The Influence of Hydroxyapatite Nanoparticles on Human Mesenchymal Stromal Cells: Application in Tissue Engineered Constructs

Simon William Partridge

A thesis submitted in partial fulfilment of the requirements for the degree of Doctor of Philosophy

Arthritis Research UK – Tissue Engineering Centre

Institute of Cellular Medicine – Faculty of Medical Sciences

Newcastle University

June 2016

Abstract

The Influence of Hydroxyapatite Nanoparticles on Human Mesenchymal Stromal Cells: Application for Tissue Engineered Constructs

Simon William Partridge

Arthritis Research UK – Tissue Engineering Centre, Institute of Cellular Medicine, Faculty of Medical Sciences, Newcastle University

Osteoarthritis (OA) is a debilitating disease characterised by degradation of the articular cartilage and changes in the subchondral bone. Presently the gold standard treatment for OA is total joint replacement using metal, ceramic and non-degradable polymer materials. Tissue engineering using novel bioresorbable biomaterials has the potential to stimulate regeneration of bone and cartilage for early stage intervention in OA suffers. This thesis investigates the synthesis of hydroxyapatite nanoparticles (HAp) and techniques to generate poly (lactic acid) (PLA) HAp nanocomposites. The effect of the synthesised HAp on isolated OA donor derived human mesenchymal stem cells (hMSC) was investigated in both 2D and 3D culture conditions. A highly controllable sol-gel synthesis method demonstrated control over HAp morphology and composition, with modification of titration rate, addition methodology and reaction pH. Two novel nanocomposite fabrication techniques were developed and characterised with transmission electron microscopy (TEM) demonstrating HAp dispersion at the nanoscale throughout PLA. Dip-coated HAp PLA and fibrin substrates were fabricated and demonstrated maintenance of hMSC adherence, proliferation and osteogenesis on 2D substrates. Investigations into fibrin encapsulated hMSC illustrated HAp uptake within the cell following 24 hours incubation. Further studies examining fibrin/HAp encapsulated hMSC showed increased osteogenic gene expression, peripheral matrix deposition and mineralisation following 21 days in culture. 3D printed PLA constructs infused with fibrin and fibrin/HAp encapsulated hMSC demonstrated significant osteogenic gene expression differences at day 21. However, these data were variable between cell isolations from different patients further illustrating hMSC heterogeneity and hMSC donor–donor variability *in-vitro*.

Acknowledgements

I would like to thank my supervisors, Kenny for your good humour, pragmatism and guidance and Mark, for your understanding, optimism and expertise. To Prof. McCaskie for helping me keep in mind the clinical side of the research and of course your excellent guitar playing. I will ensure I keep “rocking the umbrella” regardless of the weather. A huge thanks to Deepak, for his humour and help at the start of the PhD and to Kathleen, for her help with the cell work.

I want to specifically thank Matt B, for helping me wade through all the ‘good’ associated with a PhD. To Kenny’s ever growing group Steve, Marina, Elena, Natacha, Silvia and Ricardo, most of you are next! Matt German, for your wit, knowledge and guidance throughout my PhD. Chaozong thanks for your inspiration, humility and the green tea!

To the MRG, to all the PhD’s, post-docs and PI’s (past and present) that have helped me with so much in the labs, thank you. Thank you Tracy and Kath for all your help with all things SEM/TEM. Marta Pujol and Daniel Coleman for helping and letting me use their groups ZetaSizer. David Dunbar for ICP expertise, and Maggie White for her help with all of the XRD. Thank you to the anonymous hip donors particularly the ones I managed to isolate cells from!

To my family for thanks for listening to me talk for hours and not fall asleep. To my Mum and Dad for your continued emotional and fiscal support! To Jessie and Maisie for calming me down! To my brother Dave, Sarah and Nina for keeping me sane. A special thank you to Ria, for every step we took together and for every morning coffee!

I would also like to thank the donors of ARUK for funding my PhD and giving me the opportunity to help others through research. I have had a great experience at Newcastle University and the staff have helped make the PhD process less painful!

Table of Contents

Table of Figures, Tables and Equations

Table of Figures

Table of Tables

Table of Equations

Abbreviations

Abbreviation	Denotation
ALP	Alkaline phosphatase
DLS	Dynamic light scattering
DMA	Dynamic materials analysis
FFF	Fused filament fabrication
FTIR	Fourier transformed infrared spectroscopy
MSC	Human mesenchymal stem cell
MTT	3-(4, 5-dimethylthiazol-2-yl)-2, 5-diphenyltetrazolium
OA	Osteoarthritis
PCR	Polymer chain replication
SEM	Scanning electron microscope
TEM	Transmission electron microscope
TGA	Thermogravimetric analysis
XRD	X-Ray diffraction
BMP	Bone morphogenic protein
HAp	Hydroxyapatite
CTAB	Cetyltrimethylammonium bromide
PLA	Poly (lactic) acid
DMF	Dimethylformamide
FACS	Fluorescence-Activated Cell Sorting

Chapter 1 – Introduction

The ageing population coupled with the lifespan of existing prosthetic treatments for OA, contribute to the need for early stage interventions in the treatment of OA. To many, the total repair of tissues without the use of biomaterial scaffolding is the holy grail of regenerative medicine. However, tissue engineering exploits biomaterial properties and their potential to contribute to cellular repair mechanisms, which is a tangible approach already providing treatment to a number of disease conditions.

OA disease progression is not only characterised by loss of cartilage, but also presents alterations in the underlying subchondral bone. This thesis presents data that aimed to investigate the synthesis and characterisation of materials suitable to be reorganised by endogenous repair mechanisms and to regenerate bone tissue in a number of biomedical applications. To assess the biological influence of these materials, discrete cell populations from donors diagnosed with OA were used *in-vitro* to characterise biological behaviour.

Hydroxyapatite nanoparticles (HAp) is the main form of calcium phosphate mineral providing strength to collagen type I within our bones. Artificial hydroxyapatite has a number of biomedical applications, most notably for the enhancement of implant integration within bone tissues. Artificial HAp properties are known to have a greater effect on bone cell biology than traditional sintered/large grain sized hydroxyapatite. Consequently, there is renewed interest in HAp research for bone tissue engineering.

Alone hydroxyapatite is very brittle but bone is a natural nanocomposite material with multiple orders of HAp/collagen type 1 organisation. Techniques to distribute HAp within a matrix, l*et al*one self-assemble multifaceted 3D architecture are in their infancy. Bioresorbable polymers potentially present a flexible material for an artificial resorbable hard yet flexible nanocomposite.

Cellular therapies are already demonstrating efficacy in the clinic for the treatment of a number of disease conditions, nevertheless there is apprehension over the stability of cell locality following surgery. Fibrin is a naturally occurring protein responsible for haemostasis during injury and is currently used as glue in surgical procedures. Fibrin is also present during bone fracture healing, making it an ideal candidate for cell delivery into hard prefabricated scaffold materials.

Currently, the procedures for the *in-vitro* assessment of biomaterials for use in bone tissue engineering are highly variable. An often adopted approach is to assess biomaterial interaction with isolated adult human multipotent mesenchymal stromal cells (hMSC). The approach presented in this thesis focuses on the development/characterisation of biomaterials and their subsequent influence on hMSC adhesion, proliferation and osteogenic potential.

This thesis is organised as follows:

Chapter 2 aims to cover musculoskeletal biology and how tissue engineering is being used for the early treatment of OA with a significant focus on the application of hydroxyapatite nanoparticles (HAp) and bioresorbable polymers for bone regeneration.

Chapter 3 outlines standardised materials and methods used throughout the results chapters 4 – 7.

Chapter 4 presents the investigation of HAp synthesis parameters and cytotoxicity assays using patient derived hMSC.

Chapter 5 demonstrates two novel nanocomposite fabrication methods of PLA with monodispersed HAp. The influence of PLA and HAp materials on hMSC adherence, growth and differentiation are assessed.

Chapter 6 assesses the influence of fibrin and HAp materials on hMSC adherence growth and differentiation.

Chapter 7 presents the development of a cell delivery fibrin “formulation” and the 3D influence of HAp on cells encapsulated within a fibrin matrix. Finally, the influence of fibrin/HAp encapsulated cells within a 3D printed PLA construct were investigated.

Chapter 8 presents an overall discussion of the results displayed in the thesis, and their interpretation within the context of the wider field of tissue engineering and the treatment of OA.

1.1 Aims and objectives

- The first aim is to synthesise and characterise HAp identifying key parameters that influence HAp crystal morphologies and compositions.
- To assess the direct cytotoxicity of synthesised HAp *in-vitro* on OA patient derived human mesenchymal stem cell (hMSC) populations.
- To investigate the influence of HAp filled within a PLA matrix and to develop techniques to improve HAp particle distribution.
- To assess the potential influence of HAp on patient derived hMSC osteogenesis in the context of 2D PLA and fibrin substrates.
- Investigate the interaction of patient derived hMSC with HAp at the nanoscale within a 3D fibrin matrix.
- To investigate the potential for fibrin hydrogels filled with and without HAp as a carrier for hMSC delivery into prefabricated 3D printed PLA scaffolds.

Chapter 2 – Literature survey

2.1 Osteoarthritis

Osteoarthritis (OA) is a highly prevalent chronic disease of the articulating joint affecting more than 8 million people in the UK alone. With age being a significant risk factor for OA and the average population life span increasing there is a growing burden of disease. Loss or restriction in mobility can both drastically reduce the quality of life and increase the risk of secondary disease conditions. Consequently, there is a significant need for early stage intervention in OA treatment. Currently the treatment of OA is moderate exercise, dietary supplementation, topical/oral anti-inflammatories pain relief and finally referral to a joint replacement surgeon if symptoms impact greatly on the patients' quality of life (NICE 2008). Factors associated with increased risk of OA are summarised below (Fauci, 2008).

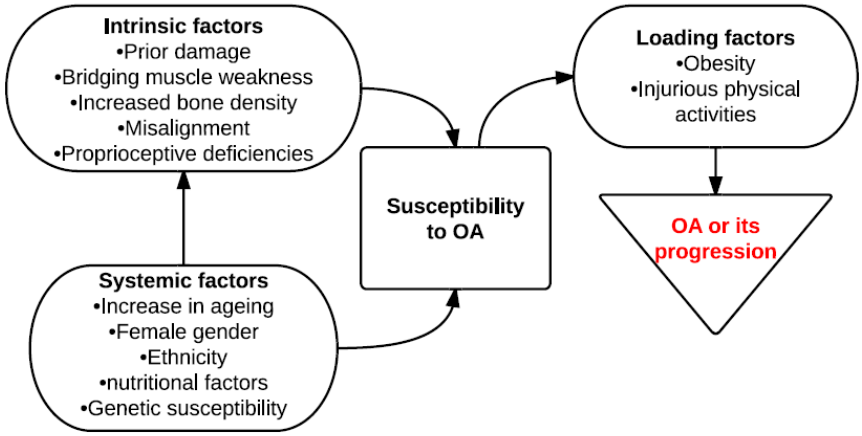

Figure 2-1: Risk factors that increase the joint to susceptibility of OA (systemic and intrinsic factors) or that increase the risk through increased join load. Modified from Fauci (2008) page 2160 figure 326-4.

Cartilage, the tough durable tissue that provides the smooth articulating surface in joints is known to thin with age. This is partly due to the failure of adequate synthesis of matrix in response to loading. Reduction in matrix leads to increased shear stress of the basal layers and perpetuates cartilage damage (Goldring and Goldring, 2010). It has long been known that cartilage has a limited ability to repair itself when damaged (Hunter, 1742, Buckwalter and Lohmander, 1994).

There are a variety of theories surrounding OA pathogenesis. It is assumed that damage to the cartilage induces the chemotaxis of local chondrocytes, these chondrocytes are impounded in

their own matrix and are unable to migrate to injury sites. The chondrocytes secrete metalloproteases to degrade the cartilage and migrate to the site of injury which further exacerbates OA pathogenesis (Goldring and Goldring, 2010). It is also hypothesised that irregularities in the subchondral bone interface is a potential cause for cartilaginous lesions and have been found in many patients with OA (Grynpas *et al.*, 1991).

Metals are traditionally used for joint replacement surgery and are usually successful however, studies show that patients undergo foreign body responses (fibrosis) and in some cases hypersensitivity to metallic implants (Steinemann, 1996, Deutman *et al.*, 1977). Mechanical mismatch of materials can be induced by the prosthesis, and cause stress shielding of natural bone, this in turn leads to bone degradation with inevitable implant failure (Lewis *et al.*, 1984).

Considerable efforts have been made to improve integration of metals with the bone itself to avoid stress shielding. Ceramics are of significant interest in orthopaedics as they can be resorbable, allowing for osseointegration with natural bone tissue (Hench, 1989). Ceramics, unlike metals, have the ability to combine with inorganic phosphates to help promote further deposition of calcium phosphate minerals when implanted in body fluids. For example; Bioglass®, glass- ceramic Ceravital®, sintered hydroxyapatite, glass- ceramic apatite-wollastonite and glass-ceramic Bioverit®. Efforts have been made to coat metal prosthesis with porous ceramics to improve osseointegration with host tissues and currently there are a number of ceramic coated metallic implants on the market (Kamitakahara *et al.*, 2007).

2.2 Articular Cartilage

The human musculoskeletal system refers to the organ systems that govern structural support, stability and movement of the body. The system comprises a variety of tissues including bone, cartilage, muscle, tendons, and ligaments, synovial and non-synovial joint systems which are still not fully understood. The musculoskeletal system is subject to a host of mechanical forces, tension, compression, bending, shear and torsion on a day-to-day basis. Bone tissue specifically is in a constant state of remodelling, augmenting the architecture and density of material to provide support in the most energy conservative manner. The adaptive nature of the musculoskeletal tissue is most notably demonstrated by its ability to regenerate following injury. Harnessing the body's ability to repair, replace or enhance tissue function undoubtedly requires an understanding of regular physiological processes that govern these actions.

Hyaline (Greek: glassy) articular cartilage has no neural, vascular or lymphatic system and is a connective tissue which covers the articulating surfaces of freely movable joints (Poole, 1997). Chondrocytes maintain the cartilage which is composed of a fibrillar matrix of proteoglycans (~30% dry w/w), collagens (50-90% dry w/w), non-collagenous proteins (NCP) and water (~70% wet w/w) (Bollet and Nance, 1966, Maroudas *et al.*, 1980, Heinegard and Oldberg, 1989).

Proteoglycans are protein chains with glycosaminoglycan's (chondroitin and keratan sulphates) attached in an array, forming a 'bottlebrush-like' structure (figure 2-2). These proteoglycan units can aggregate to form a macromolecule with a molecular weight of up to 200,000 kDa (Mow and Lai, 1980). The proteoglycan concentration is relatively low at the articulating surface and increases closer to the subchondral bone, which correlates inversely with water content (Mow *et al.*, 1984).

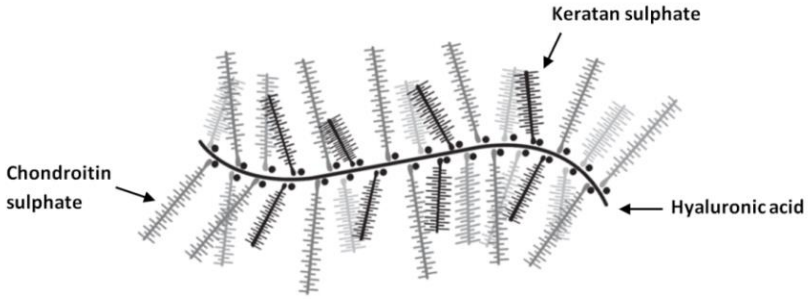

Figure 2-2: A hyaluronic acid backbone with proteoglycan aggregates. Negatively charged sites on the chondroitin and keratan sulphate chains cause this aggregation to expand and occupy a large space aqueous solution. Image modified from (McCormack and Mansour, 1997).

Collagen type II is the most predominant collagen in cartilage with other types present in smaller amounts. The collagen fibre architecture varies through the depth of the tissue however it is known to consist of type II collagen with type XI within the fibril and type IX integrated in the fibril surface making a complex heterofibril as demonstrated in figure 2-3 (Eyre, 2002, Goldring and Goldring, 2010).

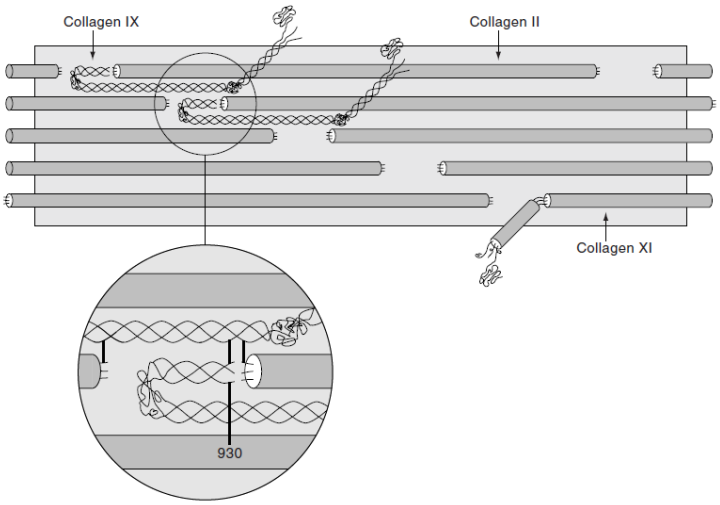

Figure 2-3: A molecular model of collagen type II demonstrating interaction sites and known cross-linking sites between collagen II and IX molecules (Eyre, 2002).

The morphology of articular cartilage is often described as having four zones between the articular surface and the subchondral bone. The structure of articular cartilage can be described using a 'split line' method (figure 2-4). The cartilage collagen is organised into broad layers arranged perpendicular to the split line axis. (Jeffery *et al.*, 1991). The zone nearest the subchondral bone contains calcified and non-calcified collagen radially orientated and

arranged in tightly packed cross-linked bundles. The radial zone contains collagen maintaining a tightly packed radial arrangement, which becomes less distinct towards the intermediate zone with fibre networks encapsulating chondrocytes. In the superficial zone the fibres are thinner and the collagen structure is organised into several layers. The cells in this layer produce superficial zone protein (SZP also known as proteoglycan-4 or lubricin) that acts as a lubricant for joint mobility (Khalafi *et al.*, 2007, Jeffery *et al.*, 1991). Chondrocyte morphology and surrounding ECM composition varies throughout the distinct zones (Goldring and Goldring, 2010).

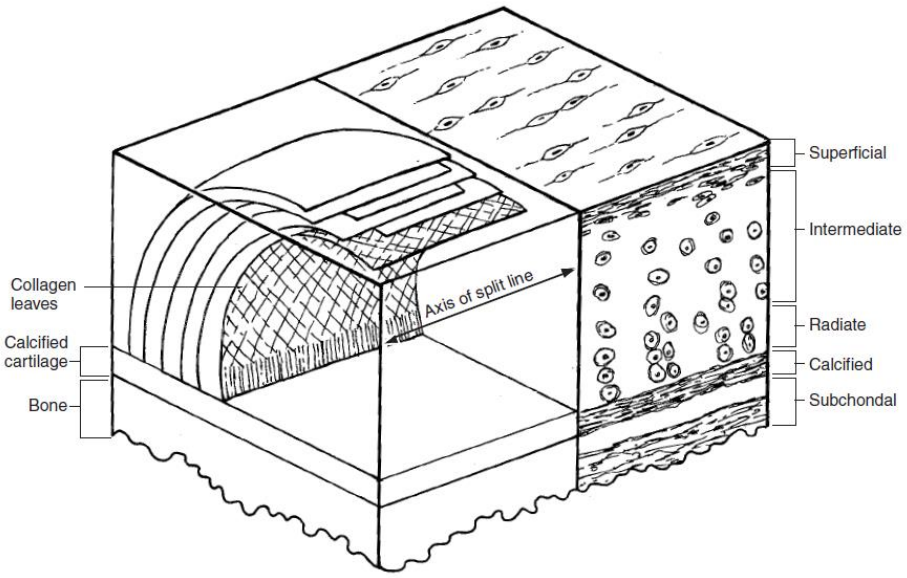

Figure 2-4: A split line axis orientated cross-section of articular cartilage. The left half of the image represents the organisation of collagen leaves with respect to the split line axis. The right image represents the characteristic histological zones of cartilage: superficial, radiate and calcified (McCormack and Mansour, 1997).

This complex architecture of connective tissue provides a low friction-bearing surface capable of absorbing and transmitting compressive, tensile and shear forces across the joint. Cartilage has been characterised as a biphasic material as it holds two properties when mechanically challenged. As loading of cartilage occurs there is a rapid displacement of water. This is a direct influence of matrix water permeability. Upon displacement, equilibrium of fluid flow is reached and the modulus of the matrix aggregate is then challenged. The aggregate modulus of cartilage is in the range of 0.45-0.59 MPa however taking into account the biphasic nature of cartilage, this value is closer to 0.45-0.8 MPa (Athanasiou *et al.*, 1991, McCormack and Mansour, 1997).

2.3 Bone Biology

2.3.1 *Bone Structure and Composition*

Bone has a vital role in vertebrate physiology. Not only forming the structural endoskeleton, it houses a stable microenvironment for haematopoiesis (blood production) and homeostasis of essential minerals. Bone itself is a highly vascularised connective tissue which can be organised into several layers of structural hierarchy (figure 2-5) (Weiner and Wagner, 1998).

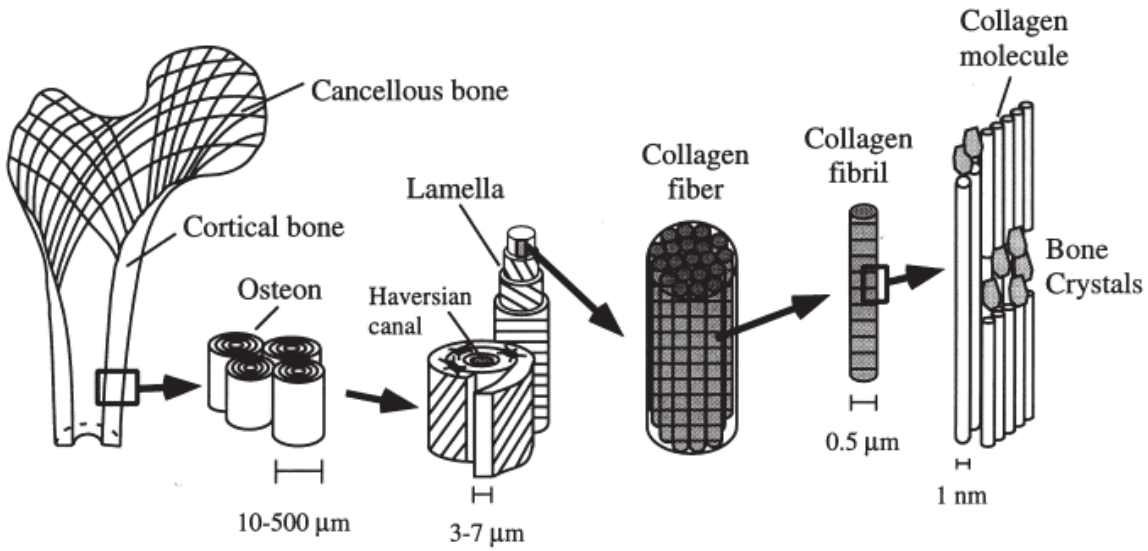

Figure 2-5: Hierarchical structure of bone (Weiner and Wagner, 1998).

The outer layer of cortical bone in very dense, whereas the internal structure has a spongy appearance and is called cancellous bone. Vertebrate bone is, in essence, a composite composed of 70% calcium phosphate bone mineral. The main form of which is hydroxyapatite, 27% collagen type I protein and 3% other non-collagenous proteins (Weiner and Wagner, 1998). Collagen type I is an extracellular protein consisting of three tropocollagen polypeptides coiled to form a triple helical structure approximately 300nm long. This protein self assembles into fibrils in the presence of phosphates and sodium chloride. These fibrils combine into bundles called fibres which present characteristic D pattern banding (figure 2-6) (Kadler *et al.*, 1996).

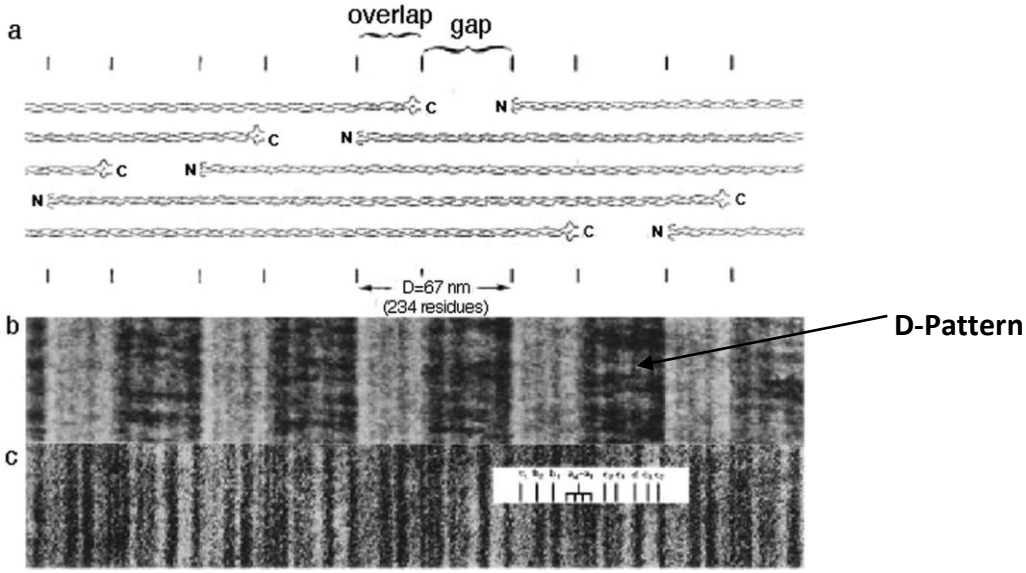

Figure 2-6: a) Schematic of a collagen type I fibril. b & c) TEM image of collagen from positive and negative stain methodologies respectively (Kadler et al., 1996).

The electron dense D-band pattern shown in the transmission electron micrograph is overlapping collagen presenting as a denser section (figure 2-6). The hierarchical design of bone organisation from the nano-macro scale makes it a marvel of nature. The intercalation of HAp within the collagen type 1 fibrils and orientation at the nanoscale makes bone an extremely complex nanocomposite material.

2.3.2 *Cell adherence*

Cells are surrounded by fat-based phospholipid membrane studded with proteins. These proteins are responsible for the sensitivity of the cell to the surround environment. Transporter proteins act as valves to regulate the movement of substances in and out of the cell. Membrane receptor proteins sense and communicate signals from neighbouring cells and the environment. Cell adhesion molecules (CAMs) are responsible for anchoring the cell to neighbouring cells or the ECM.

Integrins are transmembrane proteins responsible for cells-ECM interaction. Cells cultured *in-vitro* use integrins to adhere to ECM proteins from the culture media adsorbed to the growth substrate. Integrins bind to proteins containing a specific peptide sequence arginylglycylaspartic acid (RGD). Ergo the ability of cells to adhere to materials depends on the adsorption of proteins containing this sequence (Burridge & Chrzanowska-Wodnicka 1996; Gumbiner 1996).

2.3.3 *Biomineralisation*

Biomineralisation of HAp *in-vivo* has been described to occur in a matrix vesicle; formed and released from osteoblasts and other related cells. Nucleation of calcium and phosphate precursors is thought to occur within the vesicle. As the crystal grows it ruptures the membrane and is exposed to the extracellular environment. This theory describes two phases of HAp synthesis control: cellular and extracellular matrix (ECM) (Anderson, 1995). These crystals intercalate and align with tropocollagen protein gap domains within collagen type 1 matrix (Palmer *et al.* 2009). There is evidence that other matrix non-collagenous proteins orchestrate nucleation and control growth of HAp crystals (Boskey, 1996).

2.3.4 *Specialised bone cells*

Bone is maintained by two main cell types: osteoblasts (osteocytes when fully matured) and osteoclasts, these cells act antagonistically locally generating and resorbing bone respectively. This is tightly regulated by a mechanism of hormones, growth factors, physical stimuli, and ionic concentrations. This, in turn, maintains structural integrity of the skeleton and mineral ion concentration of the body (Weiner and Wagner, 1998).

Osteoclasts are large multinucleated cells derived from hematopoietic stem cells (HSCs) found in the bone marrow and are critical in the regulation of bone formation. During bone remodelling osteoclasts form resorption pits in trabecular bone. In cortical bone osteoclasts cluster and burrow through old or damaged bone forming a tunnel. This tunnel is vascularised and lined with recruited osteoblasts which concentrically deposit new bone forming new osteons (Alberts *et al.* 2008).

Osteoblasts are anchorage dependent cells; highly responsive to mechanical and chemical stimulation relayed through cell-cell and cell-ECM interactions. Specific receptors and trans-membrane proteins such as integrin's, cadherin's and connexins mediate these stimuli leading to production of ECM and biomineralisation (Pirraco *et al.* 2010). Some osteoblasts become entrapped within the mineralised matrix and fully differentiate into osteocytes. Osteocytes are smaller than osteoblasts and maintain communication with surrounding osteoblasts through specialised filopodia, which also ensure mass transport with the extracellular fluid. The filopodia form a network of canaliculi between the dense bone regions. This is believed to be responsible for mechanical stimuli transduction and bone homeostasis (Pirraco *et al.* 2010).

The osteoblastic lineage is derived from multipotent mesenchymal stromal cells or mesenchymal stromal cells (hMSC). hMSC have the capacity to form an assortment cell types in tissue culture (figure 2-7). hMSC not only contribute to tissue formation, they play a vital role in HSC self-renewal and proliferation (Kemp *et al.* 2010).

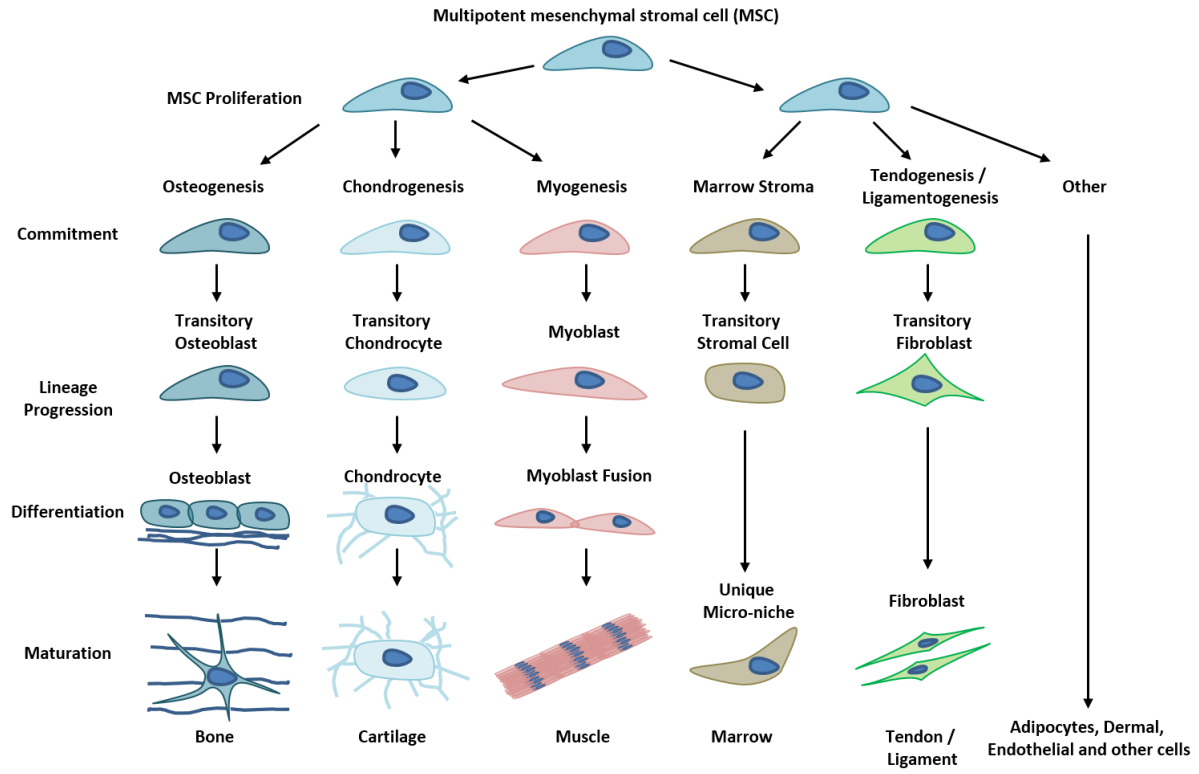

Figure 2-7: Illustration of the multipotent potential of hMSC with different lineage progression pathways. Modified from (Alberts et al. 2008).

Conventionally hMSC are characterised by their ability to adhere to tissue culture plastic from bone marrow aspirates. Significant efforts have been made to isolate hMSC with a reproducible capacity for differentiation into the various tissue lineages. However, currently there is no specific marker or characteristic that defines differentiation capacity. In an attempt to standardise hMSC for clinical applications, panels of positive and negative surface markers have been developed to reduce variability (Dominici *et al.* 2006).

It is widely accepted that the functionality of hMSC depends on an assortment of subpopulation progenitors partially committed to one or two lineages. There is a lack of clarity with regards to the specific functionality of these hMSC subpopulations. This is exacerbated by donor-to-donor variation and intra-population heterogeneity (Phinney 2012).

The proliferative and multipotent capacity of hMSC populations is also known to decline though *in-vitro* expansion (Muraglia *et al.* 2000; Sarugaser *et al.* 2009). Monolayer cultivation of hMSC on tissue culture plastic is known to favour both fibroblastic and osteoblastic differentiation (Engler *et al*. 2006).

Recently it has been demonstrated that specific differences in cytoskeletal structure are dependent on the substrate elasticity (Gupta *et al*. 2015). Findings by Gupta *et al.* (2015) reveals that the actin cytoskeleton acts as a rigidity sensor and behaves like a fluid-like material on soft substrates and as a solid-like material on stiffer ones, of which is morphologically evident in the cells actin filaments (figure 2-8A).

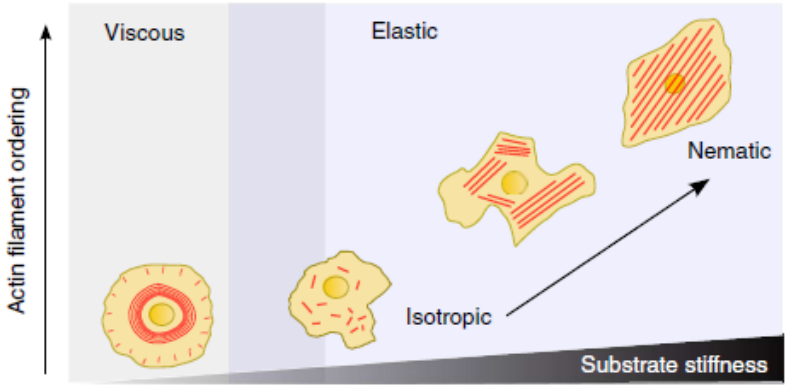

Figure 2-8: The influence of substrate stiffness on actin filament ordering (Gupta et al. 2015).

Stem cells have been found to differentiate into various lineage commitments based on the associated stiffness of the anatomical tissue (figure 2-9A). The observed changes in the differentiation of stem cells as a response to substrate stiffness is no doubt linked to these reported changes in focal adhesion and cytoskeletal structure (Engler *et al.* 2006) (figure 2-9B).

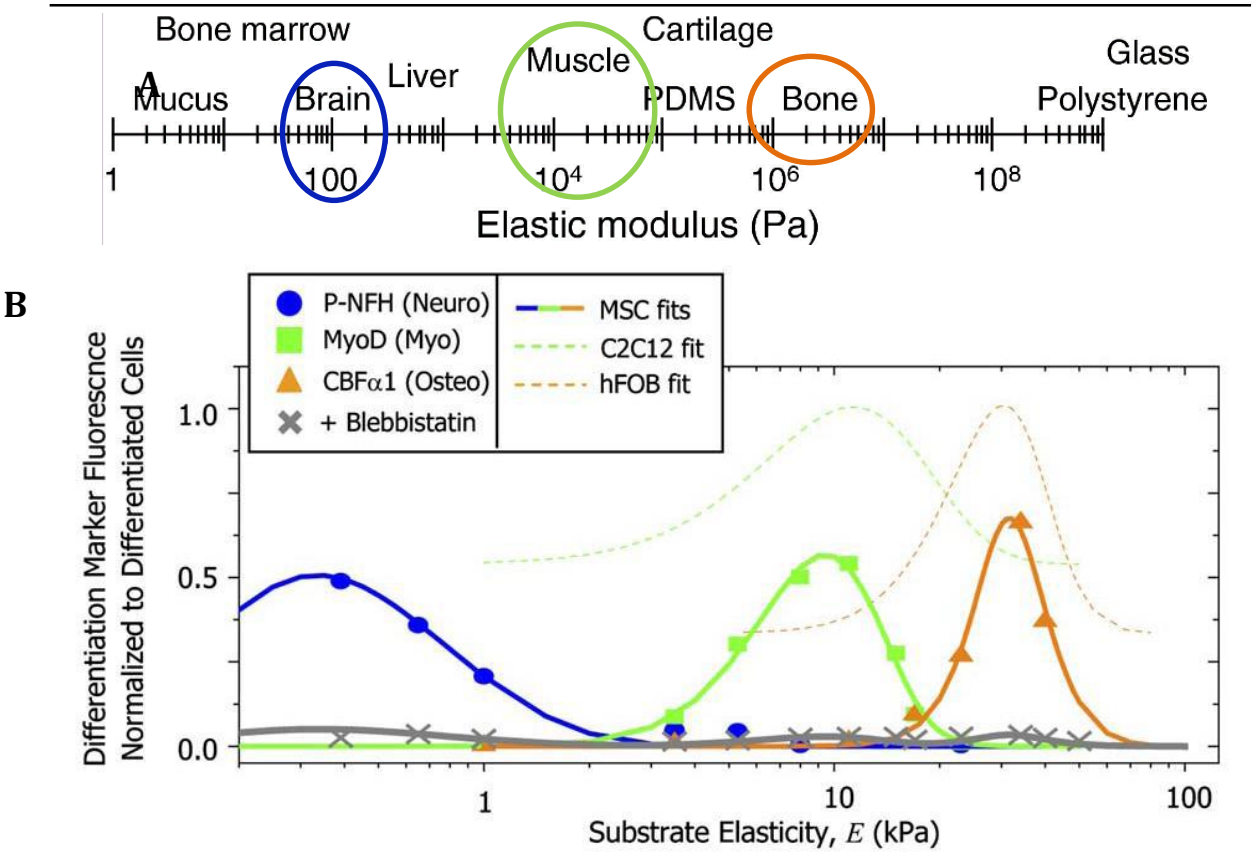

Figure 2-9: A) Scale of biological elastic modulus modified with coloured circles to show changes in hMSC gene expression on different substrate elasticities (B) (Janmey & Miller 2011). B) Changes in hMSC marker expression of neurogenic (brain), myogenic (muscle) and osteogenic (bone) lineages when cultured on substrates with various elasticities. Blebbistatin is a control which inhibits myosin II synthesis, which is hypothesised to render the cells insensitive to elasticity. C2C12 fit and hFOB dotted lines represent differentiated myogenic and osteogenic cell types (Engler et al. 2006).

The objective of this thesis was to use hMSC to provide an insight into endogenous cell responses to biomaterials for bone tissue engineering. The reparative and destructive processes associated with OA have been linked to functional alteration in hMSC populations (Luyten 2004). Ergo, the approach was to use hMSC located from the cancellous cavity of the femoral head donated from patients undergoing total hip replacement surgery as a consequence of OA progression. These cells hypothetically offer a more representative population for the *in-vitro* assessment for biomaterials aimed at the treatment of osteochondral defects in OA suffers.

2.3.5 *Mechanisms of Bone Formation and Repair*

There are two major types of bone formation: intramembranous ossification and endochondral ossification.

Endochondral ossification is observed during bone development and can be divided into five distinct stages (figure 2-10). Firstly, hMSC migrate to the bone region and commit to becoming cartilage cells (A). Secondly, the cartilage cells form dense nodules and differentiate into chondrocytes. In the third phase the chondrocytes proliferate and secrete cartilage specific ECM in the shape of the bone (B). During the fourth phase chondrocytes become hypertrophic, which alter the ECM to include collagen X and adding more fibronectin. These alterations result in mineralisation and vascularisation that converts hMSC into blood vessels (C-D). The hypertrophic chondrocytes undergo a metabolic change from aerobic to anaerobic respiration; they then die through apoptosis. The fifth and final stage is the progressive vascularisation of dying hypertrophic chondrocytes and differentiation of surrounding cells into osteoblasts to mineralise the bone collar (E-H) (Gilbert 2010).

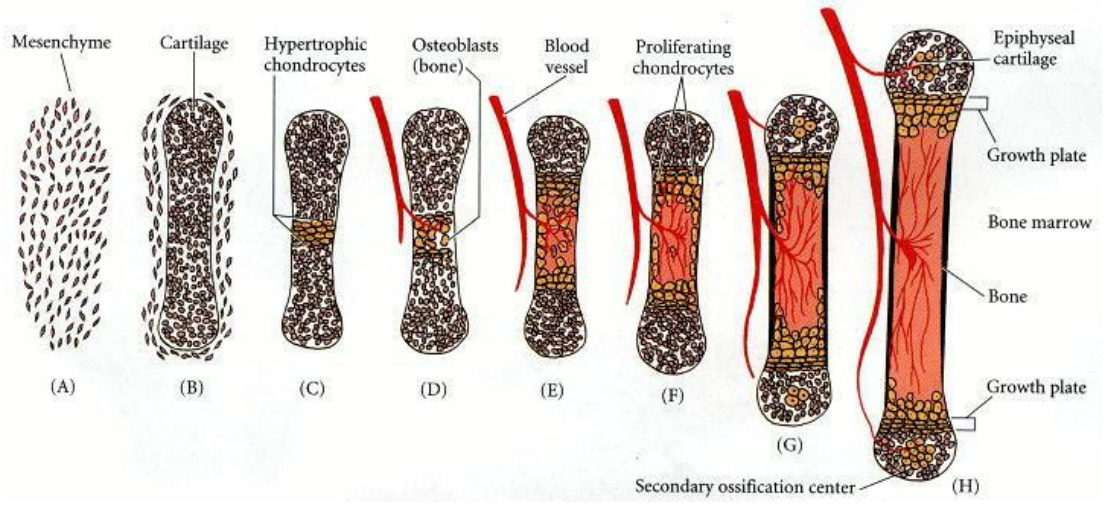

Figure 2-10: Schematic diagram of endochondral ossification. (Gilbert 2000)

There are three main types of intramembranous ossification. Formation as a result of mechanical stimulation is called sesamoid bone, bone thickening is termed periosteal bone, and bone formed in the dermis of the skin is called dermal bone. hMSC first proliferate and condense to form nodules which, through growth factor stimulation, become pre-osteoblasts and begin to deposit and mineralise ECM.

Bone healing is a complex process involving the migration, proliferation, differentiation and activation of several cell types (Street *et al.* 2002). Bone healing occurs in two stages: firstly, the early inflammatory stage, the repair stage and finally the late remodelling stage. During the first few hours a fibrin hematoma develops containing inflammatory cells and fibroblasts. Furthermore, this encourages vascularisation and migration of hMSC. Fracture healing comprises a mixture of both endochondral and intramembranous ossification (figure 2-11) (Bahney *et al.* 2015a). Restoration of mechanical integrity occurs during the remodelling stage, which happens slowly over months to years, and is dependent on mechanical stress (Kalfas 2001).

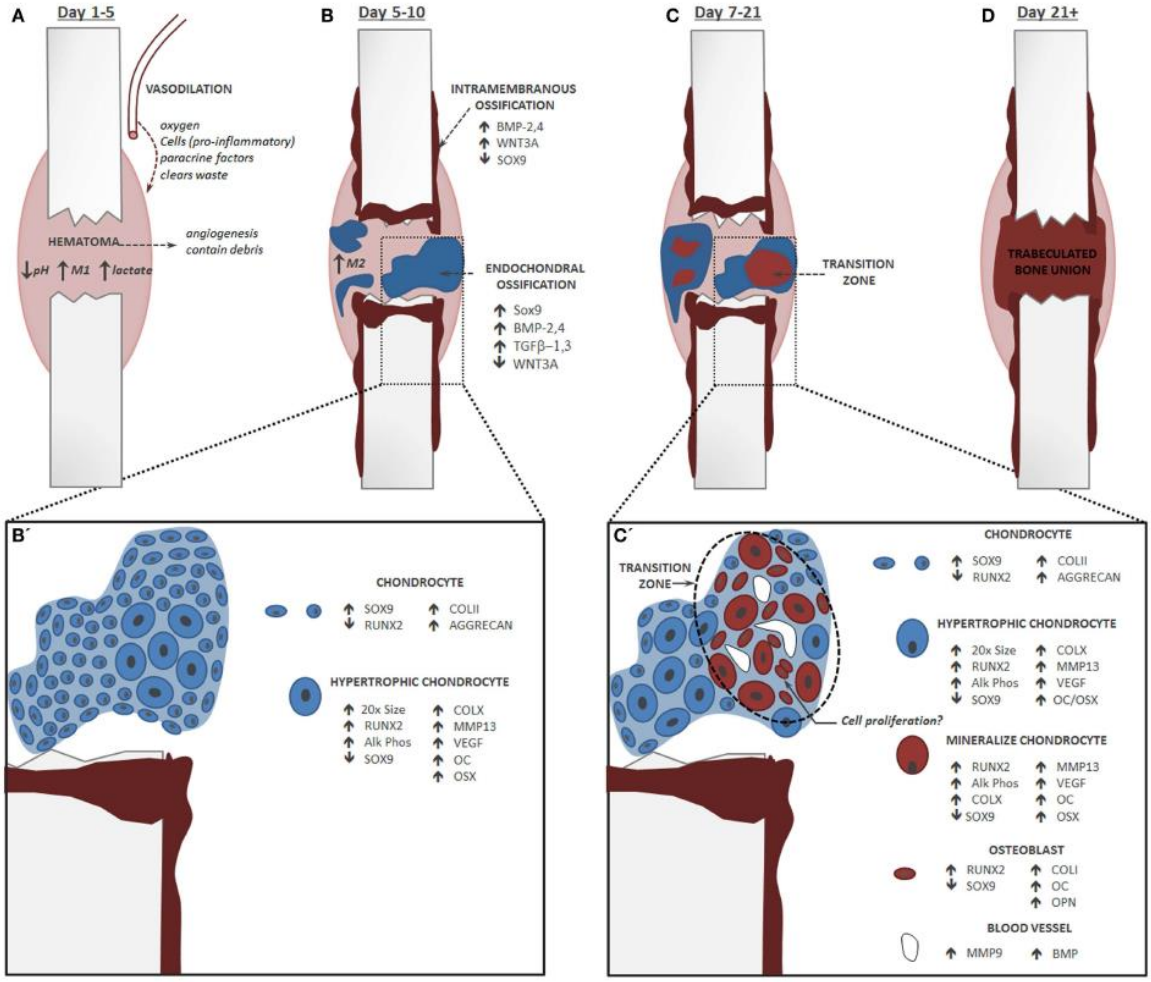

Figure 2-11: Fracture healing illustration. A) Haematoma formation, B) intramembranous ossification occurs at the periosteum and endosteum of the fracture site. Within the callus cartilage cells condense and proliferate. C) Vascularisation, mineralisation of ECM, apoptosis of hypertrophic chondrocytes and proliferation of osteoblasts. D) Conversion of cartilage into bone, bridging the fracture site (Bahney et al. 2015b).

2.3.6 *Regulation of osteoblastic differentiation by growth factors*

Growth factors are proteins secreted by cells that act as molecular signalling agents for cells. Growth factors are essential for the control of assorted functions including: proliferation, ECM production and differentiation. These proteins have three modes of action: (1) autocrine; whereby the factor effects the same cells which produce it, (2) paracrine; in which the factors influence cells in close proximity, and (3) endocrine; where the growth factor influences cells from a different anatomical site. Growth factors can influence a diverse number of cell types and can orchestrate a number of cellular functions in a range of different tissues.

Bone morphogenetic proteins (BMP) refers to a group of growth factors responsible for the morphological formation of bone and cartilage. Runx2 (also known as CBFA1) is a master regulator of bone formation activated by BMPs and its expression is essential for the expression of many downstream genes important for osteoblast differentiation (Ducy *et al.* 1997). There are two isoforms of Runx2 involved in osteogenesis type1 (T1) and type 2 (T2). T1 Runx2 is expressed during early differentiation of osteoblasts and promotes expression of BMP2. Subsequently, this upregulates transcription of T2 Runx2 to stimulate osteoblast differentiation and maturation. Previous studies have found that although T1 Runx2 is continually expressed in many cells it is rarely enhanced during osteogenesis and bone formation (Xiao *et al.* 1998). T2 Runx2 expression is believed to play a more crucial role in osteoblastic differentiation (Yang *et al.* 2011).

During intramembranous ossification hMSC are exposed to relatively low level BMP, which promotes osteogenesis through expression of Runx2 and collagen II and IX. At later stages Runx2 is downregulated and OPN is upregulated, similar to developing chondrocytes, and are sometimes termed chondrocyte-like osteoblasts. Autocrine secretion of Indian hedgehog protein further matures the osteoblasts (Gilbert 2010).

At the start of endochondral ossification stimulation of nearby sclerotome cells by Sonic hedgehog protein results in the commitment of hMSC into cartilage cells. During condensation of cartilage cells, BMP (in orchestration with other growth factors) appears vital for inducing the expression of N-cadherin, N-CAM and Sox9. N-cadherin and C-CAM are responsible for initiation and maintenance of the condensation. Sox9 is responsible for the production of cartilage ECM (collagen II and aggrecan) and proliferation of cartilage cells. Runx2 mediates transformation of cartilage cells into hypertrophic cartilage cells. These hypertrophic cartilage

cells secrete vascular endothelial growth factor (VEGF), which promotes hMSC differentiation into endothelial cells and vascular taxis (Carlevaro *et al.* 2000).

2.3.7 *Osteopontin*

Osteopontin (OPN) also known as bone sialoprotein 1 or ETA -1 is a very important phosphorylated glycoprotein secreted by a number of cells; most notably osteoblasts. OPN is present where ever calcification occurs. It is important for the control of biomineralisation. Low levels of OPN have been linked to critical HAp nucleation where high levels of OPN is linked to HAp nucleation and growth inhibition (Gericke *et al.* 2005). OPN is postulated to bind to HAp through phosphorylated residues (Sodek *et al.* 2000). OPN also contains an integrin receptor binding arg-gly-asp (RGD) peptide domain; responsible for cell adhesion. OPN has transglutaminase-reactive glutamine residues that enable it to be cross-linked to form OPN polymers, which bind to HAp (Gericke *et al.* 2005).

2.3.8 *Alkaline Phosphatase*

ALP is an enzyme responsible for the liberation of phosphate from different molecules. In humans there are four isozymes: intestinal, placental, placental-like and tissue nonspecific (bone, liver and kidney). The tissue nonspecific isoform of ALP is abundantly expressed in osteoblasts and is used as a marker of osteoblastic differentiation. Actively dividing osteoblasts conserve ALP expression. However, when proliferation stops, ALP is expressed in high levels and appears necessary for the mineralisation of the ECM (Fernández-Tresguerres-Hernández-Gil *et al.* 2006).

2.4 Tissue Engineering Biomaterials

Tissue engineering refers to a field of research aimed at the repair, replacement or enhancement of defective or dysfunctional tissues.

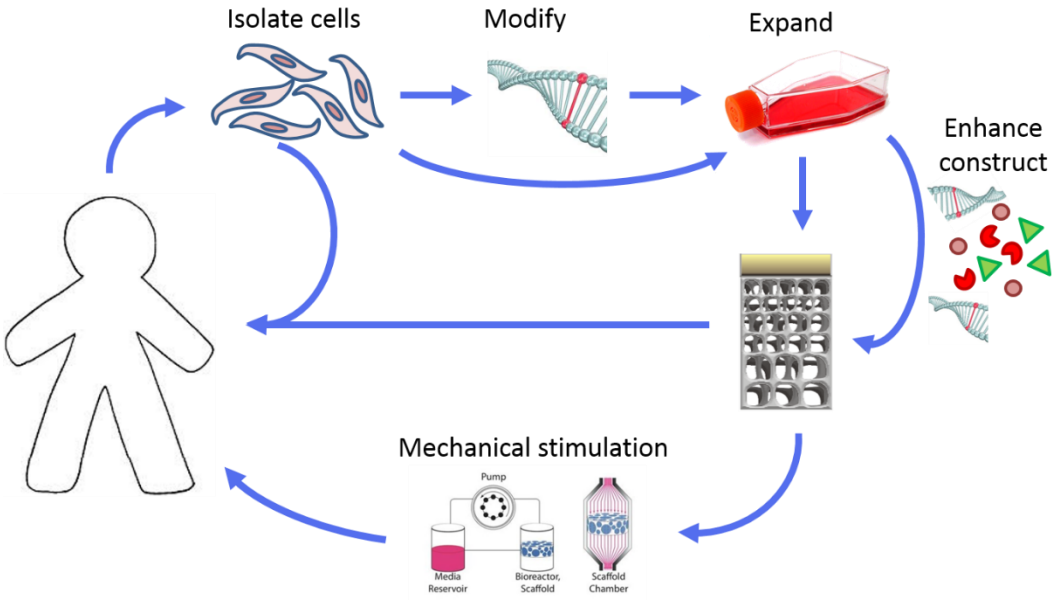

Figure 2-12: illustration of various treatment approaches used in tissue engineering.

Figure 2-12 demonstrates various treatments strategies used in tissue engineering; the simplest being direct implantation of a biomaterial scaffold or enriched host cells. More complex approaches include *ex-vivo* expansion/modification of autologous, allogenic or xenogeneic cells in combination with scaffolds. Recently strategies have been employed to improve scaffold functionality pre-implantation using biomolecules or pre-mechanical stimulation (Huang & Ogawa 2010).

The ideal biodegradable scaffold for bone regeneration would include a number of material and biological considerations. Firstly the material should have suitable mechanical properties to withstand physiological loads during the transition to the surrounding host tissue (Gerhardt & Boccaccini 2010). Secondly the degradation products of the material should be biocompatible and stimulate host bone tissue regeneration (Hannink & Arts 2011). Thirdly material surface chemistry should allow for host cell attachment, migration and bone formation (Tang *et al.* 2016). Fourthly the structure of the implant should include porosity to both encourage osteogenesis and host tissue integration (Hannink & Arts 2011).

The human body is consisted of 213 bones without including the sesamoid bones (Clarke 2008). Each bone has a variety of pore sizes depending on its function and on the individual

sex/age. Many groups have investigated different pore sizes to identify what pore range promotes specific cellular activities. It has been reported that pores <50 µm enhance hypoxic conditions promoting chondrogenesis. In addition, small pore size stimulates protein and cell adhesion as well as cellular migration and osseointegration. Pores with size <50 µm promote vascularisation and ossification (Perez & Mestres 2016). It has been reported that pore size <300 µm promote endochondral ossification (Hutmacher *et al*. 2007), pores >300 µm favour angiogenesis (Mantila Roosa *et al*. 2010) (Karageorgiou & Kaplan 2005; Mantila Roosa *et al*. 2010). pores around 500 µm enhance tissue formation (Karageorgiou & Kaplan 2005) and pores around 1000 µm stimulate the osteoblast phenotype expression (Sicchieri *et al*. 2012). However, an optimal scaffold for bone tissue engineering should be made with a combination of pore sizes to trigger different functions simultaneously.

The potential for MSCs to regenerate a variety of tissues has made them a subject of intense research in the fields of cellular therapy and regenerative medicine. The applications for MSCs in bone tissue engineering are as follows:

1. To provide an indication into the influences of biomaterial properties such as architecture and chemical properties on stem cell behaviour.

2. Autologous or allogenic co-delivery with pre-fabricated or *in-situ* fabricated biomaterial scaffold implants.

3. Conditioning of biomaterial scaffolds prior to implantation.

Specifically this thesis addresses the use of bioresorbable biomaterials to transiently replace bone and encourage endogenous reparative processes to locally regenerate host tissues (Hutmacher 2000).

2.4.1 *Hydroxyapatite*

Hydroxyapatite and other calcium phosphates such as tri-calcium phosphate (TCP) and calcium carbonate have a long history as implant materials from the 1920s to the 1930s (Shepherd *et al.* 2012). Hydroxyapatite is a naturally occurring ceramic, calcium apatite mineral $Ca_5(PO_4)_3(OH)$, however the crystal unit cell contains two hydroxyapatite units and is often depicted $Ca_{10}(PO_4)_6(OH)_2$ with a Ca/P ratio of 1.67. Natural bone hydroxyapatite has a crystalline, non-stoichiometric nanostructure (exhibits Ca/P ratio of >1.67) containing various carbonate (CO_2^{3-}) and phosphate (HPO_4^{2-}), zinc (Zn^{2+}), sodium (Na^+), magnesium (Mg^{2+}), strontium (Sr^{2+}), potassium (K^+), chloride (Cl^-) and fluoride (F^-) ions integrated with its structure (Markovic *et al.*, 2011).

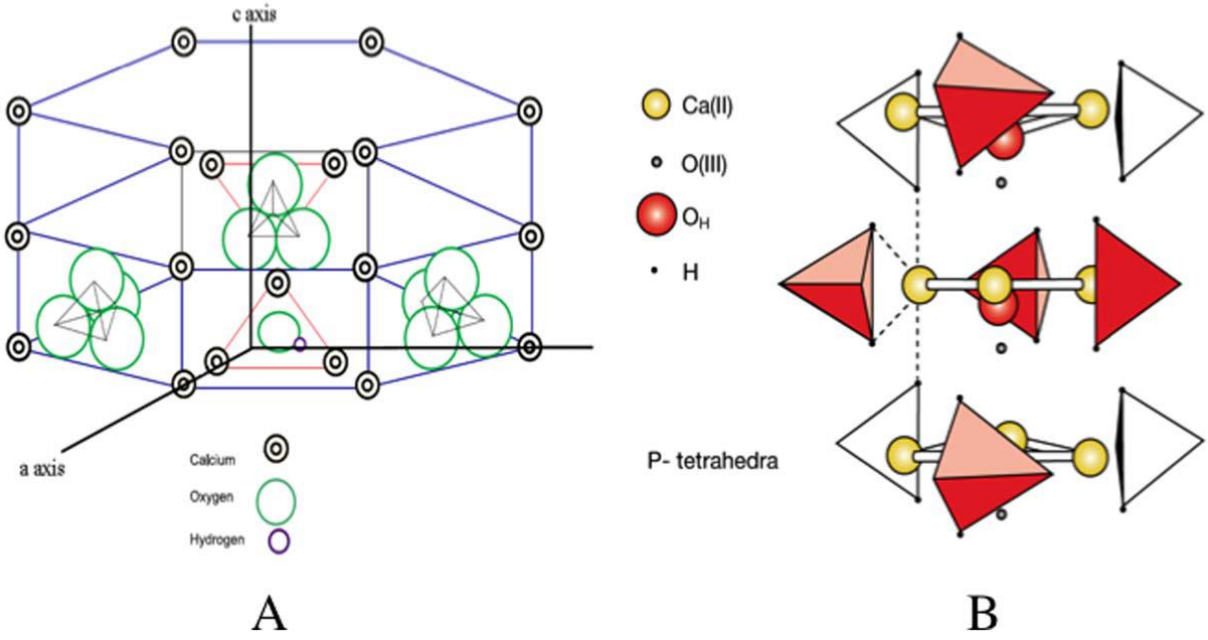

Figure 2-13: A) The theoretical arrangement of the hydroxyapatite unit cell. B) Types of calcium ion sites within the hydroxyapatite lattice. Four columnar calcium Ca(I) sites (c-axis 0 and ½) and six Ca(II) sites (z-axis ¼ and c-axis ¾). Modified from (Ratnayake et al. 2016).

X-ray diffraction studies of hydroxyapatite $Ca_{10}(PO_4)_6(OH)_2$ has shown a crystalline hexagonal arrangement of $Ca^{2+}$and PO_4^{3-} ions around columns of OH^- ions. The structure of the hydroxyapatite unit cells is a six-fold space group ($P6_3/m$) with unit cell dimensions of c = 6.884 nm and a = b = 9.421 nm. Figure 2-13 demonstrates the theoretical arrangement of the hydroxyapatite unit cell (A) and organisation of different calcium ion sites (B) (Ratnayake *et al.* 2016).

Ionic substitutions of artificially synthesised hydroxyapatite have been a subject of intensive research during the past few decades to improve material, mechanical and biological properties (Ratnayake *et al.* 2016). Significant research has been carried out specifically in zinc, magnesium, strontium, fluoride, carbonate and silicon for use in both dental and orthopaedic applications.

Zinc that can be found naturally in bone (110-300 µg/kg) is known to decrease with age and correlates with decreased bone strength (Shepherd *et al.* 2012). Zinc substituted HAp has demonstrated *in-vitro* enhanced activity of osteoblasts and inhibition of osteoclast function (Webster *et al.* 2004; Kishi & Yamaguchi 1994).

Magnesium is highly prevalent in the body and has been found in the enamel (0.44 wt. %), dentin (1.23 wt. %) and bone (0.72 wt. %) (Shepherd *et al.* 2012). Magnesium is thought to play a role in bone remodelling as it is found in high concentration at the start of remodelling and decreases with increased calcification (Bigi *et al.* 1992).

Strontium is present in the mineral phase of bone (0.008 – 0.01 wt. %) and is correlated with areas of high metabolic turnover (Blake *et al.* 1986). Strontium ranelate has been used therapeutically and combines two atoms of stable strontium with the organic moiety, ranelic acid used as a carrier for the strontium cations (Basu *et al*. 2015). Studies have demonstrated that administration of strontium ranelate increases the proliferation and activity of osteoblasts whilst decreasing osteoclast differentiation *in-vitro* (Peng *et al.* 2009; Caverzasio 2008). These findings are also supported by *in-vivo* studies, which show strontium ranelate to decrease bone resorption and increase bone formation (Buehler *et al.* 2001).

Fluorine is an important element for bone/dental growth and has successfully been used to treat patients with osteoporosis, however excessive intake could lead to osteosclerosis (abnormal hardening). Farley *et al. (*1987) demonstrated increased ALP activity and proliferation of osteoblasts in response to fluoride ions *in-vitro* (Farley *et al.* 1983). Another study showed a similar result in rat osteoblasts from rats treated with NaF ions present in the rats drinking water (Chavassieux *et al.* 1993).

Silicon is also present in active bone growth areas with a 0.5 wt. % in mice and rats. Abnormal skeletal growth was also observed when Si was deficient from the diet (Carlisle 1970). More recent studies have demonstrated increased collagen type I and enhanced osteoblastic

differentiation in human osteoblast like cells in response to physiological levels of Si (10-20 μM) in the form of orthosilicic acid (Reffitt *et al.* 2003). Bioglass and apatite-wollastonite are bioactive ceramics containing 40-34 wt. % SiO_2 which plays a crucial role in their surface reactivity and can change their *in-vitro* and *in-vitro* activity (Gibson *et al.* 1999).

Carbonate is the most abundant form of substitution in biological apatites and has been found at levels of 7.4 wt. % in bone, 5.6 wt. % in dentine and 3.5% in enamel (Bigi *et al.* 1997; Montel *et al.* 1981). Carbonated hydroxyapatite is supposedly vital for its role in bone metabolism and as such has been a significant effort in the use of carbonated apatites for orthopaedic applications (Ratnayake *et al.* 2016; Shepherd *et al.* 2012).

High temperature sintering of hydroxyapatite powders to form solid implants and plasma spraying to coat metal implants require thermal stability of the ceramic powder (Cheang & Khor 1996). Typically hydroxyapatite is sintered at temperatures ranging from 800^{o}C to 1200^{o}C (Shepherd *et al.* 2012). The sintering of hydroxyapatite has been reported to convert some calcium phosphates into tri-calcium phosphate and octa-calcium phosphate. Impurities in the case of TCP are shown to strengthen the ceramic material, although the β form of TCP is a reported biodegradable bioceramic known to dissolve in physiological media and *in-vivo* (Royer *et al.* 1993; Best *et al.* 2008).

Sintered hydroxyapatite has been used in combination with a polymeric template to produce blocks with fully interconnected pores (average diameter of 500 μm) with 77% porosity. These scaffolds were able to improve bone integration with a intramedullary titanium cylinder when implanted in a rabbit model (D'Lima *et al.* 1998).

Previous *in-vitro* work has demonstrated osteoblast adherence, proliferation and ECM secretion on hydroxyapatite surfaces (Bagambisa & Joos 1990; Best *et al.* 1997; Kim 2003). Osteoclasts have also been observed forming resorption sites with characteristic actin ring formation on the surface of hydroxyapatite implants (Redey *et al.* 1999). Although numerous studies have demonstrated resorption sites, very few have demonstrated resorption lacunae indicating limited *in-vivo* remodelling potential of solid hydroxyapatite implants (Monchau *et al.* 2002; Webster *et al.* 2001)

A number of commercially available hydroxyapatite coatings have been developed and is currently used in a variety of orthopaedic implants. A number of hip replacements utilise a

hydroxyapatite coating on metal implants to improve biological integration. One of the first is the Furlong® hip system, JRI orthopaedics. Johnson & Johnson – Depuy: Corail total hip system, Stryker: Restoration HA™ and Biomet: Porous HA coatings. Hydroxyapatite based bone substitute fillers have also been used in the clinic: Medtronic: bone cement with hydroxyapatite, Zimmer: CopiOs® bone void filler, Stryker: BoneSource® & HydroSet.

2.4.2 *Artificial Hydroxyapatite Nanoparticle (HAp) Fabrication*

A number of studies have illustrated the bioactivity of nanoscale HAp over traditional hydroxyapatite to promote osteogenesis and bone-material interfaces (Webster *et al.* 2001; Yoshida *et al.* 2000; Hench 1991; Davies 2007; Ducheyne & Qiu 1999). However, control over particle dimensions, crystallinity and composition are likely contributing factors to their success in the clinic (Cai *et al.* 2007a).

The influence of substitutions on artificial HAp with different ionic groups has significant impact on the final HAp crystal lattice parameters, morphology, crystallinity, solubility and thermal stability (table 2-1).

Substitution	Empirical formula	Substitutes	Lattice change		Solubility
			a	c	
Magnesium (MgHA) (47)	$Ca_{10-x}Mg_x(PO_4)_6(OH)_2$	Calcium	−	−	+
Silver (AgHA) (58, 61, 62)	$Ca_{10-x}Ag_x(PO_4)_6(OH)_2$	Calcium	+	+	+
Strontium (SrHA) (74–77)	$Ca_{10-x}Sr_x(PO_4)_6(OH)_2$	Calcium	+	+	+
Carbonate CHA (A-Type) (118, 119)	$Ca_{10}(PO_4)_{6-x}C_x(OH)_2$	Phosphate	+	−	+
Carbonate CHA (B-Type) (120)	$Ca_{10}(PO_4)_6(OH)_{2-x}C_x$	Hydroxyl	−	+	+
Fluoride (FHA) (43, 145, 147, 149–152)	$Ca_{10}(PO_4)_6(OH)_{2-x}F_x$	Hydroxyl	−	+	−
Silicate (SiHA) (169)	$Ca_{10}(PO_4)_{6-x}Si_x(OH)_2$	Phosphate	−	+	+

Table 2-1: Substitutions in hydroxyapatite and the effect on crystal lattice parameters and solubility (Shepherd et al. 2012).

Table 2-2 describes different synthetic routes for the production of artificial hydroxyapatite nanoparticles with different morphologies, crystallinities and stoichiometry.

Given the complexity of substituted HAp fabrication, the first step in the development of the sol-gel methodology was to investigate parameters that influence the production of non-substituted HAp. This will deepen the understanding on how different parameters influence the HAp physiochemical properties and will enable further research for better control over the fabrication of potentially more bioactive forms of HAp.

Sol-gel precipitation involves the conversion of monomers into a colloidal solution of solid particles. Sol-gel is the most widely used method involving the mixing of calcium and phosphate precursor solutions under controlled environments. Typically, the resulting calcium phosphate crystals synthesised through this methodology are later calcined at high temperature (800 ^{o}C-1200^{o}C) to produce crystalline HAp ceramic nanocrystals.

Investigation into the processing parameters using the sol-gel methodology for the fabrication of hydroxyapatite nanoparticles has not been entirely characterised. A variety of techniques for the fabrication HAp has been described in the literature (Bakan *et al.* 2013; Jadalannagari *et al.* 2011; Marković *et al.* 2011; Yubao *et al.* 1994; Wang *et al.* 2010; Iyyappan *et al.* 2016; Wang *et al.* 2007; Kumar *et al.* 2004; Ramesh *et al.* 2015; Vázquez-Hernández *et al.* 2010; Ha *et al.* 2015; Huang *et al.* 2012), where individual parameters have been studied without taking into consideration the influence and interactions of other parameters that influence the particle size, morphology and chemistry of the resulting particles. Despite the variety of techniques described in the literature, very few comment on the effects of multiple processing parameters on particle size and morphology (Salimi *et al.* 2012).

Knowledge of calcium phosphate nucleation and growth kinetics is vital not only for understanding *in-vivo* systems, but also for *in-vitro* or *ex-vivo* synthesis of biomimetic HAp nanocrystals for tissue regeneration applications. *In-vivo* biomineralisation by osteoblasts and osteocytes require sufficient supersaturation of mineral precursors and is controlled though the action of control proteins and local pH regulation. This biomineralisation results in plate-like, nanocrystalline, carbonated HAp nanoparticles (Marković *et al.* 2011).

Several sol-gel processing methodologies have been investigated using a variety of precursor solutions. These are based on an aqueous system using calcium, phosphate and alkaline solutions to regulate the reaction. For calcium these include calcium chloride, calcium nitrate, calcium alkoxides, calcium acetate and calcium hydroxide. Precursors for phosphate include potassium di/tri-hydrogen phosphate, phosphate alkoxides, sodium phosphate tribasic (Liu *et al.* 2001). Alkaline solutions that have been used in the literature include sodium hydroxide, ammonia, ammonia hydroxide, potassium hydroxide (Cunniffe *et al.* 2010; Bakan *et al.* 2013; Yubao *et al.* 1994; Vázquez-Hernández *et al.* 2010)

The reaction between these different calcium, phosphate and alkaline precursor solutions yield different by-products. These by-products are likely to influence HAp nucleation and growth. Efforts have been made in an attempt to coat metal implants with hydroxyapatite using sol-gel methodologies as an alternative to thermal spraying (Asri *et al.* 2016).

Temperature has been observed as a fundamental parameter of sol-gel synthesis governing crystal shape yielding needle-like morphology at low temperatures (35^{o}C) and a more regular rounded shapes at higher temperatures (85^{o}C) (Bouyer *et al.* 2000).

Ion availability within the sol-gel solution is known to influence HAp crystal structure, indeed the affinity for specific ions during HAp nucleation and growth is known to vary according the conformation of the crystal lattice (Elliott *et al.* 2002). This will have ramifications on the HAp synthesised with different addition methodologies or titration rates.

Methodology	Sub-methodology	Description	Advantages & disadvantages	Example author
Chemical precipitation	**Sol-gel**	Addition of calcium and phosphate precursor solutions	Basic method, economically viable and homogeneous crystal morphology. Potential particulate aggregation.	(Jarcho *et al.*, 1976, Bouyer *et al.*, 2000)
	Hydrothermal	Aqueous sol-gel method heated in a reaction vessel +/- pressure.	Control of temperature on crystal formation. Can require specialist equipment.	(Earl *et al.*, 2006, Wang *et al.*, 2006, Li *et al.*, 1994, Bouyer *et al.*, 2000)
	Solvothermal	Non-aqueous hydrothermal method	Control of particle distribution during fabrication. Enhanced complexity of crystal growth.	(Chen *et al.*, 2011, Furuzono *et al.*, 2001)
	Electrochemical deposition	Sol-gel method employing an electric charge on surface to encourage particle deposition	Control of nucleation surface. Aggregation of crystals. Depositional differences in crystal formation	(Eliaz *et al.*, 2005)
	Hydrothermal-Electrochemical	Electrochemical deposition with hydrothermal treatment	Control of nucleation surface and crystal morphology	(Ban and Maruno, 1998)
	Simulated body fluid (SBF) influenced	SBF used as a medium for chemical precipitation	Biomimetic conditions for HAp precipitation, complies with the second phase of biomineralisation (Anderson, 1995). Enhanced complexity of crystal growth.	(Tas, 2000)
	Dispersant Aided	Dispersants used in media for chemical precipitation	Avoid aggregation of crystals. Enhanced complexity of crystal growth.	(Wang *et al.*, 2006, Moulik *et al.*, 1996)
	Direct precipitation	Scaffold fabricated or soaked with a precursor solution before incubation with counterpart solution.	Potential multi-layering of HAp on surface. Surface coated HAp. Treatment of polymeric scaffolds could jeopardize structural integrity.	(Kawai *et al.*, 2004, Cui *et al.*, 2010, Nirmala *et al.*, 2010, Chen *et al.*, 2006)
	Spray drying	Aqueous precursor solutions sprayed in a column.	Bundles of agglomerated nano-rod HAp. Enhanced complexity of crystal growth.	(Chow *et al.*, 2004)
Solid state	**Mineral conversion**	Monetite dissolution and re-precipitation using NaOH yielding HAp.	Bundles of agglomerated nano-rod HAp. Enhanced complexity of crystal growth.	(Ma *et al.*, 2006)

Table 2-2: Summary of various HAp production methodologies

Bouyer *et al.* (2000) investigated the influence of various addition rates of the phosphate component into a calcium precursor reservoir. This lead to differences in HAp morphology.

Reaction pH i.e. OH^- availability is a key component for HAp crystal formation (figure 2-14). Weakly acidic titration conditions of pH 4-6 is known to form a calcium phosphate phase known as dicalcium phosphate dehydrate (DCPD) $CaHPO_4 \cdot 2H_2O$ or brushite at physiological temperatures. This phase is unstable and the DCPD loses its bonded molecular water to form monetite during storage, DCPD is rapidly transformed into HAp under physiological conditions (Kumta *et al.* 2005). It was noted that calcium phosphate titrated at pH < 6 and with elevated temperatures (80°C – 100°C) resulted in formation of calcium deficient HAp with a Ca/P ratio of <1.67 (LeGeros *et al.* 2003). Octacalcium phosphate (OCP) is an intermediate between the DCPD to HAp transformation process and is thought to be regulated through local OH^- ion changes. Alkaline solution conditions >pH 9 were reported to mediate a transformation from OCP to amorphous HAp (Lazić 1995). Previous research by Zhang *et al.* (2009) has clearly shown the importance of reaction pH on HAp crystal morphology (figure ***2-14***). The preparation method used here differs from the one described by Zhang and colleagues, ergo alterations in reaction pH were investigated.

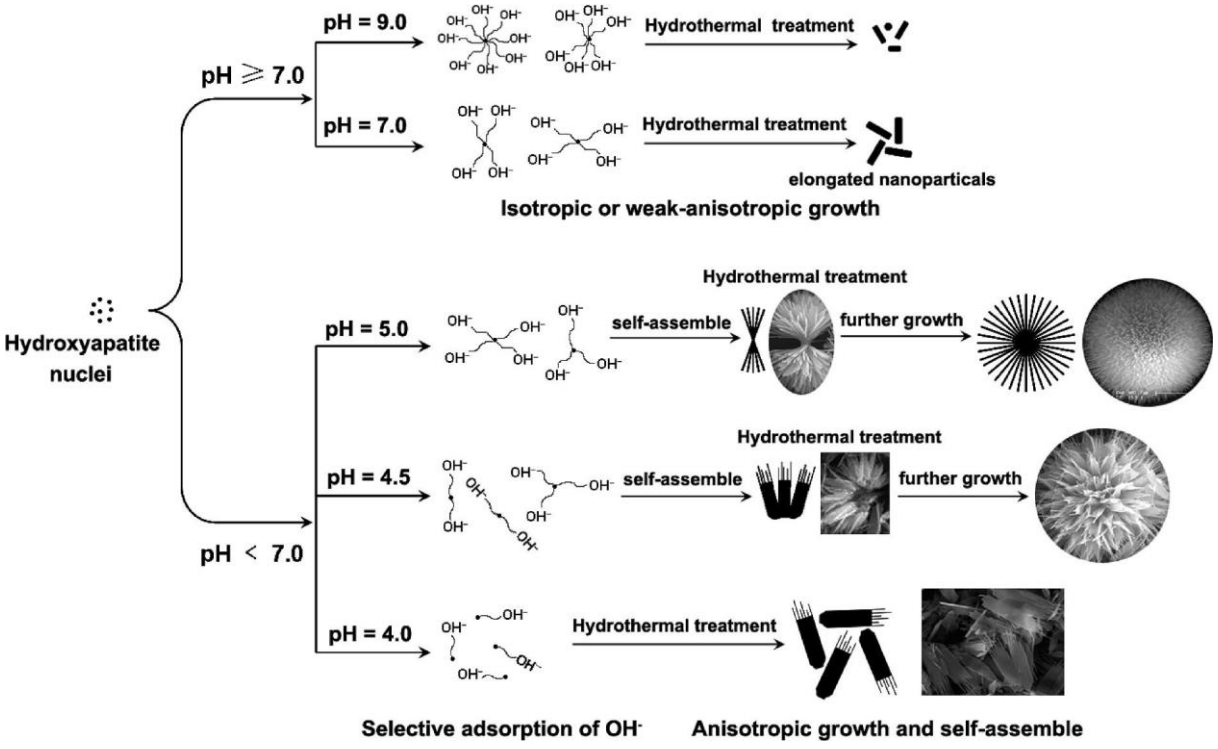

Figure 2-14: The role of OH^- on hydroxyapatite nucleation and growth (Zhang et al. 2009)

The order of the crystal lattice is influenced over time increasing the stability of the final HAp crystal, this maturation is a consequence of time and pH (Kumta *et al.* 2005). Commonly calcium phosphates undergo post-process sintering to form highly crystalline hydroxyapatite; this is known to result in secondary crystal growth (Sanosh *et al.* 2009).

Modification of crystal morphology, size and zeta potential are important factors in governing how cells interact with nanoparticles (Mahmoudi *et al.* 2011). Previous studies have used micelle facilitated crystal growth to limit growth size and spherical morphology of HAp (Cai *et al.* 2007b). A more biomimetic approach investigated the use of amino acid combinations, which are known to orchestrate *in-vivo* biomineralisation of collagen type 1 (Jahromi *et al.* 2013).

Recent developments in supercritical water hydrothermal synthesis (scWHS) technology could potentially produce a more scalable approach to the production of nanoparticles. The scWHS method uses a continual flow system which can be optimised to produce a variety of different material nanoparticles including HAp (Lester *et al.* 2006). This technology is currently under development by Promethean Particles Ltd (UK) SHYMAN funded by the EU FP7 framework project. Investigating the influence of HAp nanoparticles on mammalian cells *in-vitro* is a challenging process. A number of methods have been used to evaluate nanoscale HAp *in-vitro*; each with their advantages and disadvantages. Growing cells in a monolayer on tissue culture plastic and adding a suspension of HAp does not assess direct cell – surface nanoparticle interaction. Cultivating cells directly on loose powder runs the risk of monolayer disruption during medium replacement. Sintering the particles into pellets conceals any potential outcome of particle – cell interactions and alters the as synthesised crystallinity. Coating a substrate with HAp allows cellular interaction not only with the HAp but also the material substrate. The dip coating methodology theoretically simulates HAp liberation from the proposed bioresorbable polymer/HAp composite substrate resembling that which would occur at a composite – tissue interface.

2.4.3 *Synthetic polymers*

Current understanding of the important influences of extracellular matrices on cell fate highlights the necessecity for control of these processes using artificial materials. Synthetic polymers hold a number of advantages over natural polymers, these include scaleability, consistency, reproducability and in some cases cost. The biodegradability of many synthetic polymers is appealing for bone tissue engineering, as it allows for ingrowth of bone from the native tissue, thereby eliminating potential stress sheilding (Chen & Liu 2014).

Poly (α-hydroxyacids) are amongst the most commonly used polyesters in bio materials. Poly (lactic acid) (PLA) is synthesised from starch and sugars by a ring-opening polymerisation process and exhibits semicrystalline behaviour (Savioli Lopes *et al.* 2012). The lactic acid within PLA exsists as two enantiomers L- and D-lactic acid. The mechanical and biodegradation properties are directly influenced by the arrangement or tacticity of these enantiomers of which determines the polymer crystallinity. Pure L-lactic acid PLA results in a highly crystalline polymer, where as a L:D ratio of 50% in syndiotactic form results in an amorphous PLA material (Kister *et al.* 1998).

L-lactic acid D-lactic acid

Figure 2-15: Enantiomers of lactic acid (Nampoothiri et al. 2010)

In general amorphous polymers biodegrade more readily due to loose association of the polymer chains, conversely crystalline polymers take considerably longer to biodegrade. Ergo medical grade polymers require consistancy in their structure to avoid uneven biodegradation, of which could lead to release of large regions of crystalline polymer.

PLA is degraded though the hydrolysis of the ester bonds; the hydrolytic products of this process are transformed into non-toxic by-products. PLA has been demonstrated as a suitable bioresorbable polymer for fixation devices and has been used extensively as suture meshes (Lovald *et al.* 2009). Biodegradable implants are advantageous over metal as there is no requirement for removal and would allow the bone to gradually take over mechanical loading, which is vital to allow appropriate bone healing and remodelling within the scaffold region.

Other biodegradable polymers are studied for use in medical devices include polyglycolic acid (PGA), polyanhidrides, polyorthoester, polycaprolactone (PCL) and polyethylene glycol (PEG). Many have sought to combine these polymers to tailor the material degradation properties. For example L-PLA and PGA (Tai *et al.* 2007).

For the purposes of studying the influence of polymer and HAp *in-vitro,* food grade PLA was selected as it is similar to medical grade PLA and as a model for process development. The degradation of PLA would also not occur in the *in-vitro* time scales of the experiments performed in this thesis. Future work would of course use medical grade polymers for *in-vitro* and *in-vivo* applications.

2.4.3.1 Polymer nanocomposites

Polymer nanocomposites are composed of a polymeric phase with one or more materials comprising nanoscale features of organic or inorganic phase distributed within the matrix. Nature is a master of nanocomposite materials, the most relevant example of which is bone. Evidence from the early 1990s demonstrated a significant improvement in mechanical and thermal properties with only a small addition of a nanoscale filler material (Hussain 2006). The properties of the nanocomposite material are not only dependent on the individual material properties, but also the morphology, distribution and interfacial characteristics of the two components. (Hussain 2006). Uneven distribution and lack of interfacial strength of nanoparticles within the polymeric matrix can lead to mechanical discrepancies and failure (Šupová 2009).Consequently, achieving a consistent dispersion of nanoparticles within polymer matrices will allow for optimal property improvements.

Physically nanomaterials vary from traditional composite materials due to the fillers large surface area for a given volume. A number of important chemical and physical interactions depend on nanoparticle surface properties and morphology. As such nanostructured materials can have considerably different properties from materials with larger-dimensional fillers of the same composition. The surface area per unit volume of nanoparticles is inversely proportional to the materials diameter, therefore the smaller the particle diameter the greater the surface area per unit volume (Chen *et al.* 2013).

Nanocomposites can be made by several techniques. Thermo-mechanical methods including compounding, milling and compression or injection moulding are often employed to produce

nanocomposites. These methods are advantageous as they can be used with existing manufacturing processes and are highly scalable. The large material quantities required for extrusion processing can often be a limiting factor to when it comes experimental work. Researchers have however, produced hydroxyapatite polymer nanocomposites with good dispersion using these techniques (Mathieu *et al.* 2006).

Physico-chemical methods involve the use of a solvent to solubilise the polymer and allow for nanoparticles dispersion before consolidation (Šupová 2009). The advantage of this method is that it allows direct control over dispersion and distribution of the particles using lower temperatures and smaller quantities of material for experimental work. The disadvantages include potential contamination of the final composite material with residual solvents and the generation of contaminated wash waste requiring specialist disposal. For the purposes of the experimental work presented in this thesis, a physico-chemical dispersion approach was adopted and thus introduced.

Dispersion of a solid <1000 nm particles within a liquid is termed a colloid and is mainly governed by three forces:

1: Van der Waals force refers to a number of physical interactions that can occur between elements and molecules, including the London dispersion force, dipole interaction and hydrogen bonds. Van der Waals forces can generally be attributed to the probability of electron distribution based on the electronegativity of the element alone and elements present within a molecule. In the case of HAp, electrons distribute to form a positive and negative dipole within the particle. The smaller the nanoparticle the more particles will be present in a given volume, thus increasing the frequency of dipole moments at any given time. HAp also has a number of hydroxyl groups present, of which are capable of forming hydrogen bonds with other electronegative paired hydrogen atoms (Luckham 2004).

2: Electrostatic interaction of particles with one another and with the medium in which it resides, originates due to the presence of fixed or induced charges at the particle surface. The electrical double layer theory suggests that in a liquid, charged ionic moieties are attracted to an oppositely charged interface and form a diffuse layer near the surface (Adamczyk 2003).

3: Steric forces or simply the blocking of solid movement by the physical packing of surrounding molecules that will influence solid phase dispersion. An example of steric

interaction would be the adsorption of a polymer chain to the surface of the HAp. The adsorbed polymer does not lie flat, instead parts adsorb to the surface with others extending away into the medium. Those repelled from the particle surface would therefore repel from similar neighbouring moieties resulting in repulsion of particles from one another (Rozenberg & Tenne 2008).

Researchers have used a number of different techniques to overcome these forces and disperse nanoparticles within polymers. These include solution chemistry to functionalise the nanoparticle surface (Tanaka *et al.* 1999), the use of polymers to coat the surface of the nanoparticle (Lee & Shofner 2013; Rozenberg & Tenne 2008), *in situ* polymerisation of the nanocomposite (Li *et al.* 2003; Li *et al.* 2004), ultrasonic dispersion in solution (Safadi *et al.* 2002), the use of surfactants (Kim *et al.* 2006; Tanaka *et al.* 1999) and gelation/crystallisation (used with carbon nanotubes) (Bin *et al.* 2003).

Utilisation of a solvent with suitable polarity will also facilitate solid – liquid interaction. The viscosity of the medium is a good example of steric hindrance of particle dispersion and can be reduced by increasing the volume of solvent used to dissolve the polymer.

Mixing of the solid phase with the liquid phase requires the input of energy into the system to initiate particle movement. The dispersion of nanoparticles requires very high energy to encourage initial separation from one another. Ultrasonic vibration (15-400 kHz) with the use of an ultrasonic water bath provides high energy throughout the solid and liquid phase maximising solid – solid phase separation.

Surfactants are amphiphilic molecules containing both hydrophobic and hydrophilic domains. The polarity of the hydrophilic ‘head’ of the molecule determines its nomenclature (figure 2-16).

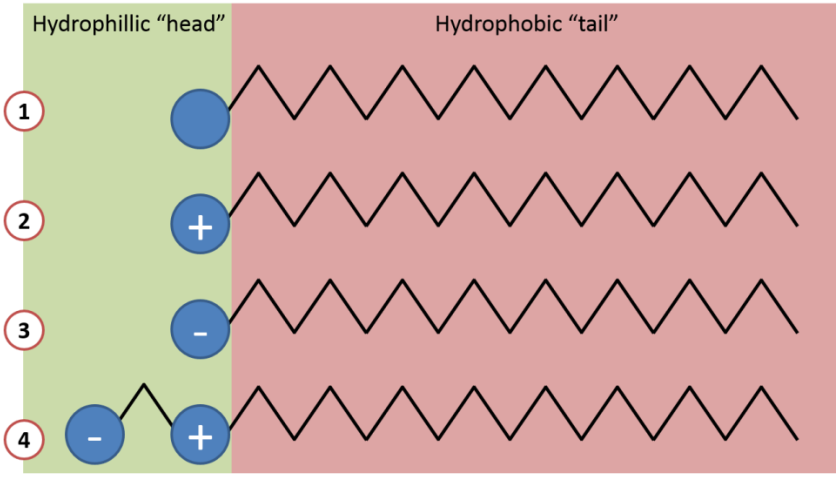

Figure 2-16: Surfactant classification 1: Non-ionic, 2: cationic, 3: anionic and 4: amphoteric.

Surfactants have previously been used to disperse nanoparticles prior to a number of processing techniques including electrospinning (Kim *et al.* 2006). Surfactants at a specific concentration self-assemble into hydrophilic/hydrophobic spheres called micelles depending on the preference of the medium. The concentration in which surfactants are able to form micelles is termed the critical micelle concentration (CMC). Cetrimonium bromide (CTAB) is a commonly used surfactant for the production on HAp and was therefore used for experiments (Cai *et al.* 2007b). Micelles can be used to stabilise solid – liquid suspensions through providing a physical and electrostatic barrier between the solid and liquid phases.

2.4.4 *Fibrin*

Minimally invasive techniques are a fast developing area of research, given the cost benefits achieved through lowering patient recovery time and reducing likelihood of infection (Bensaïd *et al.* 2003). Localising cells with the ability promote osteogenesis within the implant site would reduce the healing dependency on endogenous cell recruitment.

Fibrin is an insoluble protein involved in the clotting of blood during injury. Fibrin is formed from soluble fibrinogen molecule precursors and locally activated thrombin enzymes. Thrombin acts by exposing a specific polymerisation site in the middle (E domain) of the fibrinogen molecule. This facilitates hydrogen bonds to form between the E domain and terminal D domains of other fibrinogen molecules (figure 2-17) (Mosesson 2005).

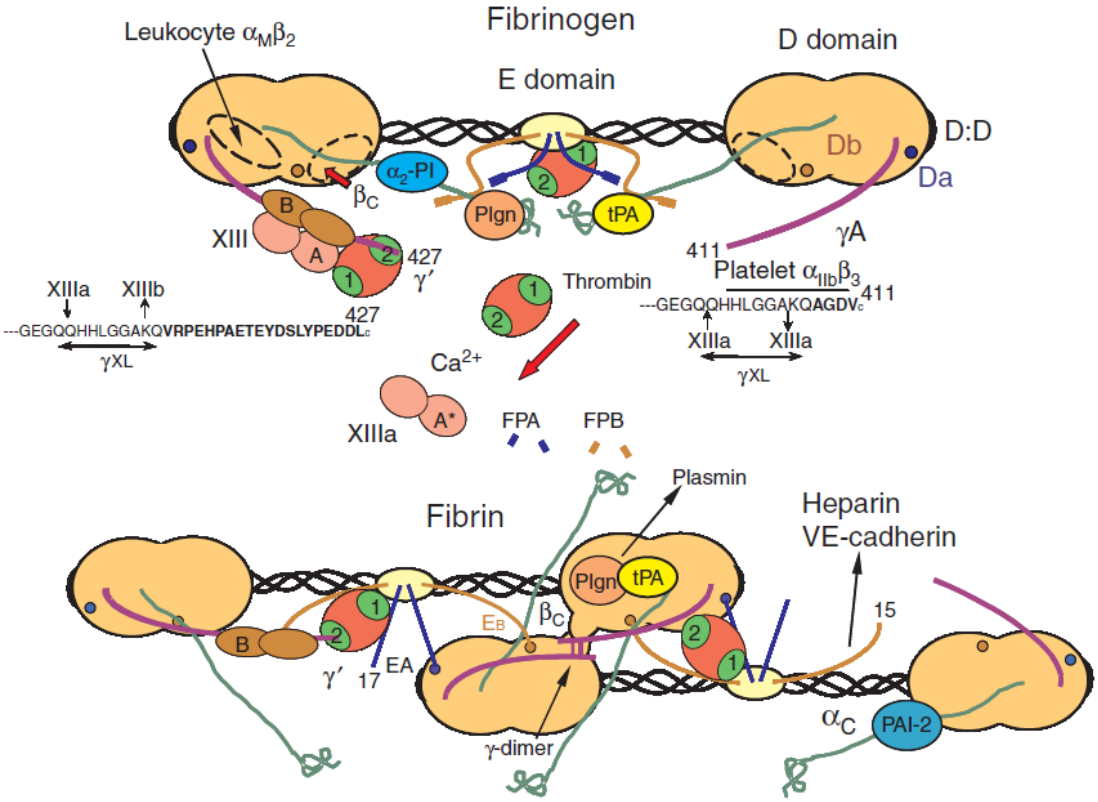

Figure 2-17: Diagram of fibrinogen structure and its conversion into fibrin (Mosesson 2005)

Polymerisation of fibrinogen molecules produces a lattice of overlapping E-D domain bonded chains, which are prone to branching, directly influencing the porosity of the fibrin network. With relatively low levels of activated thrombin the fibrinogen polymerisation site exposed at a slower rate resulting in more branching with a less porous matrix and vice versa (Blombäck *et al.* 1994). The fibrinogen molecules are covalently cross-linked by plasma protransglutaminase (factor XIII) which forms a disulphide bridge between D-D domains on adjacent molecules (Mosesson 2005).

The crosslinking controlled by thrombin and density of the fibrinogen monomer are likely to influence the migration of cells within the implant site. *In-vitro* synthesised fibrin scaffolds have demonstrated the potential for cell migration using ~20-30 mg/mL fibrinogen by Dikovsky *et al.* (2006). Specific studies investigating the direct influence between crosslinking and fibrinogen density have demonstrated that fibrinogen concentration can influence cells spreading and proliferation of hMSC (Bensaïd *et al.* 2003).

Fibrin is also known to facilitate endothelial cell spreading, capillary tube formation and angiogenesis making it a promising option for the regeneration of vascularised tissues (Mosesson 2005). Literature has demonstrated cell attachment and proliferation to fibrin

material for both angiogenic and osteogenic promotion (Osathanon *et al.* 2008; Bensaïd *et al.* 2003; Catelas *et al.* 2006). Fibrin is also used to seal chondrocytes within the defect site during autologous chondrocyte implantation surgery (Richardson 2015).

The mechanical properties of fibrin alone are insufficient to withstand direct loadbearing (80.9 – 16.1 kPa) implantation and would therefore require support by a load bearing scaffold (Thomson *et al.* 2013). Fibrin has a significant disadvantage which is its gradual disintegration in the presence of cells, losing its shape and volume before the cells can replace the hydrogel with tissue. This disadvantage however can be overcome by balancing the degradation with specific cell concentrations and/or adding specific protease inhibitors (Ahmed *et al.* 2008). One such protease inhibitor currently used in fibrin glue is aprotinin (Yamada *et al.* 2003). The fibrin investigated in this thesis did not contain protease inhibitors, as the degradation of the hydrogel by the cells was favourable to promote extracellular matrix deposition by the encapsulated cells. The concentration of fibrinogen and thrombin used was based on previous research by Osathanon *et al.* (2008) to produce a hydrogel that would temporally localise specific cells within a hypothetical implant.

2.4.5 *Scaffold fabrication techniques for bone TE applications*

The choice of the biomaterial used for a TE application primarily influences the biocompatibility, bioactivity, biodegradation/ bioresorption, osteoconductivity and osteoinductivity of the scaffold. However, the architectural characteristics in combination with the selected material will affect the mechanical properties, the porosity, interconnectivity, surface roughness that are vital for the structural integrity of the scaffold and the regeneration of the damaged tissue. To date a variety of scaffold fabrication techniques have been developed to produce scaffolds that simulate the native tissue characteristics. Representative techniques of widely used polymeric scaffold fabrication techniques are reported in table ***2-3***. In all the techniques mentioned ceramic or glass- ceramic particles can be incorporated to prepare composite materials.

Method	Description
Solvent casting/ particulate leaching	A polymer that has been dissolved using an organic solvent is mixed with water-soluble (e.g. salt, PVA) or acid-soluble particles (e.g. chitosan) with specific particle range. The solution is cast into a mould and the solvent is evaporated to produce a compact polymer structure. The dry polymeric construct is immersed in the solution that will dissolve the particles and polymeric matrix becomes porous (Vitale-Brovarone et al. 2010).
Gas foaming	**Supercritical CO_2 foaming**: The carbon dioxide (CO_2) at a temperature and pressure above its critical point is a supercritical liquid. An amorphous glassy polymer is soaked with supercritical CO_2 ($scCO_2$) at elevated temperatures. The $scCO_2$ acts as plasticizer and decreased the T_g of the polymer making it rubbery. When the pressure drops, whilst the temperature remains stable the solution promote bubble nucleation that produces pores. As the solution is depressurised, the concentration of the plasticizer decreases, the T_g of the polymer increases and vitrification of the polymer occurs. As the pressure is decreased, the concentration of the plasticizer is also decreased. The polymer T_g increases and vitrification occurs resulting in a glassy polymer with a porous structure. (White et al. 2012)
Freeze drying	**Thermally induced phase separation (TIPS)**: A polymer is dissolved at increased temperature in a solvent. After the polymeric solution is cast in moulds, the temperature is decreased to induce phase separation between the polymer lean (containing the solvent) and polymer rich phase. The frozen construct is freeze dried to sublime the solvent leaving a highly interconnected and porous polymeric scaffold (Camarero-Espinosa et al. 2016).
	Freeze casting: A non-solvent soluble material is solubilised. The solution is cast in moulds and the temperature is reducing to promote ice-crystal formation. The frozen polymer is freeze dried resulting in an interconnected porous polymeric scaffold (Deville et al. 2006).

Nonwoven	**Electrospinning**: A polymer is dissolved in a solvent and poured in a syringe that is placed on the syringe pump. Electric or magnetic field is used to evaporate the solvent as is extruded from the syringe resulting polymeric fibres that are collected onto a conductive surface (Tuin et al. 2013; Rogers et al. 2014).
	Centrifugal spinning: A dissolved polymer is loaded into the reservoir of the spinner is heated at high temperature. The molten or dissolved polymer is drawn from the orifices and is collected from the spinner (Zhang & Lu 2014).
Solid Freeform Fabrication (SFF)	A group of computer aided manufacturing (CAM) techniques use computer aided design (CAD) programs to rapidly generate 3D structures. The different SFF systems are divided to: laser based, nozzle-based and printer based (Bose et al. 2013; Billiet et al. 2012). Below a couple of the most widely used SFF techniques are reported.
	Stereolithography (SLA): A liquid photocurable polymer is in a SLA apparatus, a laser source is moving on the x, y axis and polymerises the material layer by layer. SLA is a laser-based system.
	Fused filament fabrication (FFF): A polymeric filament passes through a nozzle that has a hot end to melt the polymer. The molten polymer deposits on the stage as the extruder moves on the x, y and z axis build the construct layer by layer. FFF is a nozzle-based system.

Table 2-3: Examples of 3D scaffold polymeric techniques.

2.5 Current regenerative approaches for the treatment of OA

Mosaicplasty or osteochondral grafting is a surgical technique where by cylindrical plugs of non-load bearing regions of cartilage are removed from the defect site. This is a lengthy, difficult to standardise procedure leading to some donor site morbidity. The results are largely successful with viability of the transplanted tissue and results in a fibrocartilage matrix deposited within the gaps between the implanted plugs (Richardson 2015).

Microfracture is a surgical technique whereby the extent of the osteochondral defect is prepared by removal of defective cartilaginous tissue and debridement of the subchondral bone surface. Small holes are punctured in the subchondral bone surface to allow bone marrow to bleed into the prepared site. Microfracture results in tissue growth which, over time, forms cartilage 'tufts' and eventually fibrocartilage that is believed not to be as mechanically robust as hyaline cartilage (Richardson 2015).

Autologous chondrocyte implantation (ACI) is a technique requiring two surgical procedures. The first includes removal of healthy cartilage from a non-load bearing region. Chondrocytes are isolated from this tissue and expanded *in-vitro* in a highly controlled good manufacturing practice (GMP) facility. Following up to two months of cell expansion, the second surgery involves preparation of the defect site removing defective tissue. A membrane is then sutured in place and sealed using fibrin glue forming a cavity into which the chondrocytes are injected (Richardson 2015).

A similar procedure to ACI called matrix-assisted autologous chondrocyte implantation (MACI) is currently being trialled however, ongoing results have demonstrated little difference between the two methodologies (Richardson 2015).

Recent efforts have been made using bioresorbable scaffolds, particularly aimed at larger defects, to maintain mechanical stability and functionality of the articulating joint surface. These scaffolds are designed to encourage host cells to regenerate and replace the material using natural reparative processes. Current clinical trials are taking place to investigate the potential for a number of artificial osteochondral scaffold (Nukavarapu & Dorcemus 2013). The foreseeable advances in the repair of osteochondral lesions are likely to include a mixture of current surgical, material and cellular therapies.

Chapter 3 – Materials and Methods

3.1 Materials

Materials used in the following methods were purchased from Sigma Aldrich Co. (St. Louis, USA) unless otherwise stated.

3.2 General laboratory procedure

All laboratory procedures were carried out in accordance with University of Newcastle safety policy and publications. All experimental processes were performed subsequent to full risk assessment form and in compliance with Control of Substances Hazardous to Health regulations (COSHH). This comprises assessment covering the use, storage, disposal and general protection of staff and students. All laboratory work was carried out in compliance with the 'University Safety Policy' and the 'Departmental Safety Policy'. Biological agents were used in compliance with university safety office (USO) regulations for containment of class II pathogens. All solutions were made using distilled water as a solvent unless stated otherwise.

3.3 Materials and analysis

A range of analytical techniques were employed to assess a variety of materials from ceramic powder to polymers and polymer ceramic composites.

3.3.1 *Poly (lactic acid)*

Poly (lactic acid) (PLA) filament 3mm diameter was requisitioned from NatureWorks LLC (Ingeo 4032D) with 60-68%L/40-32% D isomers and with relative viscosity 4.0. The molecular weight was 156,651 Dalton according to gas phase chromatography data performed by a fellow student. The use of this polymer allows for the processing parameters of various methods to be optimised at a fraction of the cost. This grade of polymer would not be used clinically due to the lack of characterisation with regards to its degradation. As a material substrate for *in-vitro* assessment (21 days), it can be argued that overall surface chemistry would be similar to that of medical grade PLLA or PDLA.

3.3.2 *Fourier transformed infrared spectroscopy (FTIR)*

Attenuated total reflection (ATR) is a sampling technique used in conjunction with infrared spectroscopy which enables samples to be examined directly.

Solid material samples were analysed using an ATR-FTIR Perkin Elmer Spectrum 100 with PerkinElmer's Spectrum™ v6 FT-IR software. Spectra were collected by first cleaning the diamond/ZnSe crystal surface with acetone or 100% ethanol before and after use. The machine is first calibrated to background noise prior to data collection. Material samples were then loaded onto the detection area (enough to cover the surface with no more than a few millimetres thickness) and locked in place using the pressure arm. Spectra were then recorded from start 4000 cm^{-1} to 650 cm^{-1} with a resolution of 4 cm^{-1} and a minimum of 32 scans per sample.

3.3.3 *Transmission electron microscopy (TEM)*

Transmission electron microscopy (TEM) is a technique used to visualise the two-dimensional silhouette of a material obstructing a focused beam of electrons. TEM has a higher resolving power than optical microscopes permitting the visualisation of nanoscale features.

Copper grids were first coated with pioloform. Pioloform was prepared to 0.5% solution in trichloromethane (TCM) (C2432). A glass slide was coated in Pioloform and allowed to dry for 1 minute. The Pioloform was then lifted from the glass into a water tank. Copper grids were then positioned on top of the floating film and were collected using parafilm. Coated grids were then stored in a clean petri dish and plasma cleaned in a vacuum for 5 minutes using a Plasma Cleaner PDC 32G (HARRICK PLASMA ltd., Ithaca, New York, USA) prior to use.

Powder samples were prepared by diluting particles in solvent (ethanol) to approximately 1-5 mg/mL (or almost fully translucent, concentration not crucial). The sample solutions were then ultrasonically agitated for a minimum of 10 minutes using a USC 300TH Ultrasonic Cleaner (VWR International LLC., Radnor, Pennsylvania, USA).

Material samples were embedded for sectioning in 100% epoxy resin (TAAB Labs, Aldermaston, Berks) at 60°C for 24 hours. Ultrathin sections of approximately 70 nm were cut using a diamond knife on a RMC MT-XL ultramicrotome (Boeckeler Instruments Inc., Tucson, Arizona, USA). Sections were then stretched using TCM to eliminate compression and mounted on Pioloform-filmed copper grids.

Prepared grids were examined using a Phillips CM100 Compustage (FEI) transmission electron microscope (1000 kV). Digital images were collected using an AMT CCD camera (Deben, Ltd, Suffolk, UK) at the Electron Microscopy Research Services, Newcastle University, UK.

3.3.4 *Scanning electron microscopy (SEM) & energy dispersive X-ray spectroscopy (EDX)*

All biological samples were prepared for scanning electron microscopy (SEM) by a chemical drying procedure and subsequent gold coating. Initially culture medium was aspirated and samples were washed three times in PBS (17-516F, Lonza, UK). Samples were then fixed using 2.5% glutaldehyde for 30 minutes at 4°C. Samples were washed again with PBS and dehydrated using graded ethanol (25%, 50%, 75% and 100%) 5 minutes in each. Samples were then treated with hexamethyldisloxane (HMDS) diluted to graded concentrations using 100% ethanol. Samples were immersed in 25%, 50%, 75% and 100% HMDS for 10 minutes each and finally kept in 100% HMDS overnight to evaporate. The dry biological and non-biological samples were preserved in a desiccator with silica beads pending gold coating.

All samples were mounted onto aluminium stubs with sticky carbon discs. Gold coating was performed when necessary using a polaron SEM coating unit (Quorum Technologies, Sussex, UK) to a thickness of 15nm least otherwise stated.

Samples were examined using a Cambridge stereoscan 240 scanning electron microscope, housed within the Catherin Cookson building, Faculty of Medical Sciences, Electron Microscopy Research Services at Newcastle University. Digital images were collected using Orion6.60.6 software (1000 kV and Mode).

Samples for EDX analysis were prepared by sticking powder to carbon tape (Elektron Technologies, AGG3939B). Samples were examined using either a Hitachi TM3030 analytical benchtop SEM. Calcium to phosphate ratios were measured using energy dispersive X-ray spectroscopy, values were processed by NEXUS services, School of Mechanical Systems Engineering, Stephenson building, Newcastle University.

3.4 Ethics

Donated tissue was collected via the Newcastle Bone and Joint Biobank 09/H0906/72. Ethical approval for the use of consented patient tissue was attained through the NHS National Research Ethics Service within the National Patient Safety Agency and Research Ethics Committees in England. Research numbers were designated to isolated cell samples to ensure patient anonymity.

3.5 Cell Culture

Cell culture is the process by which isolated cell types are cultivated *ex-vivo* in controlled conditions outside of their natural environment. Specific cell types are adherent to certain substrates and can be propagated to form a monolayer which can be subcultured to expand the cell population. To achieve this the medium in which they are grown in should contain necessary components, these include specific osmolality, pH, essential minerals, vitamins and growth factors, glucose and oxygen dissolution.

"Tissue culture treated" plastics have since replaced glass substrates as disposable cultivation surfaces for adherent tissue culture. The process involves corona discharge/gas-plasma to add oxygen containing chemical groups or to open benzene rings on the polymer surface to enhance protein interaction. Tissue culture substrates were purchased from coring plc. (New York, USA), unless otherwise stated.

Dulbecco's modified eagle medium (DMEM) developed by Harry Eagle during the 1970s contains a mixture of: amino acids, salts, calcium chloride, potassium chloride, magnesium sulphate, sodium chloride, monosodium phosphate, glucose, vitamins folic acid, nicotinamide, riboflavin, vitamin B-12 and phenol red. Medium is supplemented with fresh foetal bovine serum (FBS), L-glutamine/glutaMAX™ (Life Technologies) and penicillin/streptomycin. FBS contains essential growth factors and proteins for cell adhesion and proliferation. Glutamine is necessary for cell metabolism as well as protein and nucleic acid synthesis. Penicillin/streptomycin is added to help avoid unwanted bacterial and fungal contamination.

Aseptic technique was used throughout any cell culture procedures using a class II microbiological safety cabinet (Contained Air Solutions Ltd, Manchester, UK). Solutions and reagents were either purchased sterile and endotoxin free or sterilised according to section 3.5.2 . All liquids that came in contact with cells during cultivation were pre-warmed to 37^{o}C using a Clifton unstirred thermostatic bath (NE1-8, Nickle – Electro Ltd., Western-super-Mare, UK) unless otherwise stated.

3.5.1 *Medium and Supplements*

Medium name	Medium
Phosphate Buffered Saline (PBS)	PBS without Ca^{++}, Mg^{++} or phenol red (17-516F, Lonza, UK)
hMSC medium / Basal medium	DMEM 1000 mg/mL glucose (D5523), 10% v/v FBS (F9665, batch 062M3397), penicillin/streptomycin 1,000 U/mL and 20 mM GlutaMAX™ (15140 & 35050, Invitrogen-Gibco, UK).
Transportation buffer	Hank's buffered salt saline with phenol red without Ca and Mg (BE10-543F, Lonza Group Ltd, Basel, Switzerland), penicillin/streptomycin 1,000 U/mL and nystatin suspension 1,000 unit/mL (N1638).
Osteogenic medium	100 nm Dexamethasone, 10 mM /β Glycerophosphate disodium salt hydrate (G9422), 50 µg/mL L-Ascorbic acid (A4544).
Chondrogenic medium	hMSC media, 40 µg/mL Proline (P5607), 10 ng/mL TGFβ-3 (PHG9305, Life-Technologies, UK) and 1X ITS™+ premix (Insulin, Transferrin and Selenous acid) (354352, BD Biosciences, New Jersey, USA).
Adipogenic induction medium	hMSC media, 25 ng/mL h-insulin (I2643), 0.5 mM IBMX (3-isobutyl-1-methylxanthine) (I5879), 15 µM IGF-1 (insulin-like growth factor 1) (R&D Systems, Inc., USA), 40 nM Dexamethasone (D4902), 2 nM Rosiglitazone (R2408) and 60 µM Indomethacin (I7378).

Table 3-1: Cell culture medium formulations.

Table 3-1 outlines media used for tissue culture passaging and experimentation.

3.5.2 *Sterilisation*

Liquids and equipment were sterilised prior to use in tissue culture using an Astell (UK) steam-air autoclave with a sterilisation cycle including a peak temperature of 121^{o}C with 1.037 pressure bar for 30 minutes.

Temperature sensitive liquids were sterilised by filtration. 1 mL – 50 mL volumes were filtered using an appropriate sterile syringe and a Millex-GP filter unit, 0.22 µm, polysulfone, 33mm, gamma-sterilised adapter (SLGP033RK, EMD Millipore™, MA, USA). Volumes exceeding 50 mL were filtered using a Steritop-GP® filter unit, 0.22 µm, polyethersulfone, 250 mL radio-sterilised (SCGPU02RE, EMD Millipore™, MA, USA) attached to a vacuum pump.

Materials were sterilised using a UV Steristorm 2537å (Coast-Air, London, UK) lamp for 30 minutes in a class II safety cabinet. More complex three dimensional materials were first soaked in 70% ethanol for 1 hour and washed three times with PBS prior to cell seeding.

3.5.3 *hMSC Isolation*

hMSC were isolated from donated femoral heads from arthroplastic surgery. Femoral heads from arthroplasty were stored at 4°C and collected twice daily, from the Freeman hospital, Newcastle, UK. The donated tissue was transported in sterile 500 mL containers containing transportation buffer. This was packaged with absorbent tissue, autoclavable polyethylene biohazard bag within a sealed plastic container with strap.

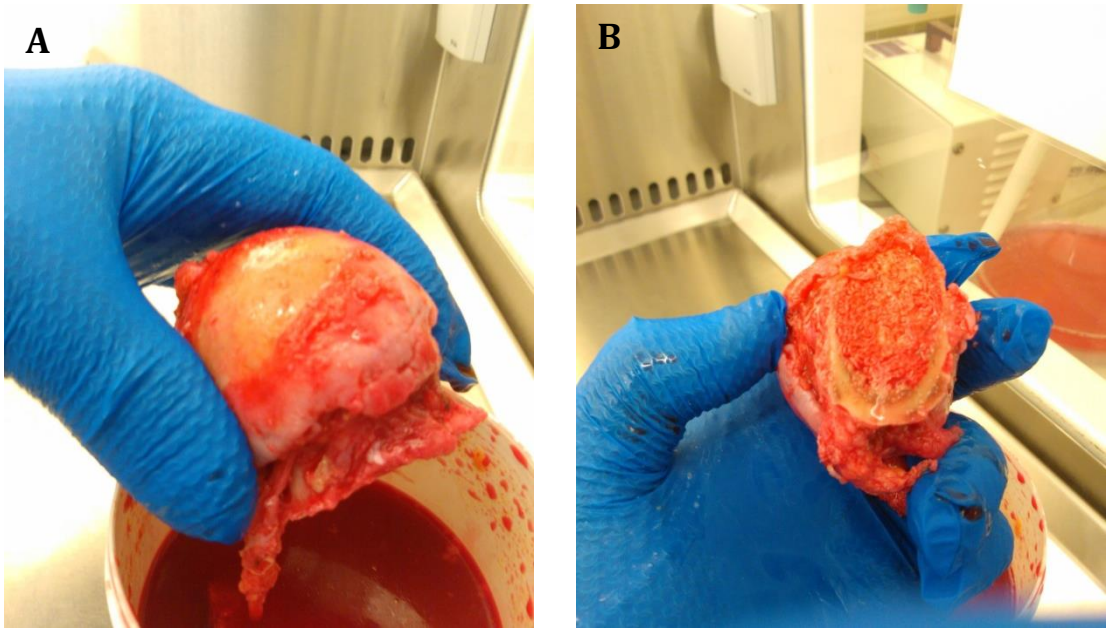

Figure 3-1: Images of patient femoral head following hip arthroplasty. A) Femoral head showing exposed bone and remains of cartilaginous covering. B) Bone marrow cavity located within the neck of the femoral head.

In a class II microbiological safety cabinet the femoral head was examined and held using a chainmail gloved hand. Debris of connective tissue was first removed from the cancellous bone region at the neck of the femoral head. A bone cutter was then used to mechanically homogenise and extract cancellous bone fragments into a universal tube containing 10 mL PBS. The bone and PBS was mixed to liberate free bone marrow; this solution was then filtered using a cell strainer to remove bone fragments. The washed bone marrow solution was then separated (figure 3-2A) using an equal volume of Ficoll-Paque PREMIUM (GE Healthcare Life Sciences, Buckinghamshire, UK) and centrifuged in a Sigma 2-6E centrifuge at 800g for 40 minutes at 4°C figure 3-2. A P1000 pipette was used to carefully extract the buffy layer containing the mononuclear cells (MNC's). This was washed twice using a 0.2% BSA, PBS, without Ca/Mg, 0.5 mM EDTA solution and centrifuged at 300 g for 10 minutes to remove any

contaminating Ficoll-Paque. The pellet was then suspended in hMSC media and transferred to adhere in a T-75 flask. After 2 days the remained non adherent cells were removed and fresh media was added. This process was repeated until the flask was confluent. If the cell density was too high in any specific regions throughout the flask, the cells were lifted via trypsinisation and seeded into the same flask. Cells were grown to ~70% confluence before passaging into P1.

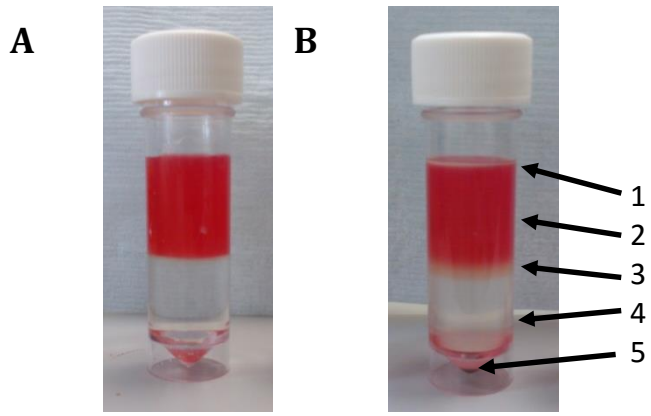

Figure 3-2: Examples of washed bone marrow solution (top) separated using a ficol gradient (bottom). Before (A) and following centrifugation (B). 1 = lipids, 2 =less dense nucleated cells, 3 = buffy coat, 4 = ficoll-Paque, 5 = pelleted non-nucleated cells.

3.5.4 *hMSC Culture*

The hMSC were subcultured upon reaching ~70% confluence. hMSC media was aspirated and the flask was washed using PBS 2.5 mL/25 cm^2 to remove traces of serum. 0.5 mL/25 cm^2 of 0.05% trypsin-EDTA (1x) (Life-Technologies, UK) was added and the flask was incubated on a level surface at 37^oC, in humidified atmosphere for 2-4 minutes (depending on cell morphology). hMSC media was used to inactivate the trypsin, an aliquot was obtained for a cell count and the remaining cell suspension was centrifuged at 200g for 5 minutes. Cells were counted within the 5-minute centrifugation period to minimise time spent outside incubation conditions. The supernatant was aspirated and the pellet suspended in a volume of hMSC media appropriate for seeding at a specific density or divided to subculture at one third (1/3) the density of confluence. Cells were fed with fresh hMSC media every 3-4 days with the addition of 10 ng/mL bFGF from passage one.

Notes: Prolonged incubation with trypsin will damage cell membranes and induce cell death.

Cell line number	hTERT Immortalised	Primary cell line	Date of isolation	Patient sex	Patient age	Source
Y201	Yes	Yes	-	?	?	THR
Lonza	No	Yes	-	?	?	BM-Asp
3070	No	Yes	26/02/2013	F	70	THR
3175	No	Yes	25/06/2013	F	66	THR
3286	No	Yes	23/10/2013	F	79	THR
3287	No	Yes	23/10/2013	F	57	THR
3303	No	Yes	05/11/2013	F	61	THR
3388	No	Yes	05/02/2014	F	56	THR
3502	No	Yes	21/05/2014	F	73	THR
3503	No	Yes	21/05/2014	F	61	THR
3505	No	Yes	22/05/2014	F	60	THR

Table 3-2: hMSC information and details of isolation and patient information. Total hip replacement (THR). Bone marrow aspirate (BM-Asp). Human telomerase reverse transcriptase (hTERT) modified immortalised cell line.

3.5.5 *Cryopreservation and retrieval*

Cells were cultured to confluence in cell culture flasks 25, 75, 225 cm^2. Upon ~70% confluence cells were detached from tissue culture plastic substrate using 0.05% trypsin-EDTA (Life-Technologies, UK) centrifuged at 200g. Cells were suspended in freezing medium containing 10% v/v DMSO in FBS and kept on ice. The cell suspension was then transferred into cryopreservation tubes (Coring) and transferred into an insulated container for initial freezing at -80^oC for 5 days. Cryotubes were later relocated into a liquid-nitrogen storage unit -196^oC for up to 5 years.

Cells were retrieved from cryogenic storage by quickly thawing the cryotube in a 37^oC water bath until it is half liquid. The liquid was then suspended in fresh media and seeded into a cell culture flash. After 24 hours the diluted cryopreservation media was replaced with fresh media and cells were cultured as described above.

3.6 Biological Analysis

Analysis of biological material is necessary to determine the status of cells under a variety of parameters. In this thesis the influence of material surfaces and matrices were investigated *in-vitro* to determine their potential for tissue regeneration.

3.6.1 *Cell Counting*

Cells were counted using a Fuchs-Rosenthal haemocytometer (Marienfeld, Lauda-Königshofen, Germany) with a depth of 0.200 mm. Cells collected from trypsinisation were homogenised using a pipette. A 20µl sample was taken from the cell suspension and applied to the haemocytometer to fill the viewing chamber via capillary action. 5 or more 1 mm^2 areas were counted and the average is then divided by two and multiplied by the dilution volume to provide total cell number x x 10^4. Cells were viewed using a Leica DMIL (Leica microsystems, Wetzlar, Germany) inverted light microscope with phase contrast filters.

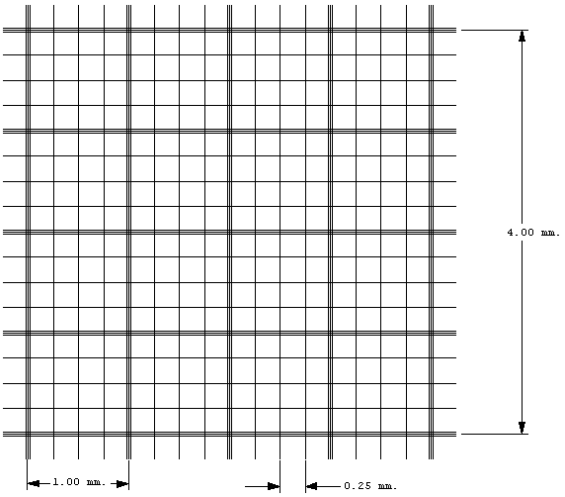

Figure 3-3: Dimensions and layout of a Fuchs-Rosenthal haemocytometer.

3.6.2 *Biochemical assays*

Biochemical assays were employed for qualitative and quantitative assessment of cellular responses to materials.

3.6.2.1 Alkaline Phosphatase Activity

Alkaline phosphatase (ALP) of cells cultivated on material substrates was evaluated with methods similar to that of Jaiswal *et al.* (1997). Cells were seeded at ~100% confluence 100,000 cells/well in a 24 well plate for 7, 14 and 21 days.

At each time point media was removed from samples and incubated with 4% paraformaldehyde in PBS for 20 minutes at room temperature. Cells were then washed with PBS and incubated with PBS 0.1M TRIS buffer pH 8.3 for 10 minutes. Samples were incubated in the dark at room temperature with 300 µL p-nitrophenyl phosphate (pNPP) liquid substrate system (N7653) for 5-30 minutes (time was noted). The solution was then transferred into 96 well plate and absorbance was measured at a wavelength of 405 nm using a Tecan plate reader. A calibration curve was used to determine pNPP concentration relative to absorbance (Appendix 8.6.3). Average pNPP conversion rate/well was presented when average cell number was not possible.

3.6.2.2 Cell Viability

The tetrazolium reduction assays were used to detect cellular viability of cells following cultivation on various substrates. The exact cellular mechanism of tetrazolium reduction is not fully understood, however it is thought to be involved with reducing molecules like nicotinamide adenosine dinucleotide (NADH) and potentially specific enzymes in the mitochondria capable of transferring electrons to MTT.

Two fundamentally different tetrazolium compounds have been used; (1) MTT is positively charged and contains (3-(4,5-dimethylthiazol-2-yl)-2,5-diphenyltetrazolium bromide) which readily penetrates viable eukaryotic cells. (2) MTS [3-(4,5-dimethylthiazol-2-yl)-5-(3-carboxymethoxyphenyl)-2-(4-sulfophenyl)-2H-tetrazolium, inner salt; MTS] is negatively charged and requires an electron coupling reagent (Phenzein ethosulfate; PES) to transfer electrons from the cell cytoplasm to facilitate the reduction. The main divergence between these two compounds is that MTT forms an insoluble precipitate inside which requires solubilisation using prior to absorbance reading and whereas MTS forms a soluble formazan

coloured solution. Ergo the MTS assay can be used consecutively while the MTT assay is an end point assay.

Prolonged exposure of cells to tetrazolium compounds results in cytotoxicity due to depletion of reducing equivalents such as NADH from the cell. Therefore, it is important to balance assay sensitivity and potential cytotoxicity with incubation time. Calibration of MTT was performed to quantify cell number however it is widely accepted that this assay assumes homogeneous cellular metabolism, which accounts for potential changes in cell phenotype from substrate interaction (Riss *et al.* 2013).

For 2D proliferation experiments cells were seeded on 13 mm coverslips with various materials at 10,000 cells/well in a 24 well plate. MTT (M5655) solution was prepared to 0.5 mg/mL in hMSC media and filter sterilised prior to use. Samples were incubated with 1 mL of MTT solution at 37^{o}C, in a 5% CO_2 and humidified atmosphere for 2 hours. Samples were washed using PBS and 300 µl of DMSO (D4540) applied to lyse the cells and dissolve formazan crystals. 200 µl of DMSO lysate was transferred into a flat bottomed 96-plate and absorbance was measured using a TECAN sunrise-basic plate reader (Austria, GmbH) at an absorbance of 570 nm.

3.6.3 *Histology*

Samples were prepared for histology by first fixing in warmed (37^{o}C) 4% w/v paraformaldehyde (P6148) or 10% formalin solution - neutral buffered (HT501128) for 20 minutes or overnight at 4^{o}C. Samples were then stored in 70% ethanol/water solution at 4^{o}C before sectioning.

Samples requiring sectioning were delivered to the Newcastle Centre Biobank (NCB) for embedding tissue in paraffin blocks. Blocks were sectioned by Mrs. Sharon Watson at the Musculoskeletal Research Group (MRG), Institute of Cellular Medicine (ICM), Newcastle University.

3.6.3.1 Trilineage differentiation of human mesenchymal stem cells

Human hMSC were prepared for adipogenic and osteogenic differentiation with the same methodology. Cells were cultured to confluence in a 75 cm^2 flask. Upon confluence cells were raised from tissue culture plastic substrate using 0.05% trypsin-EDTA (Life-Technologies, UK) centrifuged at 200g. The pellet was suspended into a volume to provide a confluent cell number in a 24 well plate (surface area = 1.9 cm^2 (39.45 mL)). Supplements for each type of differentiation media is found in (table ***3-1***)

Oil red O staining was performed on hMSC following 14 days cultivation with adipogenic medium. 13 mm slides were incubated with 60% isopropanol diluted in PBS for 5 minutes prior to staining. 200 µL working oil red O solution was added to each sample for 10 minutes. Excess oil red O solution was removed and samples washed in 60% isopropanol. Samples were then rinsed in distilled water before mounting on microscope slides using VECTASHIELD® mounting medium (Vector Laboratories Ltd., H-1000) and covered with a coverslip. Samples were imaged directly after staining.

Von Kossa staining was performed on hMSC following 14-day incubation with osteogenic medium. Samples were first washed in dH_2O three times. Samples were incubated with 1% silver nitrate solution (1g silver nitrate in 100 mL dH_2O) in a 24 well plate under a UV Steristorm 2537å (Coast-Air, London, UK) for 20 minutes. Samples were washed three times in dH_2O. Unreacted silver was removed using 5% sodium thiosulphate (5g sodium thiosulphate in 100 mL dH_2O) for 5 minutes and washed in dH_2O. Samples were mounted on microscope slides using VECTASHIELD® mounting medium (Vector Laboratories Ltd., H-1000) and covered with a coverslip. Samples were imaged directly after staining.

Chondrogenic differentiation measured using hMSC pelleted in a V-well 96-well plate at a density of 200,000 cells/well. Following 14 days incubation with chondrogenic medium samples were removed and prepared for histology according to methods outlined in section 3.6.3 Alcian blue staining was performed by first deparaffinising slides using xylene followed by rehydration in graded ethanol to dH_2O. Samples were incubated with alcian blue solution (alcian blue 8GX 1g and 3% acetic acid solution 100 mL [pH 2.5 was attained using acetic acid]). Samples were washed in tap water and rinsed in dH_2O. Samples were counterstained using 0.1% nuclear fast red solution (0.1 g nuclear fast red, 5 g aluminium sulphate and 100 mL

dH_2O). Samples were washed in tap water and dehydrated through grade ethanol. Samples were moved into xylene and a coverslip was mounted using DPX mounting medium (44581).

3.6.4 *Immunofluorescence*

For morphological evaluation cells were seeded 10,000 cells/well in a 24 well plate. Samples were incubated with the substrates for 24 hours at 37^oC with a 5% CO_2 atmosphere. Samples were prepared for immunofluorescent labelling by fixation in warmed (37^oC) 4% w/v paraformaldehyde (P6148) for 20 minutes. Samples were then washed in 0.1% v/v Tween20® (P2287) PBS for 5 minutes and incubated with phalloidin–tetramethylrhodamine B isothiocyanate (P1951) (rhodamine phalloidin) 1:1000 dilution in 0.1% Tween20® PBS. Samples were then rinsed in PBS before mounting on microscope slides using VECTASHIELD® mounting medium (Vector Laboratories Ltd., H-1000) and covered with a coverslip.

3.6.5 *RT-PCR Gene Expression*

3.6.5.1 TRIzol® RNA Isolation

RNA isolation was performed in a chemical safety cabinet using TRIzol® reagent (15596-018, Life-Technologies, UK). For 2D cultures TRIzol® lysates were prepared by first removing growth medium and adding 1 mL of TRIzol®. Lysation was assisted using a p1000 pipette and transferred into a 1.5 mL Eppendorf. RNA was isolated from TRIzol® lysates by adding 200 µL TCM (C2432) and shaking for 15 seconds. Samples were centrifuged in a Fisher-Scientific micro-centrifuge AccuSpin Micro 17 (Fisher Scientific, UK) at 13,000 rpm (16,200g) for 15 minutes.

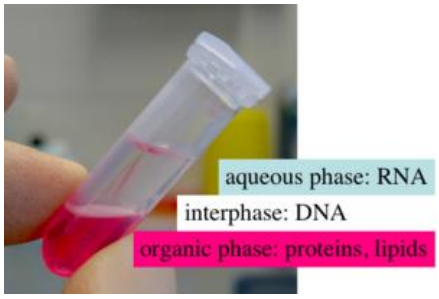

Figure 3-4: Trichloromethane separated TRIzol® lysate following centrifugation. Labels denote phases and contents.

Eppendorf's were carefully removed from the centrifuge and the aqueous phase was transferred into a fresh 1.5 mL Eppendorf. 500 µL of 100% isopropanol was added to the supernatant and incubated at room temperature for 10 minutes to precipitate the RNA. Samples were centrifuged for 15 minutes at 13,000 rpm with aligned hinges to pellet the RNA in the Eppendorf's. Supernatant was removed and pellet was washed with 1 mL of 70% ethanol and centrifuged for 15 minutes at 13,000 rpm. Supernatant was removed and pellet was allowed to air dry upside down on a clean surface. Pellet was suspended in 15 µL RNase-free water, Eppendorf's were incubated in a water bath for 10 minutes at 65^{o}C to aid pellet resuspension. Eppendorf's were then cooled on ice for 5 minutes to condense the RNA-water suspension and 'pulse' centrifuged for 5 seconds to collect the sample at the bottom of the tube. RNA was stored at -80^{o}C thereafter.

3.6.5.2 Complementary DNA synthesis

Complementary DNA (cDNA) synthesis is a technique used to convert mRNA into cDNA using reverse transcriptase and DNA polymerase enzymes. Sample RNA was first thawed and 1 µg added into a 0.2 mL RNase-free Eppendorf tube. 4 µL of mix 1 (table 3-3) was added to each sample and tubes were incubated at 70^{o}C for 5 minutes using a PTC-200 Peltier thermal cycler with 96-well alpha unit block assembly (MJ Research, Minnesota, USA). Tubes were cooled on ice for 2 minutes and briefly centrifuged to pool the condensate. 8 µL of mix 2 (table 3-3) was added to each sample to make a final volume of 20 µL. The tubes were then incubated at 37^{o}C for 50 minutes and at 70^{o}C for 15 minutes. cDNA was stored at -20^{o}C. cDNA samples were then diluted to 50 µL with DPEC-treated water.

Mix number	Reagent	Volume/sample (µL)
Mix 1	20 ng/µL – Random hexamers	1
	10 mM – dNTP mix	3
Mix 2	5X – First strand buffer	4
	0.1 M – DTT	0.125
	40 U/mL – RNaseOUT™	0.1
	MMLV	0.5
	DPEC-treated water	1.375

Table 3-3: Reagent mixtures for complementary DNA synthesis

3.6.5.3 Real Time – Polymer Chain Replication

2 µL of sample cDNA was added to into a 96 well clear MicroAmp® Optical 96-well reaction plate (Applied Biosystems, Life Technologies, I02N4Q). 8µL of 3' and 5' primer mixtures reaction plate (containing 1 mM/µL in DPEC-treated H_2O water) were added to the sample DNA for each gene. 10µL SYBR Green PCR Master Mix (Life-Technologies, 4309155) advantage reagent was added to every well and the plate was centrifuged using a Megafuge40 (Heraeus™, Frankfurt, Germany) centrifuge to remove and bubbles from the liquid. The reaction plate was loaded into an Applied Biosystems Real-Time PCR instrument (model: 7900HT, serial: 201456) and the appropriate method was selected on SDS2 (Applied Biosystems) software.

The method consisted of 3 stages:

1. Holding stage consisted of 50^{o}C for 2 minutes and 95^{o}C for 10 minutes.

2. Cycling steps included 95^{o}C for 15 seconds and 60^{o}C for 1 minute for 40 cycles.

3. Dissociation stage 95^{o}C for 15 seconds, 60^{o}C for 15 seconds and 95^{o}C for 15 seconds.

A dissociation stage was added following the cycling stage to determine that the correct amplicon was detected. SYBR green amplifies any double stranded DNA so it is important to assess the end products.

Human gene	Primer sequence sense/antisense	Reference
Internal control		
GAPDH	CTCTGCTCCTCCTGTTCGACA ACGACCAAATCCGTTGACTC	(Yang *et al.* 2011)
Osteogenic markers		
T2 Runx2	GGTTAATCTCCGCAGGTCAC GTCACTGTGCTGAAGAGGCT	(Yang *et al.* 2011)
OPN	TTTTCTGGATCCTCCATTGC CAAAAGCCATATGCTGCTCA	(Yang *et al.* 2011)
COL 1A1	ATGCCTGGTGAACGTGGT AGGAGAGCCATCAGCACCT	(Sarugaser *et al.* 2009)

Table 3-4: Human gene primer sequences

3.7 Microscopy

Cell culture progression was assessed using a Leica DMIL inverted light microscope with phase contrast filters. The resolution of transmission optical microscopes is limited due to the wavelength of light (λ) used and the refractive properties of the objective lens and the numerical aperture.

Cells were visualised using a Leica DM4000 B with a Leica EL6000 external light source for fluorescence excitation. Images were captured using a Leica DF310 FX camera and processed using the Leica application suite advanced fluorescence 3.1.0 build 8587 software (Leica microsystems, Wetzlar, Germany).

3.8 Image Analysis

ImageJ is a free software used for a variety of post-image processing applications. ImageJ was used to determine the shape factor circularity, a function of the perimeter P and the area A.

$$f_{circ} = \frac{4\pi . A}{P^2}$$

Equation 3-1: ImageJ shape factor calculation.

TIFF images (A) were first colour stacked to separate RBG channels (image→color→split channels). The red stack (stained actin) was used for morphological assessment (*B). The red image was first inverted (ctrl+shit+i) (C), cells at the periphery of the image were removed gating cells of interest and removing the outside (“clear outside”) (*D). Joined cells were then separated using the polygon tool to move cells to a free area (ctrl+x, ctrl+v) (*D). The cut cell area where cells were clearly overlapping was filled using the polygon tool (ctrl+f) (*D). A threshold (*E) was applied to each image to yield a solid black and white image (*F) for particle analysis. ROI manager was used to determine correct identification and analysis of single cells (*G) (*figure 3-5).

Following data collection 60 cells were randomly selected from the data set using Microsoft Excel 2013. This was achieved by generating a random number from 0-1 using “=rand()” for each data point. The data set was then indexed and ranked to 60 according to the randomly assigned number using the formula “=index(“random number range”,rank(“data range”))”.

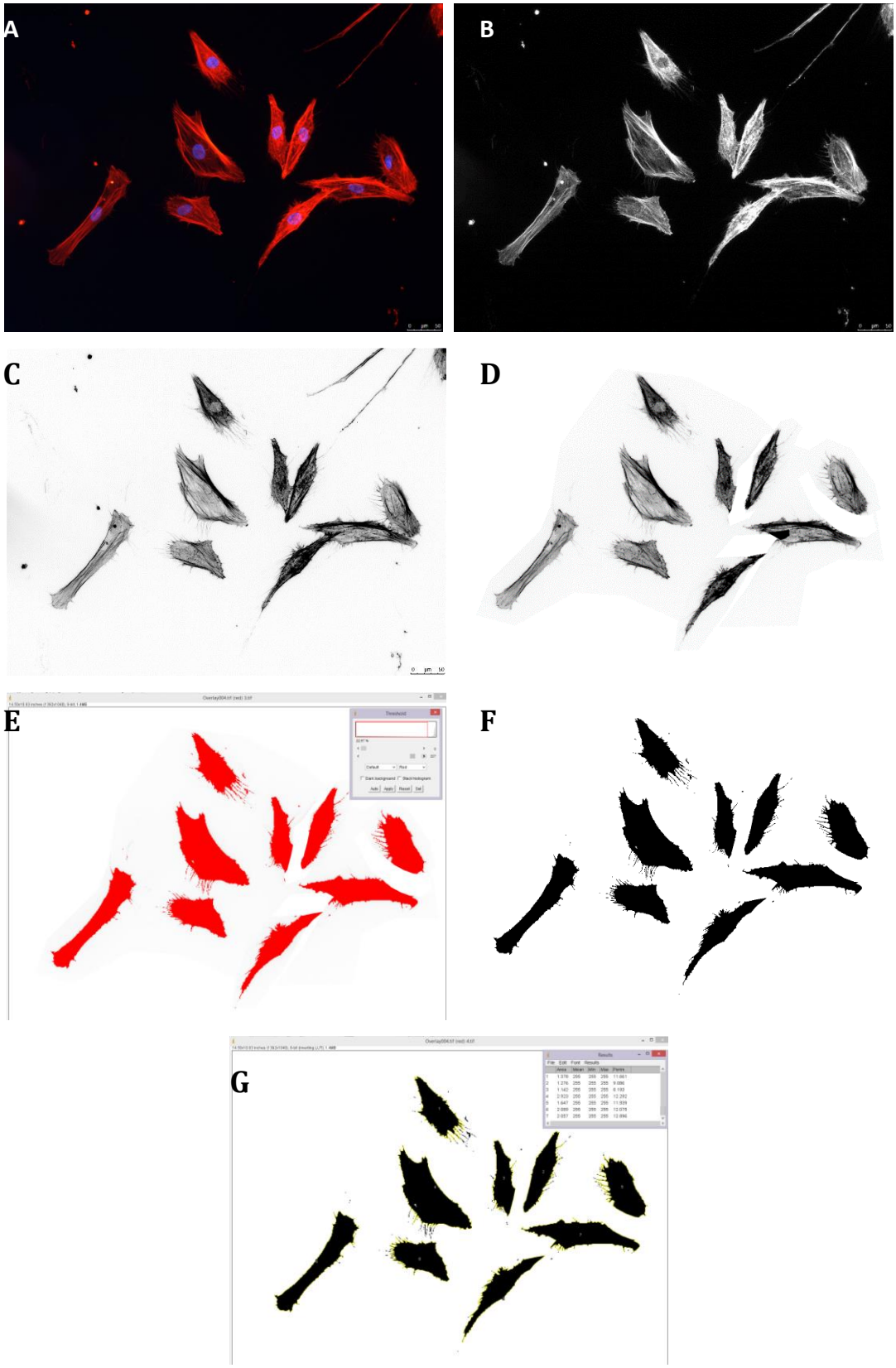

Figure 3-5: Example of image processing using ImageJ. A) RBG image, B) Red colour separated, C) B inverted, D) removal of peripheral cells and cell separation, E) thresholding, F) black and white image and G) analysis of particles and result output.

3.9 Statistical analysis

Data collected were first processed and formatted using Microsoft Excel 2013. Statistical data analysis was performed using both Minitab 16® and GraphPad Prism 5®. Anderson-Darling test was used to assess normality prior to statistical evaluation. One-way analysis of variance (ANOVA) were performed using a Tukey's HSD post-hoc test, two-way ANOVAs were performed when possible to determine variation between data sets. For missing values in a two and one-way ANOVA GraphPad Prism5® calculates the type III sum-of-squares using three times multiple regression (Glantz & Slinker 1990).

Chapter 4 – Sol-gel Synthesis and Characterisation of Hydroxyapatite Nanoparticles

4.1 Introduction

This chapter first aims to investigate key parameters influencing HAp crystal characteristics using a low temperature sol-gel synthesis technique. Key parameters include titration addition methodology, component addition rate and reaction vessel pH. Using the identified parameters, the aim is to tailor the sol-gel method to produce HAp crystals with specific characteristics. A variety of material characterisation techniques will be used to help characterise the physical properties of the HAp nanoparticles. The cytotoxicity of the HAp will be evaluated using an *in-vitro* viability assay with patient derived hMSC.

The aforementioned parameters were investigated due to the variation that exists throughout the literature without pinpointing an optimised procedure for fabricating reliably reproducible HAp particles by investigating the interaction on the multiple parameters that could potential influence the process. The pH of the reaction system is arguably one of the most critical factors governing crystal formation by influencing the organisation of the HAp at the atomic level. The availability of Ca^{2+} and PO_4^{3-} within the reaction vessel is equally as important as the pH which will be influenced by both the method of titration and also the addition rate.

There are a number of other variables which were not included, of which some have been investigated. The mixing of the components by sonication (Utara & Klinkaewnarong 2015), temperature (Bouyer *et al.* 2000), surfactants to govern crystal growth (Iyyappan *et al.* 2016; Wang *et al.* 2006) and addition of proteins to act as templates for HAp formation (Semino 2008; Uskoković *et al.* 2011; Jahromi *et al.* 2013).

The aspect ratio of nanoparticles has been linked to a number of important influences on optical properties in gold nanoparticles (Link *et al.* 1999) nanocomposite mechanical properties (Fu *et al.* 2008), cytotoxicity (Murphy *et al.* 2008) and cellular uptake (Qiu *et al*. 2010).

4.2 Materials and Methods

4.2.1 *Preparation of Hydroxyapatite*

HAp was prepared using a modified sol-gel similar to those described by other authors (Bakan *et al.* 2013; Jadalannagari *et al.* 2011; Marković *et al.* 2011; Yubao *et al.* 1994; Wang *et al.* 2010; Iyyappan *et al.* 2016; Wang *et al.* 2007; Kumar *et al.* 2004; Ramesh *et al.* 2015; Vázquez-Hernández *et al.* 2010; Ha *et al.* 2015; Huang *et al.* 2012). Aqueous solutions of $CaCl_2$ 200 mM (calcium chloride), Na_2HPO_4 120 mM (sodium phosphate dibasic) and NaOH 50mM (sodium hydroxide) were prepared using deionised water. These solutions were stored and used for up to 1 week. The precipitation reaction between the calcium and phosphate precursor solutions produces acid by-products and pH was controlled by the automated addition of the sodium hydroxide solution. Precursor components were titrated at a specific addition rate and pH was regulated with the use of the 907 Titrando Metrohm dual burette 800 DOSINO system and Tiamo 2.0 software. The order of precursor component additions was also modified to investigate method differences in resulting HAp powders.

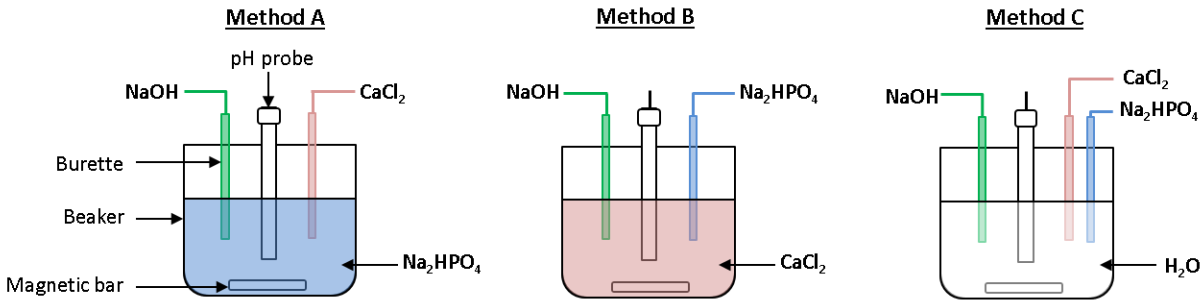

Figure 4-1: Schematic representation of titration methodologies A, B and C. Method A) calcium is titrated into an excess of phosphate. Method B) Phosphate is titrated into an excess of calcium. Method C) calcium and phosphate are titrated simultaneously into a medium of water.

A variety of methodologies were generated within the Tiamo 2.0 to investigate differences in precipitation parameters on crystal morphology, crystallinity, composition and chemical interactions (section **Error! Reference source not found.**).

The following is an example procedure for the control HAp titration method (method A, 0.1 mL/min addition rate and stabilised at pH 10). 50 mL of Na_2HPO_4 120 mM was loaded into a 500 mL Pyrex beaker with magnetic stirrer bar. The beaker with solution and magnetic stirrer bar was placed on a IKA® C-MAG HS7 hot plate (Staufen, Germany) at stirred at '3'. The 800

DOSINO burettes and pH meter were fastened in place in the beaker using a retort clamp and clamp stand. The Tiamo2.0 software method was then started with following program.

Set pH 10: pH of the Na_2HPO_4 120 mM solution was monitored for 30 seconds before NaOH is added incrementally with a maximum addition rate of 2.5 mL/min to achieve pH 9.8. Upon attainment of pH 9.8 the method waited for 30 seconds to allow for pH drift. The software then initiated two protocols 1: maintain pH 10 and 2: dose component. The maintain pH protocol aimed to keep the pH of the reaction to pH 10 ± 0.05 for the duration of the titration. The dose component was set up to titrate 50 mL of the $CaCl_2$ 200 mM solution into the Na_2HPO_4 120 mM reservoir at an addition rate of 0.1 mL/min. The total time taken for the titration was 500 minutes or 8 hours 20 minutes.

4.2.1 *Titration parameters*

Calcium phosphates generated using method outlined in section 4.2.1 were titrated using different parameters defined in **Error! Reference source not found.**. The default- control set of parameters are described as method A and the other methods contain small alteration in one parameter at a time.

		Titration parameter				
	Method	pH	Rate (ml/min)	Volume (mL)	Time (minutes)	Temperature (°C)
Control	A	10	0.1	50	500	25
4.3.2 Addition Method	**B**	10	0.1	50	500	25
	C	10	0.1	50	500	25
4.3.3 Addition Rate	A	10	**1.0**	50	50	25
	A	10	**10.0**	50	5	25
4.3.4 Addition pH	A	**9**	0.1	50	500	25
	A	**8**	0.1	50	500	25
4.3.5 "Tailored HA"	A	**8**	**1.0**	50	50	25

Table 4-1: Hydroxyapatite reaction vessel and titration parameters.

4.2.2 *Post-titration processing*

The reaction fluid was dialysed using cellulose dialysis tubing in >1 L dH_2O for 72 hours and water was replaced every 24 hours. The precipitate was then autoclaved using an Astell (UK) steam-air autoclave at 121°C temp and 1.037 bar pressure for 30 minutes. Following the precipitate was frozen at -80°C for 24 hours and freeze dried in an ALPHA 1-2 LDplus (Martin Christ Freeze Dryers GmbH, UK) for 24 hours at -52°C <0.0005 mbar. The resultant powder was stored in a desiccator for subsequent materials analysis and scaffold fabrication.

4.2.3 *X-Ray Diffraction (XRD)*

X-Ray diffraction spectra of hydroxyapatite powders were measured using a PANalytical X'Pert Pro MPD and powered by a Phillips PW3040/60 X-ray generator. X-rays were filtered using a real time multiple strip technology X'Celerator detector. Diffraction data was acquired by exposing powder samples to Cu-K_α X-ray radiation with a characteristic wavelength (λ) of 1.5418 Á. X-rays were generated using a Cu anode supplied with 40 kV and a current of 40 mA.

Data was collected over a ranged of 2 – 80 °2θ with a step size of 0.0334225 °2θ and a nominal time per step of 200.025 milliseconds, using the scanning X'Celerator detector. Fixed anti-scatter and divergence slits of 0.38 mm were used together with a beam mask of 10 mm and all scans were carried out in 'continuous' mode.

Phase identification was carried out by means of X'Pert accompanying software program PANalyical High Score Plus in conjunction with the ICDD Powder Diffraction File 2 Database (1999), ICDD Powder Diffraction File 4 – Minerals (2012), the American Mineralogist Crystal Structure Database (March 2010) and the Crystallography Open Database (February 2013; www.crysallography.net).

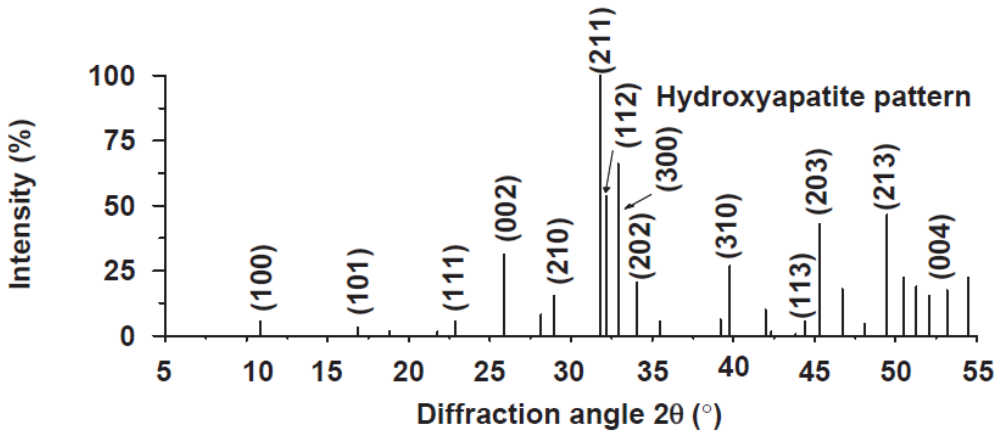

Figure 4-2: Highly crystalline hydroxyapatite characteristic XRD line pattern (Rusu et al. 2005).

Crystals are regular arrays of atoms and elastic scattering of X-ray from atoms can be used to determine crystal planes. These crystal planes lie orthogonal to the reflective angle denoted by the miller indices with curved brackets (hkl). These crystal planes lie parallel along an axis called the crystal direction and has the same hkl nomenclature as the planes, however is denoted by square brackets [hkl].

With nanoscale materials the size of a specific direction forming a crystal plane can be estimated by using the Scherrer formula. However XRD is sensitive to the size of coherent scattering domains which can significantly differ from particle size, with lattice defects or amorphous surface layers (Borchert *et al.* 2005).

Crystallite size was calculated using Scherrer formula (equation 4-1). The full width at half maximum (FWHM) of Si (111) at position 2.8443 °2θ was used to calibrate FWHM peak values of hydroxyapatite at (002) (~29.91°2θ) and (110) (~16.84°2θ).

$$\tau = \frac{K\lambda}{\beta \cos\theta}$$

Equation 4-1: τ, refers to the mean size of the ordered crystalline domains. K, is the shape factor, which varies with the actual shape of the crystallite. λ, is the X-Ray wavelength. β, is the distance in °2θ at the full width at half maximum (FWHM) of a unique peak. θ, is the Bragg angle.

The crystallite direction at [002] was chosen to allow characterisation of the *c*-axis length and perpendicular *ab*-axis at [110] of the crystallite direction (Jevtic *et al.* 2008).

4.2.4 *Fourier Transformed Infrared Spectroscopy*

FTIR was performed according to materials and methods section 0. Similar to literature published by Marković *et al.* (2011) carbonate vibrational modes have been labelled according to their crystal position. A-type carbonate ions refer to CO_3^{2-} occupying the OH^- sites and B-type, where CO_3^{2-} ions occupy PO_4^{3-} sites.

4.2.5 *Cell viability assay (MTT)*

Osteoarthritic patient derived hMSC were isolated from donated femoral heads subsequent to total hip replacement surgery (methods section 3.5.3). hMSC were seeded into a 48 – well plate at 20,000 cells/well and allowed to attach for 24 hours.

HAp was weighed, washed with 100% ethanol and ultrasonically agitated for 1 hour. The HAp ethanol solution was centrifuged at 400g for 5 minutes (to pellet the HAp) and washed with PBS, this was repeated three times for each HAp powder to remove any ethanol from the solution. hMSC medium was added the HAp pellet to make a 500 mg/mL stock solution, this was then serially diluted in hMSC to make the media for the experiment. hMSC media ranging from 0 – 500 mg/mL were ultrasonically agitated for 10 minutes prior to their application to the pre-seeded 48 well hMSC seeded monolayers.

Following 24 hours incubation the media was removed and replaced with 0.5 mg/mL MTT working solution (see section 3.6) for 2 hours. The MTT solution was carefully removed and the monolayer washed with PBS. 300 µL of DMSO was added to each well and the plate was agitated at room temperature wrapped in aluminium foil for 10 minutes. 200 µL of the DMSO/dye was added to a 96 well plate and absorbance was read at 570nm. Results were displayed as percentage cell viability relative to control (0 mg/mL HAp = 100%).

4.3 Results

HAp synthesised from the parameters shown in table ***4-1*** were first characterised using a variety of techniques to assess the size, morphology, chemical composition and crystallinity of the synthesise nanocrystals. As a reference, HAp powder synthesised with method A, at pH 10, with 0.1 mL/min rate of component addition with standard post processing procedures was used as a control.

4.3.1 *Transmission electron microscopy*

TEM was used throughout the course of this study to observe the morphology of fabricated calcium phosphate crystals. Figure 4-3 shows images of the same cluster of HAp with minimal and prolonged exposure to electron bombardment at 1000 kV.

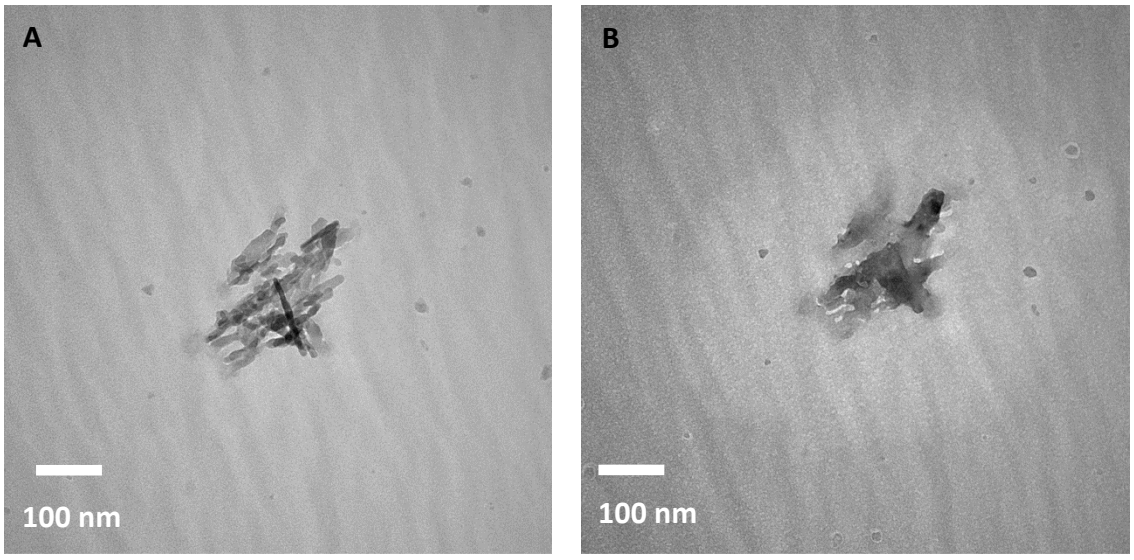

Figure 4-3: TEM images of control hydroxyapatite degradation with exposure to electron bombardment. A) First image B) 2 minutes, 5 seconds post image A. Images were collected on 30/07/2013. A) [13:25:16] & B) [13:27:21].

The TEM imaging of HAp particles yielded the loss of graphical definition of individual crystals with prolonged observation (figure 4-3).

4.3.2 *Influence of component addition methodology*

This section investigates the influence of component addition method on the variation in resultant HAp crystal morphology, crystal size and Ca/P ratio. The influence of section 4.2.1 methods A, B and C were observed whilst maintaining control pH, and titration rate. Variables examined throughout this section are summarised below in table 4-2).

KEY	Method	pH	Rate (ml/min)	Volume (mL)	Time (minutes)	Temperature (°C)
Addition method	A – Calcium ↓ Phosphate	10	0.1	50	500	25
	B – Phosphate ↓ Calcium	10	0.1	50	500	25
	C – Calcium + Phosphate	10	0.1	50	500	25

Table 4-2: Section key for titration parameters investigating addition methodology.

4.3.2.1 Energy-Dispersive X-Ray Spectroscopy

EDX analysis was used to determine elemental composition and extrapolate calcium/phosphate ratio.

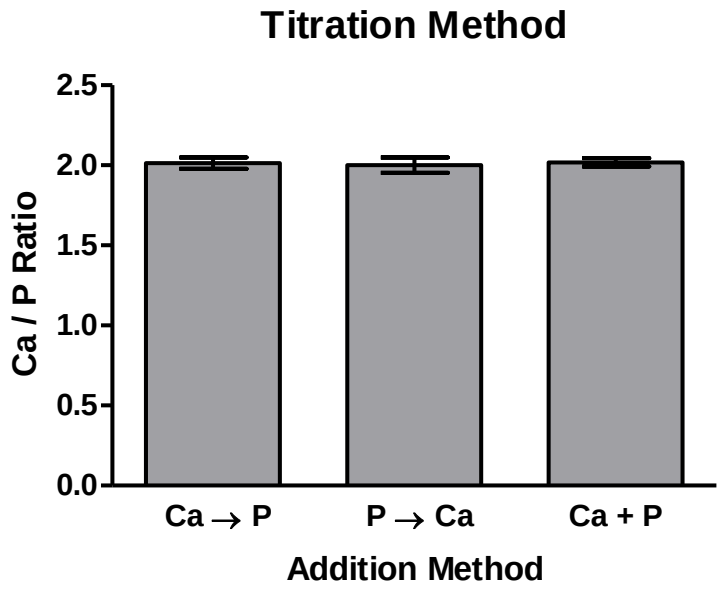

Figure 4-4: EDX analysis of titrated hydroxyapatite powders Calcium to Phosphate ratio. (n = 3)

EDX analysis of titration rates shown in figure 4-4 revealed a Ca/P ratio of ~2.0 with no significant variation found between HAp synthesised at all titration rates.

4.3.2.2 Transmission Electron Microscopy

TEM was used to provide information on HAp crystal morphology to provide an insight into how the various methodologies are influencing crystal synthesis.

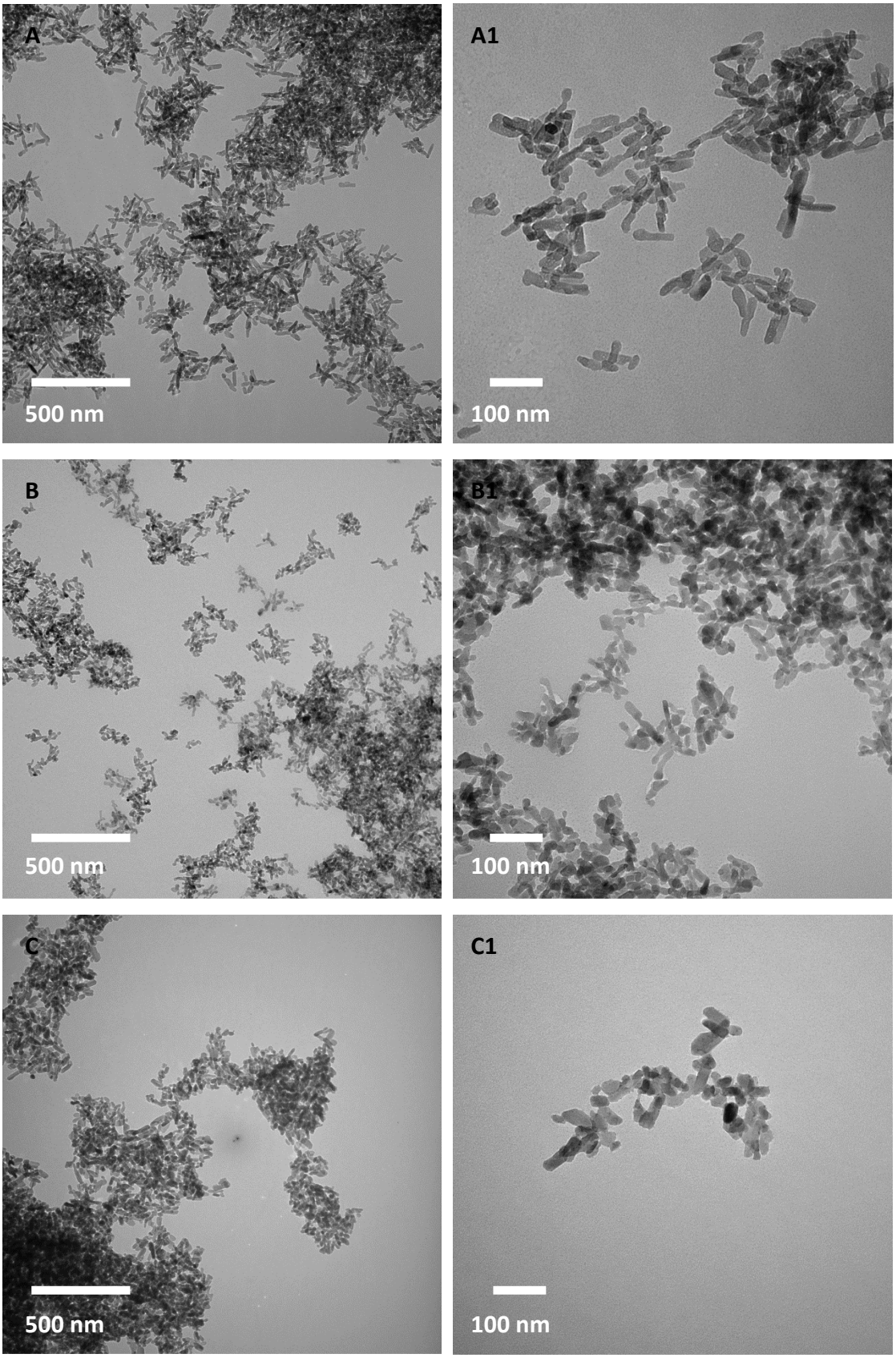

Figure 4-5: Representative TEM images of HAp synthesised with different precipitation rates. A) Method A, B) Method B, C) Method C. Images were collected on A) 18/12/12, B & C) 30/07/13.

Observations from figure 4-5 show subtle variations in crystal morphology throughout the different methodologies. The reference nanocrystals (figure 4-5 A) titrated at pH 10, 0.1 mL/min with titration method A appears to have a rod-like morphology with lengths of approximately 50 nm. Crystals formed via method B and C (figure 4-5 B & C) seem to form a similar morphology to reference HAp, with apparent heterogeneity in size.

4.3.2.3 X-Ray Diffraction

XRD analysis was used to characterise phase composition and crystallinity of the titrated calcium phosphate powder.

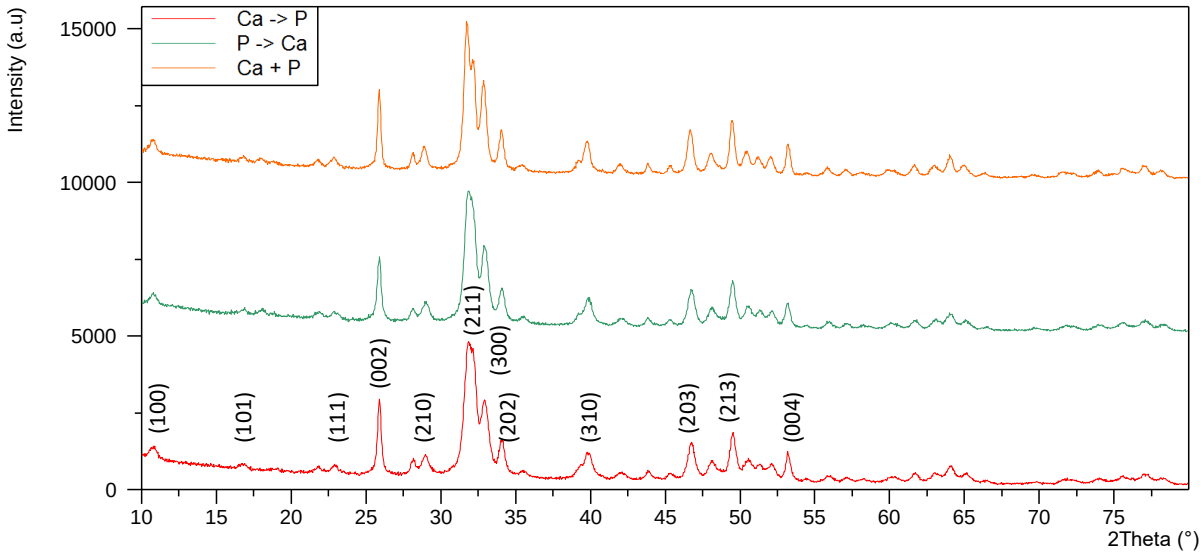

Figure 4-6: Representative XRD spectra for hydroxyapatite powders synthesised with various titration methodologies.

The XRD patterns (figure 4-6) of the powders synthesised using various addition methodologies are labelled with notable crystal planes. The powders demonstrated broad X-Ray diffraction peaks. No significant diffraction peak was observed at $2\theta = 45.5^{o}$ demonstrating removal of NaCl by the wash process. Using Scherer's formula (equation 4-1) from section 4.2.3 average crystal dimensions were calculated to provide quantitative information on HAp precipitated with different titration methodologies.

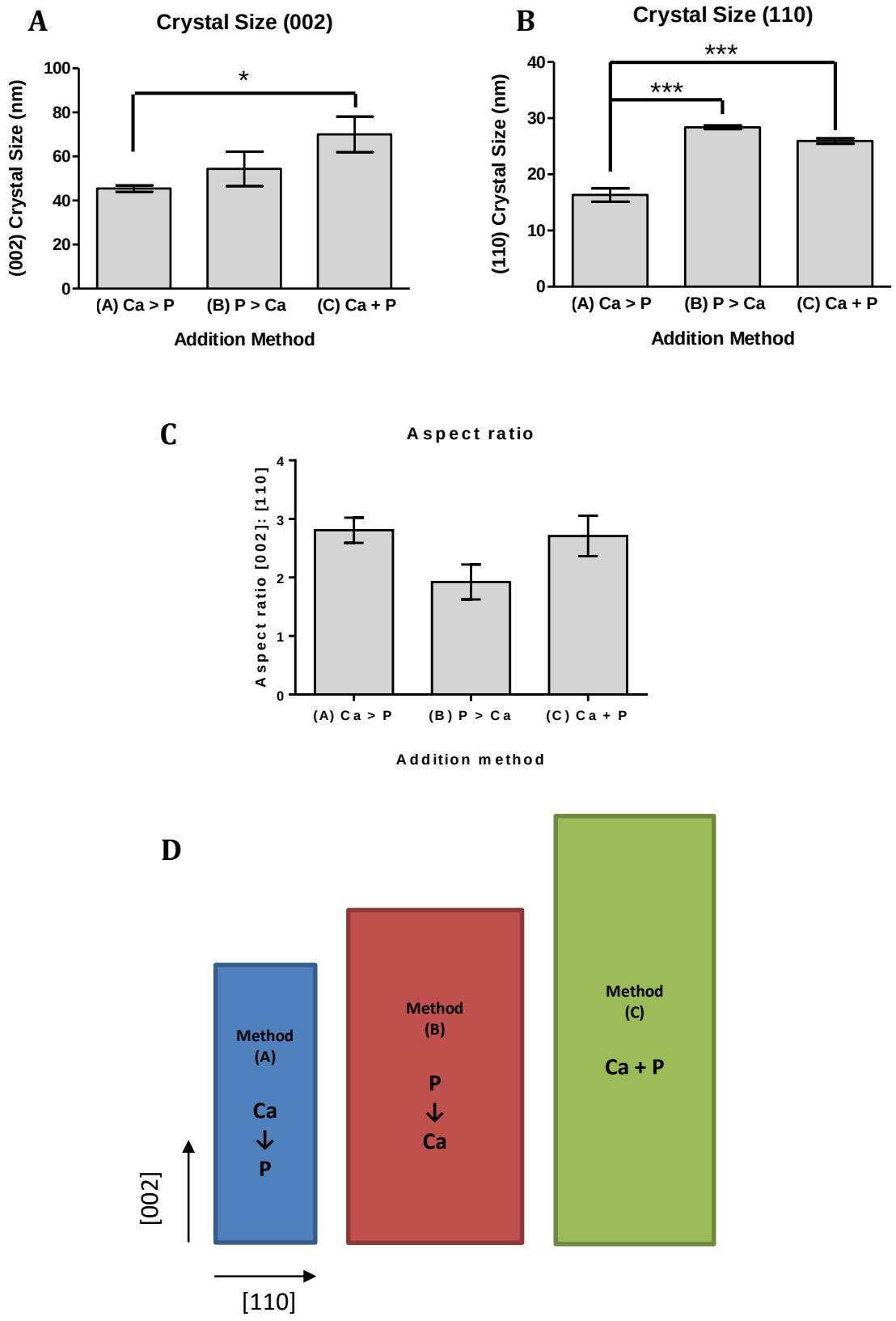

Figure 4-7: XRD derived crystallite size calculated using equation 4-1). A & B) Bars show the mean ± SEM [002] & [110] crystal direction of HAp synthesised with various titration methodologies (n=3). C) Average aspect ratio of the HAp nanoparticles D) 1 x 10^6 scale graphical representation of HAp crystal dimensions.

Figure 4-7A displays increased crystal length [002] with dual titration methodology in comparison to the alternative single reservoir addition methods with significant differences observed in between control. Figure 4-7B shows a significant increase in crystal width in HAp titrated with both phosphates into excess calcium and dual titration methodologies in comparison with control. HAp aspect ratios demonstrated a range from 1.92 (P → Ca) to 2.8 (Ca → P), however no significant differences were observed between the groups (figure 4-7 C).

Fourier Transformed Infrared Spectroscopy

FTIR analysis was used to determine influences to molecular groups included in the unit cells of the HAp structure. The three HAp powders from the different component addition methodologies are shown in figure 4-8.

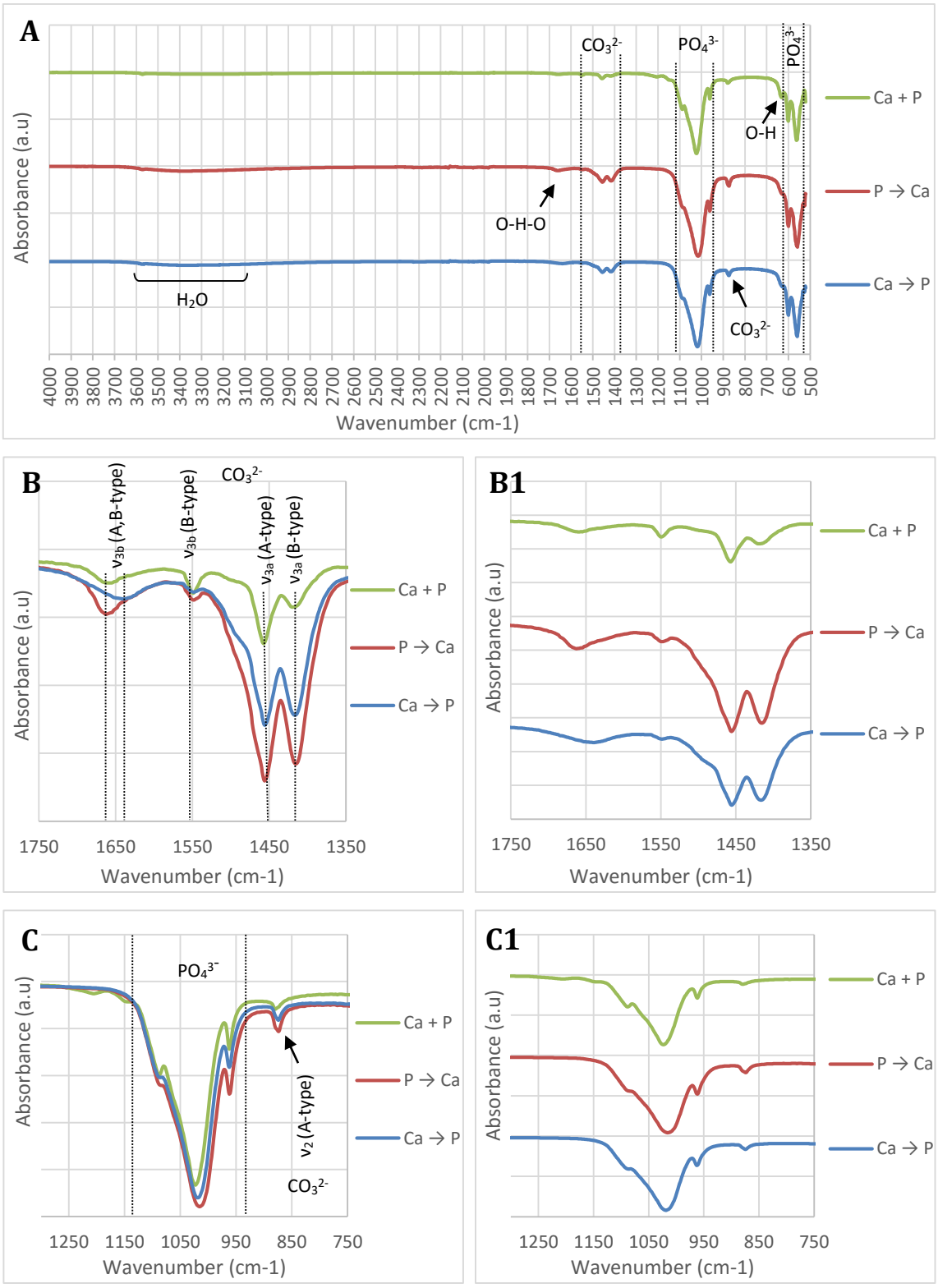

Figure 4-8: FTIR spectrum of dry hydroxyapatite powder. Each line represents the mean of three titration samples. Ca → P, P → Ca and Ca + P refer to addition methodologies (A-C respectively). A) Full 500-4000 cm^{-1} stacked spectrums B) narrow scan 1750-1350 $cm^{-1}$of A. B1) spectra from B stacked. C) Narrow scan 1300-750 cm^{-1} of A, C1) Spectra from C stacked.

Figure 4-8(A) shows the FTIR spectrum of the three synthesised HAp powders using various titration methodologies. All powders show strong absorption bands that can be attributed to HAp: $v_3PO_4^{3-}$ at 1045 -1092 cm^{-1} and v_2PO_4 at 474 cm^{-1}, v_1PO_4 symmetric stretch at 963 cm^{-1}, v_4PO_4 from 602- 572 cm^{-1}. Absorption peaks at 1415 cm^{-1} and 1455 cm^{-1} appeared lower in HAp titrated using the dual addition methodology relative to HAp titrated using reservoir addition methods.

4.3.3 *Influence of component addition rate*

Changing the addition rate of titration components is one of the key variables in manufacturing large quantities of HAp for biomedical uses. Controlling the component addition rate and the reaction pH during the titration is the main advantage of using this system, this section characterises HAp synthesised using three titration rates (table 4-3). The hypothesis for this section is that titration rate will significantly alter final HAp crystal characteristics. Variables examined throughout this section are summarised below in (table 4-3).

KEY	Method	pH	Rate (ml/min)	Volume (mL)	Time (minutes)	Temperature (°C)
Addition rate	A – Calcium ↓ Phosphate	10	0.1	50	5	25
	A – Calcium ↓ Phosphate	10	1.0	50	50	25
	A – Calcium ↓ Phosphate	10	10.0	50	500	25

Table 4-3: Section key for titration parameters investigating component addition rate.

4.3.3.1 Energy-Dispersive X-Ray Spectroscopy

EDX analysis was used to determine elemental composition and extrapolate calcium/phosphate ratio.

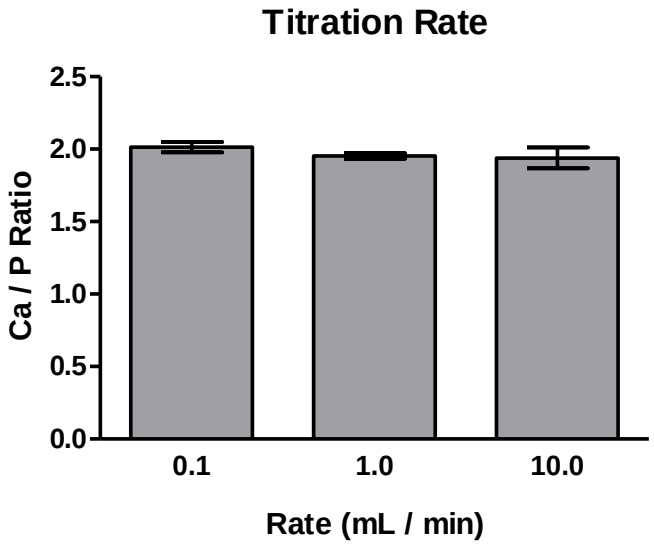

Figure 4-9: EDX analysis of titrated hydroxyapatite powders Calcium to Phosphate ratio. (n = 3).

EDX analysis of titration rates shown in figure 4-9 revealed a Ca/P ratio of ~2.0 with no significant variation found between HAp synthesised at all titration rates.

4.3.3.2 Transmission Electron Microscopy

The morphology of HAp titrated at different titration rates was investigated using TEM. A summary of the titration parameters for the HAp discussed in this section are outlined in table 4-3.

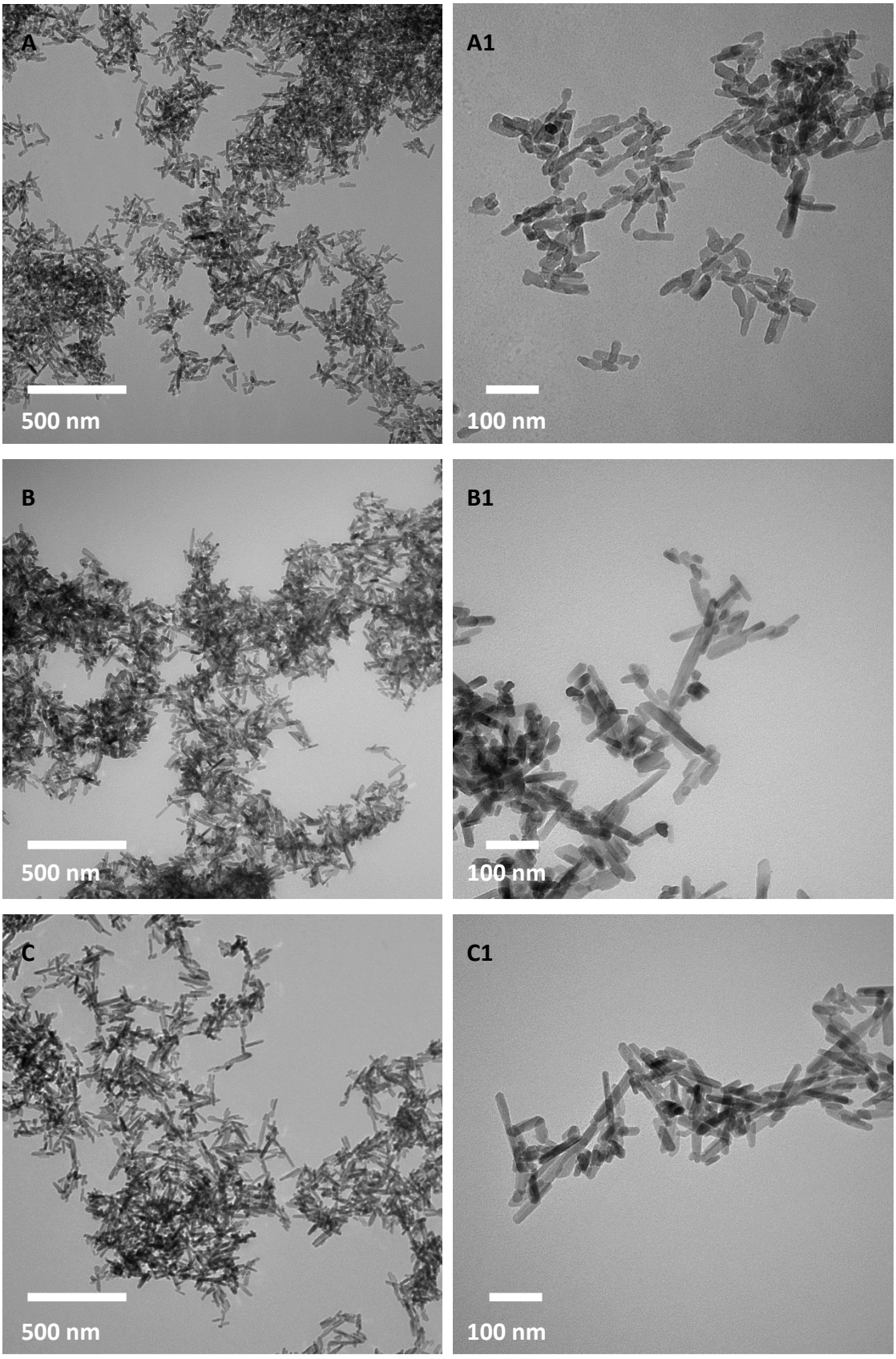

Figure 4-10: Representative TEM images of HAp synthesised with different precipitation rates. A) 0.1 mL/min, B) 1.0 mL/min, C) 10 mL/min. Images were collected on A) 18/12/12, B & C) 30/07/13.

Images from figure 4-10 revealed similar rod-like morphologies with HAp titrated at 1 mL/min and 10 mL/min compared with control HAp 0.1 mL/min. HAp crystal sizes appear to be larger with increased titration rates evident in figure 4-10 B1 and C1.

4.3.3.3 X-Ray Diffraction

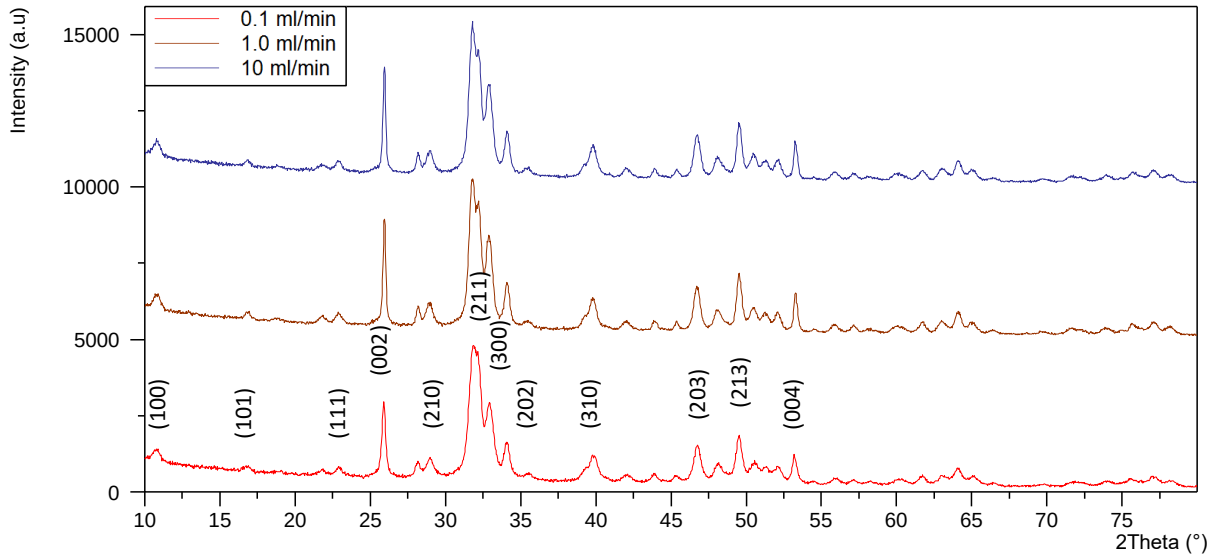

Figure 4-11: Representative XRD spectra for hydroxyapatite powders synthesised with various titration rates.

XRD patterns of HAp synthesised using various component titration rates are displayed with labelled notable crystal planes (figure 4-11). The powders demonstrated broad X-Ray diffraction peaks. No significant diffraction peak was observed at $2\theta = 45.5^{o}$ demonstrating removal of NaCl by the wash process. Using Scherer's formula (equation 4-1) from section 4.2.3 average crystal dimensions were calculated to provide quantitative information on HAp precipitated with different titration methodologies.

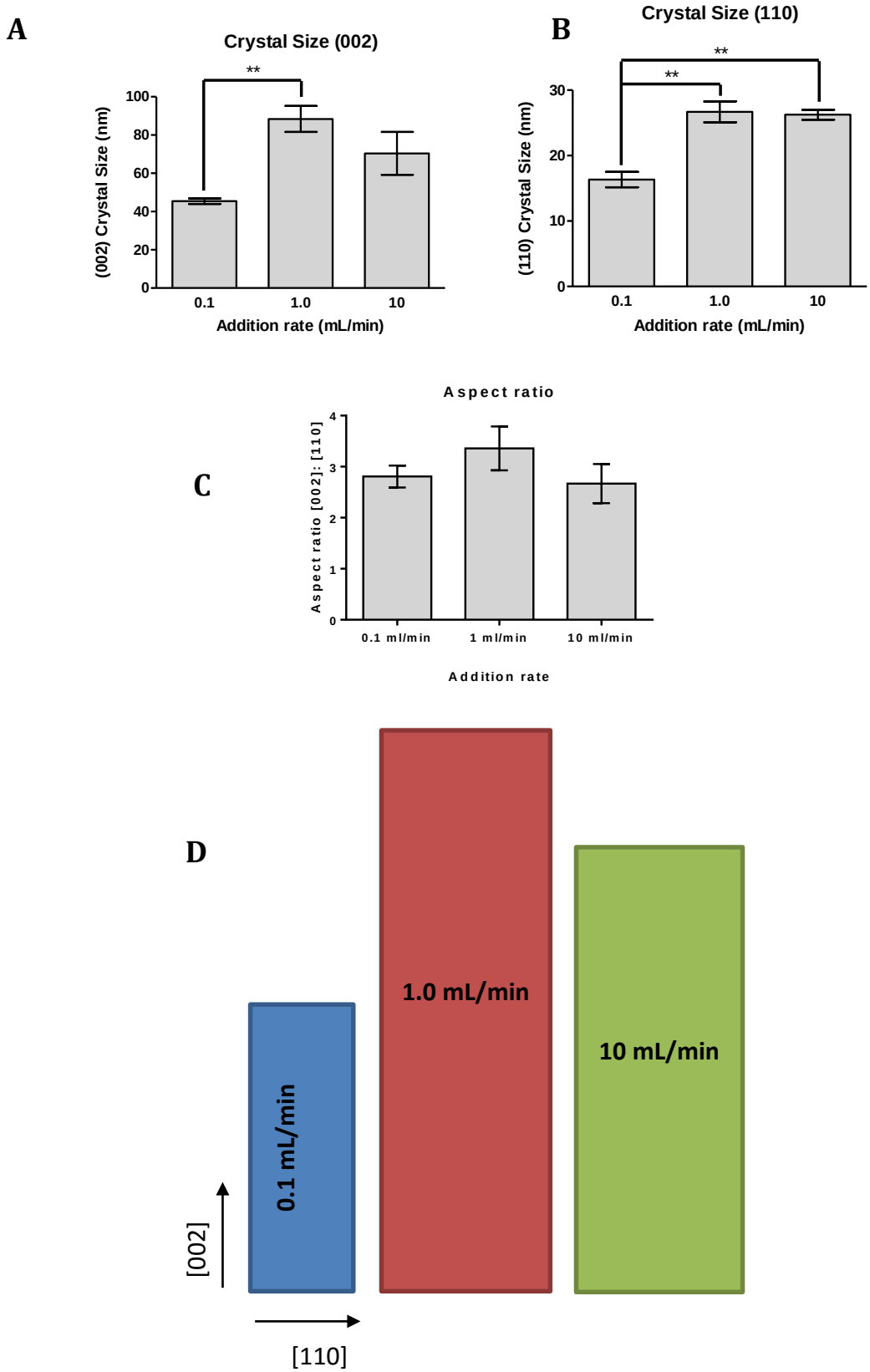

Figure 4-12: XRD derived crystallite size calculated using equation 4-1). A & B) Bars show the mean ± SEM [002] & [110] crystal direction of hydroxyapatite powder synthesised with various titration rates (n=3). C) Average aspect ratio of the HAp nanoparticles D) 1 x 10^6 scale graphical representation of HAp crystal dimensions.

Average crystallite planes shown in figure 4-12 A & B show variation in HAp dimensions with synthesis at different titration rates. Figure 4-12 A shows a significant increase the particle size in [002] crystal direction of HAp with 1.0 mL/min titration rate in comparison to control (0.1 mL/min). No significance was observed in [002] crystal direction of HAp titrated at 10 mL/min compared with both 0.1 and 1 mL/min addition rates. Figure 4-12 B shows a significant increase in crystal [110] direction in HAp titrated at 1.0 and 10 mL/min compared with control (0.1mL/min). HAp aspect ratios demonstrated a range from 2.67 (10 mL/min) to 3.36 (1 mL/min), however no significant differences were observed between the groups (figure 4-12 C).

4.3.3.4 Fourier Transformed Infrared Spectroscopy

FTIR analysis was used to determine influences to molecular groups included in the unit cells of the HAp structure. The three HAp powders from the different titration rates are shown in figure 4-13.

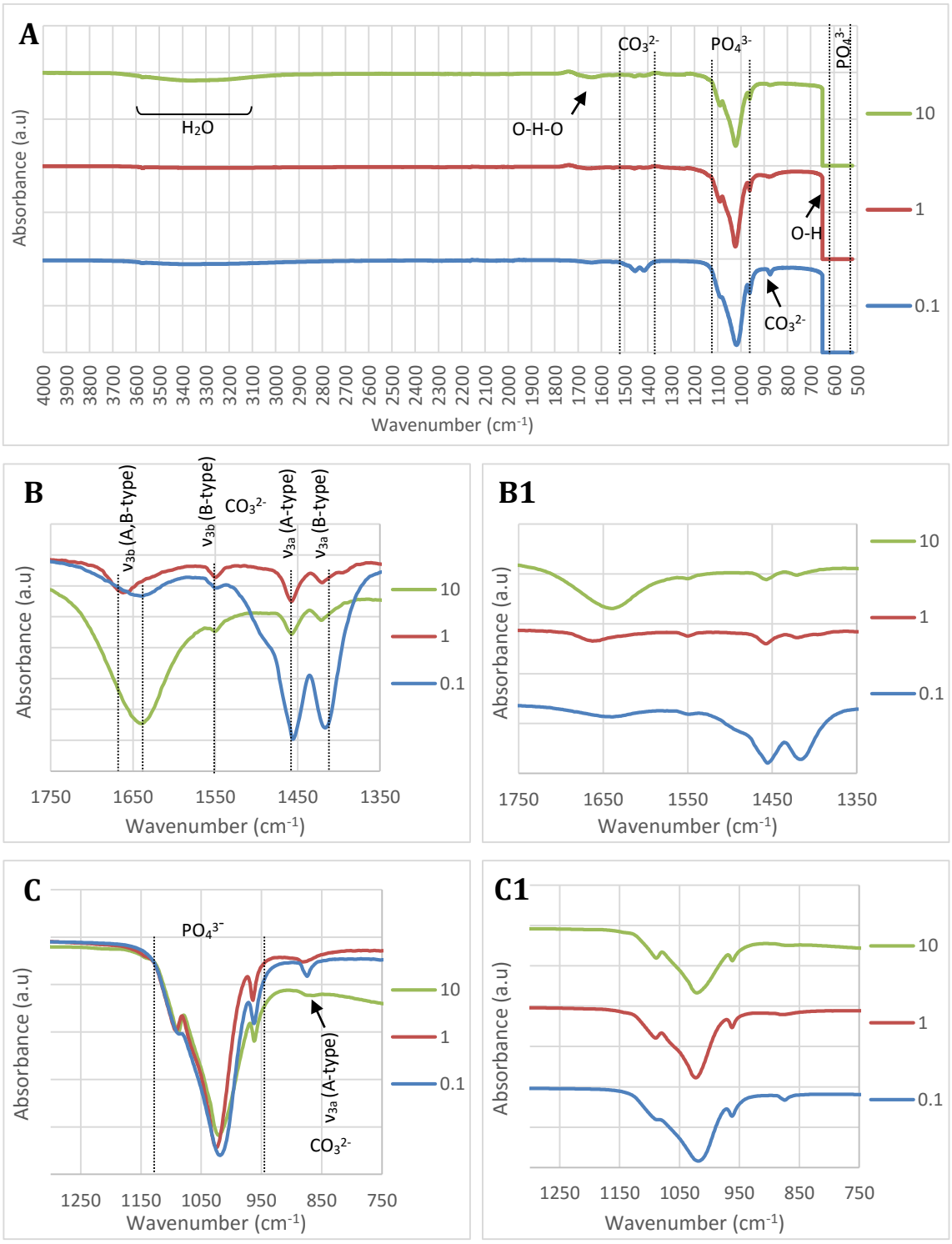

Figure 4-13: FTIR spectrum of dry hydroxyapatite powder. Each line represents the mean of three titration samples. 0.1, 1 and 10 refer to component addition rate in mL/min. [A] Full 650-4000 cm^{-1} stacked spectrums [B] narrow scan 1750-1350 $cm^{-1}$of A. [B1] spectra from [B] stacked. [C] Narrow scan 1300-750 cm^{-1} of [A], [C1] Spectra from [C] stacked.

Figure 4-13 A shows the FTIR spectrum of three HAp powders synthesised at different titration rates. All powders show similar phosphate absorption bands vibrational bonds $v_3PO_4^{3-}$ at 1045-1092 cm^{-1} and v_2PO_4 at 474 cm^{-1}, v_1PO_4 symmetric stretch at 963 cm^{-1}, v_4PO4 from 602-572 cm^{-1}. Broad absorption peaks were observed in HAp titrated at 10 mL/min from ~3100 cm^{-1} – ~3600 cm^{-1} and at ~1650 cm^{-1} with higher absorption peaks relative to HAp titrated at 0.1 and 1.0 mL/min. Absorption peaks at 1415 and 1455 cm^{-1} appeared lower in HAp titrated at 1.0 and 10.0 mL/min compared with control.

4.3.4 *Influence of reaction pH*

The reaction pH of HAp particle synthesis is a fundamental parameter governing HAp morphology, ergo reaction pH was varied using methods outlined in section 4.2.1 The hypothesis for this section is that titration pH will significantly alter final HAp crystal characteristics. A summary of the titration parameters for the HAp discussed in this section are outlined in table 4-4.

KEY	Method	**pH**	Rate (ml/min)	Volume (mL)	Time (minutes)	Temperature (°C)
Reaction pH	A – Calcium ↓ Phosphate	**10**	0.1	50	500	25
	A – Calcium ↓ Phosphate	**9**	0.1	50	500	25
	A – Calcium ↓ Phosphate	**8**	0.1	50	500	25

Table 4-4: Section Key of reaction pH variables.

4.3.4.1 Energy-Dispersive X-Ray Spectroscopy

EDX analysis was used to determine elemental composition and extrapolate calcium/phosphate ratio.

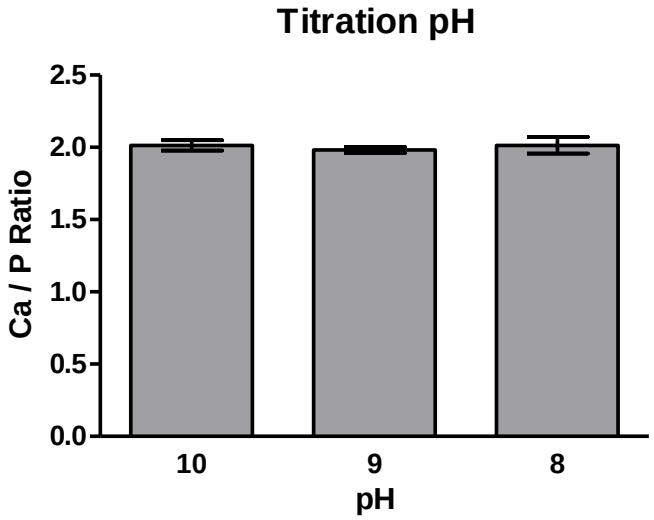

Figure 4-14: EDX analysis of titrated hydroxyapatite powders Calcium to Phosphate ratio. (n = 3)

EDX analysis of titration rates shown in figure 4-14 revealed a Ca/P ratio of ~2.0 with no significant variation found between HAp synthesised at all titration rates.

4.3.4.2 Transmission Electron Microscopy

The morphology of HAp titrated at different reaction vessel pH was investigated using TEM.

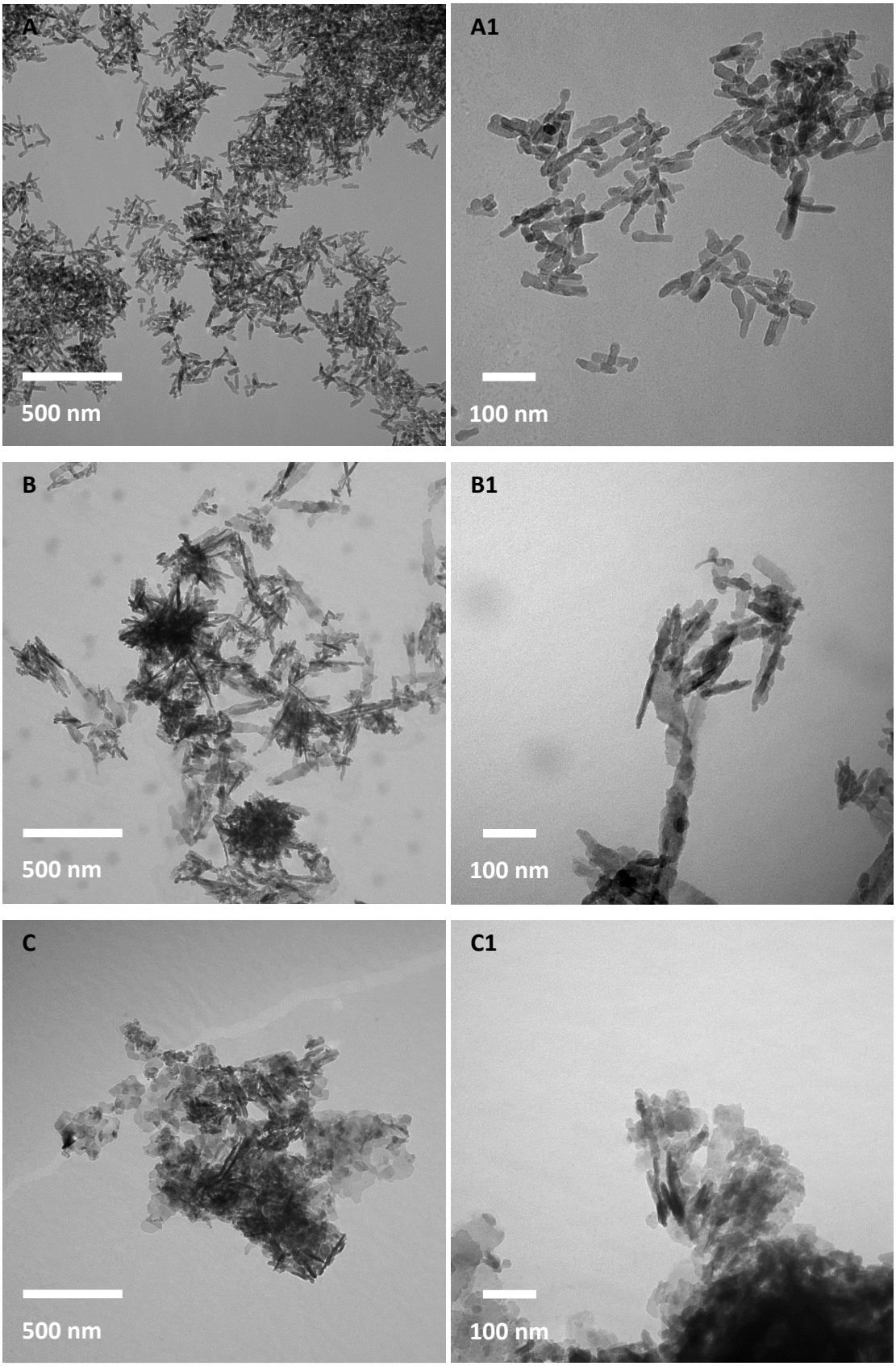

Figure 4-15: Representative TEM images of HAp synthesised with different reaction vessel pH. A) pH 10, B) pH 9, C) pH 8. Images were collected on A) 18/12/12, B & C) 30/07/13.

Figure 4-15 illustrates representative images of HAp crystals synthesised under various reaction vessel pH. The rod-like morphology of the HAp appears more plate-like with the reduction in titration pH from figure 4-15 A-C. Crystal sizes appeared to become more heterogeneous in nature with decreased pH titration environments.

4.3.4.3 X-Ray Diffraction

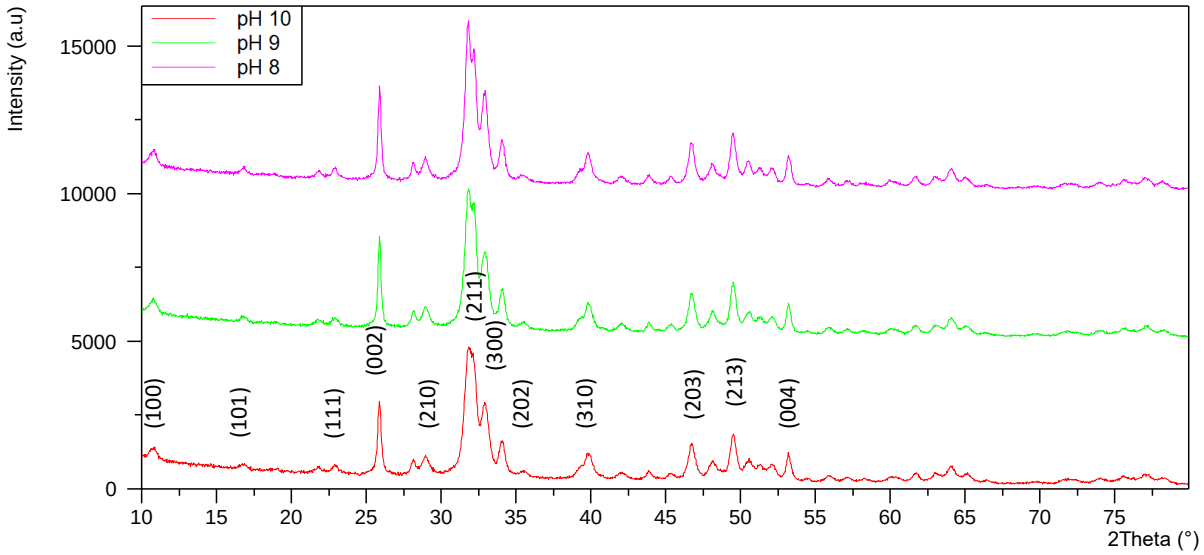

Figure 4-16: Representative XRD spectra for hydroxyapatite powders synthesised with various titration methodologies.

XRD patterns of HAp synthesised using various component titration rates are displayed with labelled notable crystal planes (figure 4-16). The powders demonstrated board X-Ray diffraction peaks. No significant diffraction peak was observed at $2\theta = 45.5^{o}$ demonstrating removal of NaCl by the wash process. Using Scherer's formula (equation 4-1) from section 4.2.3 average crystal dimensions were calculated to provide quantitative information on HAp precipitated at different pH.

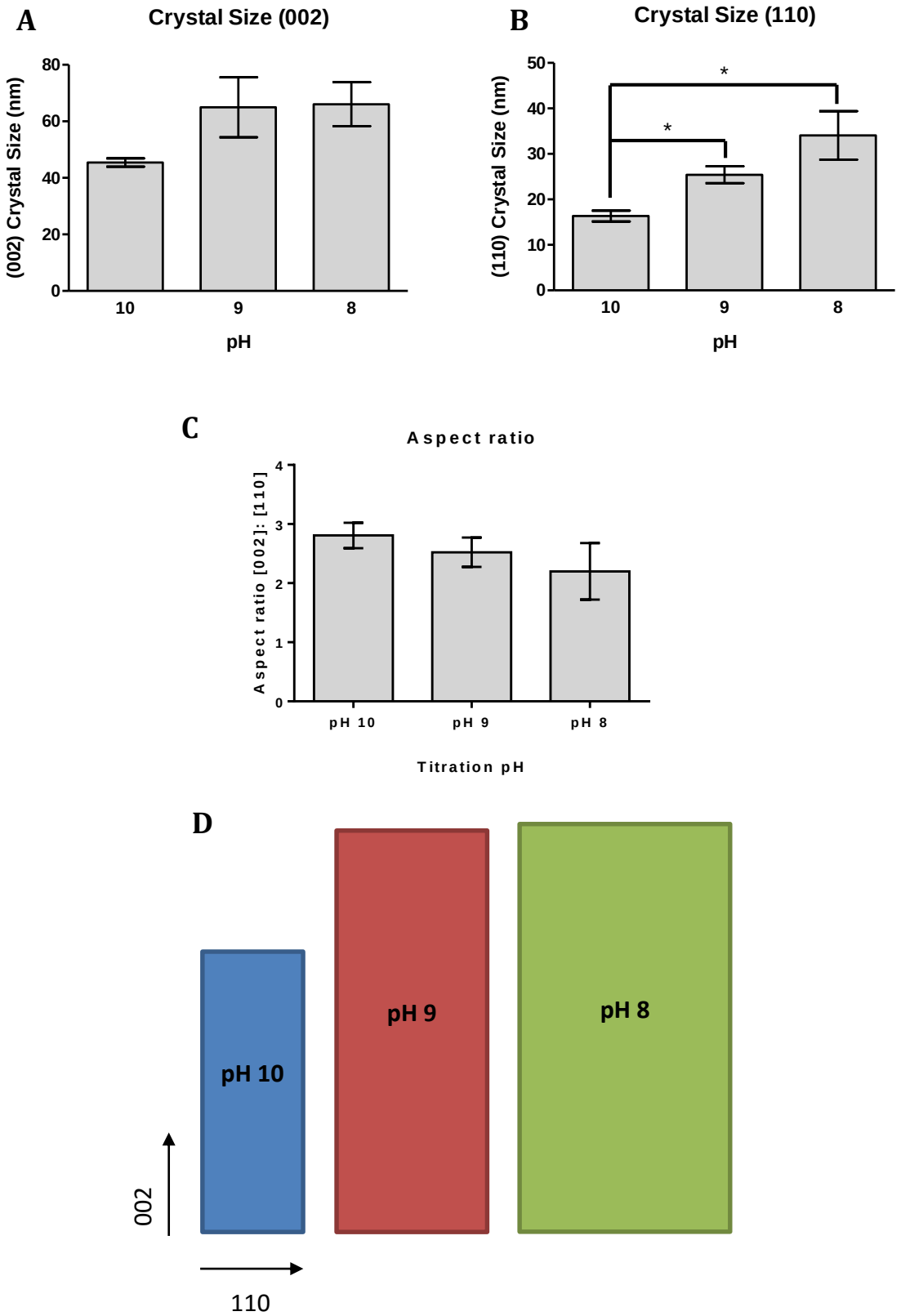

Figure 4-17: XRD derived crystallite size calculated using equation 4-1). A & B) Bars show the mean ± SEM [002] & [110] crystal direction of hydroxyapatite powder synthesised with various titration pH (n=3). C) Average aspect ratio of the HAp nanoparticles D) 1 x 10^6 scale graphical representation of HAp crystal dimensions.

Figure 4-17A shows no significant differences in average [002] crystal direction size in HAp titrated at all three pH ranges. [002] crystal direction of HAp titrated at pH 10 was the lowest at 45.42 ± 1.46 nm, the largest being HAp titrated at pH 8 at 66.04 ± 7.77 nm. Figure 4-17B illustrates a significant increase in HAp [110] crystal direction with decreased titration pH. HAp titrated at pH 10 has the smallest [110] crystal direction size of 16.34 ± 1.18 nm with pH 8 having the largest at 34.05 ± 5.33 nm. HAp aspect ratios demonstrated a range from 2.20 (pH 8) to 2.80 (pH 10), however no significant differences were observed between the groups (figure 4-17 C).

4.3.4.4 Fourier Transformed Infrared Spectroscopy

FTIR analysis was used to determine influences to molecular groups included in the unit cells of the HAp structure. The three HAp powders synthesised with different reaction pH are shown in figure 4-18.

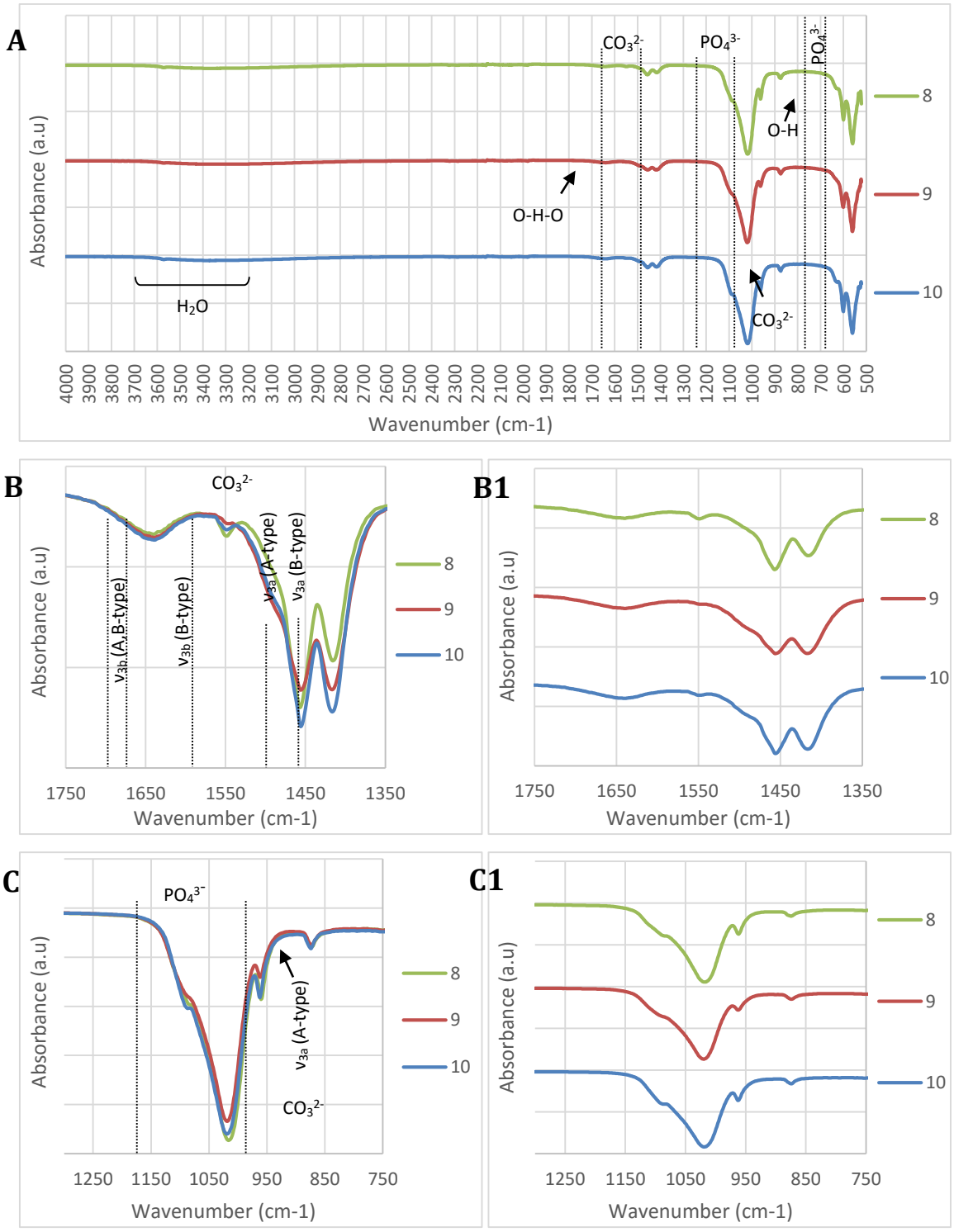

Figure 4-18: FTIR spectrum of dry hydroxyapatite powder. Each line represents the mean of three titration samples. 8, 9 and 10 refer to the titration pH of the reaction. [A] Full 500-4000 cm^{-1} stacked spectrums [B] narrow scan 1750-1350 $cm^{-1}$of A. [B1] spectra from [B] stacked. [C] Narrow scan 1300-750 cm^{-1} of [A], [C1] Spectra from [C] stacked.

Figure 4-18A shows the FTIR spectrum of three HAp powders synthesised with different pH conditions. All powders show similar phosphate absorption bands vibrational bonds $v_3PO_4^{3-}$ at 1045-1092 cm^{-1} and v_2PO_4 at 474 cm^{-1}, v_1PO_4 symmetric stretch at 963 cm^{-1}, v_4PO4 from 602-572 cm^{-1}. No significant differences were observed in absorption peaks between the HAp synthesised at the three pH conditions.

4.3.5 *Tailoring hydroxyapatite morphology and composition*

To investigate the influence of two parameters on HAp formation, titration conditions were specifically combined with an aim to vary in shape and carbonate content.

The influence of the combination of two factors were investigated to provide insights into any interaction between the titration variables. The titration 1 mL/min was selected based on the observed increase in [002] crystal direction length relative to the 0.1 mL/min titration rate. pH 8 was selected as the second variable due to the observed increase in the [002] crystal direction length relative the pH 10 control.

HAp key	**Rod-Like**	**Plate-Like**
Carbonated	**A**) pH 10 – 0.1 ml/min	**B**) pH 8 – 0.1 ml/min
Non-carbonated	**C**) pH 10 – 1.0 ml/min	**D**) pH 8 – 1.0 ml/min

Table 4-5: Hydroxyapatite titration parameters and designated nomenclature.

4.3.5.1 Energy-Dispersive X-Ray Spectroscopy

EDX analysis was used to determine elemental composition and extrapolate calcium/phosphate ratio.

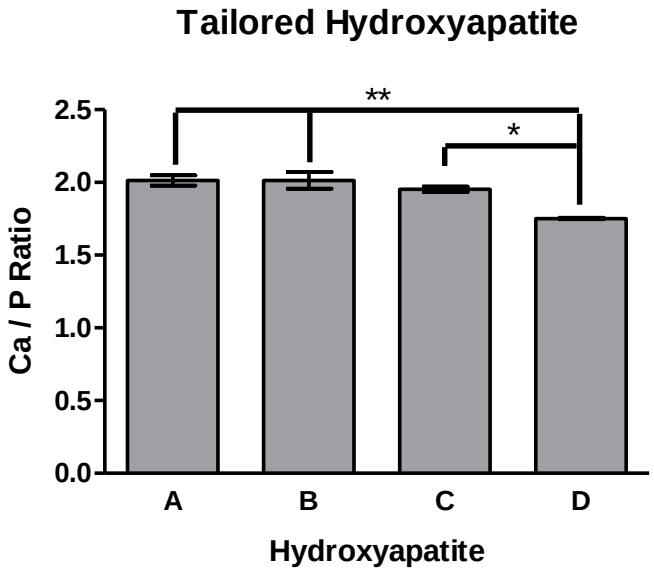

Figure 4-19: EDX analysis of A) rod-like carbonated, B) plate-like carbonated, C) rod-like non-carbonated and D) plate-like non-carbonated HAp titrated hydroxyapatite powders Calcium to Phosphate ratio. (n = 3)

Figure 4-19 shows a decrease in calcium content incorporated into the HAp lattice when synthesised at lower pH with a faster titration rate. HAp A has a Ca/P ratio of 2.01 ± 0.36 whereas D has a Ca/P ratio of 1.75 ± 0.01.

4.3.5.2 Transmission Electron Microscopy

TEM was used to compare qualitative differences in HAp morphology in relation to their respective titration methodology.

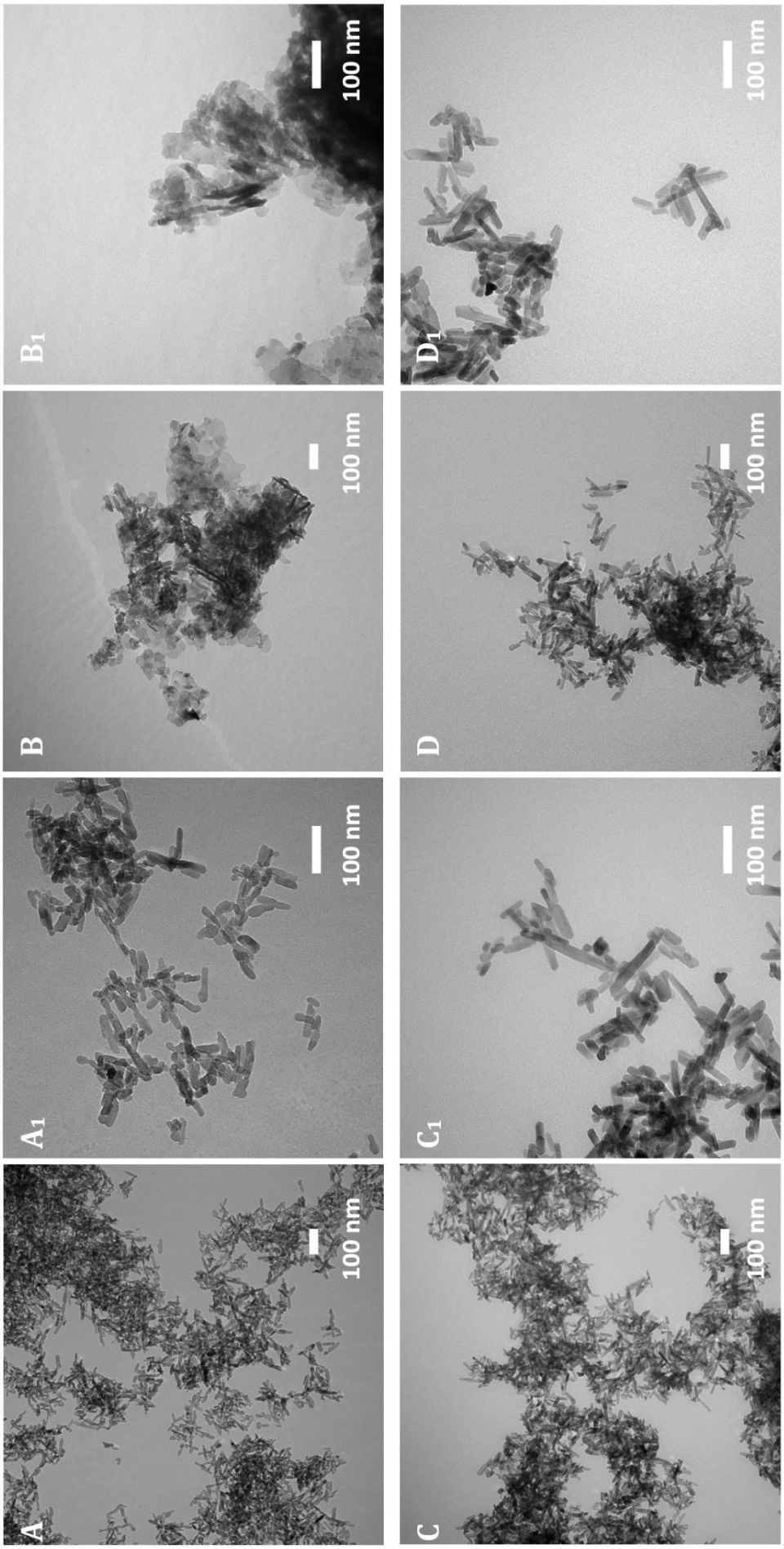

Figure 4-***20: Representative TEM images of HAp synthesised with different titration methodologies. A) pH 10, 0.1 mL/min, B) pH 8, 0.1 mL/min, C) pH 10, 1.0 mL/min D) pH 8, 1.0 mL/min. A-D = 64,000x magnification and A_1-D_1 = 130,000x magnification.***

Figure 4-20 shows TEM images form HAp titrated using methodologies outlined in table 4-5. Figure 4-20 A-C illustrates HAp discussed in previous sections, figure 4-20 D shows HAp synthesised with a combination of two previously investigated parameters. The HAp crystals D appear to have a similar morphology to that of A and C.

4.3.5.3 X-Ray Diffraction

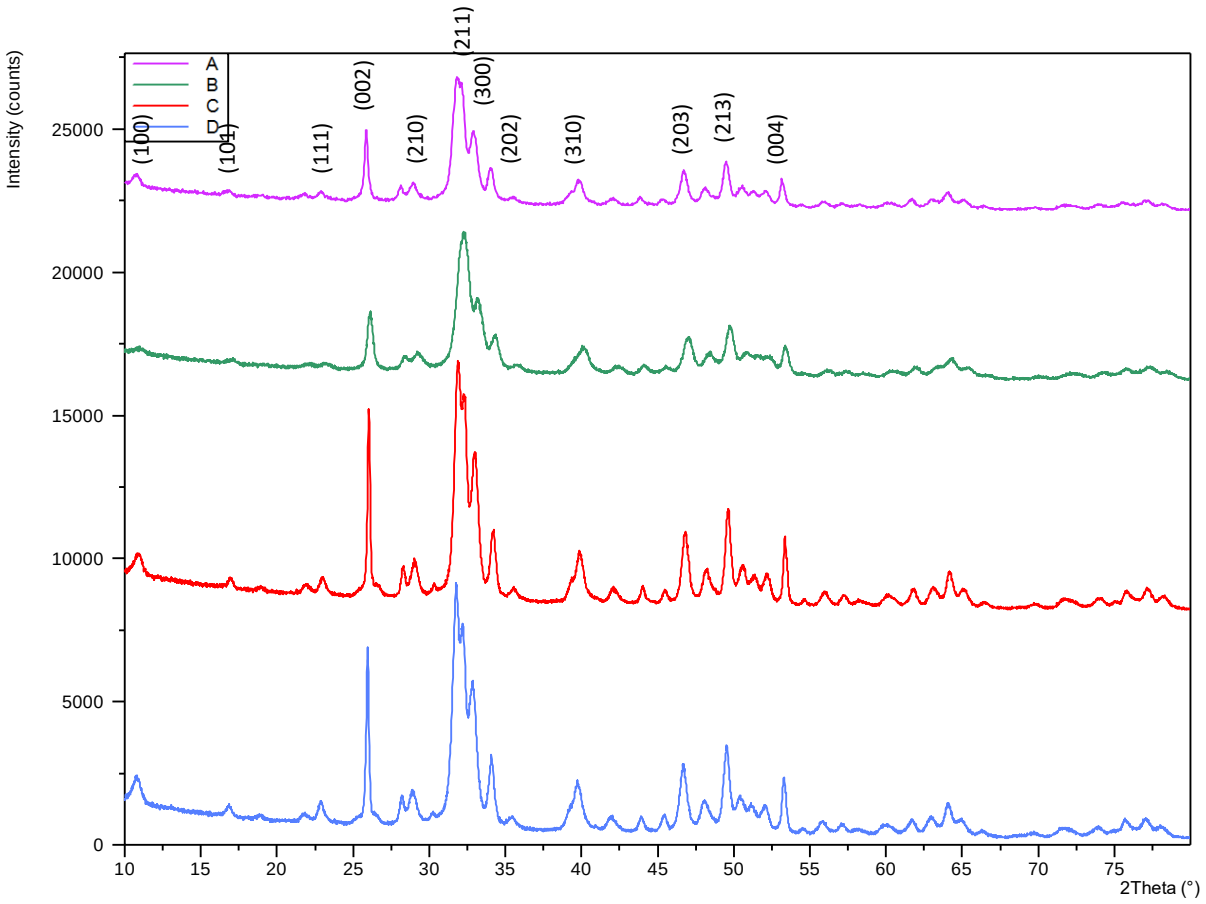

Figure 4-21: XRD spectrum of dry hydroxyapatite powder. Each series is a representative spectrum from a triplicate titration.

XRD patterns of HAp synthesised using various component titration rates are displayed with labelled notable crystal planes (figure 4-21). The powders demonstrated board X-Ray diffraction peaks. No significant diffraction peak was observed at 2θ = 45.5° demonstrating removal of NaCl by the wash process.

Using Scherer's formula (equation 4-1) from section 4.2.3 average crystal dimensions were calculated to provide quantitative information on HAp precipitated at different pH.

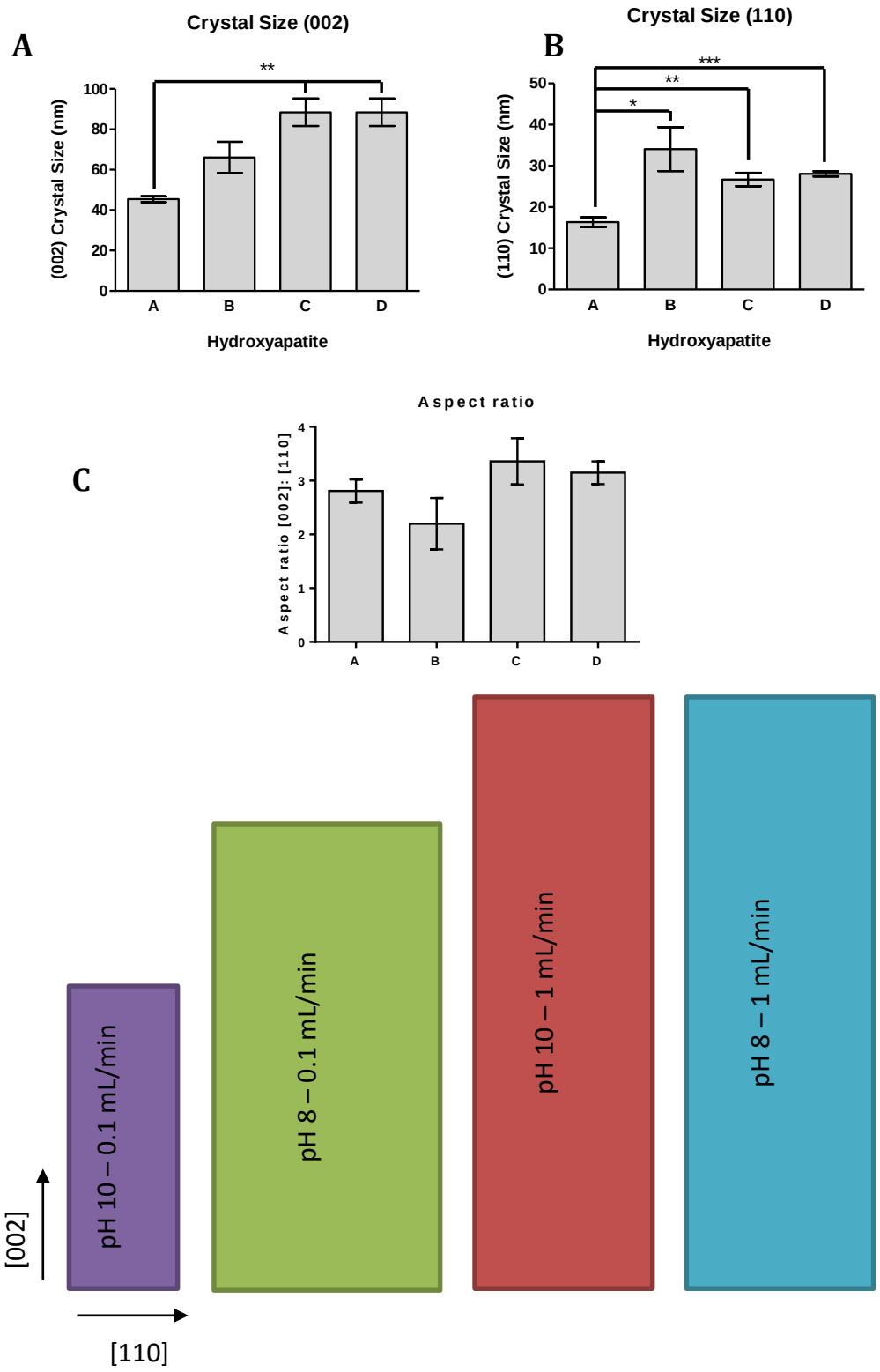

Figure 4-22: XRD derived crystallite size calculated using equation 4-1). A & B) Bars show the mean ± SEM [002] & [110] crystal direction of hydroxyapatite powder synthesised with various titration methodologies (n=3). C) Average aspect ratio of the HAp nanoparticles D) 1 x 10^6 scale graphical representation of HAp crystal dimensions.

Figure 4-22 shows average crystallite size calculated from the XRD data from powders A-D. There is a significant difference in average crystallite size between A 45.42 ± 1.46 nm and both C & D 88.39 ± 6.81 nm and 88.39 ± 6.80 nm respectively. Both C and D were synthesised using 1 mL titration rate, which appears to significantly influence the crystal size irrespective of titration pH. HAp aspect ratios demonstrated a range from 2.20 (HAp B) to 3.36 (HAp C), however no significant differences were observed between the groups.

4.3.5.4 Fourier Transformed Infrared Spectroscopy

FTIR analysis was used to determine influences to molecular groups included in the unit cells of the HAp structure. The four HAp powders synthesised with various titration methods are displayed in figure 4-23.

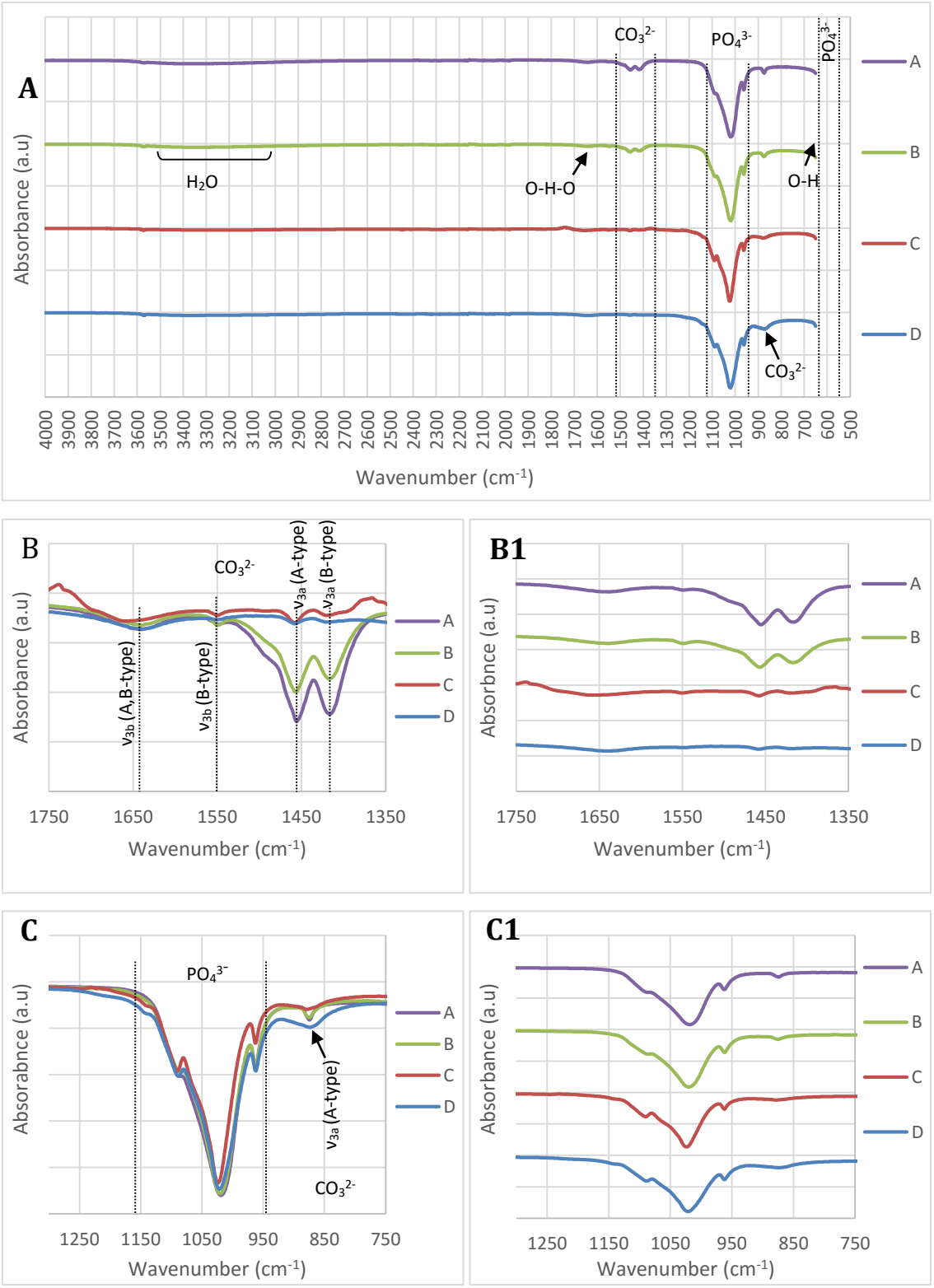

Figure 4-23: FTIR spectrum of dry hydroxyapatite powder. Each line represents the mean of three titration samples. A) pH 10, 0.1 mL/min, B) pH 8, 0.1 mL/min, C) pH 10, 1 mL/min and D) pH 8, 1 mL/min. [A] Full 500-4000 cm^{-1} stacked spectrums [B] narrow scan 1750-1350 cm^{-1} of A. [B1] spectra from [B] stacked. [C] Narrow can 1300-750 cm^{-1} of [A], [C1] Spectra from [C] stacked.

Figure 4-23A shows the FTIR spectrum of four HAp powders synthesised using various titration parameters. All powders display comparable phosphate vibrational bonds v3PO_4^{3-} at 1045-1092 cm-1 and v2 PO_4^{3-} at 474 cm-1, v1 PO_4^{3-} symmetric stretch at 963 cm-1, v4 PO_4^{3-} from 602-572 cm-1.

Carbonate bonds associated with v_3 vibrational mode were noticibly different between HAp titration at different titration rates irrespective of reaction pH. Specifically absorption linked to carbonate ion v_{3a} 1455 and 1415 cm^{-1} were increased in HAp titrated with 1.0 mL/min titration rate relative to HAp from 0.1 mL/min (figure 4-23B). CO_3^{2-} absorption peaks present at 1645 and 1655 cm^{-1} were similar in HAp titrated using the aforementioned titration parameters.

4.3.5.5 Cytotoxicity

Using HAp fabricated according to 4.3.5 table 4-5 cytotoxicity was assessed using patient derived hMSC. MTT, a cell viability assay was used to determine hMSC viability following 24 hours incubation with a series of HAp nanoparticle dilutions comparable to Müller *et al.* (2014).

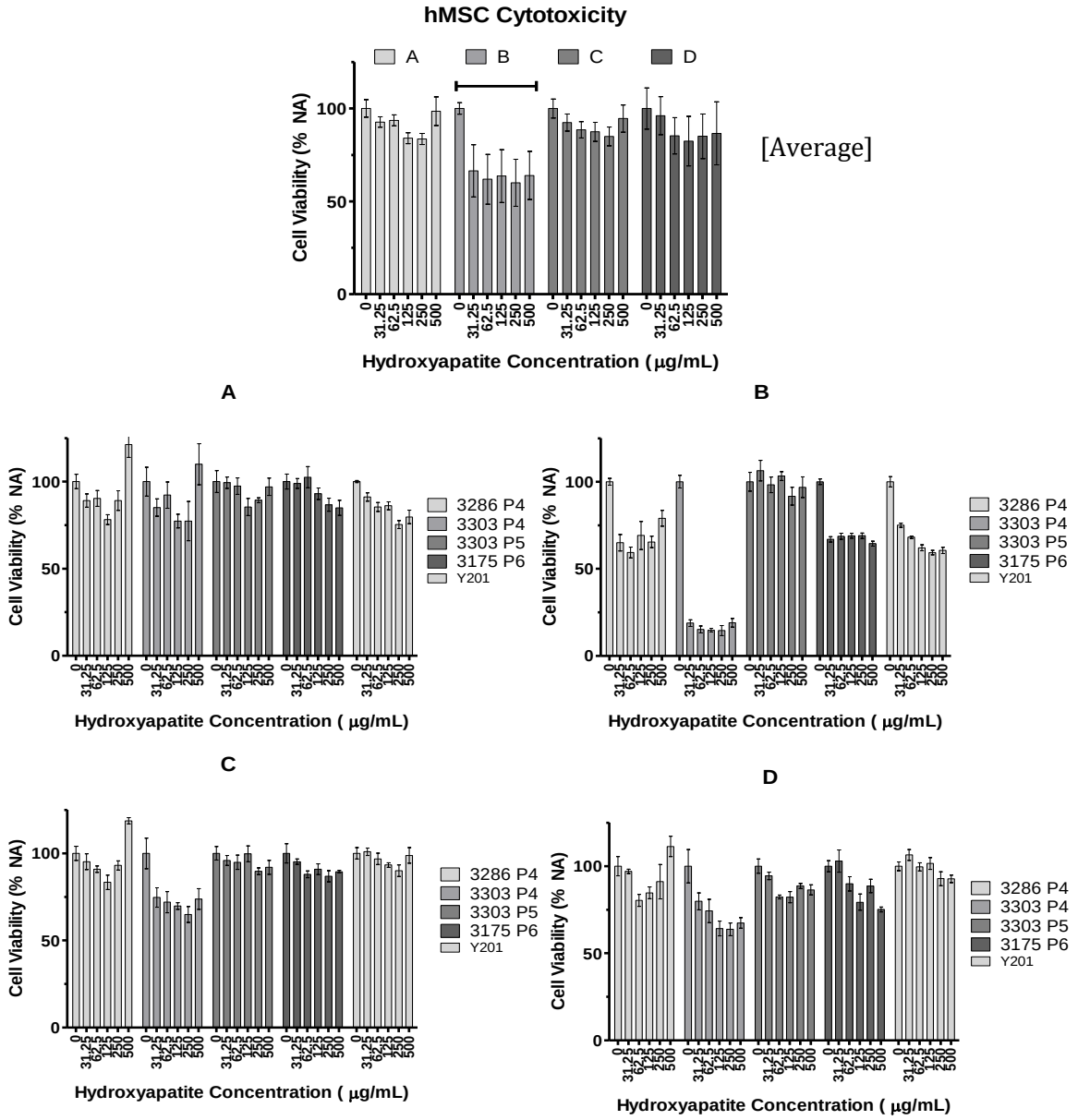

Figure 4-24: Cytotoxicity of HAp to patient derived hMSC (patient number 3286, 3303, 3175 and Y201 with corresponding passage number: denoted as PX). Cells were incubated with a serial dilution from 500 µg/mL to 31.25 µg/mL concentrations of A) rod-like carbonated, B) plate-like carbonated, C) rod-like non-carbonated and D) plate-like non-carbonated HAp for 24 h prior to measuring cell viability using MTT assay. Values represent the mean ± SEM of 5 technical replicates.

Figure 4-24 shows average cellular viability in response to the different nanoparticles pools data from a number of experiments investigating hMSC cytotoxicity to HAp concentrations. From the "[average] graph" cell viability to HAp shows an average 17.42 ± 2.76% reduction in cellular viability in response to all types and concentrations of HAp. The largest reduction in hMSC viability was observed in response to 'HAp B' 36.81 ± 1.08% which was found to be significantly different than hMSC responses to other forms of HAp (10.95 ± 1.33%).

Looking at individual hMSC responses to different concentrations and types of HAp we can see an array of varied reactions. Figure 4-24 'HAp A, B, C & D' shows the response of 4 cell types to different concentrations and types of HAp. Similar responses were observed in A, C and D throughout cell type and passage with an apparent downward trend in cellular viability with increase HAp concentration.

Figure 4-24 'HAp B' showed a marked decrease in cell viability in response to all concentrations of HAp in all cell types except 3303 P5. The 3303 cell type investigated at P4 was repeated with cells from P5 due to the observed reduction in viability in response to HAp titrated at pH 8 (D). When this experiment was repeated with the latter passage, this cytotoxic effect was not observed. It was observed that the DMEM based hMSC media containing HAp D did not sediment over time like the other HAp groups in the initial experiment. Additionally, it was observed that upon repeating this experiment with the 3303 P5 cells that the stock solution containing the HAp D began to sediment, unlike the previous experiment.

The HAp synthesised at a lower pH with a slower titration rate i.e. HAp D appeared to form a more uniform suspension of nanoparticles in the DMEM based medium, however this property appeared altered when the stock solutions were stored at -20^{o}C.

4.4 Discussion

The sol-gel method developed in this thesis resulted in nanocrystalline forms of non-stoichiometric HAp nanocrystals fabricated at room temperature with a variety of addition methodologies, titration rates and pH conditions. Initial TEM investigation demonstrated sensitivity of HAp to electron microscopic observation. Final HAp crystal dimensions varied significantly with various titration parameters, with an increase observed in [002] and [110] crystal directions. Aspect ratios of the HAp produced in this chapter demonstrated a range from 3.36 – 1.92, however there were no significant differences between any of the variables investigated. Carbonate content was found to decrease with increased titration rates and the titration addition order.

'Tailored' HAp D synthesised with the aim to increase particle [110] direction and decrease carbonate content was successful, however XRD information demonstrated a significant increase in [002] crystal direction. Ca/P ratios of HAp did not vary with single factor variation, however two factor variation revealed a significant decrease in Ca/P ratio still within the stoichiometric remit of HAp (≥1.67). Investigations into HAp cytotoxicity showed good cell viability (~75% +), with a slight reduction in viability in response to HAp synthesised at lower pH with carbonate incorporation (~60%).

EDX is not the ideal method for the measurement of calcium and phosphorous elements, inductively coupled plasma atomic emission spectroscopy (ICP-AES) is a more accurate method, however the machine was not operation at the time of this work. EDX analysis revealed an approximate Ca/P value of 2.0 for single factor synthesised HAp powders, synonymous with non-stoichiometric HAp (≥ 1.667) (figure 4-4, figure 4-9 and figure 4-14). Although the components were added in a molar ratio of 1.667 Ca/P, the Ca/P ratio was higher, indicating phosphate exclusion or greater calcium inclusion in the final HAp crystal lattice. Assuming this measurement is accurate, this evidence conflicts with previous observations by Lazić (1995), whom demonstrated calcium phosphate titrated at lower pH yielded calcium deficient apatite's.

XRD spectral analysis allows us to determine that the resultant powder contains nanocrystalline crystal peaks similar to that illustrated by characteristic hydroxyapatite diffraction library spectra (figure 4-2) and to crystals synthesised by Jevtic *et al.* (2008). The

absence of a significant diffraction peak at $2\theta = 45.5^{o}$ in the XRD spectra demonstrates removal of NaCl from the resultant HAp product via the dialysis washing method outlined in section 0.

TEM images (figure 4-3) show loss of particle definition with prolonged observation with electron microscopy. Material degradation by electron bombardment is a known consequence of electron microscopy on non-gold coated samples using TEM. This observation demonstrates the delicate nature of observing nanoscale materials and illustrates the limitations of this technique for morphological analysis without a cryogenically cooled sample stage (Bouyer *et al.* 2000). This indication also alludes to the thermal instability of the material in observation, which is confirmed by XRD analysis and supported by previous studies in low temperatures sol-gel HAp production (Monmaturapoj 2008).

4.4.1 *Influence of titration parameters on HAp crystal dimensions*

A number of methodologies have been used to measure HAp crystal size including XRD, dynamic light scattering (DLS), atomic force microscopy (AFM) and TEM quantification (Munarin *et al.* 2015; Marković *et al.* 2011; Cunniffe *et al.* 2010).

Cunniffe *et al.* (2010) used DLS and AFM to quantify HAp size. Data demonstrated large HAp agglomeration using a similar titration method to the one presented in this thesis. DLS measurement is a useful tool for the assessment of dispersity of a solid in a fluid, however is a poor tool for the quantification of HAp crystal size without a homogeneous dispersion. Furthermore, AFM measurement of HAp crystals can be misleading as intercalation of individual HAp particles can mask single crystal measurements and provides low-throughput qualitative information. Agglomeration of the HAp was observed throughout the work conducted in this thesis and is supported by observations and TEM.

4.4.1.1 Literature comparison

The following publications were selected as they produced HAp with similar morphological and crystallographic characteristics with the HAp produced in this chapter. The sol-gel methodologies varied by the addition order, type of precursor solutions and not all specify the rate at which the components were combined.

Bakan *et al.* (2013) produced HAp by titrating the $Ca(NO_3)_2$ solution at 3 mL/min into a $NH_4H_2PO_4$ reservoir at pH 9. The Hap was then aged for 24 hours prior to assessment. This method produced carbonated HAp with an average crystallite size of 26.46 nm [002] XRD. HAp produced by Bakan *et al. (2013)* contradicts evidence presented in this work as the crystallite size is much smaller in relation to HAp produced in this chapter using similar parameters (figure 4-7, figure 4-12 and figure 4-17). The main differences between the methodologies include the precursor solutions, titration rate and lack of pH regulation. Results from this thesis demonstrate that HAp nanoparticles produced at greater than 0.1 mL/min titration rates have significantly increased crystallite size (figure 4-12). However, the specific factor that is influencing HAp crystal size is likely masked by the number of deviating variables.

Jadalannagari *et al.* (2011) synthesised HAp through the titration of the H_3PO_4 precursor dropwise into a $CaCl_2$ reservoir at pH 10. The HAp was then dialysed for 12 hours prior to assessment. The reported HAp crystal size ranged from 110 – 115 nm with TEM observation according to the assumed [002] c-axis direction. The main differences between the methodologies include the phosphate precursor solution and lack of definitive titration rate/pH regulation. Results from this thesis have demonstrated HAp synthesised using a similar methodology to Jadalannagari *et al* (2011). Titration of phosphate into a calcium reservoir (method B: figure 4-5) demonstrated morphologically similar HAp to that produced by Jadalannagari *et al.* (2011), however the average crystallite size was 54.39 nm with respect to the assumed [002] direction. This difference in HAp [002] size could potentially be caused by the differences in titration addition rate, as results from this chapter demonstrated a similar increase in [002] crystal direction with increased titration rates (figure 4-12). However, lack of addition rate quantification makes it difficult to determine underlying causes for the differences observed in HAp crystal sizes.

Marković *et al.* (2011) fabricated carbonated HAp through the titration of the $Ca(NO_3)_2$ solution dropwise into a H_3PO_4 reservoir with a Na_2CO_3 carbonate precursor at 50^oC with pH

11. The HAp was then aged at 90^{o}C for 1 hour. The carbonated HAp was reported to have an average crystallite size of 11.1 nm [002] XRD. The key differences between methods used by Markovic *et al.* (2011) and those used in this chapter include the addition of a carbonate precursor, the calcium and phosphate precursors, the pH and the 'dropwise' addition. Results from this chapter yielded HAp with a larger crystallite size this is likely due to the differences in precursor solutions, particularly the carbonate incorporation and the elevated titration temperature. It is likely that the deliberate incorporation of carbonate into the HAp crystal lattice retards the growth and overall size of the resulting nanoparticle (Kanno *et al.* 1999). This is supported by results from this thesis, which demonstrates reduced crystal dimensions with increased carbonate incorporation (see discussion section 4.4.2).

Yubao *et al.* (1994) fabricated HAp by titrating a $NH_4H_2PO_4$ solution dropwise into $Ca(NO_3)_2$ reservoir at pH 10-12. The HAp was hydrothermally treated at 140^{o}C 0.3 MPa for 2 hours prior to analysis. The average crystal size of HAp synthesised using this method was 23.7 nm by 90 nm giving an aspect ratio of 3.8. The most similar HAp produced in this chapter was produced at pH 10 adding calcium into a phosphate reservoir with an addition rate of 1 mL/min. The resulting HAp had an aspect ratio of 3.36 with dimensions of 26.69 nm by 88.39 nm which are very similar to that reported by Yubao *et al.* (1994). The differences in hydrothermal treatment (121^{o}C vs 140^{o}C), precursor solutions and addition rate could explain the differences observed between the HAp presented by Yubao *et al.* (1994) and the control HAp produced in this chapter.

The aspect ratio of HAp produced in this chapter appears to vary similar to other studies utilising a simple sol-gel methodology (Motskin *et al.* 2009; Müller *et al.* 2014; Motskin *et al.* 2011). Others have utilised surfactants to retard crystal growth and promote elongation to produce HAp with different aspect ratios but did not investigating their influence on cell uptake (Zhang *et al.* 2009). This method could be used to significantly vary the aspect ratio, however some have reported difficulties concerning residual surfactant cytotoxicity (Motskin *et al.* 2009; Müller *et al.* 2014; Motskin *et al.* 2011).

4.4.1.2 Component addition methodology

The influences of component addition methods were previously investigated by Cunniffe, M *et al.*, (2010), they reported differences in resulting HAp particle sizes using a reservoir titration method. The addition of either calcium or phosphate component into an excess of the other will influence the ion availability within the reaction fluid, this will alter nucleation and growth kinetics of crystals formed at different stages of titration.

Average crystallite dimensions represented in figure 4-7 A & B show variation in HAp crystal directions [002] and [110] as a consequence of the titration methodology.

Calcium is also known to expand the [110] (a-axis) direction of HAp over the c-axis as they are not coordinated by the phosphate ions in the [002] (c-axis) direction (Elliott *et al.* 2002). This would explain how titration of phosphate into an excess of calcium led to favoured a-axis crystal growth with method B (figure 4-7). The differences in molarity of the precursor solutions $CaCl_2$ 200 mM and Na_2HPO_4 120 mM, would also result in greater calcium availability during crystal growth and the subsequent increase in 110 direction with method C (figure 4-7). Addition of both components simultaneously (method C) may have also been influenced by a diminishing saturation effect, where by the availability of ions is depleted over the period of titration. Dual addition will also be influenced by ever increasing concentrations of HAp, which may result in growth promotion of existing HAp particles over new nucleation.

4.4.1.3 Component addition rate

TEM and XRD analysis of HAp synthesised using titration rates of 0.1, 1 and 10 mL/min demonstrated increased growth of HAp crystals in the [110] direction and increased [002] direction with the 1 mL/min and 10 mL/min titration rates (figure 4-12). The component addition rate is the key rate limiting factor in the synthesis of HAp using a sol-gel methodology, influencing scalability. The parameters investigated are 10 and 100-fold increase in HAp production rate relative to the control (0.1 mL/min). With these large differences in titration rate, one would expect a similar fold influence on the resulting HAp crystal structure and composition. Results demonstrated a very limited shift in HAp crystal size from 45.42 nm to 88.39 nm [002] direction and 16.34 nm to 26.69 nm [110] direction (figure 4-12). The key alteration in HAp characteristic appeared to be with the decreased carbonate content in the resulting HAp from the 1.0 and 10 mL/min titration rates (figure 4-13).

As previously discussed, increased availability of calcium within the reaction vessel with higher titration rates would encourage preferential growth of the [110] crystal plane in HAp crystals. This helps explain differences observed with the faster titration rates 1.0 and 10.0 mL/min. The increase in HAp [002] direction growth is less straightforward and could be due to carbonate substitution (see section 4.4.2).

The heterogeneity in [002] crystal direction size of HAp titrated at 10 mL/min (figure 4-12) could be caused by the limitations of the pH control system used in this setup. The pH regulatory system of the Titrando unit attempts to equilibrate the pH within the boundary of the set pH (±0.05) as quickly as possible using an alkaline solution (NaOH) with a maximal addition rate of 100 mL/min. Upon attainment of the lower pH threshold the unit begins to titrate increasing volumes of NaOH until the rate of pH drift is sufficient to regain the set pH value. There is an exacerbated time lag period between the activation of the equilibration system and change in pH with increased titration rates. This could potentially lead to increased fluctuations in reaction vessel pH with the increased titration rates, ultimately influencing HAp characteristics. This theoretically could be overcome by calculating the rate of acid production by the precipitation and introducing an equal alkaline to balance the pH. Nevertheless, there does appear to be an increase [002] axis growth with increased availability of reaction components as observed in figure 4-12 A between 0.1 mL/min and 1.0 mL/min.

Cunniffe, M *et al.,* (2010) also investigated the reactive component addition rate of using a sol-gel reservoir titration method (method A), results showed little variation in HAp crystal size using dynamic light scattering analysis. Results observed by Cunniffe *et al.*, (2010) investigated titration rates of 0.083, 0.166, 5, 300 mL/min and found no significant differences in particle size using a dynamic light scattering technique. This could have been caused by particulate agglomeration following sonication resulting in particle agglomerates regardless of physical crystal sizes. Alternatively, these results were obtained titrating phosphate into a calcium reservoir method which is the inverse of the method applied in this section.

The majority of published articles do not directly state a titration rate and those that do not supply a rationale behind the rates which are used. Results from this thesis illustrates the impact titration rate has on resulting HAp crystal size and could potentially be used to regulate HAp crystal dimensions.

4.4.1.4 Reaction vessel pH

TEM and XRD analysis of HAp synthesised at pH in the range 8-10 demonstrated a significant increase in HAp crystal width [110] plane with decrease in pH environments with no significant changes in HAp crystal length [002] axis. This is likely due to OH^- facilitated organisation of the [110] crystal plane with preferential axis growth of the [110] crystal plane in lower pH environments.

4.4.2 *HAp carbonate incorporation*

FTIR analysis of titrated HAp powders revealed differences in carbonate vibrational modes correlating with differences in titration parameters including: addition methodology and titration rate.

Two carbonate ion vibrational modes can be observed in the FTIR spectra of control HAp v_2 and v_3 (figure 4-8, figure 4-13, figure 4-18). Carbonate ions with vibrational mode v_2 can be observed at 873 cm^{-1} and are associated with OH^- at the interface of the growing crystal (A type). Vibrational mode v_3 from 1300-1650 cm^{-1} is assigned to surface carbonate ions and related to carbonate ions in the lattice occupying PO_4^{3-} sites. Vibrational mode v_3 also has a peak split centred at 1645 and 1550 cm^{-1} with distribution of carbonate sites depending on the maturation and formation of the HAp (Rehman & Bonfield 1997; Marković *et al.* 2011). There are some discrepancies in the literature concerning interpretation of FTIR peaks from

1655-1640 cm^{-1} relating to either surface water absorption or v_3 carbonate vibrational bonds (Shi *et al.* 2009; Rehman & Bonfield 1997; Ugarte *et al.* 2005).

It has been reported that atmospheric carbon dioxide absorption into reaction vessel liquid during titration is responsible for the incorporation of carbonate groups into the apatite's crystal lattice (Shi *et al.* 2009). More recently increase carbonate content was observed in HAp synthesised under increasing ultra-sonication (25kHz) times which was again linked to entrapment of atmospheric carbon dioxide (Utara & Klinkaewnarong 2015). Indeed carbonation of the HAp lattice is a noted characteristic of *in-vivo* formed HAp found in mammalian bone (Delgado-López & Rodríguez *et al*; Ślósarczyk *et al.* 2005; Marković *et al.* 2011).

FTIR analysis of HAp titrated using a dual addition method revealed a decrease in carbonate vibration modes at 873, 1415 and 1455 cm^{-1} relative to reservoir addition methods (figure 4-8). A similar decrease in carbonate content was observed in HAp titrated at 1.0 and 10 mL/min relative to 0.1 mL/min HAp control (figure 4-13). This decrease in carbonate content correlates with increased crystal dimensions compared with carbonated control HAp. The data from this thesis corroborates previous reports that carbonation retards HAp crystal growth (Marković *et al.* 2011; Kanno *et al.* 1999).There is limited understanding of why the dual titration method yields lower carbonate content relative to reservoir titration methodologies, however it is likely be due to dissociation differences of atmospheric CO_2 in solvents and solutions.

The observed differences in carbonate content associated with titration rate are possibly due to reduced maturation time with the increased titration rates, leading to decreased atmospheric exposure time. Alternatively, the observed reduction in carbonate content could be caused by the speed in which the crystals were formed reducing available carbonate incorporation.

The carbonate vibrational modes present from HAp titrated at all three pH values were similar (figure 4-18B). It was observed by Kumta *et al.,* (2005) more carbonate incorporation into the calcium phosphate crystal with increased pH conditions and this is most likely due to the increased dissolution rates of atmospheric CO_3^{2-} into alkaline solutions. However, this observation was seen when fabricating brushite at pH <6, the pH ranges investigated in this section were all alkaline >pH 8 and would explain the absence of this result.

Future work may investigate exclusion of atmospheric carbonate absorption, perhaps via vacuum or by bubbling nitrogen through the sol-gel reaction during titration (Lazić 1995).

4.4.3 *Tailored HAp*

EDX analysis of HAp D synthesised using pH 8 and 1 mL/min titration rate revealed a significant decrease in Ca/P ratio (1.75) compared with HAp A, B and C (Ca/P = ~2.0). The ratios fall within the accepted stoichiometry for HAp mineral. This alludes to a potential interaction effect between reaction pH, titration rate and/or maturation time that directly influences resultant HAp Ca/P ratio.

In a study by Lazić *et al.,* (1995), time dependent depletion of free calcium and phosphate ions during HAp crystal formation were found to increase dramatically following >250 minutes maturation time (0.1 mL/min = 500 min and 1.0 mL/min = 50 min. Lazić also noted differences in the conversion kinetics of OPC into the HAp conformation in response to pH, with lower pH coverting more slowly than higher pH conditions. This observation might explain the observed differences in Ca/P ratio in D as it was produced with a faster titration rate and pH conditions.

One theory could be that at lower pH calcium has a reduced affinity for crystal binding domains, this could explain why there is a significant difference between HAp titrated at the same rate; calcium ions have a greater affinity to integrate with the crystal lattice.

FTIR analysis indicated reduced carbonation ion inclusion into the HAp crystal lattice with increase titration rate regardless of the titration pH (figure 4-18). This evidence supports the hypothesis that addition rate/maturation time influences carbonate content. Further investigation could explore the influence of maturation time on resultant HAp carbonate content.

HAp D (titrated at 1 mL/min at pH 8) demonstrated that the rate of component addition had a more profound impact on final crystal dimensions than pH. Evidence for this is demonstrated by extrapolated XRD data (figure 4-22) showing HAp D showed no significant differences in morphology when titrated at pH 8 or 10 (HAp C). This reinforces the argument that morphology is strongly governed by the availability of free calcium and phosphate in the reaction system and that pH plays a less significant role than anticipated.

The cytotoxicity of HAp A, B, C and D is demonstrated by the MTT viability assay of hMSC (figure 4-24). Results were largely homogeneous, however HAp B showed increased cytotoxicity relative to other forms of HAp. It was observed that HAp B was the only HAp to form a stable colloid suspension within the hMSC growth medium, this characteristic was lost during sample freeze – thawing. Coincidently, subsequent experimentation with HAp B revealed a loss of hMSC – HAp B cytotoxicity. The aspect ratio of HAp B was lower than the other forms of HAp, however this was not statistically significant. Future experiments could aim to produce HAp with statistically different aspect ratios and investigate their influence on cytotoxicity and dispersion characterises using dynamic light scattering (DLS).

A recent study by Müller *et al.* (2014) found that agglomerates of HAp induce higher levels of cytotoxicity than dispersed, this conflicts with the aforementioned preliminary finding. Further research is required to investigate this phenomenon.

4.5 Conclusion

A nanocrystalline non-stoichiometric form of HAp was successfully synthesised and isolated using a room temperature sol-gel methodology. Within the confines of a titration rate of 0.1 mL/min using a reservoir addition methodology $Ca^{2+} \rightarrow PO^{3-}$, we can conclude that a decrease in reaction pH yields HAp with increased a-axis width. This is itself limited to pH ≥ 8 as < pH 8 results in other calcium phosphate derivatives (Bouyer *et al.* 2000). I also conclude that it is the availability of calcium within the reaction vessel that governs HAp morphology, as modification to titration order and rate influenced both length and width of resultant HAp. These result supports the hypothesis of preferential a-axis expansion of Ca^{2+} during apatite formation described by Elliott *et al.* (2002). Carbonate content can be directly influenced by the titration rate of reaction components and there is evidence that this in turn may influence HAp crystal [002] direction length. The combination of lowered reaction vessel pH and increased component addition rate, demonstrated that either addition rate or maturation has a more significant impact on final HAp morphology than reaction vessel pH, this observation has yet to be explored. Increase titration rate and dual addition of reaction components yielded a decrease in carbonate content. The hMSC demonstrated low cytotoxicity (~75% viability) to various forms and concentrations of synthesised HAp.

The HAp produced at pH 10, 0.1 mL/min with method A (control) appeared to be most similar to naturally occurring bone mineral nanoparticles in morphology, size and carbonate substitution (Marković *et al.* 2011). This HAp was therefore used in subsequent experiments in chapter 5, chapter 6 and chapter 7.

Chapter 5 – Poly (Lactic Acid)/Hydroxyapatite Surface Fabrication and Characterisation

5.1 Introduction

The aim for this chapter was to characterise material fabrication processes and investigate substrate influence on hMSC behaviour. Initial work focused on developing routes to produce a HAp PLA composites and characterise final HAp dispersal. A series of *in-vitro* assays were performed on these materials to assess changes to hMSC adherence, morphology, growth kinetics, functionality and gene expression.

The integration of nanoparticles with polymeric materials offers the potential to produce composite materials with enhanced mechanical and bioactive properties. The mechanical properties of these materials is not only dependent on the properties of the polymer and nanoparticle but also the distribution and interfacial bonding of the two. The fabrication of monodisperse polymer – nanoparticles still remains a significant challenge for material scientists (Tjong 2006; Deng *et al.* 2007; Stankovich *et al.* 2006; Sinha Ray & Okamoto 2003; Althues *et al.* 2007).This chapter presents two methods for the production of HAp filled PLA composites using physico-chemical methods. The two approaches attempt to disperse HAp within solvents with differing properties, both capable of dissolving PLA.

The first approach presented utilises a solvent capable of dispersing both polymer and nanoparticle. N,N-dimethyl formamide (DMF) has previously been used to disperse both PLA and HAp (Deng *et al.* 2007; Patlolla *et al.* 2010). DMF is a polar-aprotic solvent. This family of solvents are known to have both high dielectric constants and high dipole moments. They are also capable for accepting hydrogen bonds which make them an ideal candidate for stabilising HAp in suspension. The disadvantages of DMF are that it can often be difficult to remove from the resulting material and the solvent does not readily evaporate making it unsuitable for solvent casting (Patlolla *et al.* 2010).

The second approach presented in this chapter applies a commonly used non-polar volatile solvent trichloromethane (TCM) to dissolve the PLA. The method of dispersing a HAp (hydrophilic) within a hydrophobic medium presents a number of complications. Firstly, dry addition of HAp into a non-polar solvent results in large scale agglomeration by overwhelming repulsion of the medium. This repulsion requires a huge amount of energy to disperse the

solid. The rationale behind the work presented in this chapter is to overcome this initial HAp agglomeration prior to introduction within the non-polar solvent utilising a surfactant.

Cetyltrimethyl ammonium bromide (CTAB) is a cationic surfactant used in the synthesis of nanoparticles and has been investigated as a dispersion agent for HAp (Zhou & Lee 2011). Cationic surfactants readily form micelles within an aqueous environment with the hydrophilic head exposed to the aqueous environment (figure 5-1). In the case of a reverse micelle, the hydrophilic head of the surfactant associates with the exposed OH^- groups on the exterior of the negatively charged nanoparticle (figure 5-1).

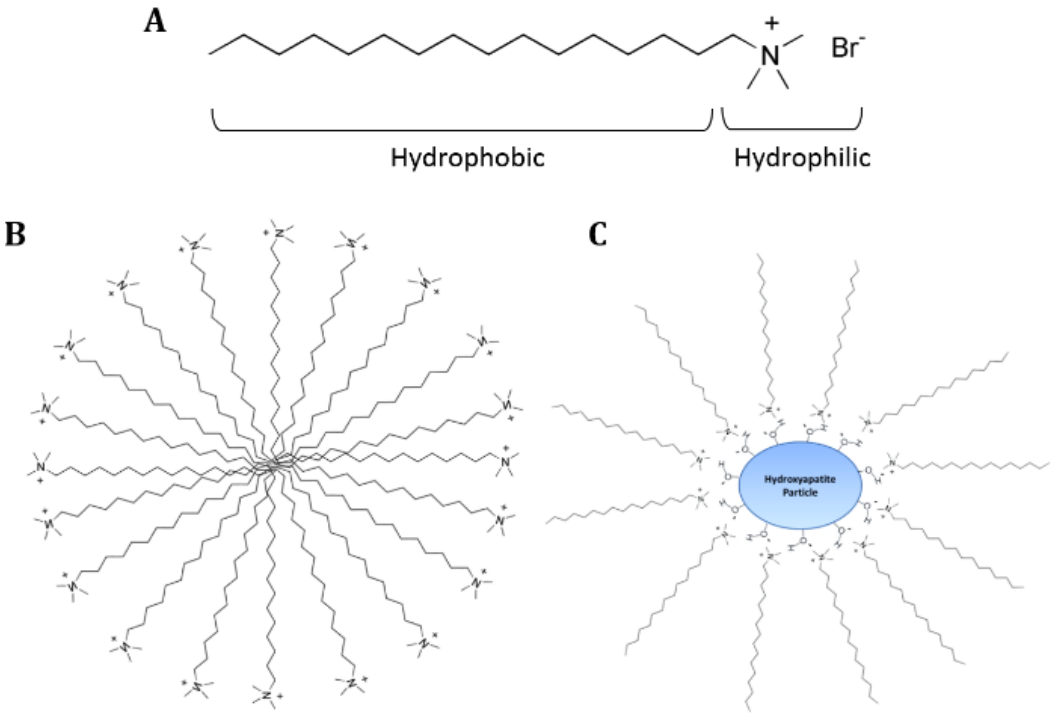

Figure 5-1: Chemical structure of A) CTAB molecule, B) CTAB micelle in H2O and illustration of HAp – CTAB reverse-micelle.

The affinity of the HAp-CTAB complex is hydrophobic providing stability of the particle within an aqueous medium. The work in this thesis investigates the potential application of this hydrophobicity to facilitate movement of dispersed HAp from an aqueous phase into a non-polar phase for composite fabrication.

The modification of nanoparticles by surfactants to facilitate transfer from one phase to another is not a novel process. Previous research has demonstrated the transfer of gold nanoparticles from an aqueous solution into organic hydrophobic solvent. Underwood &

Mulvaney (1994) showed the transfer of aqueous gold nanoparticles by complexation with 'comb stabilizers' (surfactant) present in an organic phase facilitated by gentle agitation. The methods presented in this chapter are based on a similar principle.

To investigate how hMSC interaction with PLA, the material requires processing into a film. There are a number of techniques for producing flat thin films of materials including solvent casting summarised in an excellent review by (Granqvist 2012) (table 5-1). In this thesis a bulk coating wetting process of spin coating was used to quickly evaporate a polymeric solvent solution with the aim to reduce particle sedimentation within PLA HAp composite solution preparations.

Atomistic deposition	Particulate deposition	Bulk coating	Surface modification
Vacuum environment • Evaporation • Molecular beam epitaxy • Ion beam deposition	**Thermal spraying** • Plasma spraying • Flame spraying • Detonation gun	**Wetting processes** • Printing • Dip coating • Spin coating	**Chemical conversion** • Anodic oxidation • Nitridation
Plasma environment • Sputter deposition • Ion plating • Plasma polymerization • Glow discharge deposition	**Fusion coating** • Enameling • Electrophoresis	**Printing** **Cladding** • Explosive • Roll-binding	**Leaching** **Thermal surface treatment** **Ion implantation** **Laser glazing**
Electrolytic environment • Electroplating • Electroless deposition		**Weld coating**	
Chemical vapor environment • Chemical vapor deposition • Spray pyrolysis			
Liquid phase epitaxy			

Table 5-1: Thin film deposition technologies (Granqvist 2012).

To investigate the influence of direct HAp – cell contact on PLA spin coated substrates, HAp was first stabilised in solution using a pH dispersion technique. The PLA spin coated substrates were then coated using a wetting process of dip coating to adsorb the HAp particles to the surface of the PLA films.

5.2 Materials and Methods

5.2.1 *Dynamic Light Scattering (DLS)*

DLS data was collected using a Zetasizer Nano ZSP Malvern Instruments Ltd (Worcestershire, UK). The poly dispersive index (PDI) is a measure of the distribution and homogeneity of the sample. PDI was recorded by the instrument and samples with value greater than 0.4 omitted from data analysis due to their heterogeneity.

A concentration of 0.1 mg/mL HAp was found to be appropriate for DLS measurement. Samples were prepared by ultrasonic agitation for a minimum of 10 minutes prior to measurement. For water dispersed solutions samples, 1 mL of solvent was added into a disposable PMMA cuvette. For TCM and DMF solvent dispersed solutions a quartz cuvette was used to hold the sample. The quartz cuvette was washed between measurements with dH_2O and acetone.

Samples were loaded into a measurement cuvette and three measurements were immediately recorded for each sample. The reflective index and viscosity of the various solvents and HAp were added into the Malvern database.

5.2.2 *Spin casting*

Polymer solutions for spin coating were fabricated to a concentration of 2.5% v/v. Poly (lactic acid) (PLA) has a density of approximately 1.21 g/cm^3, this was used to calculate the weight of PLA required to fabricate the polymer solution (equation 5-1).

$$Weight\ of\ PLA\ (g) = (Volume\ of\ polymer\ solution\ (mL) \times\ 2.5\%)\ \times\ 1.21\ g/cm^2$$

Equation 5-1: Weight of PLA required for 2.5% v/v solvent mixture.

A bench top rotary spin coater (MTI tech Ltd.) with a vacuum pump (Charles Austin pumps ltd. Model 8100) was use to coat 13 mm glass coverslips with a PLA film. Spin coating parameters such as polymeric temperature, concentration, volume and speed were optimised. The 13 mm glass cover slip was secured on the vacuum holder rotor and 60 µL of polymer TCM solution was applied evenly to the slide. The spin casting chamber was then flooded with/without nitrogen and spun with a two phase spin cycle; Stage 1) 3 seconds at 1000 rpm and stage 2) 10 seconds at 3000 rpm.

Substrate abbreviation	**Description**
PLA-	PLA surface cast without N_2
PLA	PLA surface cast with N_2
PLA HAp	HAp 10% v/v within a PLA matrix
PLA HAp CTAB	HAp ~10% v/v dispersed with CTAB within a PLA matrix
PLA+	Plasma treated PLA surface
PLA+ HAp Coated	Plasma treated PLA surface with HAp functionalisation.

Table 5-2: PLA substrate key

5.2.3 *Inductively Coupled Plasma Atomic Emission Spectroscopy (ICP-AES)*

Samples were prepared for ICP-AES by digesting approximately 0.1g of HAp powder in a 100ml Erlenmeyer flask. The digestion was used according to (Guzm 2005) with a solution containing 58% HNO_3, 35% H_2O_2 and 7% HCl at room temperature for 1 hour. The solution was then diluted using ultrapure distilled H_2O to 20% its original concentration. Elemental composition was then found using a Unicam 701 emission spectrometer. Results given in PPM were then converted into mg/ml using equation 5-2 below. The following two assumptions were used:

1 mg/1 L= 1PPM

Ca + P = 97.55% Mw of HAp

Equation 5-2: ICP-AES HAp quantity calculation

Ca PPM + P PPM/0.9755 = HAp PPM

HAp PPM x dilution factor = Total HAp PPM

Total HAp PPM/1000 = HAp mg/ml

5.2.4 ***Crystal Violet***

The methodology for crystal violet dye-binding method was used similar to that used by Bruder *et al.* (1997). Samples were washed with PBS and incubated for 10 minutes with 0.01% w/v crystal violet solution (0.25% methanol with dH_2O). Samples were then washed repeatedly with PBS to remove any excess dye form the surfaces. 300µL of 0.01% SDS in dH_2O was used lyse the cells and dissolve retained crystal violet, absorbance was measured at λ 570nm. Calibration curve was used to determine cell number relative to retained dye from the samples (appendix 8.6.3).

5.3 Results

The results presented in this section were divided into two areas, dispersal processes for HAp PLA nanocomposite fabrication and biological characterisation of PLA and HAp materials.

5.3.1 *Hydroxyapatite Polymer Dispersal, Coating and Characterisation*

The measurements shown in this section are focused on dispersal processing of previously fabricated HAp filled in and coated on PLA material.

5.3.1.1 DMF based dispersal

This section addresses the use of DMF as a potential solvent for the dispersal of HAp and the processing of PLA HAp composites.

The dispersion of HAp in DMF was assessed using DLS. HAp was weighed and diluted to 0.1 mg/ml in either H_2O with CTAB 10 mM or DMF. Samples were then ultrasonically agitated for and pipetted into a cuvette for measurement according to section 5.2.1 .

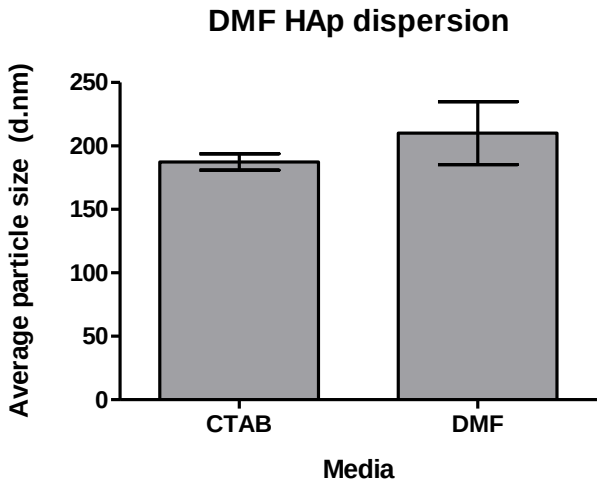

Figure 5-2: Dynamic light scattering graph showing average hydroxyapatite agglomerate size in water, water – 10 mM CTAB and DMF at 0.1 mg/ml concentration. (d.nm = diameter in nanometres)

No significant differences were observed in the dispersion of HAp in CTAB H_2O and DMF media groups. DMF dispersed HAp had an average particle size of 210.13 ± 24.80 nm. DMF dispersed PLA/HAp composites were fabricated using a developed procedure outlined in figure 5-3.

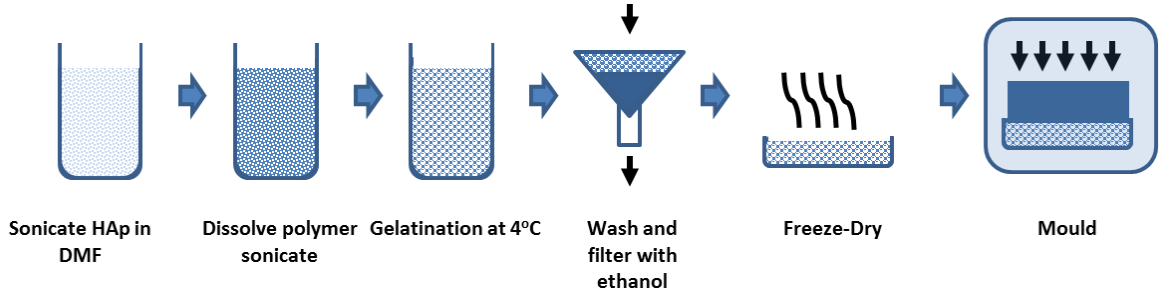

Figure 5-3: DMF processing route for monodispersed HAp/PLA composite granules.

PLA HAp composites were produced by dispersing the desired quantity of HAp in DMF and mixed by ultrasonic agitation for 1 hour. The desired quantity of PLA was then introduced in pelleted form into the HAp DMF solution and ultrasonically agitated for 4 hours until complete polymer dissolution. The PLA HAp DMF solution was then allowed to gel over night at 4°C. The resultant gel was then extracted from the preparation bottle and washed repeatedly with 100% ethanol with the use of a vacuum filter to remove the DMF. The resulting composite powder was then frozen at -20°C overnight and freeze dried using an ALPHA 1-2 LDplus (Martin Christ Freeze Dryers GmbH, UK) for 24 hours at -52°C <0.0005 mbar. The dry composite powder was then stored in a nitrogen filled desiccator.

Compression moulding was performed on the DMF dispersed PLA HAp powder to investigate composite processing technique. Composite bars were fabricated using an in house PTFE - stainless steel mould with linear compression guide bars designed and made by Dr Matt Benning at the school of mechanical systems engineering, Newcastle University figure 5-4.

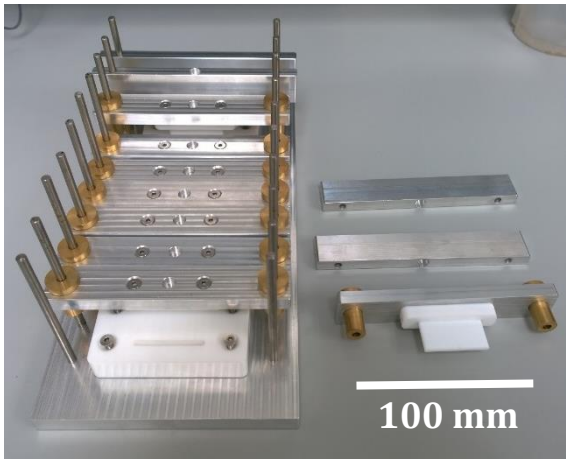

Figure 5-4: PTFE mould with linear bearing guided compression for level bar fabrication.

Composite powder was first weighed and carefully distributed into the PTFE mould channels. The powder was then loaded using a spring to exert force on the linear bar to evenly compress the powder. The assembled mould complex was then placed in an oven with 10^{o}C/min ramp to 200^{o}C and held for 2 hours before cooling at 10^{o}C/min.

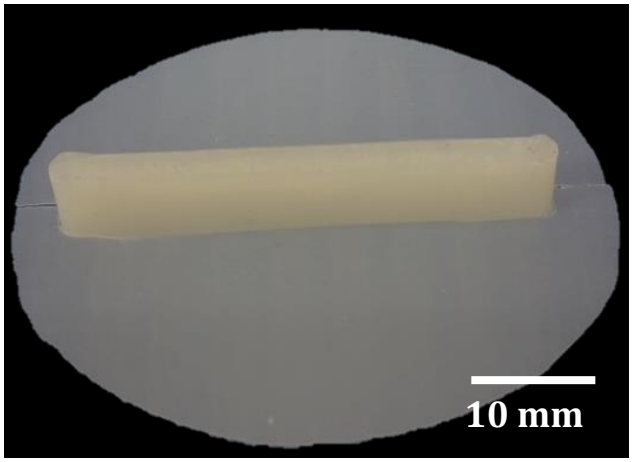

Figure 5-5: Compression moulded 10% w/w HAp/PLA composite bar with flash.

Observation of the bars fabricated using the compression moulding technique revealed some trapped air bubbles within the bar itself. No visible agglomerations were observed in the flash or within the bar.

The influence of compression moulding on the final dispersion of HAp throughout the PLA HAp material was assessed using TEM. The bar was cut into smaller pieces, resin embedded and sectioned on an ultramicrotome for TEM analysis method outlined in section 3.3.3 .

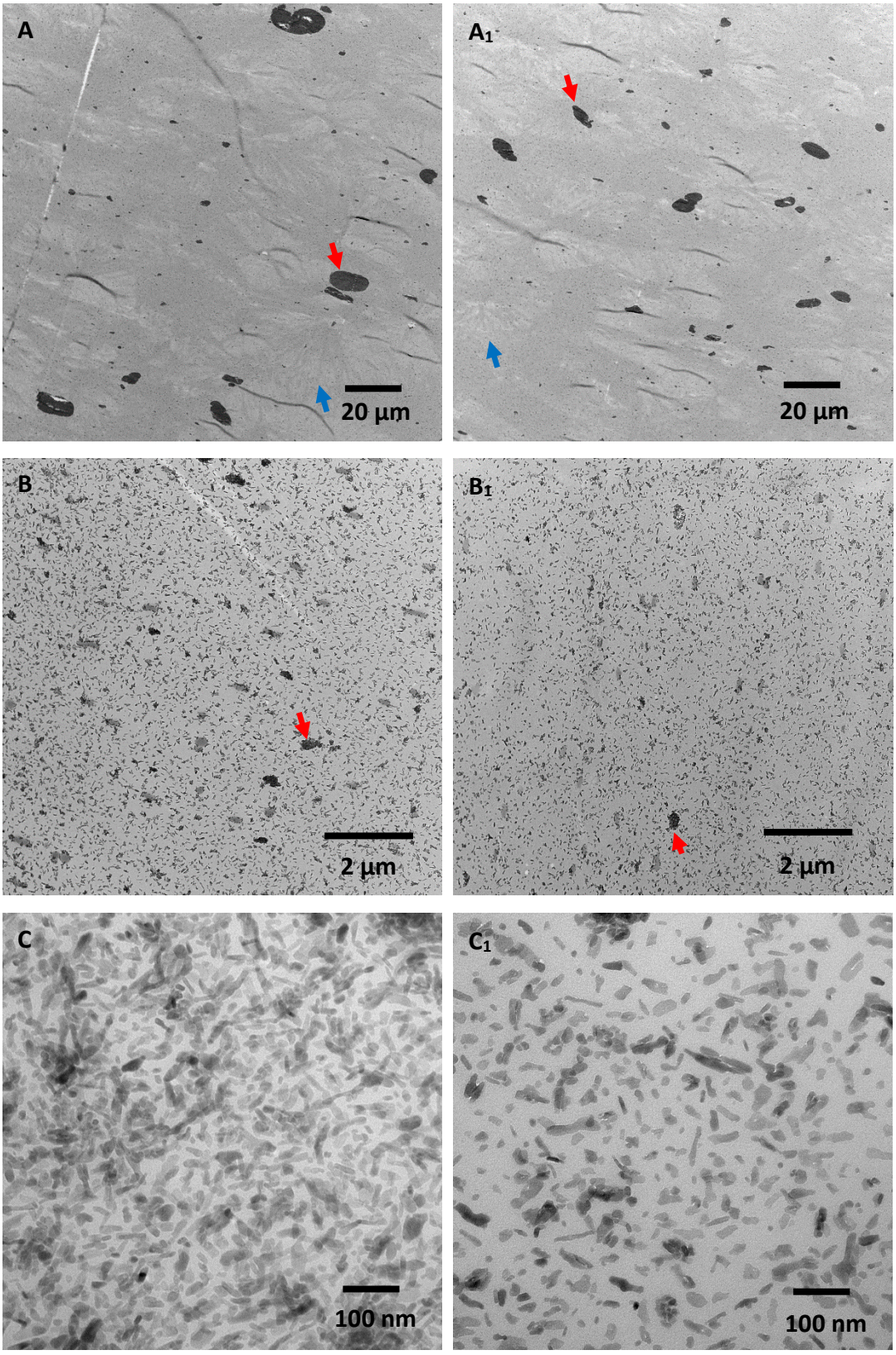

Figure 5-6: TEM images of DMF processed composite powder following compression moulding procedure. A) 800x, B) 10500x and C) 130000x magnification. A-C) Core end 1 and A_1-C_1) core end 2. Agglomerates of HAp (red arrow) and 'star-like region' (blue arrows).

The DMF dispersed PLA HAp composite bar sections revealed ~ 5 – 15 µm agglomerate of HAp at low magnification (figure 5-6 A & A_1) indicated by the red arrows. Emanating star-like regions were observed within the material cross-section (blue arrows). Images B-C show HAp monodispersion with smaller agglomerates of HAp ranging from ~ 100 – 200 nm in size (red arrows).

FTIR was used to characterise molecular vibrational changes in PLA HAp composite compared with non-DMF processed PLA and HAp powder. FTIR analysis was performed on HAp powder, flattened PLA filament and PLA HAp composite bar sections. Sample preparation for HAp powder is outlined in methods section 0, PLA filament and PLA HAp composite bar sections were flattened using a press prior to measurement.

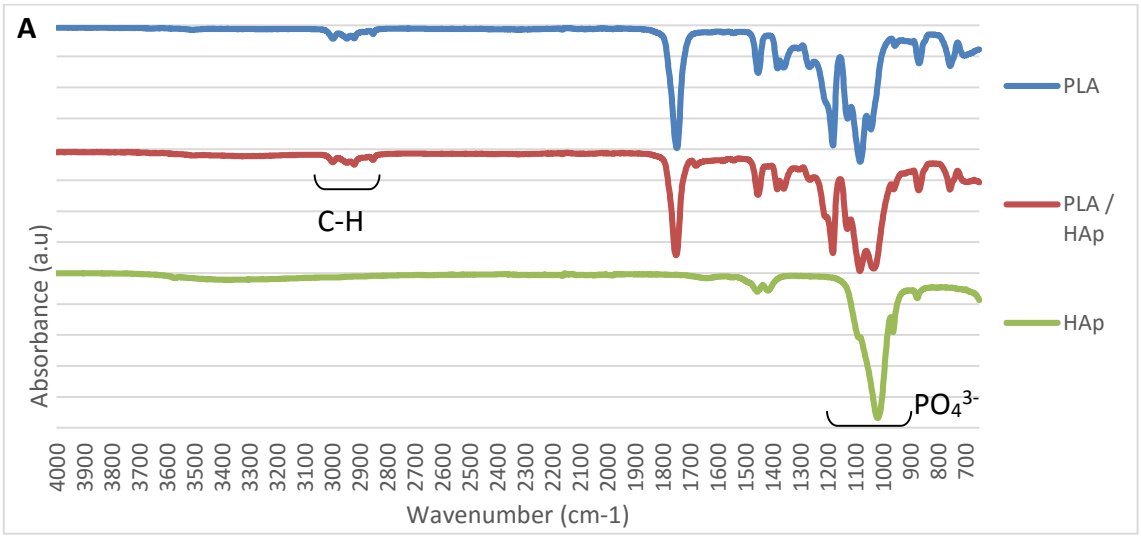

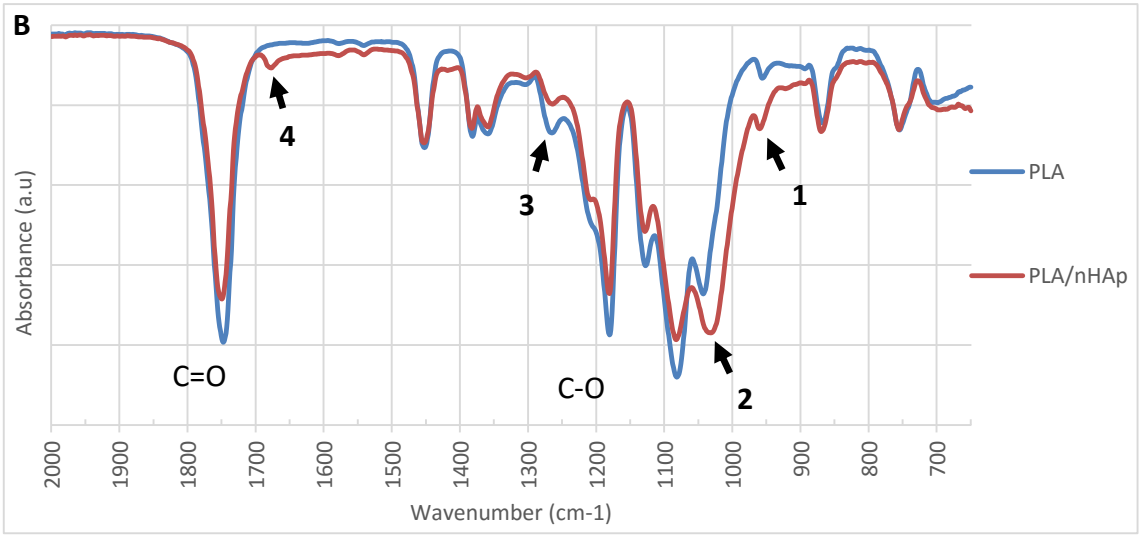

Figure 5-7: FTIR spectra of PLA, PLA/HAp and HAp powder. A) Vertically stacked spectra and B) Overlay spectra of PLA and PLA/HAp composite (650 cm^{-1} to 2000 cm^{-1}). Arrows indicate peak changes within PLA in the presence of HAp. (n=1)

FTIR analysis of the composite material revealed differences in specific peak domains (figure 5-7). Peak differences between PLA and PLA/HAp composite were observed at (1) 958 cm^{-1}, (2) 1033 cm^{-1}, (3) 1266 cm^{-1} and (4) 1672 cm^{-1}. Generic broadening in some absorption bands was observed in the overlaid FTIR spectra (figure 5-7B).

5.3.1.1 CTAB aided TCM dispersal

This section addresses the use of a surfactant as a potential route for the dispersal of HAp and the processing of PLA HAp composites.

Spin coated PLA and PLA HAp substrates were evaluated using SEM to view surface topography. All PLA substrates were cast with parameters outlined in section 5.2.2 Substrates spin coated with and without nitrogen are denoted PLA and PLA- respectively. PLA HAp solutions were prepared to a concentration of 10% v/v HAp of the final solid volume. HAp was weighed into a glass tube and ultrasonically agitated with TCM in an ultrasonic water bath for 10 minutes. Weighed PLA pellets were then added into the TCM HAp solution and ultrasonically agitated until the pellets fully dissolved (2 hours minimum).

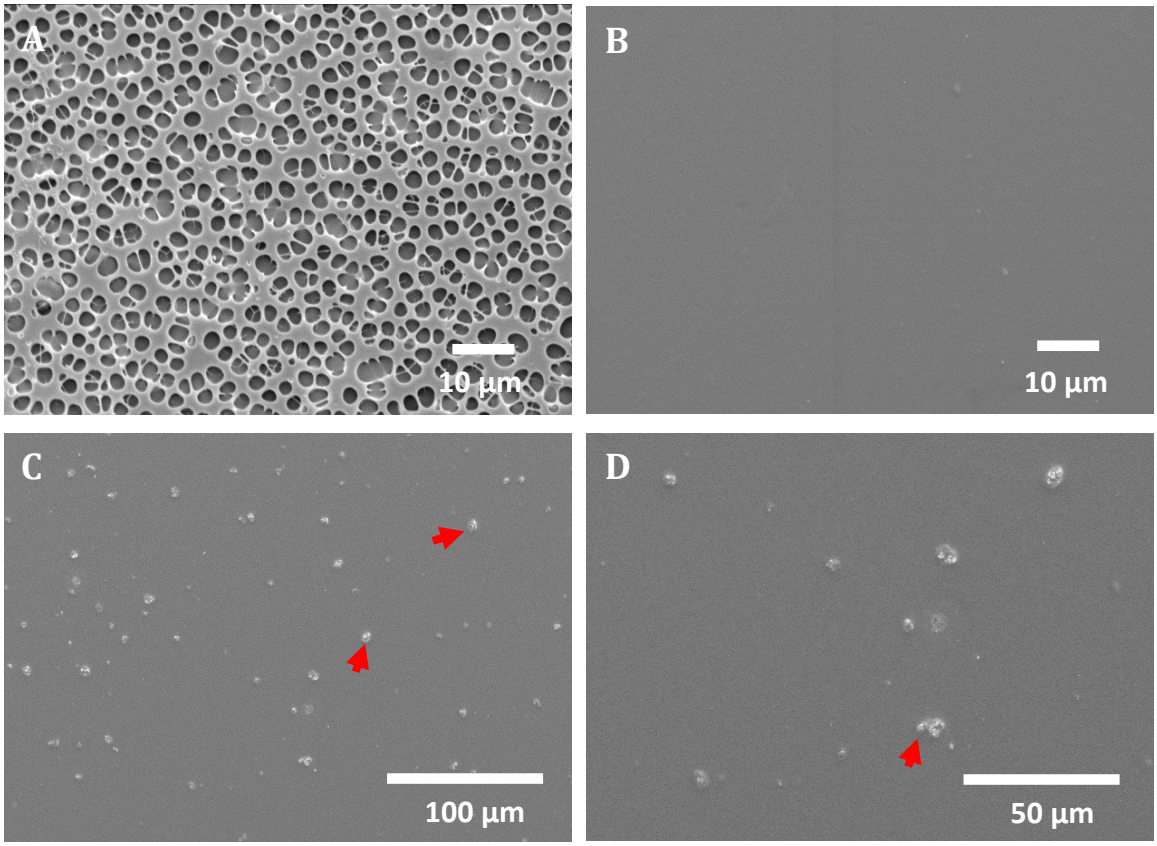

Figure 5-8: Scanning electron microscope image of TCM spin cast PLA/PLA HAp surfaces. A) PLA- cast under standard laboratory conditions, B) PLA, C & D) PLA HAp (1% v/v) surface.

Results from figure 5-8 demonstrated differences in PLA surface topography under different atmospheric conditions. A porous film was observed in image A with a uniform smooth topography in image B. SEM of PLA HAp spin cast surfaces (figure 5-8 C & D) show ~10 µm size subsurface aggregates beneath the PLA (red arrows).

The influence of CTAB surfactant on HAp particle dispersion was examined in H_2O using DLS measurement (figure 5-9). Samples were prepared for DLS by mixing a serially diluted range of CTAB dH_2O concentrations with 0.2 mg/mL HAp dH_2O solution in a 1:1 ratio. Samples were then ultrasonically agitated for and pipetted into a cuvette for measurement according to section 5.2.1 .

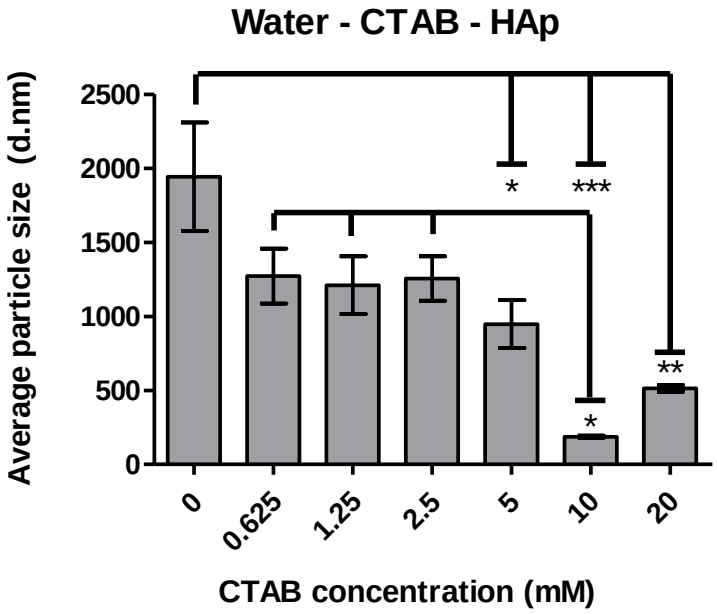

Figure 5-9: Dynamic light scattering graph showing average particle size in dH_2O, 0.1 mg/mL HAp with serial dilutions of CTAB (mM). (n=3) Average particle size ± SEM.

DLS shows particle sizes ranging from 186.37 – 1943.50 nm. Dispersion characteristics of HAp demonstrated in figure 5-9 shows the average particle size was largest in CTAB concentrations less than 2.5 mM. CTAB concentrations 5, 10 and 20 mM appeared to decrease average particle size with 10 mM being the lowest with an average size of 186.37 ± 6.41 nm. A blue hue was also observed in the mixture containing HAp with 10 mM CTAB. An increase in sample mixture viscosity was also noted in samples containing ≥ 20 mM concentrations of CTAB.

The nature of the H_2O CTAB dispersed HAp suspensions were characterised to provide information on the stability of the colloid particle suspension during the DLS measurement process.

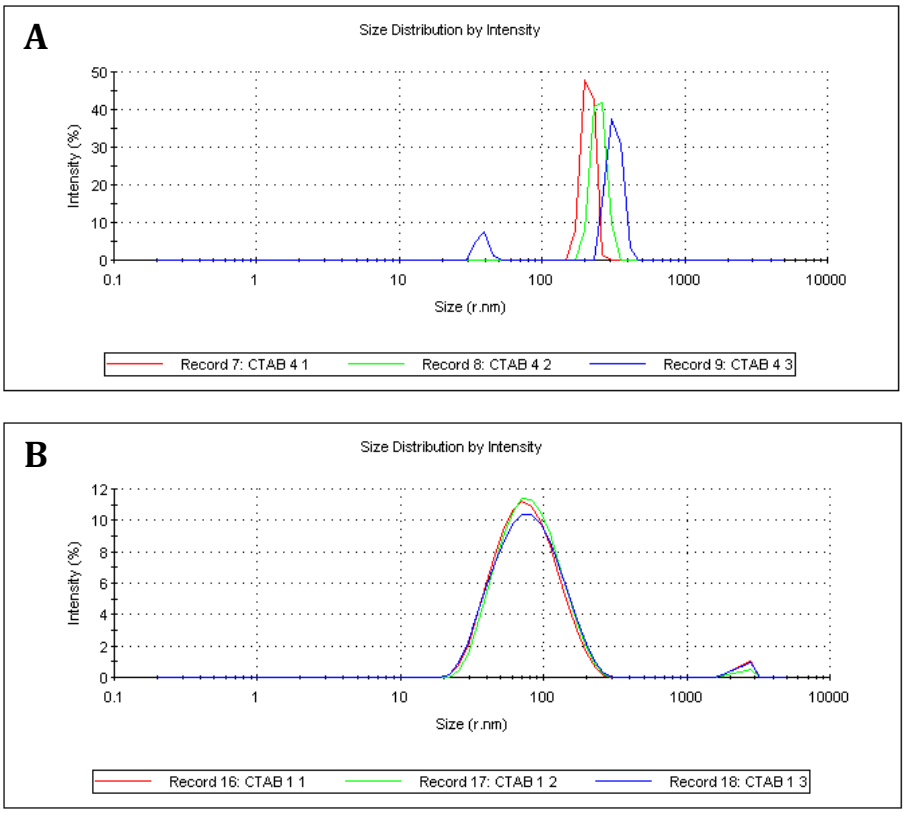

Figure 5-10: Representative DLS data of 0.1 mg/mL HAp dispersed in dH_2O with CTAB, lines represent the calculated particle size (radius nm) population in three serial measurements of sample. 1st measurement = Red, 2nd = Green and 3rd = Blue. A) HAp in dH_2O & 2.5 mM CTAB. B) HAp in dH_2O & 10 mM CTAB.

Figure 5-10 illustrates representative DLS data collected from 0.1 mg/ml HAp dispersed in dH_2O and 10 mM CTAB. The lines presented in these graphs show three consecutive measurements of 'size distribution'. Figure 5-10A shows size distribution by intensity peaks shift with each measurement and show a new smaller peak in the final measurement. Figure 5-10B shows a large intensity peak at ~80 nm radius (190 nm diameter) with a smaller peak at the micron range.

Particle agglomeration was observed with HAp directly mixed in TCM with CTAB. Prolonged utlrasonication was also insufficent to disperse the HAp within TCM CTAB solutions. Since HAp could disperse within an aqueous medium, efforts were made to first disperse HAp within water, then to transfer the proposed micelle complexes (figure 5-1) into a polymer solution with TCM similar to approaches used by Underwood & Mulvaney (1994).

CTAB dispersed HAp PLA TCM solutions were fabricated for spin casting using the procedure outlined in figure 5-11.

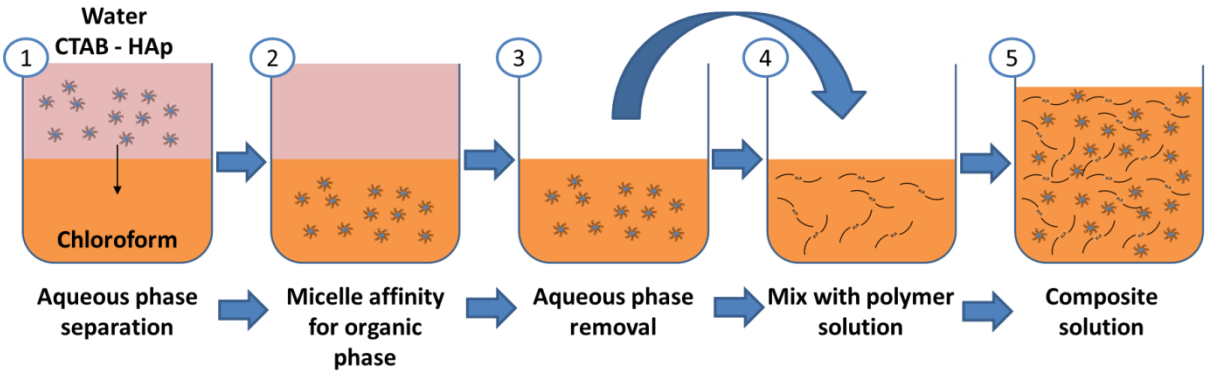

Figure 5-11: Process of reverse micelle transfer. CTAB dispersed HAp particle transfer from water to TCM and composite solution fabrication process 1-5.

10 mM CTAB was first used to disperse HAp and transfer CTAB-HAp micelles form the hydrophilic to the hydrophobic phase. Various concentrations of HAp were dispersed in dH_2O, 10 mM CTAB and separated with TCM in a 1:1 ratio. The solution was vigorously agitated to shear the interface and the HAp-CTAB TCM collected for composite fabrication and characterisation. Information from the ICP-AES analysis the required HAp quantity was calculated to form an approximate 10% v/v solid content of the final CTAB dispersed PLA/HAp product.

ICP-AES was performed to assess the quantity of HAp transferred from the H_2O to the TCM phase during the reverse micelle transfer process (section 5.3.1.1). The TCM phase following the transfer process (figure 5-11 step 3) was evaporated in a 100ml Erlenmeyer flask in a chemical fume cabinet overnight. The resultant powder was digested and analysed according to the method outlined in section 5.2.3 .

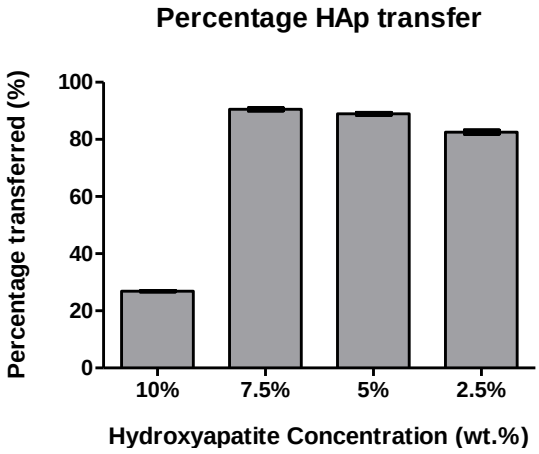

Figure 5-12: Percentage of HAp transferred into the TCM phase from 10 mM CTAB dispersed HAp of various concentrations. Data obtained through ICP-AES analysis of the TCM phase following micelle processing (n=1). Error bars = SEM of technical repeats.

During the reverse micelle transfer process, it was found that some of the material was trapped at the interface between the TCM and H_2O solvents. Results demonstrated in figure 5-12 A show the percentage of HAp in the TCM phase following reverse micelle transfer using different concentrations of HAp in the aqueous phase. The percentage of HAp transferred appeared reduced with 10% wt./v HAp concentration, however remains higher with concentrations of ≤ 7.5 wt.% Hap at ~90% - ~80%. 7.5% HAp concentration was therefore used for the reverse micelle process to make a TCM HAp solution of approximately 6.75 wt. % HAp (90% of 7.5 wt. %) – (figure 5-11, step 3).

The influence of reverse micelle transfer on resultant HAp dispersal (figure 5-11 step 3) was assessed using DLS. Both H_2O 10mM CTAB and TCM phase HAp samples were diluted to ~ 0.1 mg/mL and ultrasonically agitated for 10 minutes. 1 mL of the samples were transferred into a respective cuvettes and measured according to the method outlined in 5.2.1

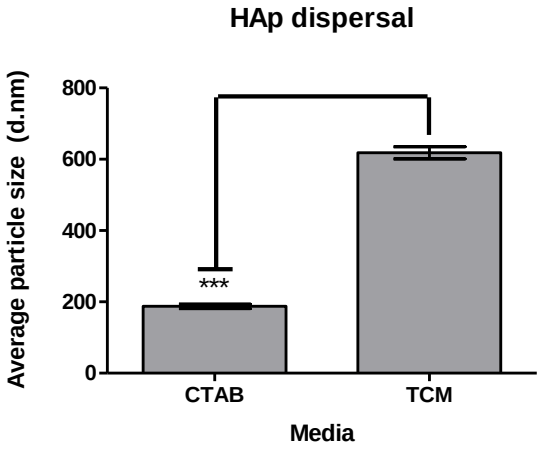

Figure 5-13: Dynamic light scattering data showing average particle size of 0.1 mg/mL HAp in 10 mM CTAB H_2O and following reverse micelle transfer. (n= 3) Average particle size ± SEM.

Figure 5-13 B shows the influence of the reverse micelle processes on the size of the CTAB – HAp agglomerates. A significant 3.30-fold increase in particle size was observed in agglomerate size following phase transfer.

The effect of adding PLA and spin cast processing on final PLA HAp CTAB composites HAp dispersal was determined using TEM. HAp at a concentration of 6.75 wt. % was diluted with TCM PLA solution to form a composite solution of 2.5% w/v solid fraction containing 90% PLA and 10% HAp (figure 5-11, step 5). This solution was used to spin cast PLA HAp CTAB surfaces later used for the biological characterisation of the material using parameters outlined in section 5.2.2

To evaluate final PLA HAp dispersion, the PLA HAp CTAB solution was spin cast onto copper grids for TEM analysis. Copper grids were first fixed to the glass coverslips prior to spin coating using a small volume of PLA TCM solution. The PLA HAp CTAB solution was then added to the glass coverslip and spin cast using parameters outlined in section 5.2.2 The grid was then peeled from the supporting glass coverslip and visualised using TEM.

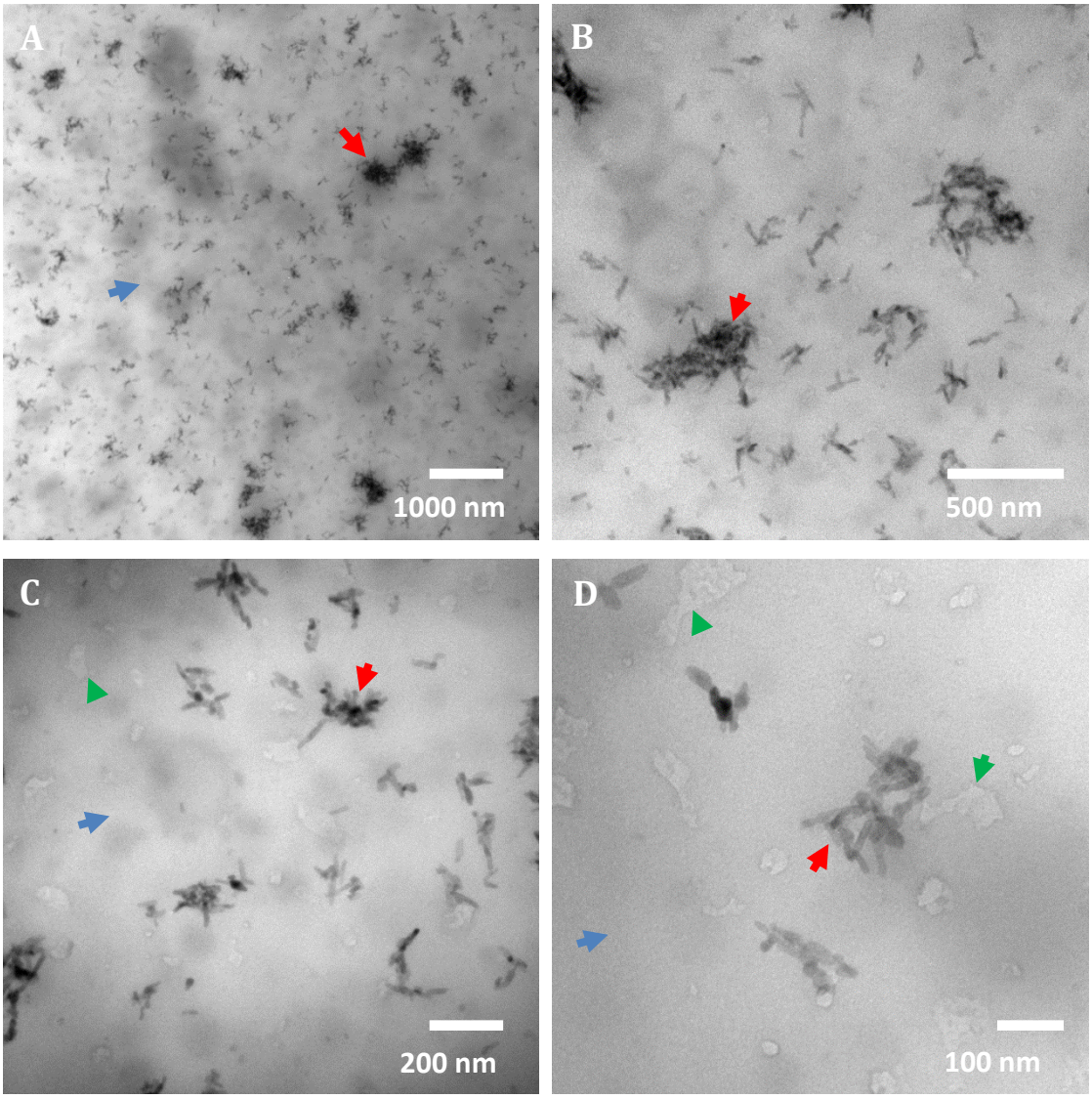

Figure 5-14: Transmission electron microscope image of spin cast PLA HAp CTAB composite film. A) 13500x, B) 46000x, C) 640000x and D) 130000x magnification. Red arrow = HAp, blue arrow = PLA matrix and green = artefact.

TEM images from figure 5-14 show relatively uniform dispersal of HAp observed through a PLA matrix (blue arrow), small aggregates of HAp were observed ranging from 200 – 1000 nm (red arrows). At higher magnification artefacts can be observed throughout the PLA matrix (green arrows).

5.3.1.2 Hydroxyapatite Polymer Surface Coating

The pH of the HAp H_2O suspension was investigated as a potential aqueous dispersal route a dip coating process.

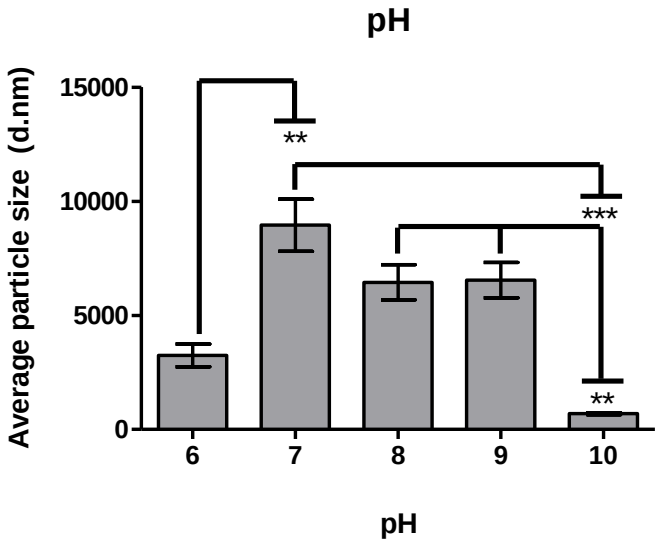

Figure 5-15: DLS data showing 0.1 mg/ml HAp dispersion in dH_2O at pH 8 – 10 (dH_2O with NaOH).

The DLS data indicated average HAp particle size was lowest in a pH 10 environment with an average particle size of 689.20 ± 44.46 nm with the largest at pH 7 with a size of 8.96 ± 1.14 µm. The zeta potential of HAp at room temperature (25°C) pH 7 was found to be -14.63 ± 1.20 mV.

Plasma treatment of PLA surfaces was performed to enhance HAp – PLA interaction during the dip coating process. PLA spin cast samples were plasma treated using a compact plasma cleaner PDC-32G (EQ-PDC-32G) (MTI Corporation, US) with an 8CFM double step rotary vacuum pump (2TW-4C) (MTI Corporation, US). Samples were loaded onto a glass microscope slides and inserted into the PT chamber. The chamber was sealed and a vacuum pump was activated and allowed to warm-up for 10 minutes before the PT procedure. PT was performed for 3 minutes on the 'medium' setting of the compact plasma cleaner PDC-32G. The chamber was then slowly brought to atmospheric pressure and samples removed directly into a 24 well plate.

HAp suspension was made by diluting NaOH in dH_2O to 50mM and ultrasonically agitated for 1 hour prior to dip coating. Spin coated PLA+ coverslips were immersed in HAp suspension for ~10 seconds and washed by dipping immediately in dH_2O three times blotting on absorbent

paper roll in between each dip. PLA+ HAp coated coverslips were then placed and covered on a hot plate at 70°C for 15 minutes to dry before placing in a 24 well plate. All samples were then sterilised by UV irradiation for 30 minutes and stored in PBS for seeding.

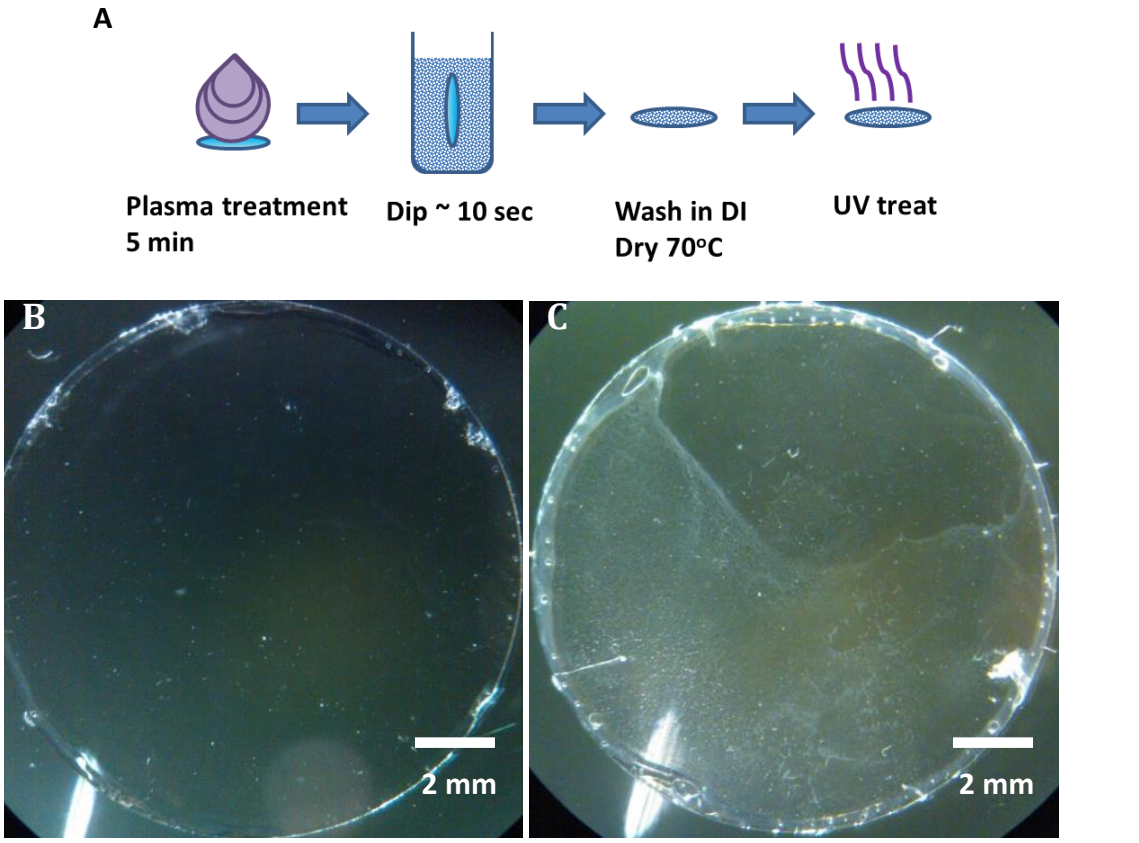

Figure 5-16: A) Diagram of PLA surface treatment and dip-coating procedure. B) PLA+ spin cast, plasma treated 13mm glass coverslip image. C) PLA+ HAp coated 13mm glass coverslip.

The image of the PLA+ HAp coated glass coverslip (C) shows a thin non-uniform white coating across the PLA surface in comparison to non-coated PLA+ substrate (B) (figure 5-16).

5.3.1 *Biological Characterisation*

This section evaluates the effects of the processed material substrates shown in section 5.3.1 on hMSC adherence, morphology, growth kinetics, and gene expression *in-vitro*.

5.3.1.1 Scanning Electron Microscopy

The influence of TCM dispersed HAp PLA substrates was assessed for basic cell adherence and substrate interaction. Cells were seeded at a density of 10,000 cells/well in a 24 well plate (approximately 5.3 cells/mm^2) using methods outlined in methods section 3.3.4 .

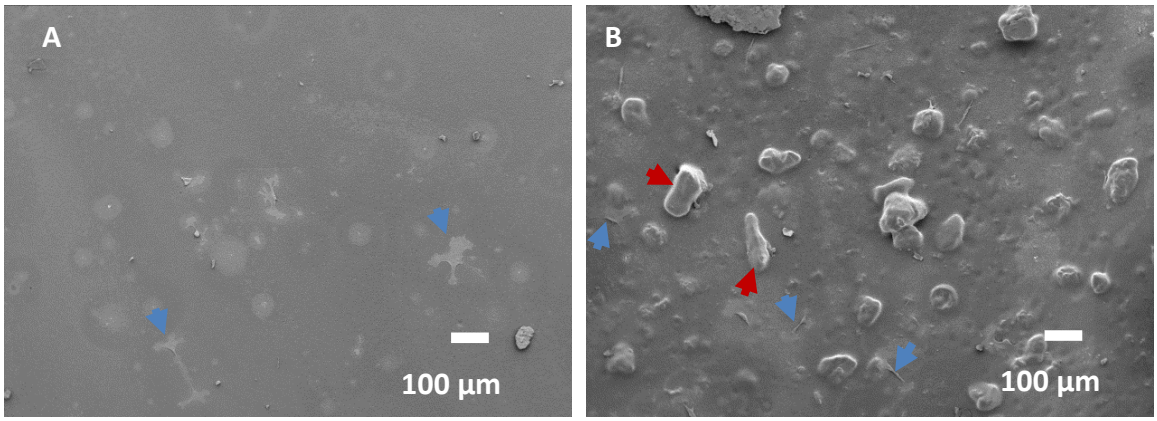

Figure 5-17: SEM image of spin cast (A) PLA & (B) PLA HAp (10% v/v) surfaces with hMSC cultivated for 24 hours. Blue arrows = cells and red arrows = subsurface particles.

From figure 5-17 cells can be observed on both PLA and PLA HAp surfaces (blue arrows) adhering and spreading. Large subsurface particles can be seen throughout the PLA coating (red arrows) in figure 5-17B.

The influence of the PLA HAp CTAB substrates were assessed for surface topography and cell adherence in figure 5-18.

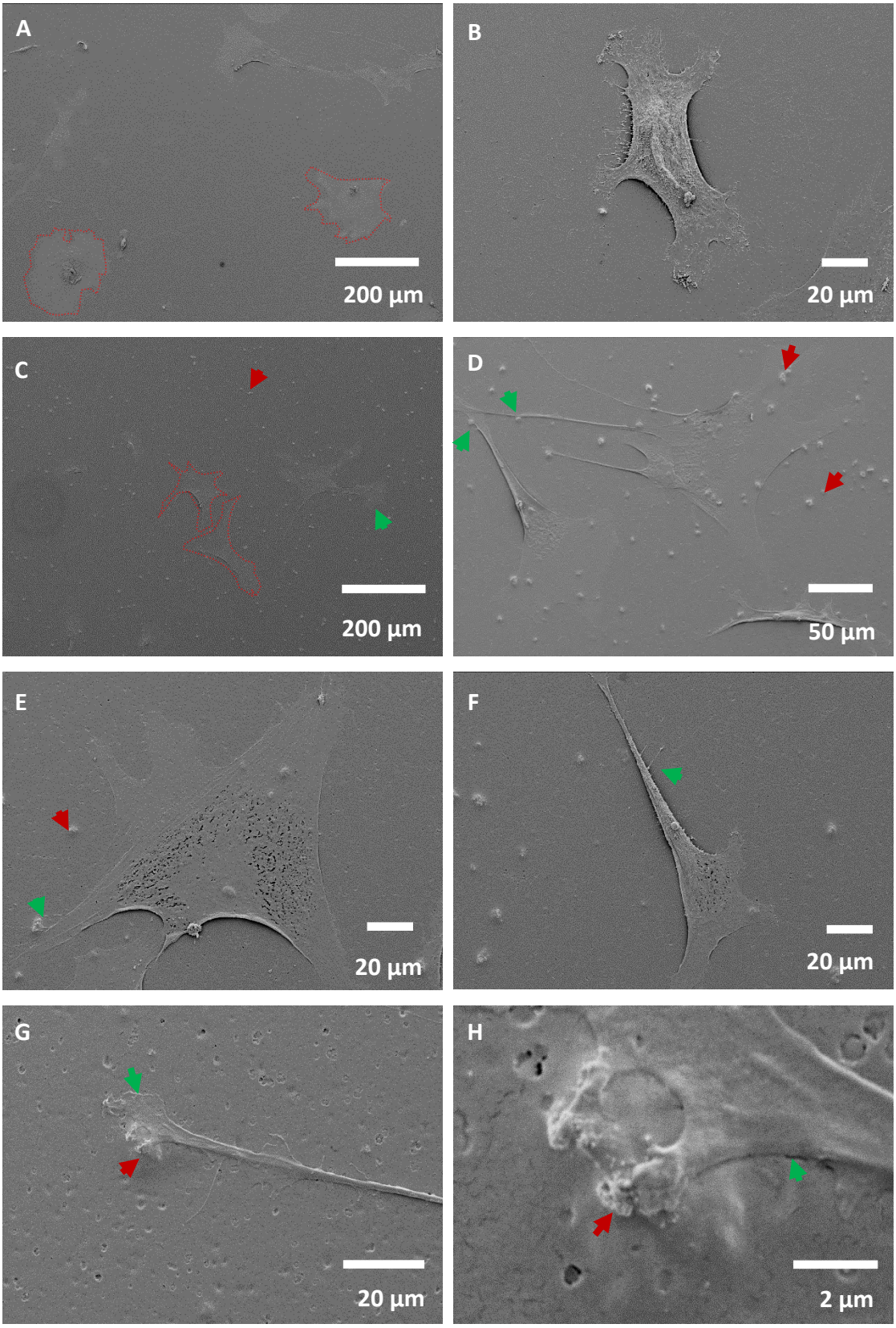

Figure 5-18: SEM images of spin cast PLA (A-B) and PLA HAp CTAB (C-H) surfaces with hMSC cultivated for 24 hours. A&C) 100x, B, E & F) 600x, D) 300x, G) 2000x, H) 10,000x

magnification. Red arrows = subsurface aberrations and green = pseudopodia. Red outline = cell perimeter.

Figure 5-18A shows a relatively smooth homogeneous PLA surface topography from low magnification. Cells can be observed adhering on both substrates (image A – F). PLA HAp CTAB substrates show subsurface aberrations ranging from 0.5 – 1 µm can be observed in images C – H (**red** arrows). Extended cell pseudopodia can be seen in images G and H interacting directly with aforementioned irregularity in surface topography (**green** arrows).

The influence of plasma treatment and HAp dip coating on spin coated PLA+ surfaces were investigated to assess both surface coating efficacy and basic cell adherence.

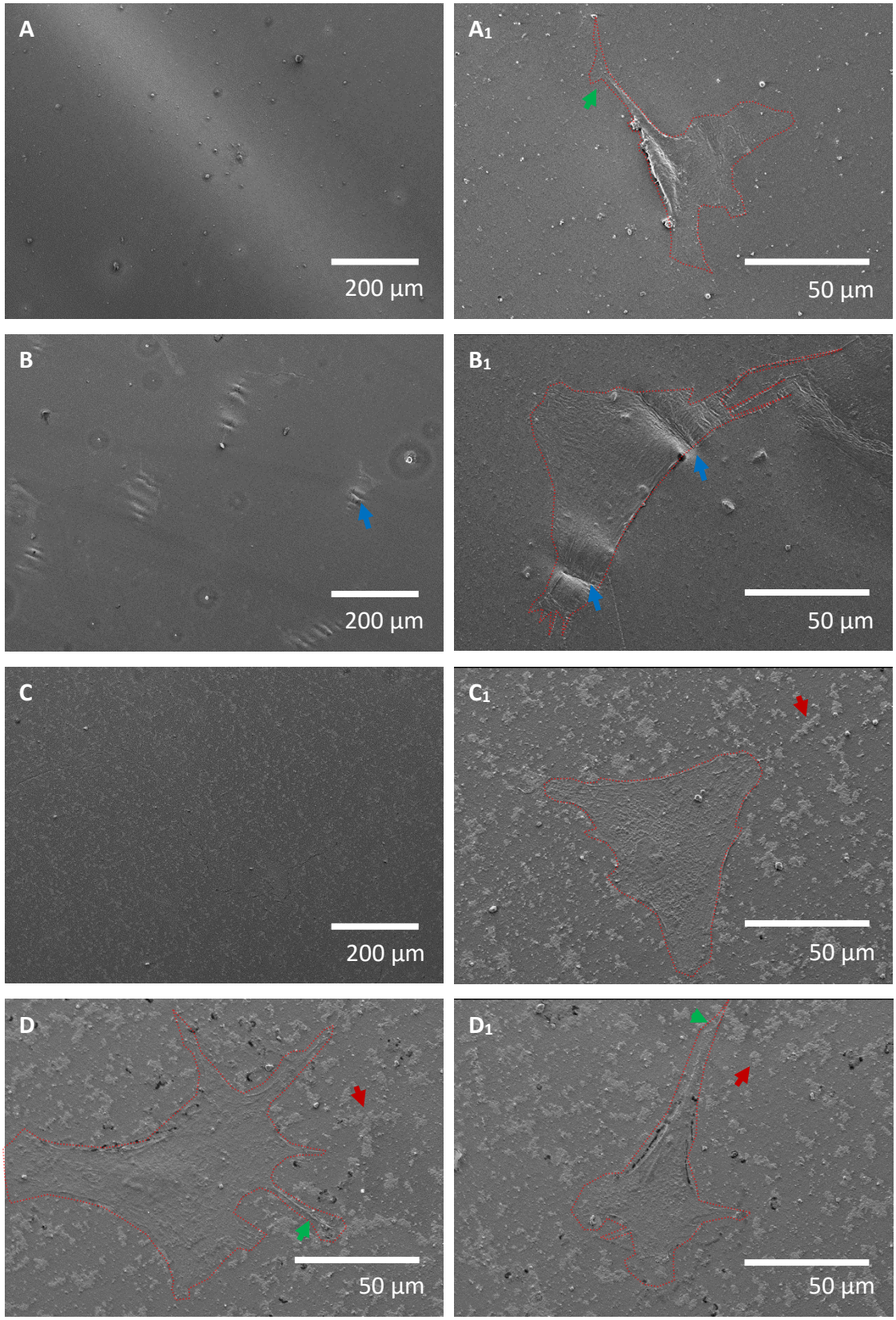

Figure 5-19: SEM images of spin coated PLA+, hMSC 3286 incubated with surfaces for 24 hours. A) PLA, B) PLA+ and C-D) PLA HAp Coating. A-D) 100x magnification and A_1-D_1) 600x

magnification. Blue arrow = 'lines of contraction', red arrow = HAp surface coating and green = pseudopodia. Red outline = cell perimeter.

The influence on cell adherence to PLA+ substrates can be observed in figure 5-19 B & B1 compared with PLA control A & A1. In figure 5-19 B & B1 cells on PLA+ appear to be well spread and have what appears to be lines of contraction (**blue** arrow), this effect is not evident the PLA+ HAp coated surface image C1, D or D1. Further examination of the PLA+ HAp coated substrates revealed a similar coating of HAp across the PLA surface with islands of HAp ranging from <1 – ~10 µm. Cells could be observed adhering to the PLA HAp coated surface, illustrated by the **red** dotted outline (figure 5-19 C_1, D & D_1).

5.3.1.1 Morphological Analysis

Images of hMSC stained with crystal violet (CV) were imaged to provide information on morphological changes of hMSC cultivated on PLA HAp CTAB surfaces following 21 days of culture in both basal and osteogenic media (figure 5-20).

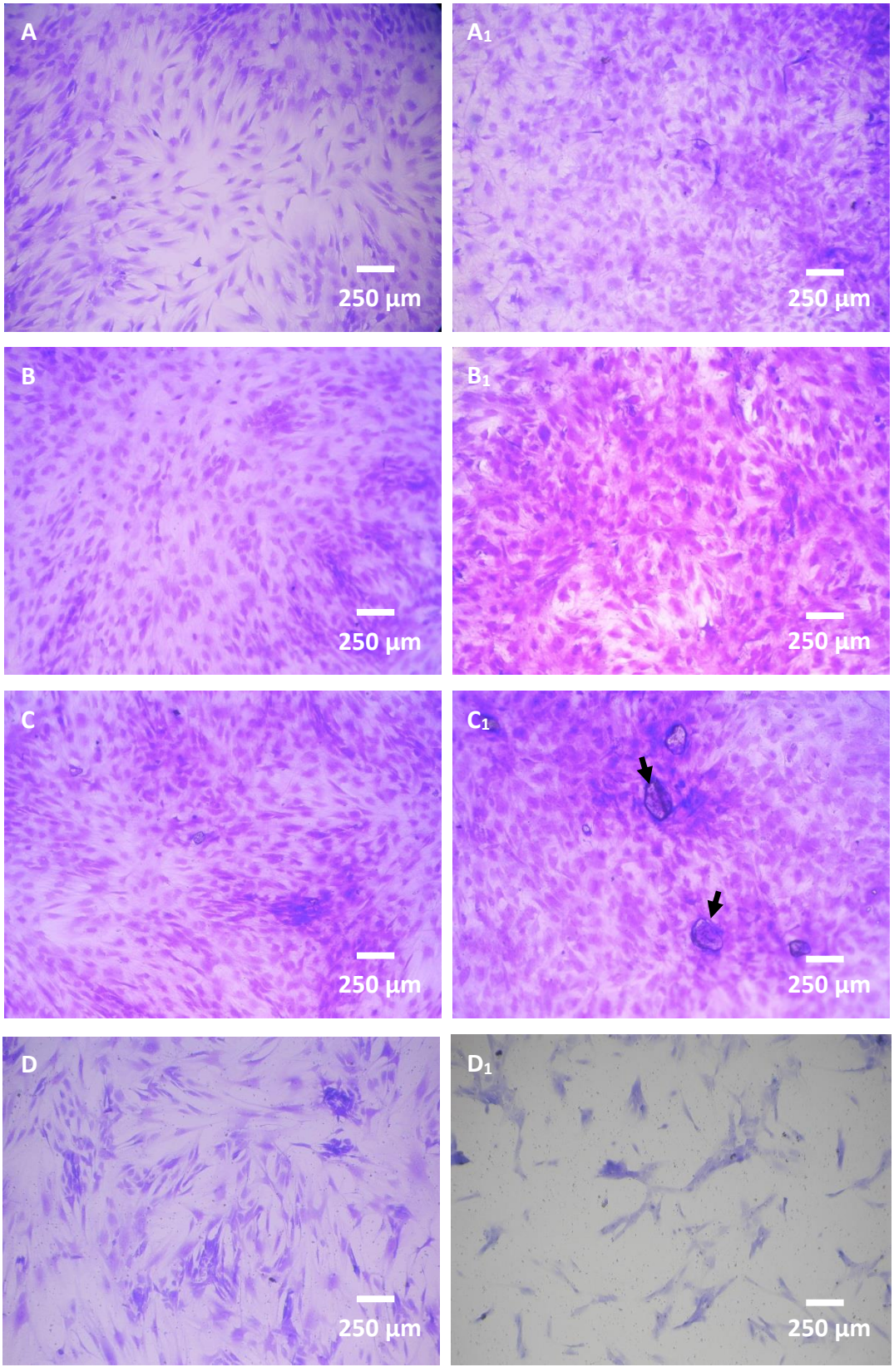

Figure 5-20: Crystal violet stained hMSC (3070) P5 cultivated on various 2D substrates for 21 days. A) Glass, B) PLA, C) PLA HAp and D) PLA HAp CTAB. A-D = basal medium and A_1-D_1 = osteogenic medium. Arrow indicates subsurface aberrations. 40X magnification.

Long term culture of hMSC on CTAB dispersed HAp within PLA matrices revealed differences in cellular morphology following 21 days' incubation in various media (figure 5-20). Cells cultivated on glass substrates (A & A_1) appear to have a variance in morphology from a striated form in A to a cobblestone-like form in A_1.

Cells cultivated on PLA substrates not containing CTAB appear to have a rounded phenotype in both media groups. Large agglomerates can be observed in PLA HAp substrates, as can be observed in C & C_1 black arrows. The density of cells cultivated on PLA HAp CTAB surfaces appeared to be substantially reduced (D & D_1) in comparison to other substrate groups. It was also observed that density varied between media groups with less cells in the osteogenic medium grouped substrates (D_1).

Immunofluorescence was used to quantify differences in cell morphology to assess cell – cell and cell – material differences between glass, PLA+ and PLA+ HAp coated surfaces. Phenotypic observations of hMSC cultivated on glass, PLA+ and PLA+ HAp coated are present in images figure 5-21 & figure 5-22, quantification of these images are displayed in figure 5-23 and figure 5-24.

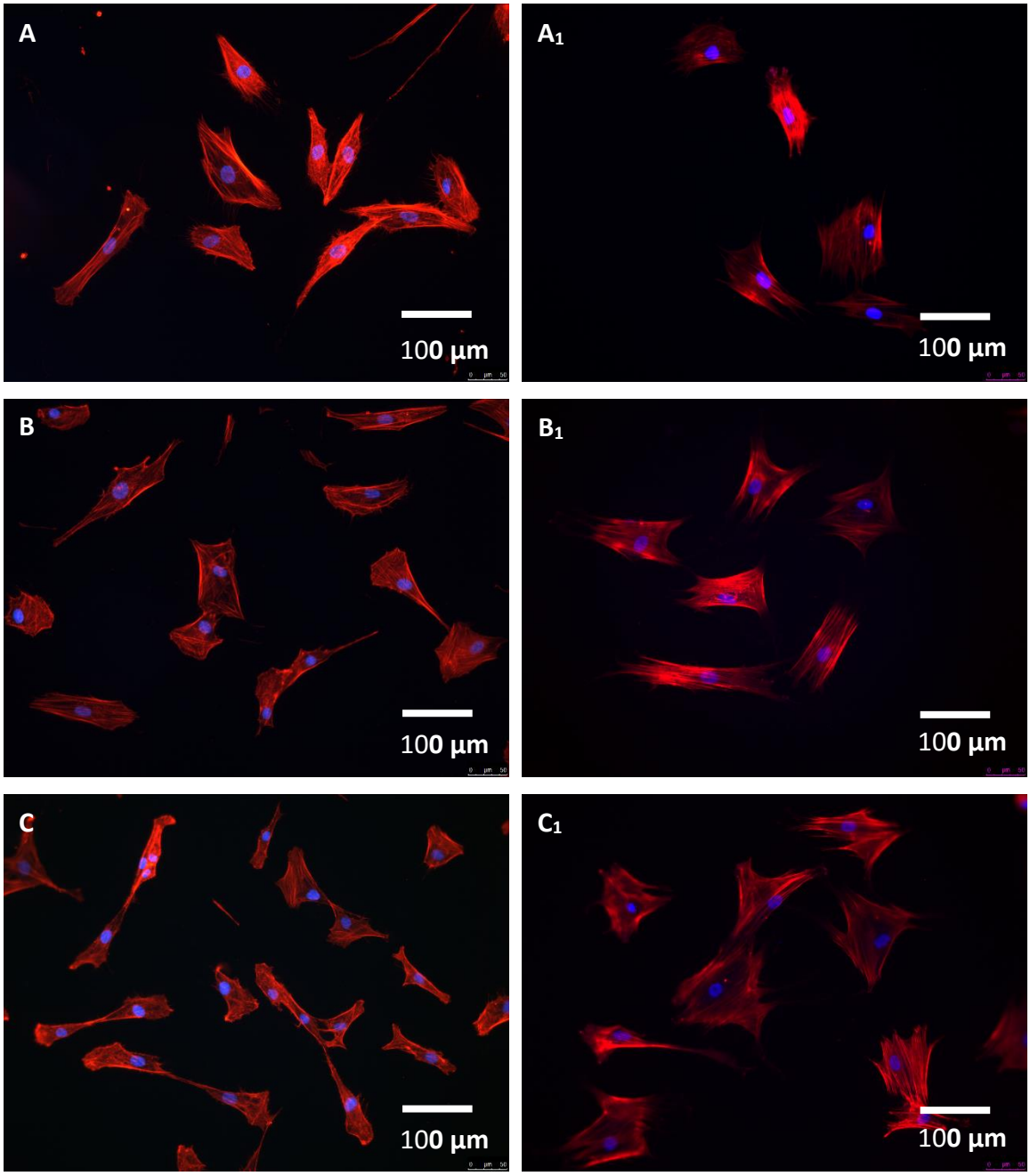

Figure 5-21: Immunofluorescence images of hMSC cultured for 24 hours on A) glass, B) PLA+ and C) PLA+ HAp coated. A-C) Y201 A_1-C_1) 3388. 200X magnification. Red = rhodamine phalloidin & Blue = DAPI.

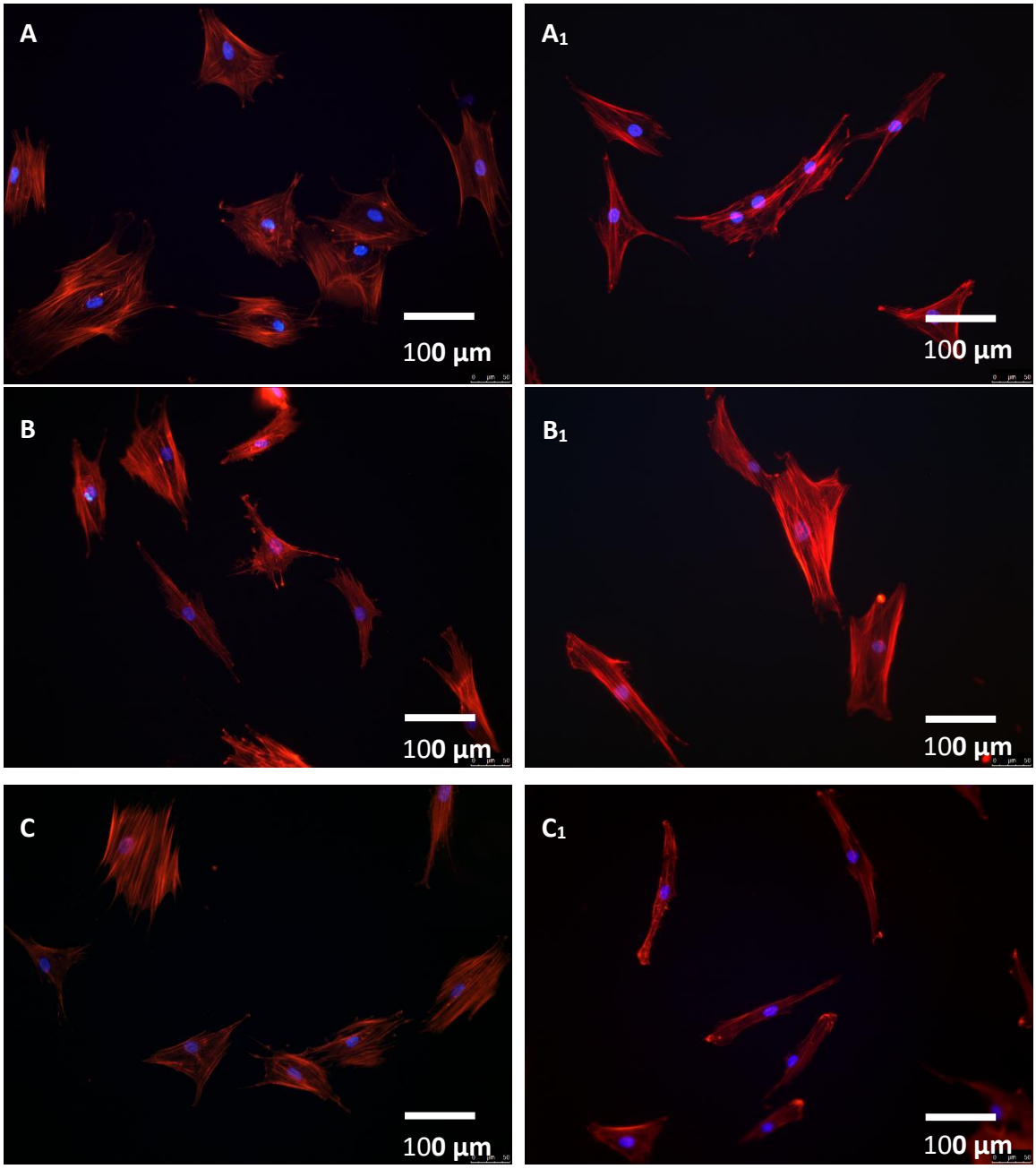

Figure 5-22: Immunofluorescence images of hMSC cultured for 24 hours on A) glass, B) PLA+ and C) PLA+ HAp coated for 24 hours. A-C) 3286 A_1-C_1) 3287. 200X magnification. Red = rhodamine phalloidin & Blue = DAPI.

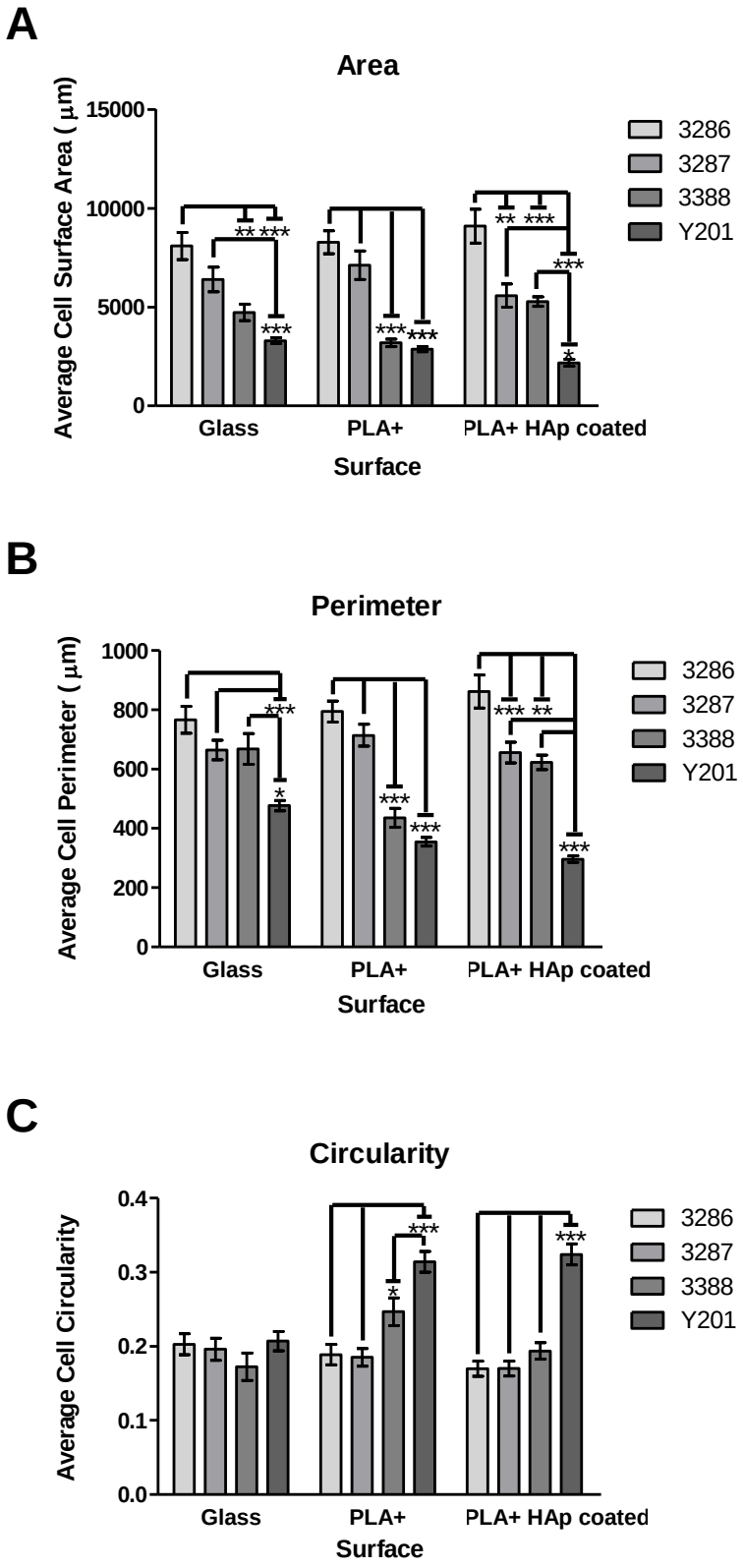

Figure 5-23: Donor-to-donor morphological analysis of hMSC cultured on a variety of surfaces for 24 hours. (A) Average cell surface area, (B) perimeter and circularity (C). (Number of cells assessed n = 60)

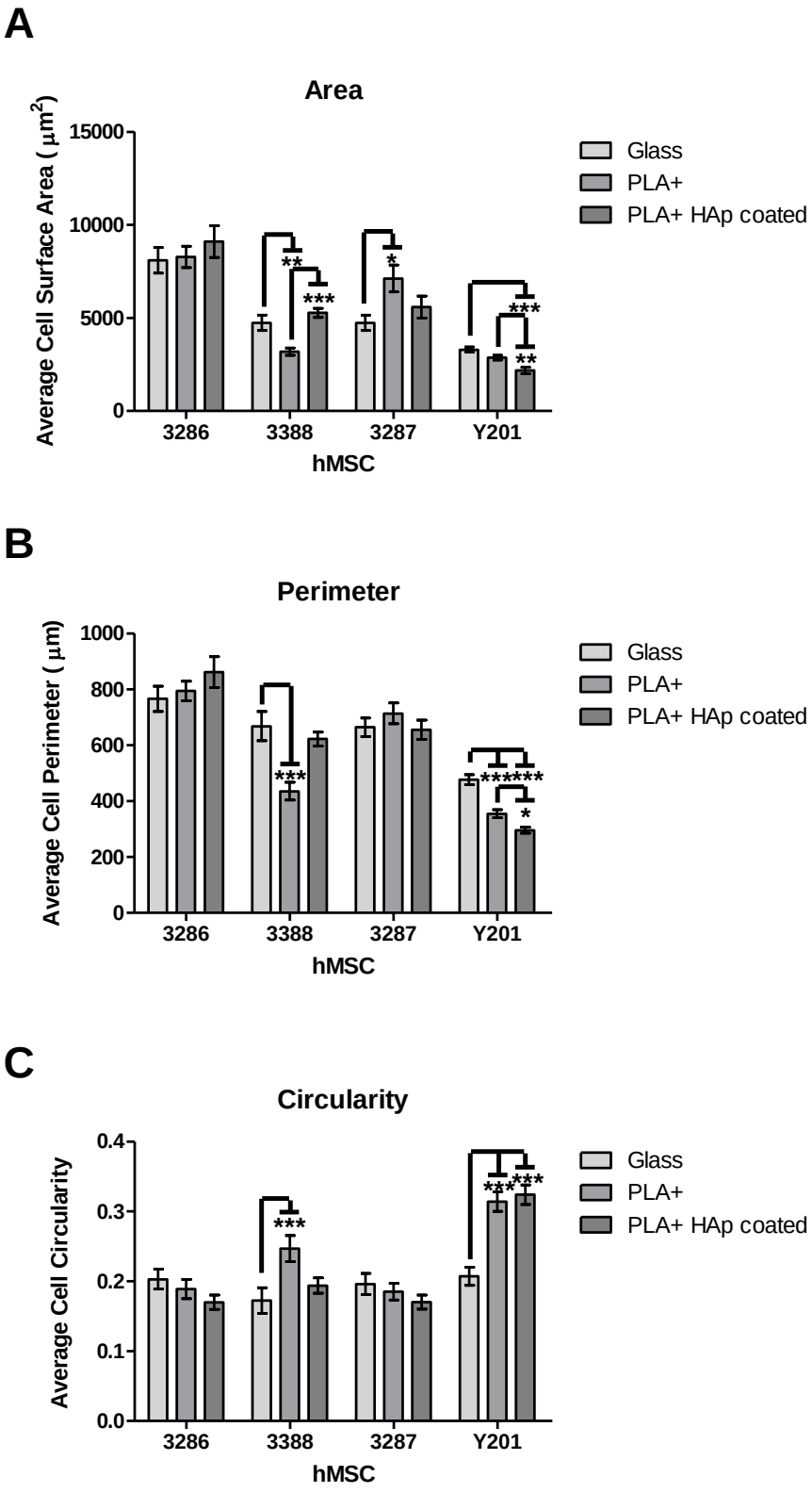

Figure 5-24: Cell-to-material morphological analysis of hMSC cultured on a variety of surfaces for 24 hours. (A) Average cell surface area, (B) perimeter and circularity (C). (Number of cells assessed n = 60)

Immunofluorescent images demonstrate sparsely adhered hMSC to various substrates, the rhodamine phalloidin highlights the cellular f-actin cytoskeleton and DAPI the cell nucleus (figure 5-23 & figure 5-24). From these representative images it was difficult to determine variances between these donor cell types and surfaces.

Inter-patient variance in hMSC morphology was assessed to provide an insight into phenotypic differences on various substrates. Figure 5-23 illustrates variances between donor cell types on different surfaces. Figure 5-23A demonstrates significant differences in donor cell surface area on the various substrates. Patient derived 3286 hMSC have the largest surface area on all substrate surfaces, these differences were significant when compared with 3388 and the Y201 cell line which had the smallest surface area on all substrate surfaces. Patient derived 3287 had the second highest surface area on all surfaces which was also significantly larger than Y201 only in the PLA+ HAp coated surface group.

Cellular perimeter results coincided with surface area in all hMSC cell types across all surfaces, except for patient derived 3388 which had a similar perimeter with 3287 but a reduced surface area when cultured on glass.

Cell circularity was similar in all patient derived hMSC with an average circularity of 0.191 ± 0.009 on glass, 0.207 ± 0.020 PLA+ and 0.178 ± 0.008 on PLA HAp C. Circularity of Y201 was not significantly different when compared with patient derived cell types when cultured on glass.

Cell – substrate interaction was examined to provide an insight into any trends in hMSC morphology to the different substrates.

hMSC cell surface area revealed no significant differences in 3286 between all substrate groups. Patient hMSC 3388 showed a significant reduction in surface area between glass and PLA+ substrate, however there was a significant increase reported between PLA+ and PLA+ HAp coated surfaces. Patient hMSC 3287 revealed a statistical increase in cell surface area between glass the PLA+ surface group. Y201 indicated a reduction in surface area in HAp coated PLA+ groups when compared with both glass and PLA+ surfaces.

hMSC cell Perimeter measurements revealed no significant differences in 3286 and 3287 cell perimeter between all substrate groups. Significant reduction in patient hMSC 3388 cell perimeter was noted between glass and PLA surface groups. Y201 cell perimeter was significantly reduced on PLA+ and PLA+ HAp coated substrates relative to glass. Y201 cell perimeter on HAp coated PLA+ was also found to be significantly lower than cells cultured on PLA+ alone.

hMSC circularity showed no significant differences in 3286 and 3287 cell circularity between all substrate groups. Patient derived hMSC 3388 demonstrated a significant increase in cell circularity between glass and PLA+ substrate group. Similar results were found in Y201 with a significant increase in both PLA+ and PLA+ HAp coated substrate groups

5.3.1.1 Cell Viability (CV/MTT)

The influence of matrix filled PLA HAp and PLA HAp CTAB composite substrates were investigated for long term cell viability using the methods outlined in section 5.2.4 (figure 5-25).

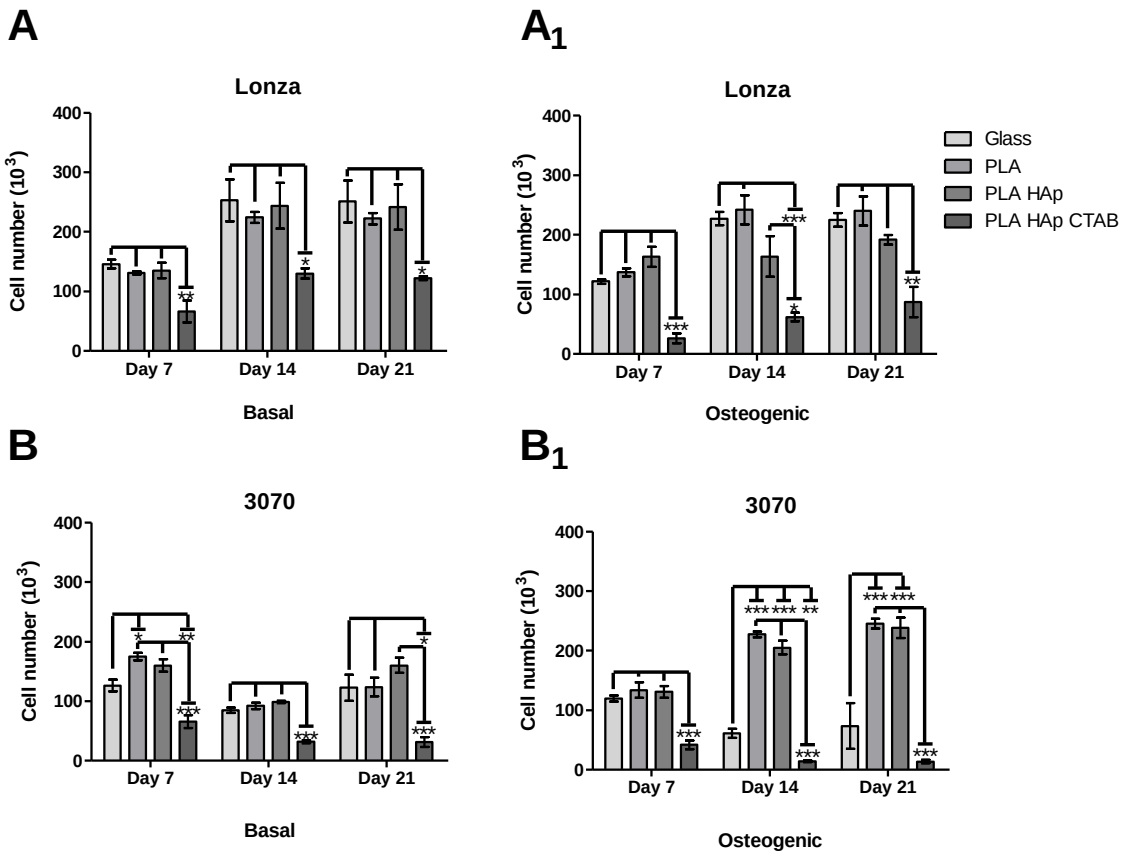

Figure 5-25: Crystal violet derived cell number of hMSC A) 'Lonza' and B) 3070 on various surfaces over 21 days. A & B hMSC cultured in basal medium and A_1 & B_1 in osteogenic medium. (n = 4)

Similar cell densities were observed on Lonza hMSC cultivated on glass, PLA and PLA HAp substrates with no significant differences at any time point in both media groups. A significant reduction in cell number was seen in Lonza hMSC cultivated on PLA HAp CTAB groups compared with all other substrates at every time point in all media groups. This reduction in cell number was mirrored in the patient derived 3070 except at day 21 in the osteogenic medium group where there was no significant difference between glass and the PLA HAp CTAB group. A statistical reduction in glass substrate cell number was observed in the 3070 group at day 14 and 21 in the osteogenic medium group.

It was observed that patient derived 3070 hMSC monolayer in the glass osteogenic medium formed a dense cell cluster after day 7 and began to condense removing the monolayer from the glass coverslip.

The cellular viability of hMSC cultivated on HAp coated PLA+ substrates was investigated for 7 days to assess *in-vitro* material adhesion, biocompatibility and proliferation.

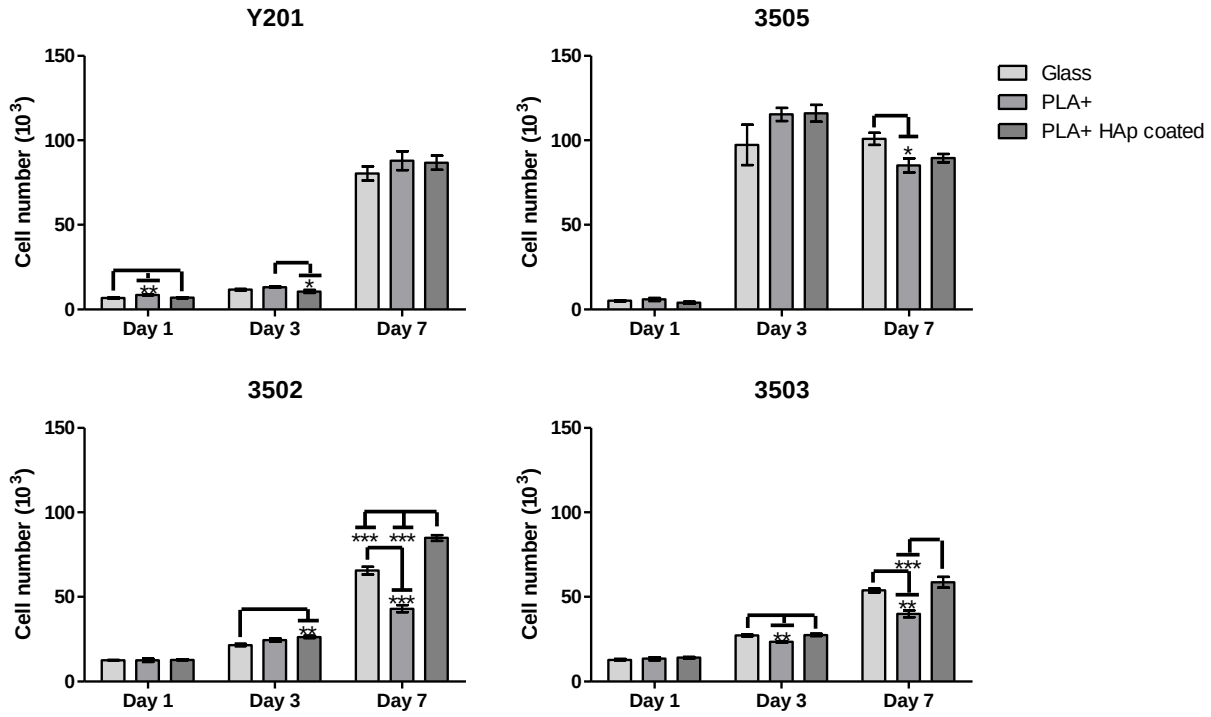

Figure 5-26: MTT derived cell number of hMSC cultured over 7 days on glass, PLA+ and PLA+ HAp coated substrates. (n=5)

Patient derived 3505 cells had a notable increase in cell number at day 3 in all substrate groups in comparison with all other donor cells from the same time point.

Some notable reduction in cell number was observed on PLA substrates in comparison to glass in 3505, 3502 and 3503 at day 7. PLA+ HAp coated substrates had some increases in cell number relative to PLA+ at day 7 in patient derived 3502 and 3503 hMSC, but no variance in Y201 or 3505.

5.3.1.2 Alkaline Phosphatase

ALP was measured to determine the influence of the material substrates on hMSC differentiation along the osteoblastic lineage. The sensitivity of the assay was assessed through the cultivation of hMSC on substrates in both basal and osteogenic media over 7 days.

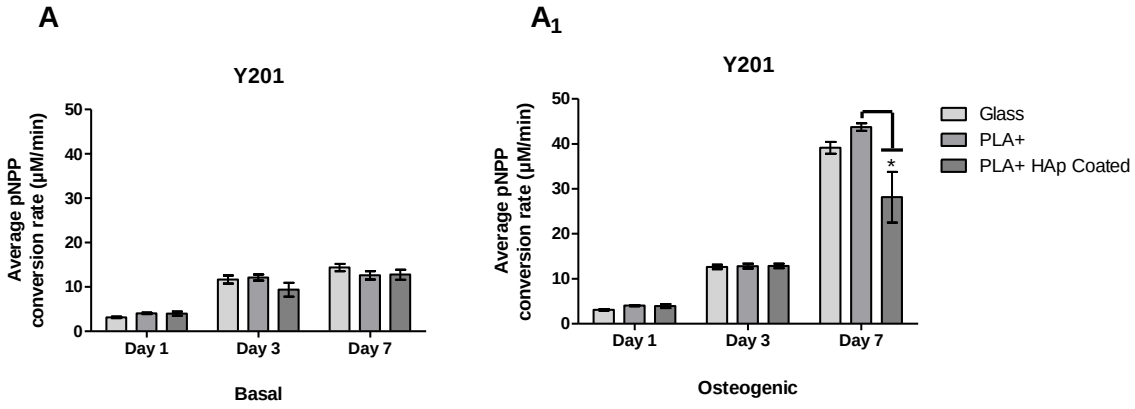

Figure 5-27: Average pNPP conversion rate from Y201 cultured on various surfaces from 1 – 7 days. (n = 4)

A significant decreased in ALP activity at day 7, in hMSC cultivated in osteogenic medium, on HAp coated PLA compared with PLA+. Two-way ANOVA analysis revealed a significant increase in ALP activity from day 1, 3 and 7 on all substrates, in both media groups. Two-way ANOVA of hMSC ALP activity in the osteogenic medium group indicated a significant difference between substrates. One-way ANOVA revealed no significant differences in ALP activity of hMSC cultured in basal media between all surface substrates. No statistical differences observed between substrate ALP activities of hMSC cultured in osteogenic medium group day 1 – 3.

The influence of the substrates shown in section 5.3.1 were assessed for long term *in-vitro* ALP activity on patient derived hMSC.

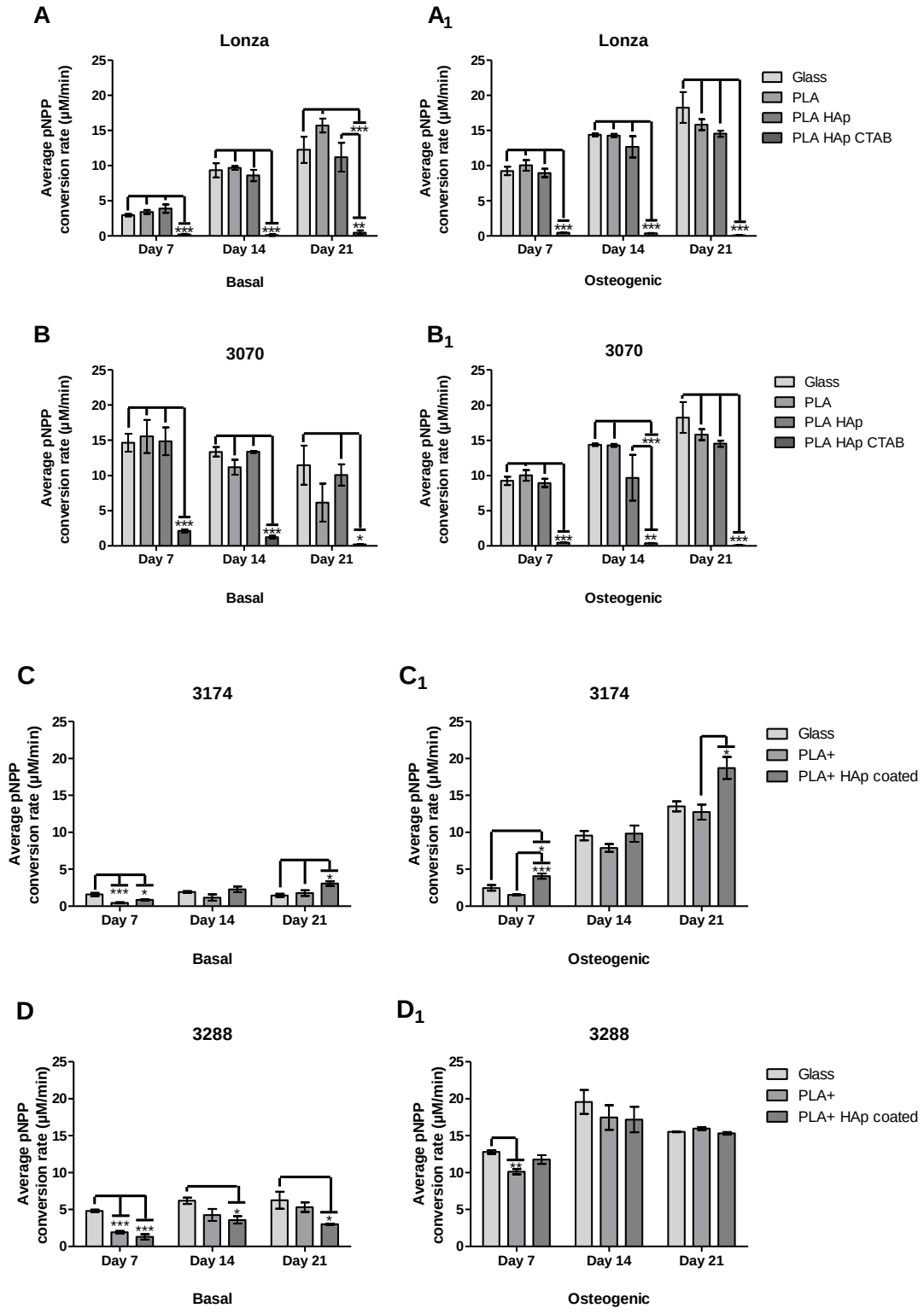

Figure 5-28: Average pNPP conversion rate µM/well/minute. A) Lonza, B) 3070, C) 3174 and D) 3288 cultured on various surfaces from 7 – 21 days. A-D cultured in basal medium and A_1-D_1 in osteogenic medium. A & B glass, PLA, PLA HAp and PLA HAp CTAB surface groups. C & D glass, PLA+ and PLA+ HAp coated surface groups. (n = 4).

A large reduction in pNPP conversion rate was found in all PLA HAp CTAB substrate groups with significant differences compared with all surface groups, at each measurement in both media groups (figure 5-28 A, A_1, B & B_1). No significant differences in pNPP conversion rate were found between glass, PLA and PLA HAp surfaces in both Lonza and 3070 at any time point and in both media groups. One-way ANOVA revealed a significant increase in the conversion rate of Lonza hMSC over 7 – 21 days in both basal and osteogenic media groups in glass control surfaces (A & A_1).

Some statistical reduction pNPP conversion rate was observed in 3174 & 3288 hMSC cultivated in basal medium, at day 7 in PLA+ and PLA+ HAp coated surface groups compared with glass control. 3288 hMSC cultured in basal medium on PLA+ HAp coated substrates had significantly lower pNPP conversion rate at each time point. A statistical increase in pNPP conversion rate was found in 3174 cultured in osteogenic on PLA+ HAp coated surfaces compared with glass, and PLA+ at day 7 and PLA+ at day 21.

5.3.1.3 Gene Expression

Reverse transcriptase – polymer chain reaction (RT-PCR) was used to quantify osteogenic differentiation at a transcriptional level, messenger ribonucleic acid (mRNA) expression of lineage-specific markers were analysed to assess influences of different material substrates on hMSC differentiation.

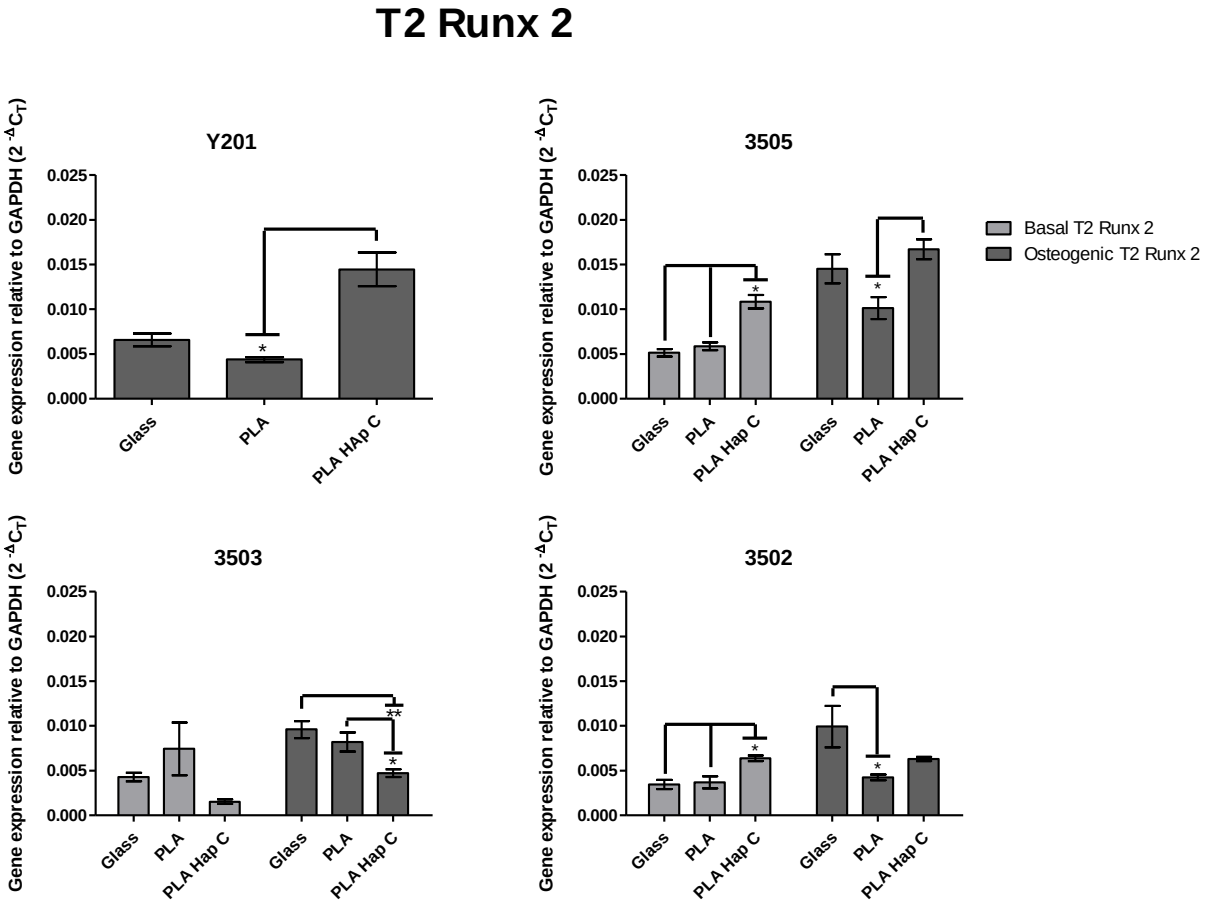

Figure 5-29: mRNA expression of T2 Runx 2 relative to GAPDH. Bars show average gene expression of Y201, 3505, 3503 and 3502 hMSC cells cultivated on glass, PLA and PLA HAp C surfaces in basal and osteogenic media groups for 7 days. (n=5)

Analysis of T2 Runx 2 mRNA expression revealed levels at ~0.005 $2^{-\Delta Ct}$ in all patient derived hMSC cultivated in basal medium on glass controls (figure ***5-29***). These mRNA levels were upregulated by two orders of magnitude when cultivated in osteogenic medium (figure ***5-29***).

Similar levels of T2 Runx 2 expression were observed in glass, osteogenic media groups in patient derived hMSC from ~0.010 – 0.014 $2^{-\Delta Ct}$ (figure ***5-29***). Runx2 expression was lower in hTERT Y201 cell line osteogenic, glass control surface, in relation to patient derived cells at ~0.010 – 0.014 $2^{-\Delta Ct}$ (figure ***5-29***).

A significant increase was observed between basal media groups, HAp coated PLA surfaces compared with glass and PLA controls in patient derived sampled '3505' and '3502' (figure ***5-29***).

A significant reduction in T2 Runx 2 expression was found in PLA HAp coated surface groups in osteogenic medium of '3505' and '3502' compared with PLA and glass surfaces respectively (figure ***5-29***). Interestingly there was no statistical difference observed in the HAp coated PLA surfaces and glass control surfaces in the same groups (figure ***5-29***).

Patient derived '3503' cells revealed a significant reduction in T2 Runx 2 gene expression in HAp coated surfaces in comparison to glass and PLA surfaces in osteogenic medium (figure ***5-29***).

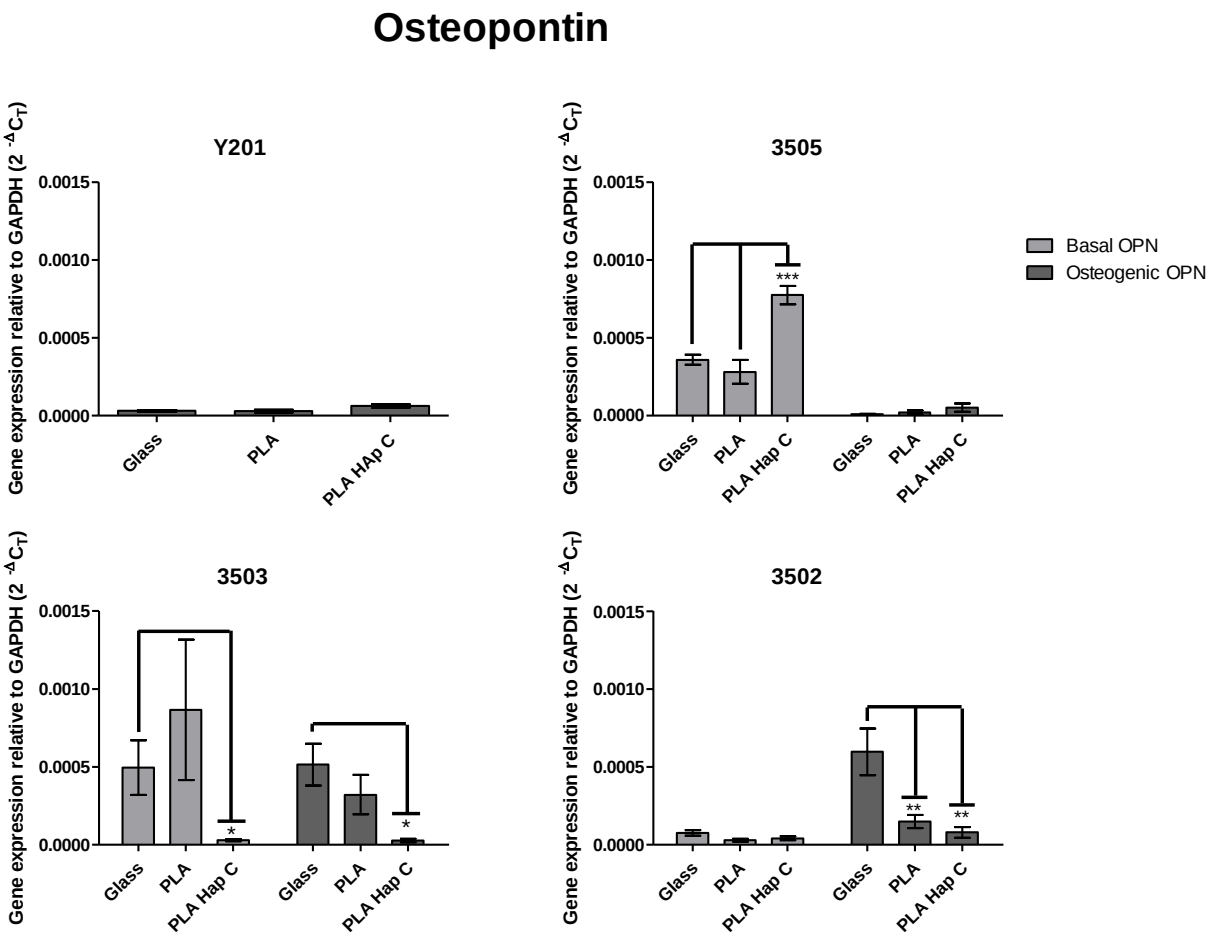

Figure 5-30: mRNA expression of osteopontin relative to GAPDH. Bars show average gene expression of Y201, 3505, 3503 and 3502 hMSC cells cultivated on glass, PLA and PLA HAp C surfaces in basal and osteogenic media groups for 7 days. (n=5)

A significant increase in OPN mRNA levels was found in '3505' hMSC cultured in basal medium, on PLA HAp coated surfaces compared with glass and PLA surfaces (figure ***5-30***).

Data from '3503' revealed a significant reduction in mRNA OPN levels in cells cultivated on HAp coated PLA surfaces in both basal (figure ***5-30***).

Both '3503' and '3502' showed a significant reduction in OPN levels between glass and HAp coated PLA surfaces in osteogenic medium compared with glass control (figure ***5-30***). Patient derived '3502' also revealed a significant decrease in OPN mRNA levels in cells cultured in osteogenic medium, on PLA surfaces in contrast to glass control (figure ***5-30***).

OPN mRNA levels were low with no significant variation between substrate groups in the basal group of '3502' and the osteogenic groups of Y201 and '3505' (figure ***5-30***).

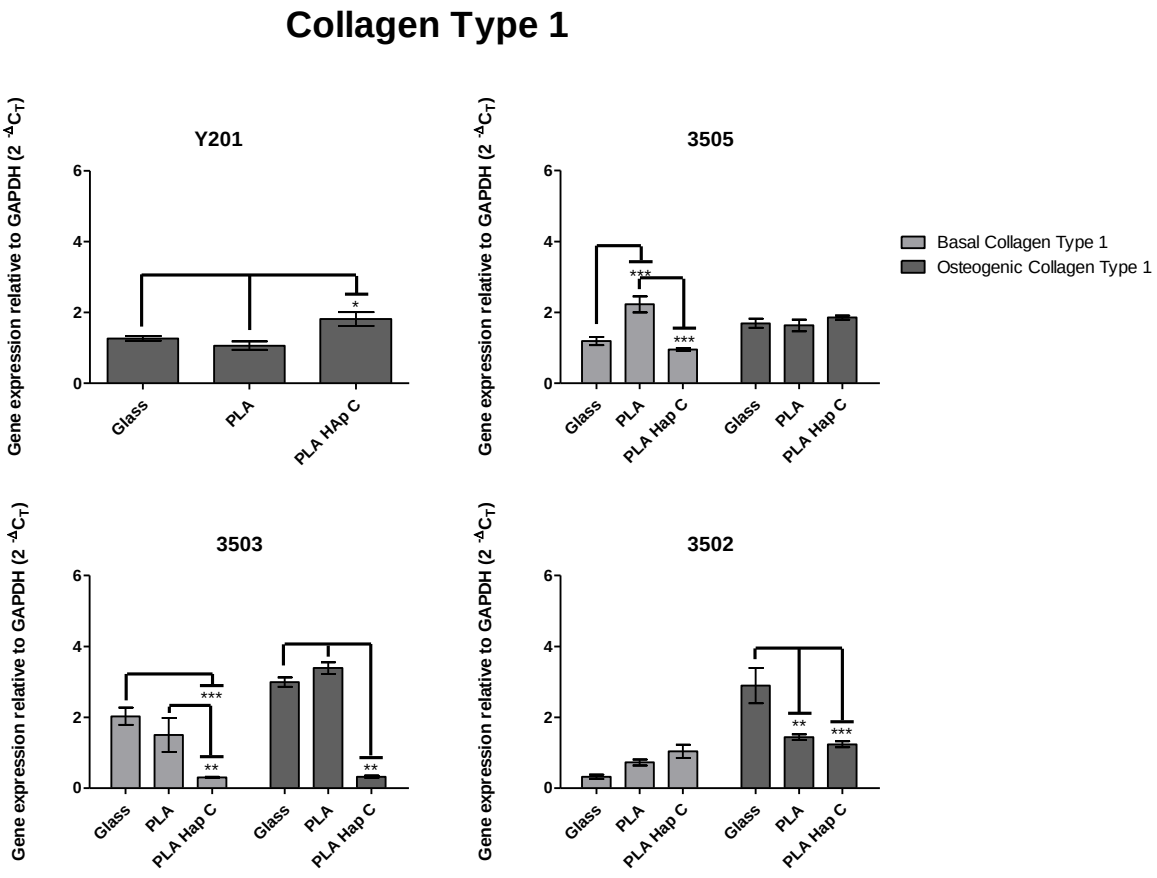

Figure 5-31: mRNA expression of COL1A1 relative to GAPDH. Bars show average gene expression of Y201, 3505, 3503 and 3502 hMSC cultivated on glass, PLA and PLA HAp C surfaces in basal and osteogenic media groups for 7 days. (n=5)

Basal medium glass control surface COL1A1 mRNA expression revealed some inter-patient variability ranging from ~ 0.5 – 2.0 $2^{-\Delta Ct}$ (figure ***5-31***). COL1A1 expression appeared elevated in osteogenic medium treatment groups on glass substrates and again varied from patient to patient (figure ***5-31***). A significant reduction in COL1A1 mRNA expression was found in both '3505' and '3503' hMSC cultured in basal media between HAp coated PLA and PLA control substrate (figure ***5-31***).

No significant differences were observed in COL1A1 expression in '3505' hMSC cultured in osteogenic medium between all substrate groups. COL1A1 mRNA levels were significantly lower in '3503' hMSC cultured in osteogenic medium, on HAp coated surfaces compared with both glass and PLA substrates (figure ***5-31***). This was similar in '3502' hMSC with a significant reduction in both PLA and HAp coated PLA COL1A1 expression relative to glass in osteogenic medium (figure ***5-31***).

A statistical increase in COL1A1 expression observed in Y201 cells cultured in osteogenic medium on HAp coated PLA compared with both glass and PLA substrates (figure ***5-31***).

5.4 Discussion

This chapter demonstrates routes to disperse HAp produced from chapter 4 in various solvents and to produce polymeric nanocomposite materials with a monodisperse HAp filling. Results demonstrate that HAp dispersed in PLA with CTAB are cytotoxic to hMSC. Biological characterisation of HAp filled and coated PLA matrices are non-toxic, however they do not show any significant variation in hMSC adherence, morphology, growth kinetics and osteogenic stimulation compared with control surfaces at the intervals investigated.

5.4.1 *Dispersion of HAp*

5.4.1.1 DMF

Data from DLS analysis allows us to determine that HAp is dispersed to the nanoscale in DMF solvent and TCM solvent following CTAB aided reverse micelle transfer (figure 5-2 and figure 5-13). Physical evidence form TEM images show nanoscale HAp dispersal following composite fabrication (figure 5-6 and figure 5-14).

DMF processing has previously been used to fabricate disperse HAp filled polymer composite materials (Deng *et al.* 2001; Deng *et al.* 2007; Patlolla *et al.* 2010). TEM data revealed some particle agglomeration in the PLA HAp composite bar which was not reported by Deng *et al.* (2001). This could potentially be due to water contamination within the composite solution prior to gelation.

DMF dispersal has its limitations and it is reportedly difficult to completely remove all of the residual toxic solvent (Hong *et al.* 2004). FTIR data of the nanocomposite PLA/HAp bar (figure 5-7) revealed some polymer – DMF interaction at ~1266 cm^{-1} (3) associated with C-N and/or C-H bonds and reduction in peak absorption at ~1675 cm^{-1} (4) (Jacob & Arof 2000; Olejnik *et al.* 1971). The DMF contamination could potentially influence this materials biocompatible properties, however Patlolla and colleges (2010) colleagues showed no detrimental effects on cells cultivated on their electrospun materials. Future work could include flexile strength testing of the composite bars, *in-vitro* assays and NMR analysis to assess the degree of DMF contamination.

TEM observation demonstrated good dispersion of HAP within the PLA HAp composite with some regions of HAp agglomeration (figure ***5-5***). The agglomeration could potentially be caused by the relatively high loading of HAp within the composite, alternatively it could be

caused by lack of ultrasonic dispersion or contamination with adsorbed water. Different loading densities, ultrasonic dispersion duration and dehydration of the HAp could be tested to investigate these speculations. Furthermore, TEM EDAX could be used to confirm the presence of the HAp.

5.4.1.2 CTAB

Data form DLS analysis demonstrated optimal dispersion of HAp within deionised H_2O medium with 10 mM to 186.37 ± 6.41 nm (figure 5-9). Stability of the HAp suspension illustrated in figure 5-10 shows characteristic sedimentation of HAp particles in a water medium, whereas the dispersion of HAp in the CTAB 10 mM water solution appears to remain consistent throughout the measurements. The transfer of the theorised HAp – CTAB complexes demonstrated an increase in average particle size following transit to the TCM phase (figure 5-13). TEM through the spin cast CTAB dispersed PLA HAp composite demonstrated dispersion of nanoparticles with some areas of agglomeration and some unknown artefacts (figure 5-14).

The dispersion and stability of HAp in the H_2O medium with 10 mM CTAB concentration is likely due to the attainment of the CMC (Cai *et al.* 2007b). The measured increase in average particle size following phase transfer could potentially be caused by dissociation of some of the CTAB from the HAp to the non-polar phase. This CTAB dissolution would likely lead to rearrangement of the HAp – CTAB complex, favouring stability of a larger complex.

The dispersion of the HAp observed in the TEM of the spin cast CTAB dispersed PLA HAp composite correlates with 2D SEM cell studies showing subsurface agglomerates (figure 5-14 and figure 5-18). The artefacts observed in figure 5-14 could potentially be caused by crystallisation of dissociated CTAB through the casting process. Further work is required to characterise this material. For example, TEM EDAX could be used to confirm the presence of the HAp and XPS could be used to determine the presence of CTAB crystals within the PLA structure.

As previously introduced, the process of transferring nanoparticles from an aqueous environment into an organic hydrophobic phase is not a new approach. However, the work presented in this chapter demonstrates a novelty in overcoming dispersion challenges associated specifically with suspension of HAp in organic hydrophobic solvents.

5.4.1.3 pH

Results from DLS analysis of HAp in water with various pH demonstrated improved dispersal in pH 10 to an average size of 689.20 ± 44.46 nm (figure 5-15). The coating of the PLA+ by HAp shown by SEM demonstrates agglomeration of the particles on the surface of the material (figure 5-16).

Balancing the electrostatic interaction of the solid and liquid phases improves dispersion of solids through alteration of the entropic threshold. Altering the pH of the dispersant medium appeared to be an effective way to balance electrostatic differences and disperse the HAp within the water. The HAp crystals were synthesised at pH 10, they would therefore order to minimise potential differences with the surrounding environment in comparison to crystals prepared at lower pH (section 4.3.4 . This would explain the improved dispersion potential at higher pH conditions (figure 5-15).

The coating of the PLA+ by HAp shown by SEM demonstrates adsorption of the HAp to the PLA surface (figure 5-19C, C_1, D and D_1). This interaction is likely caused by hydrogen bonding of hydrogen bond acceptors (O=C) on the surface of the plasma treated PLA and hydrogen bond donators (O-H) groups from the hydroxyapatite forming hydrogen bonds.

5.4.2 *CTAB aided HAp dispersed PLA composite cytotoxicity*

The cytotoxicity of CTAB dispersed HAp PLA substrates is evident from the stressed morphology and sparse density of the hMSC in (figure 5-20 D & D_1). Cell assays also demonstrated CTAB cytotoxicity with significantly reduced cell viability (figure 5-25) and ALP (figure 5-28 A & B) at day 7-21.

CTAB has a number of uses including the control over production of gold and silver nanoparticles. Indeed some concern over nanoparticle cytotoxicity is in part due to CTAB release from these nanoparticles and has been widely reported (Alkilany *et al*. 2009; Qiu *et al*. 2010)

The mechanism of CTAB cell cytotoxicity is a disputed subject although two mechanisms have recently been postulated. The first is CTAB – cell membrane phospholipid substitution, at high concentration leads to cell death, but at low concentrations allows for rearrangement of the cell membrane. Secondly, dissociated CTAB (CTA+) has an affinity of ATP synthase interfering with ATP production, leading to cessation of cell metabolism. Cell viability analysis using CV

dye extraction assay shows some cell survival, however ALP activity is drastically reduced which corroborates with the second suggested mechanism of CTAB induced cytotoxicity. (Vieira & Carmona-Ribeiro 2006; Ito *et al.* 2009).

The CV dye extraction assay only provides information on the approximate number of cells cultivated on the CTAB dispersed HAp PLA materials, an MTT assay could have been used to determine the effect on cellular metabolism. Replacement of the surfactant with one which is more biocompatible would be the focus of future research. Research by Maurin *et al.* (2002) has also demonstrated the inhibitory effects of polyunsaturated fatty acids. This would also need to be taken into account when selecting a potential surfactant candidate.

5.4.3 *PLA HAp biocompatibility and differentiation*

Evidence that the combination of PLA and HAp materials are non-toxic and have no influence on hMSC behaviour is demonstrated by the lack of significant variation between hMSC from morphological, cellular viability, ALP and gene expression analysis (figure 5-21, figure 5-22, figure 5-23, figure 5-24, figure 5-26, figure 5-27, figure 5-28, figure 5-29, figure 5-30 and figure 5-31).

Polymer HAp filled materials have previously demonstrated increased cell surface spreading with PLGA and carbonated HAp with “rice-like” (Hong *et al.* 2007). However, results from the morphological assessment of hMSC cultivated on PLA+ HAp coated and HAp filled PLA materials had no significant influence on cell surface area (figure 5-21 and figure 5-22). This is potentially due to differences in surface topography which was not measured in work presented in this chapter. Stylist profilometry or laser interferometry could have been used to measure surface topography.

Müller *et al.* (2014) investigated the effect of agglomerated hydroxyapatite nanoparticles with different morphology on mature human macrophages. Results demonstrated reduced HAp uptake in cells exposed to disperse HAp concluding that cell toxicity is correlated with the degree of HAp uptake into the cell. Although HAp uptake was not evaluated in this chapter, the form of HAp exposure to the cells differs from Müller *et al.* (2014) in that the HAp was agglomerated on the polymer surface. The morphology of the HAp on the PLA+ surfaces, show approximate 1 µm agglomerates on the surface (figure 5-19) and viability of cells on these substrates appears to be unaffected over 7 days (figure 5-26). This could be due to differences

in cellular uptake of the HAp when bound to the surface of a material. Further investigation could look at the uptake of HAp into cells on these substrates using sectioning/TEM and a parallel study similar to that used by Müller *et al.* (2014).

The ALP enzyme activity of hMSC cultured on the HAp coated PLA+ substrates had a highly variable response at day 7 between all hMSC groups (figure 5-28). ALP activity of patient derived hMSC in basal medium indicated at reduction compared with control at day 7. Evidence for the reduction in ALP activity is supported by work from Ha *et al.* (2015) using morphologically similar HAp. Results from Ha *et al.* (2015) showed a significant reduction in ALP mRNA expression in MSCs at 3 and 7 days culture with increasing concentrations of "needle-like" HAp (5-50 µg/mL). Published literature has also demonstrated the ability of "needle-like" HAp coatings to enhance ALP and osteogenic gene differentiation in human osteoblast cells. Roohani-Esfahani *et al.* (2010) demonstrated a significant increase in ALP activity, Runx2 and collagen type I gene expression in human osteoblasts on biphasic calcium phosphate (BCP) scaffolds coated with polycaprolactone and needle-like HAp coated scaffolds at day 7 compared with BCP coated PCL alone.

The mRNA gene expression results from hMSC to HAp coated PLA substrates in this chapter are highly variable. Some trends were observed in OPN and collagen type I mRNA expression, with a significant reduction observed in patient derived hMSC 3503 and 3502 in osteogenic medium. Contradicting this data Ha *et al.* (2015) demonstrated a significant increase in OPN from MSCs in response to similar HAp following 7 days culture.

Previous literature has established the enhanced proliferative and osteogenic effects of HAp nanoparticles on bone cells and hMSC over conventional ceramic substrates (Webster *et al.* 2000). Results from this chapter do not reflect the reported observations of hMSC to HAp nanoparticles.

There are a number of possible explanations for this observation. Primarily differences in HAp crystallite dimensions and surface area have been suggested to play a role in hMSC behaviour modification (Cai *et al.* 2007b). As discussed in the previous chapter, the HAp synthesised and used for this chapter has specific crystallite dimensions and crystallinity, which may influence its effect on hMSC behaviour. The quantity of HAp coated on the PLA substrate is unknown and may not be sufficient to elicit an effect on hMSC behaviour. The quantity of HAp on the

PLA substrate could have been determined using ICP-AES, however this equipment was unavailable at the time of this work.

Functional heterogeneity in discrete hMSC populations are known to vary from donor to donor and knowledge regarding these populations is not fully understood (Phinney 2012). Expression of transcriptional mRNA for specific osteogenic markers is often transient throughout the differentiation process. Heterogeneity within the hMSC population would influence the osteogenic gene expression profiles and therefore the data collected at a single time point (figure 5-29, figure 5-30 and figure 5-31).

The hMSC isolated in this thesis are derived from female donors with OA ranging from 56 – 80 years of age. The reparative and destructive processes associated with OA have been linked to functional alteration in hMSC populations (Luyten 2004). This chapter has demonstrated various responses to HAp which might allude to differences in hMSC sensitivity to HAp, however a more targeted study would be required to investigate this hypothesis.

5.5 Conclusion

In this chapter I have presented novel processing techniques to produce monodisperse PLA/HAp materials. The influence of PLA and HAp coated/filled materials on hMSC cell behaviour has been assessed in 2D *in-vitro* experiments. The biological data presented in this chapter shows that PLA/HAp material incorporation and surface functionalisation had no significant effect on the behaviour of hMSC. The CTAB dispersed PLA/HAp substrates however, were found to induce cytotoxicity with prolonged *in-vitro* cell culture.

Chapter 6 – Influence of 2D fibrin/HAp substrates on hMSC Behaviour

6.1 Introduction

In this chapter, the fabrication and characterisation of two-dimensional fibrin hydrogels containing HAp synthesised from chapter 4 will be described. 2D fibrin surface coatings on 13 mm glass coverslips were fabricated for *in-vitro* assays using hMSC to assess the influence of HAp in combination with fibrin. The aim of this chapter is to evaluate the adhesion, morphology, viability and osteogenic behaviour of hMSC to HAp in the presence of a 2D fibrin surface coating.

There are some number difficulties with the *in-vitro* investigation of cells on 2D fibrin hydrogel substrates. Gel formation within a well plate leads to the formation of a meniscus, of which may influence the cell-substrate interaction. To overcome this issue, this chapter presents a method to produce flat scaffolds by sandwiching the fibrinogen thrombin solution within 13 mm glass coverslips. Synthetic amino acid chains such as poly-L-lysine have been used to enhance substrate interactions with ECM proteins (Tsuchiya *et al*. 2001). Poly-L-lysine was therefore coated on one of the glass coverslips to encourage preferential adhesion of the fibrin hydrogel.

The fibrinogen and thrombin concentrations were based on published research with fibrin scaffolds. A fibrinogen solution concentration of 20 mg/mL was selected based on work by Dikovsky *et al.* (2006). In this study Dikovsky *et al.* (2006) investigated the effect of a PEG modified fibrinogen peptide on smooth muscle cells *in-vitro*, results demonstrated good cell proliferation and migration using a spheroid outgrowth model. In addition Bensaïd *et al.* (2003) investigated optimal fibrinogen and thrombin concentrations for hMSC spreading and proliferation. A concentration of 18 mg/mL fibrinogen concentration and 100 U/mL resulted in good proliferation, migration and osteogenic potential *in-vitro* and *vivo*. The thrombin concentration used in this thesis was 13.25 U/mL based on research by Linnes *et al*. (2007). The formulation of the two fibrinogen and thrombin solutions were also based on research by Linnes *et al*. (2007).

6.2 Experimental procedures

6.2.1 *2D fibrin hydrogel fabrication*

Fibrin surfaces were fabricated through the polymerisation of plasma derived Bovine fibrinogen (Merck Millipore - 341573) 20 mg/mL in 0.9% NaCl dH_2O by the addition of an equal volume of plasma derived Bovine thrombin (T4648) 13.25 U/L in low glucose DMEM (similar to Thomson *et al.* 2013).

Solution	Concentration	Solvent	HAp
Bovine thrombin (T4648)	13.25 U/L	DMEM	± 10 mg/mL
Bovine fibrinogen (Millipore, 341573)	20 mg/mL	0.9% w/v NaCl in dH_2O	0

Table 6-1: Fibrin precursor solutions and their constituents.

The Bovine thrombin solution was first made to 13.25 U/L concentration in DMEM and filter sterilised. Thrombin solutions containing 10 mg/mL HAp were made by first weighing out the desired quantity of HAp into a centrifuge tube. HAp was sterilised by incubating with 70% ethanol for 30 minutes, samples were then centrifuged to pellet the HAp at 1000g for 5 minutes. Supernatant was carefully aspirated and HAp was then washed three times with sterile PBS. Finally, HAp was suspended in the thrombin solution to a concentration of 10 mg/mL. Thrombin ± HAp solutions were first sonicated for a minimum of 10 minutes prior to experimentation.

13mm glass coverslips were immersed in 0.01% poly-L-lysine dH_2O solution for 24 hours prior the fabrication of fibrin surfaces. Before use, the poly-L-Lysine coated surfaces were first dried in a class II safety cabinet and UV treated for 30 minutes.

30 µL of fibrinogen and 30 µL thrombin solution (± HAp) were mixed using a pipette on the poly-L-lysine coated coverslip and a clean sterile 13mm glass coverslip was placed on top to distribute the fibrinogen/thrombin mix and incubated for 24 hours at 37^{o}C in a 5% CO_2 humid atmosphere. The clean cover slip was then removed using a needle point to wedge and lever the coverslip away from the fibrin/poly-L-lysine covered surface (figure 6-1).

Fibrin/HAp coated substrates were fabricated by dip coating fibrin substrates in a sterile solution of 0.05 M NaOH in dH_2O with 10 mg/mL HAp. Samples were then washed three times in PBS and UV treated for 30 minutes.

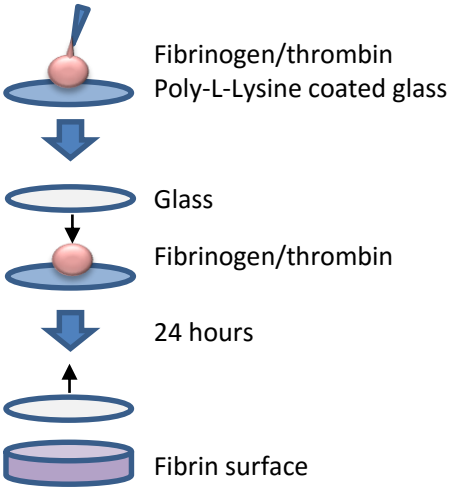

Figure 6-1: Schematic representation of 2D fibrin surface fabrication.

Substrates were washed three times with PBS and incubated with hMSC medium for 1 hour prior to cell seeding. Cells were then seeded on these surfaces and analysed as described in chapter 2.

6.3 Results

The results presented in this section show the development of 2D fibrin/HAp substrates and their evaluation *in-vitro*.

6.3.1 *Surface characterisation*

6.3.1.1 Scanning Electron Microscopy

Samples were prepared according to processes outlined in methods section 3.3.4 . SEM was performed to provide information on fibrin and fibrin/HAp surface topography.

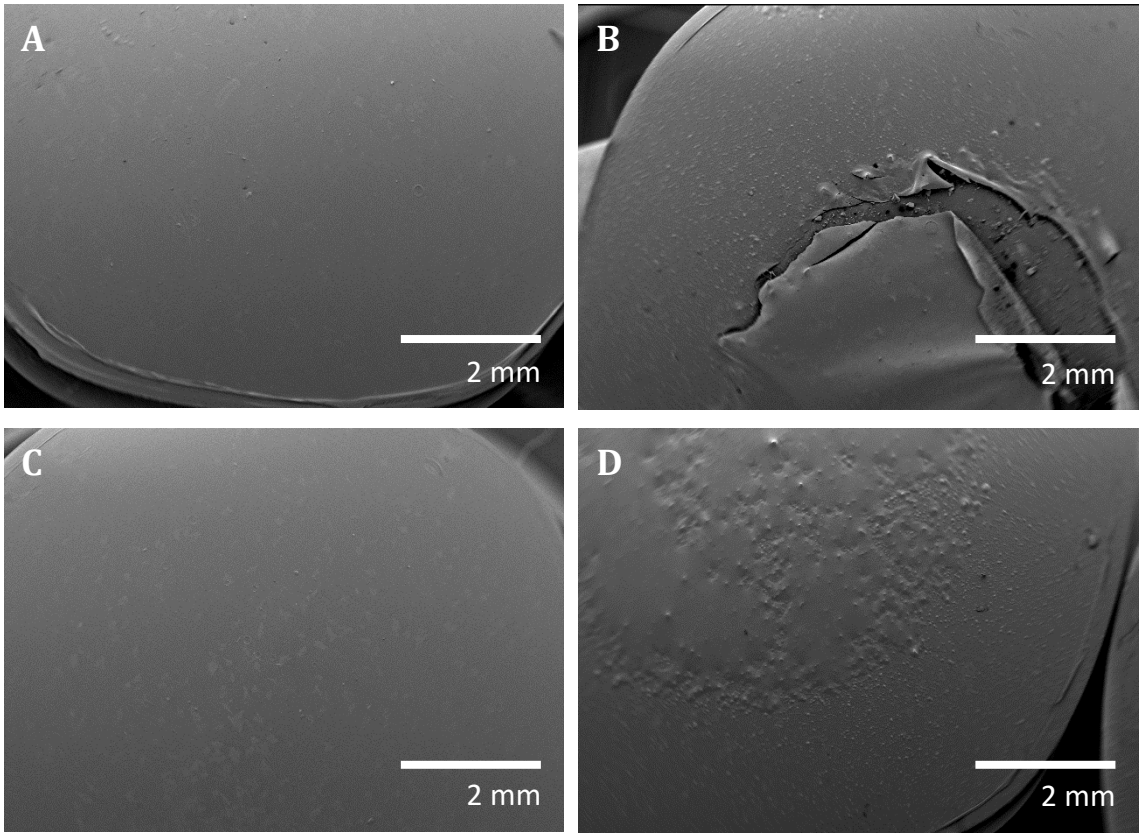

Figure 6-2: SEM images of fibrin (A & C) and fibrin/HAp filled (B & D) surfaces with hMSC cultivated for 24 hours. A – D) 13x magnification.

SEM images of fibrin substrates show a relatively flat morphology covering the 13mm glass coverslip. Figure 6-2B shows fibrin/HAp with central blister region that has lifted form the glass coverslip during processing for SEM analysis. The fibrin/HAp surfaces show differences from the centre to the edges of glass coverslip, with a bulging topography in the centre and a flatter region around the edges (figure 6-2D). The bulging region blister appears to correlate with the location of the fibrinogen and thrombin components mixing site prior to capillary spreading.

6.3.2 *Biological characterisation*

The effects of fibrin/HAp substrates on hMSC adherence, morphology, growth kinetics, and gene expression *in-vitro* was investigated.

6.3.2.1 Cell adhesion and morphology on fibrin and fibrin/HAp surfaces

The effect of fibrin alone and fibrin/HAp substrates was assessed for their role in supporting cell adherence.

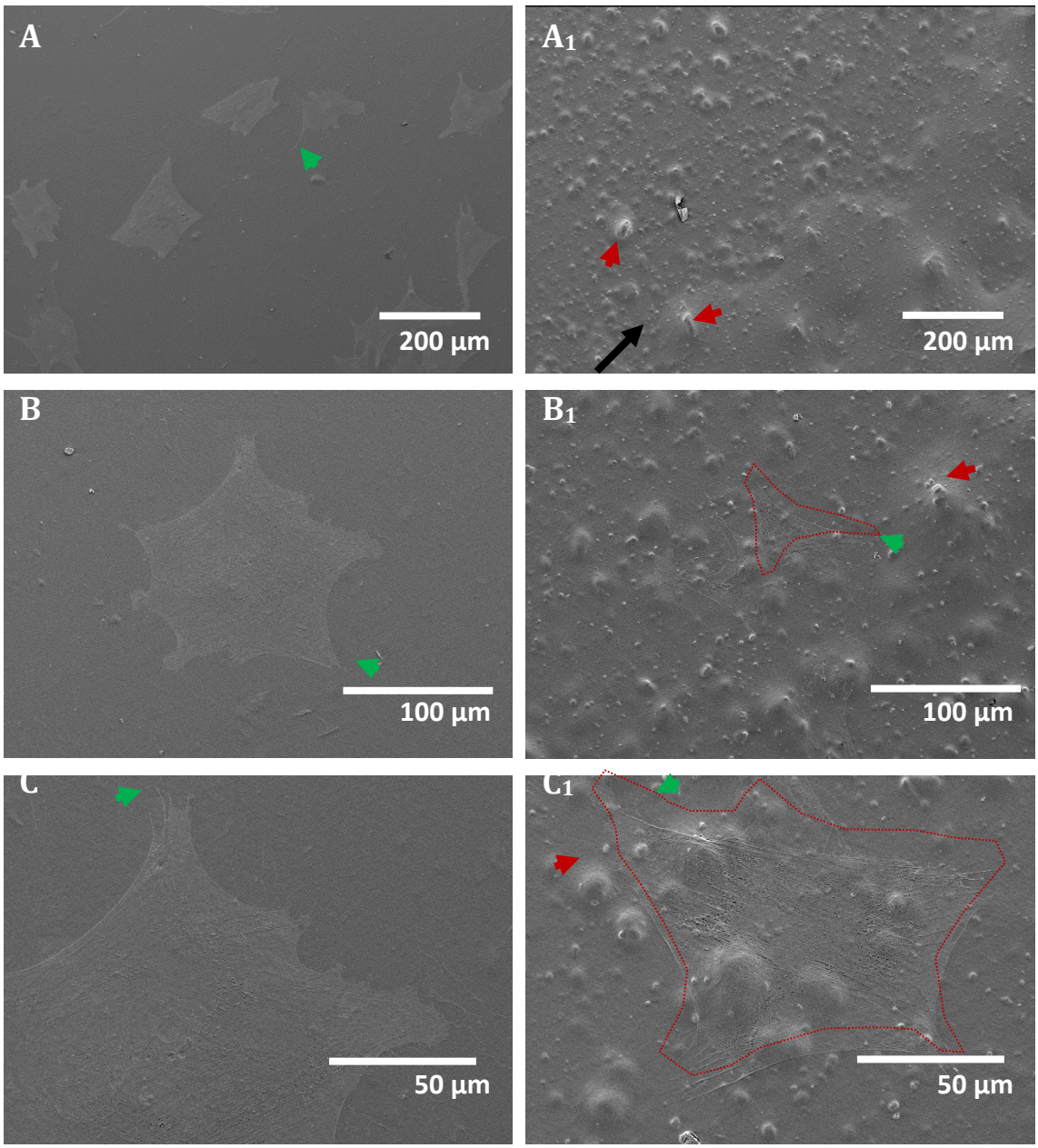

Figure 6-3: SEM images of fibrin (A-C) and fibrin/HAp filled (A_1-C_1) surfaces with hMSC cultivated for 24 hours. A & A_1) 100x, B & B_1) 300x and C & C_1) 6000x magnification. Red arrows = subsurface aberrations and green = pseudopodia. Red outline = cell perimeter.

figure 6-3 A-C shows a relatively smooth homogeneous fibrin hydrogel substrate with cells adhering and spreading. Images from A_1-C_1 demonstrate cells adhering and spreading across a fibrin/HAp surface with subsurface aberrations (red arrow). Figure 6-3C_1 shows a cell adhering, with pseudopodia extending over the fibrin surface, subsurface aberrations can be observed through the cell membrane. The black arrow in image A_1 shows the morphological separation between the bulging region and the non-bulging region of the fibrin/HAp substrate, which appears to wrap around aforementioned subsurface aberrations.

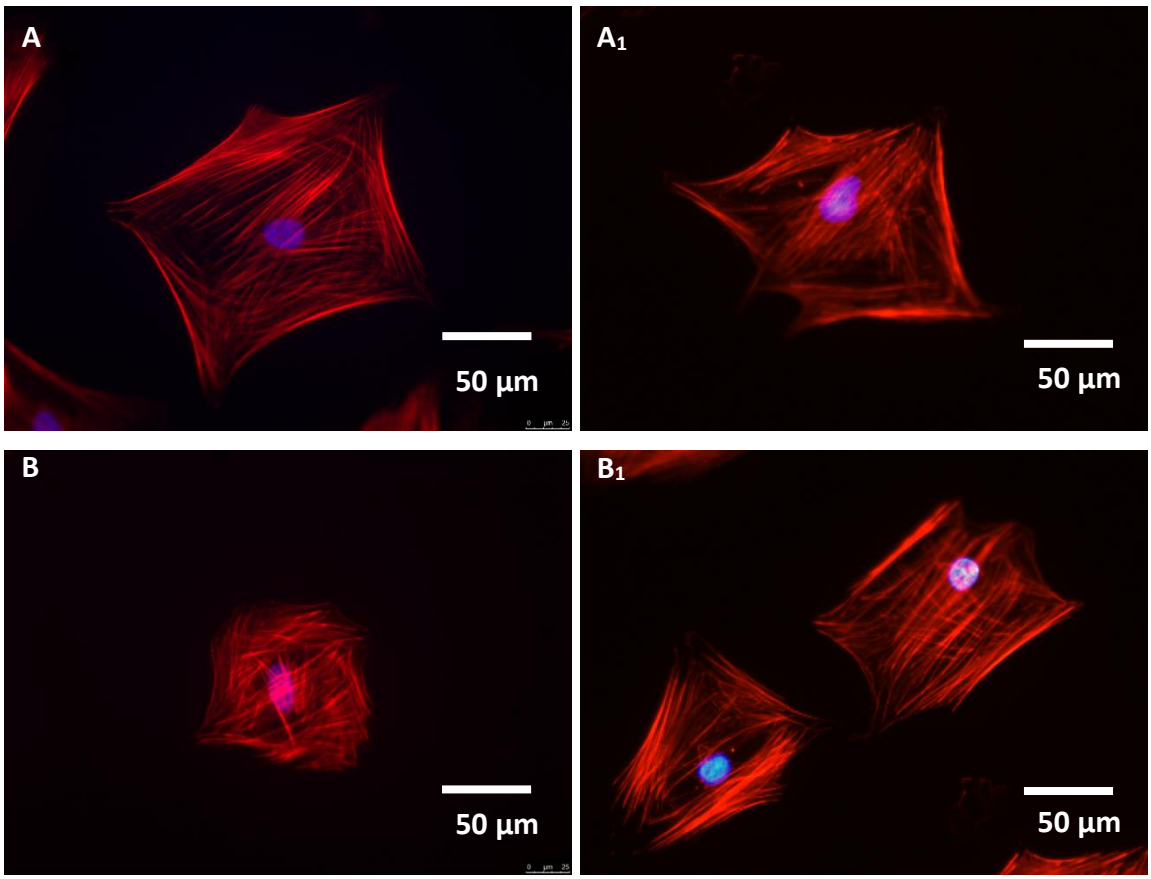

Figure 6-4: Immunofluorescence images of hMSC cultured for 24 hours on A) fibrin B) fibrin/HAp. 400X magnification. Red = rhodamine phalloidin & Blue = DAPI.

Immunofluorescence images of hMSC demonstrate the cytoskeletal structure of hMSC cultivated on fibrin and fibrin/HAp substrates (figure 6-4).

Immunofluorescence was used to assess cell morphology of cells cultured on glass, fibrin and fibrin/HAp filled substrates. Observations of hMSC cultivated on glass, fibrin and fibrin/HAp are present in figure 6-5 and figure 6-6, quantification of cells in these experiments are displayed in figure 6-7 and figure 6-8.

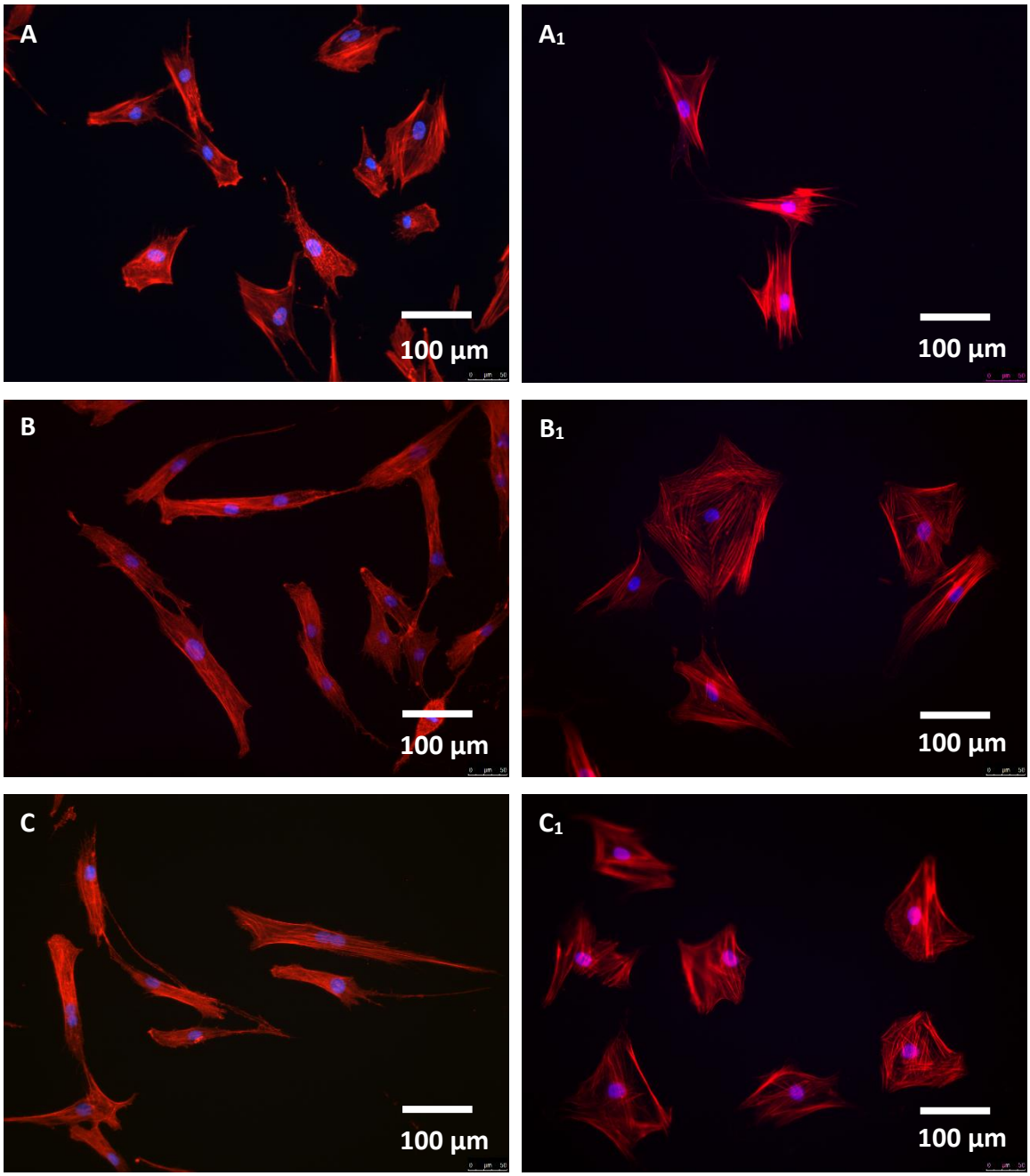

Figure 6-5: Immunofluorescence images of hMSC cultured for 24 hours on A) glass, B) fibrin and C) fibrin/HAp filled. A-C) Y201 A1-C1) 3388. 200X magnification. Red = rhodamine phalloidin & Blue = DAPI.

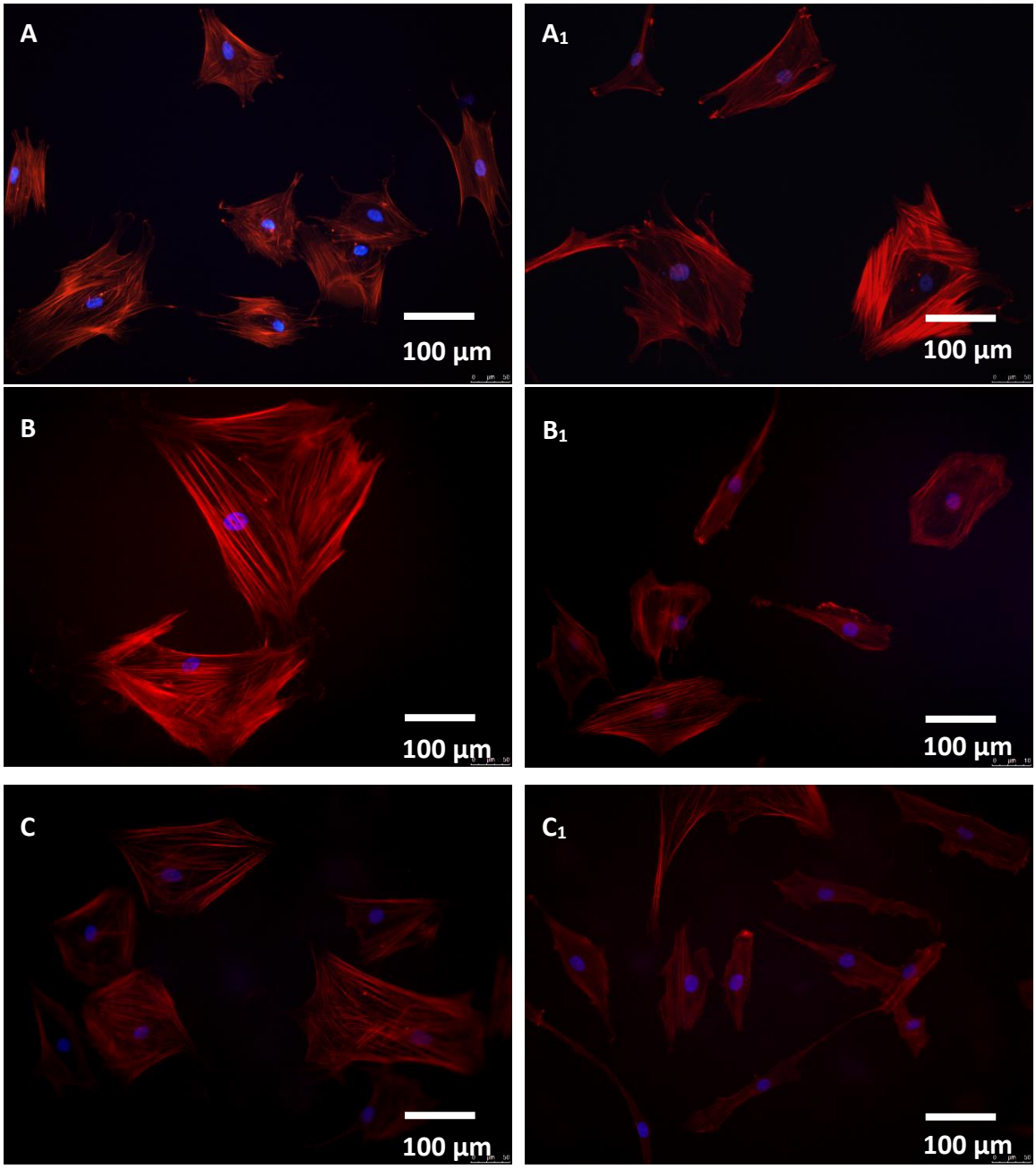

Figure 6-6: Immunofluorescence images of hMSC cultured for 24 hours on A) glass, B) fibrin and C) fibrin/HAp filled. A-C) 3286 A_1-C_1) 3287. 200X magnification. Red = rhodamine phalloidin & Blue = DAPI.

The quantification methodology for hMSC morphology is described in the methods section 3.8 . Results are presented analysing variation based upon donors (figure 6-7) and cell-material influence (figure 6-8).

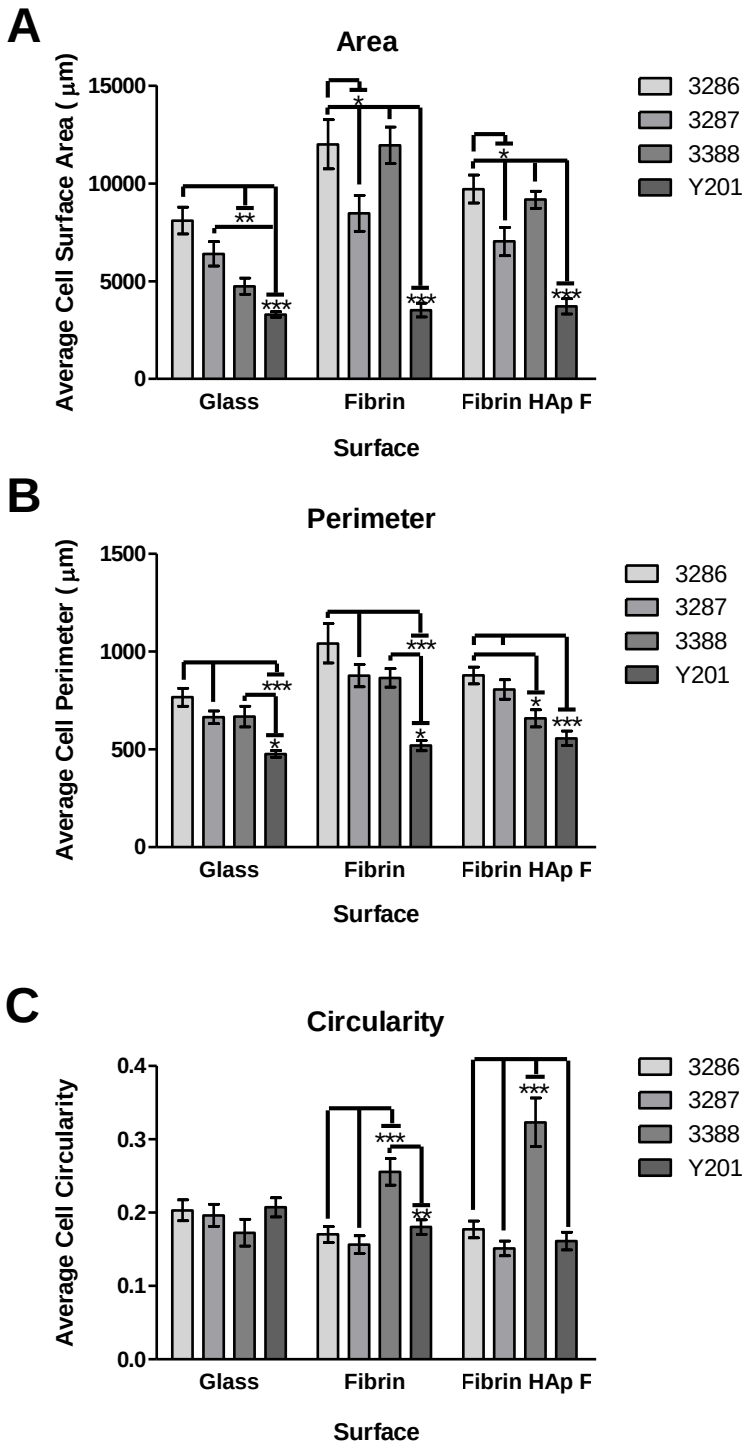

Figure 6-7: <u>Donor-to-donor</u> morphological analysis of hMSC cultured on glass, fibrin and fibrin/HAp filled surfaces for 24 hours. (A) Average cell surface area, (B) perimeter and circularity (C).

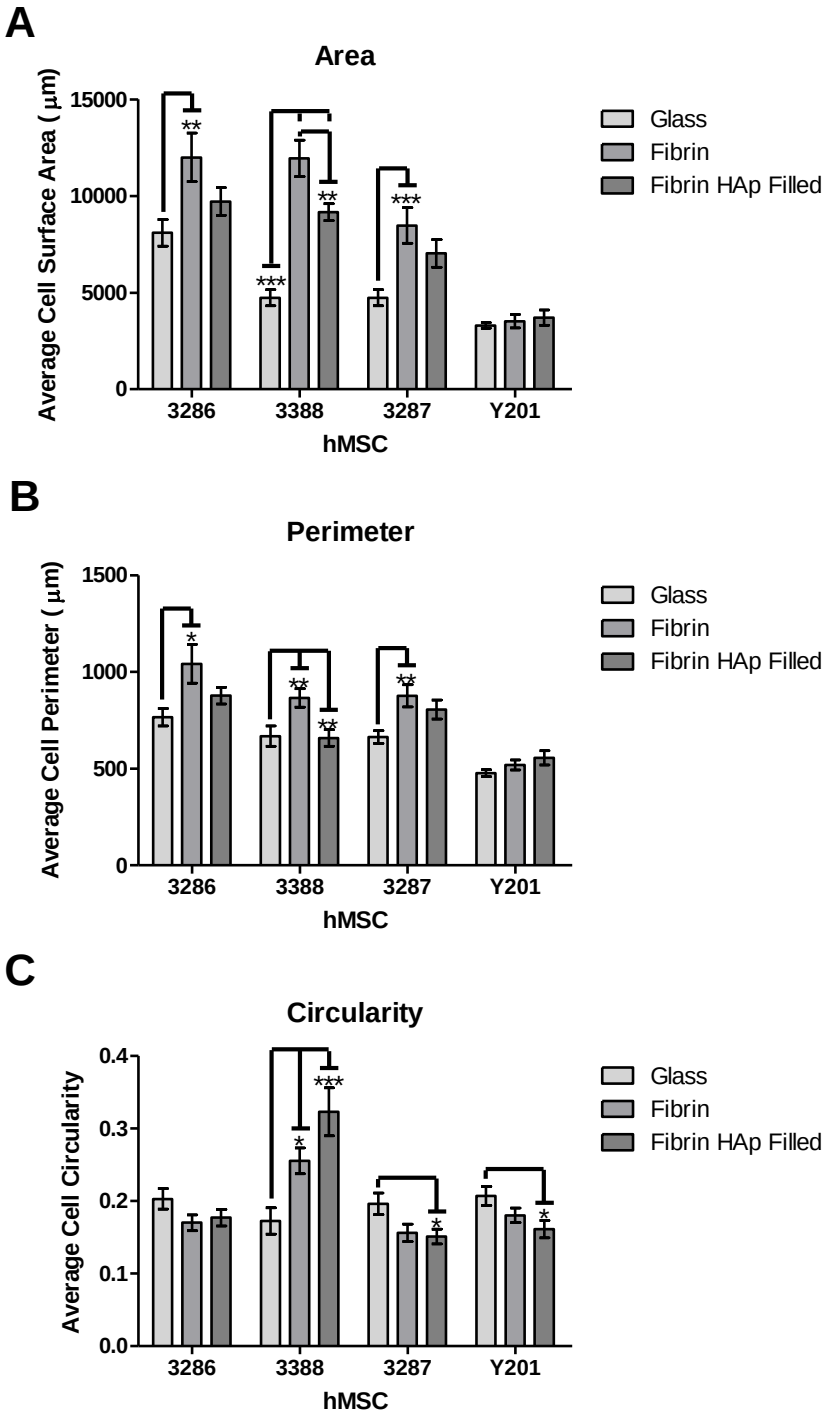

Figure 6-8: <u>Cell-to-material</u> morphological analysis of hMSC cultured on glass, fibrin and fibrin/HAp filled surfaces for 24 hours. (A) Average cell surface area, (B) perimeter and circularity (C).

Investigating cell populations from different donors showed that on glass substrates patient derived 3286 cells appeared to be spread the most over the largest area, patient derived 3287 showing no significant variation. Patient derived 3388 and Y201 cells displayed the smallest area with no significant differences between them covering approximately half the area of 3286 cells (figure 6-7).

Both fibrin and fibrin/HAp substrates had a similar influence on cell area with 3286 and 3388 cells having the largest area. 3287 cells had a significant reduction in cell area in comparison to 3286, however Y201 cells had the smallest cell area with statistical significance recorded between all patient cells on most substrates (figure 6-7).

The cell perimeter analysis indicated patient derived 3286 cells had the largest perimeter on all substrate groups in comparison to other patient's cells and the Y201 cell line. 3287 and 3388 cells tended to have a similar cell perimeter on all substrates with a slight reduction in comparison with 3286. Y201 had the smallest cell perimeters in comparison to all patient cells on most surfaces (figure 6-7).

Cell circularity of hMSC cultivated on glass substrates yielded no significant variation between all hMSC sources. Fibrin and fibrin/HAp substrates had a similar effect on cell morphology with no significant variation between all but one of the hMSC sources. Patient derived 3388 demonstrated significantly higher circularity showing a rounder cell morphology (figure 6-7).

Assessing the influence of substrates on cell morphology showed that the cell area of Y201 has no statistical variation between all surfaces. In contrast to that all of the patient derived hMSC showed a significant increase in cell surface area when cultivated on fibrin substrates in comparison to glass control. A reduction in cell surface area between fibrin and fibrin/HAp substrates was found in all patient derived cell types with significance recorded in 2 out of 3 (figure 6-8).

No significance in cell perimeter was found in the Y201 cells between all substrate groups. A significant increase in cell perimeter was found in all patient cells cultured on fibrin substrates in comparison to glass control (figure 6-8).

Cell circularity showed mixed results with no significance recorded in 3286, an increase in 3388, some decrease in 3287 and Y201 with fibrin/HAp substrates compared with glass (figure 6-8)

6.3.2.2 Cell viability (MTT)

The influence of fibrin/HAp encapsulated and fibrin/HAp coated surfaces on hMSC adhesion, biocompatibility and proliferation was assessed using an *in-vitro* cellular viability assay over a 7-day period.

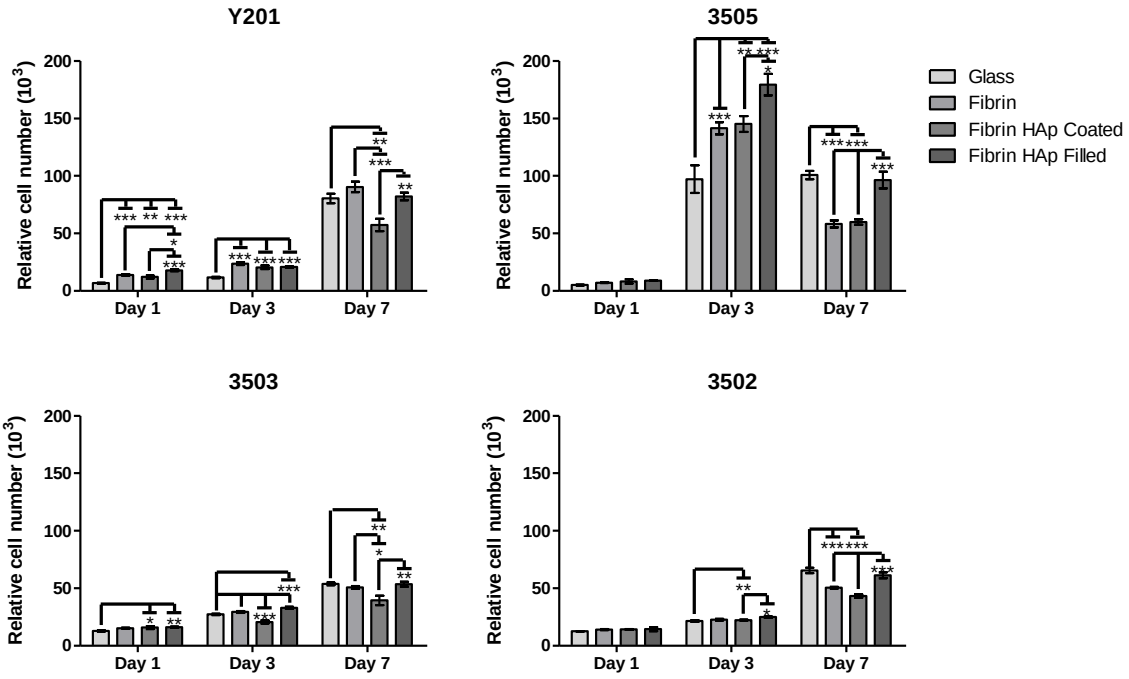

Figure 6-9: Cell viability of hMSC cultured on various substrates over 7 days. Substrate groups include glass, fibrin, fibrin/HAp coated and fibrin/HAp filled surfaces. (n=5)

Similar cell densities of all hMSC populations were observed on all substrate groups at day 1 indicating good cell adhesion to fibrin and HAp associated fibrin surfaces (figure 6-9). Growth kinetics of patient derived 3505 hMSC appeared to be greater in all substrate groups at day 3 in comparison to other patient and Y201 hMSC groups. A significant increase in hMSC number was observed in glass and fibrin/HAp substrates in comparison to HAp coated fibrin surfaces at day 7.

6.3.2.3 Alkaline phosphatase

ALP was measured to determine the influence of the fibrin/HAp material substrates on hMSC differentiation along the osteoblastic lineage. The *in-vitro* sensitivity of the assay was assessed through the cultivation of hMSC on substrates in both basal and osteogenic media over 7 days.

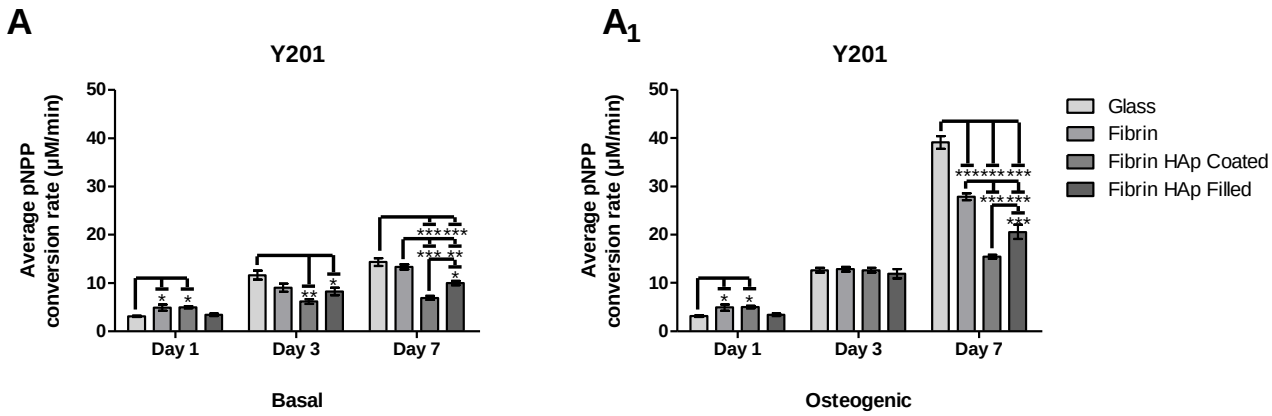

Figure 6-10: Average pNPP conversion rate from Y201 cultured on various surfaces from 1 – 7 days. A cultured in basal medium and A_1 in osteogenic medium. Substrate groups include glass, PLA, fibrin, fibrin/HAp coated and fibrin/HAp filled surfaces. (n = 4)

Increased ALP activity was found in hMSC cultured in osteogenic medium at day 7 on glass, fibrin and fibrin/HAp surfaces in comparison to basal medium groups. A significant decrease in ALP activity was observed in all fibrin contain surfaces groups in osteogenic medium at day 7 compared with glass control. hMSC cultivated on fibrin surfaces showed increased ALP activity at day 7 compared with both filled and coated HAp fibrin surfaces in both media groups. ALP activity of hMSC grown for 7 days on fibrin/HAp filled substrates was increased relative to fibrin/HAp coated surfaces in both media groups.

The influence of fibrin/HAp filled and coated substrates on ALP activity were assessed over a 21-day period in patient derived hMSC cultivated in both basal and osteogenic media.

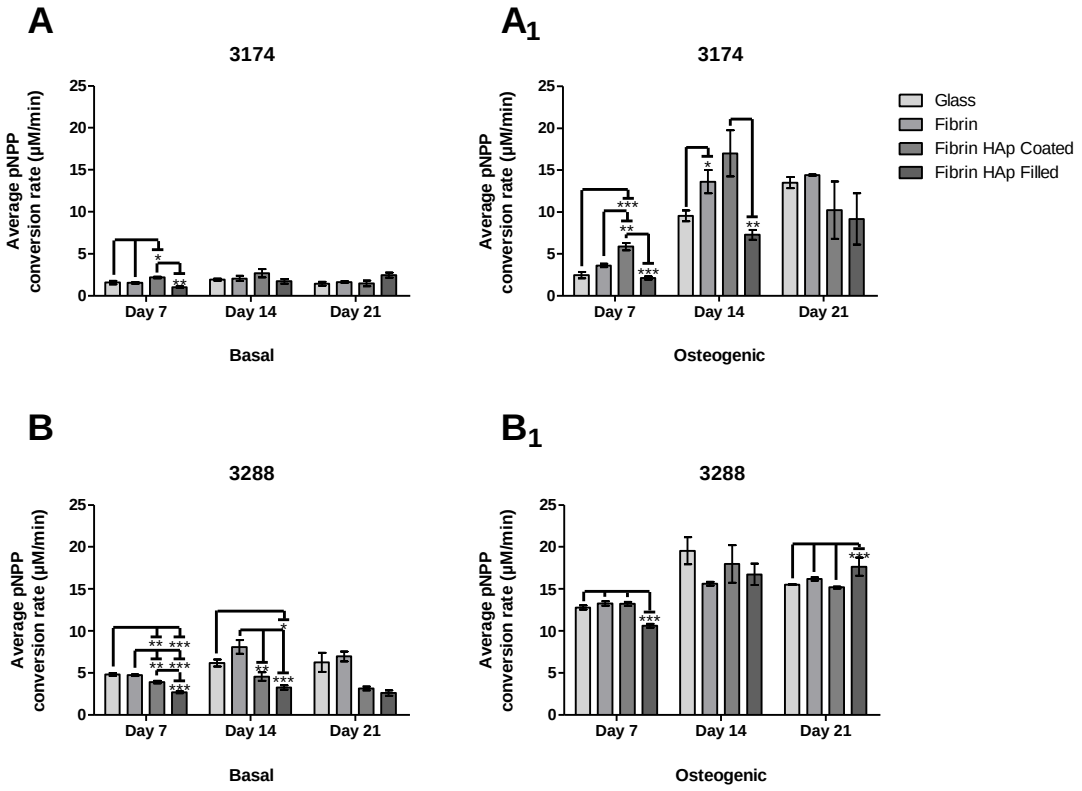

Figure 6-11: Average pNPP conversion rate. A) 3174 and B) 3288 cultured on various surfaces from 7 – 21 days. A & B cultured in basal medium and A_1 & B_1 in osteogenic medium. A & B glass, PLA, fibrin, fibrin/HAp coated and fibrin/HAp filled surface groups. (n = 4).

The pNPP conversion rate was lowest in hMSC cultured in basal medium compared with osteogenic medium groups. Patient derived 3174 cells showed a significant reduction in ALP activity when cultivated in osteogenic medium on the fibrin/HAp coated compared with fibrin filled substrates at day 7 and 14. Significant reduction in pNPP conversion rate was found in both hMSC cultivated on fibrin/HAp filled substrates compared with fibrin/HAp coated surface groups at day 7 in all media groups.

6.3.2.4 Gene Expression

RT-PCR was used to quantify osteogenic differentiation at a transcriptional level, through the analysis of messenger ribonucleic acid (mRNA) expression of lineage-specific markers to assess the influence of different material substrates on hMSC differentiation.

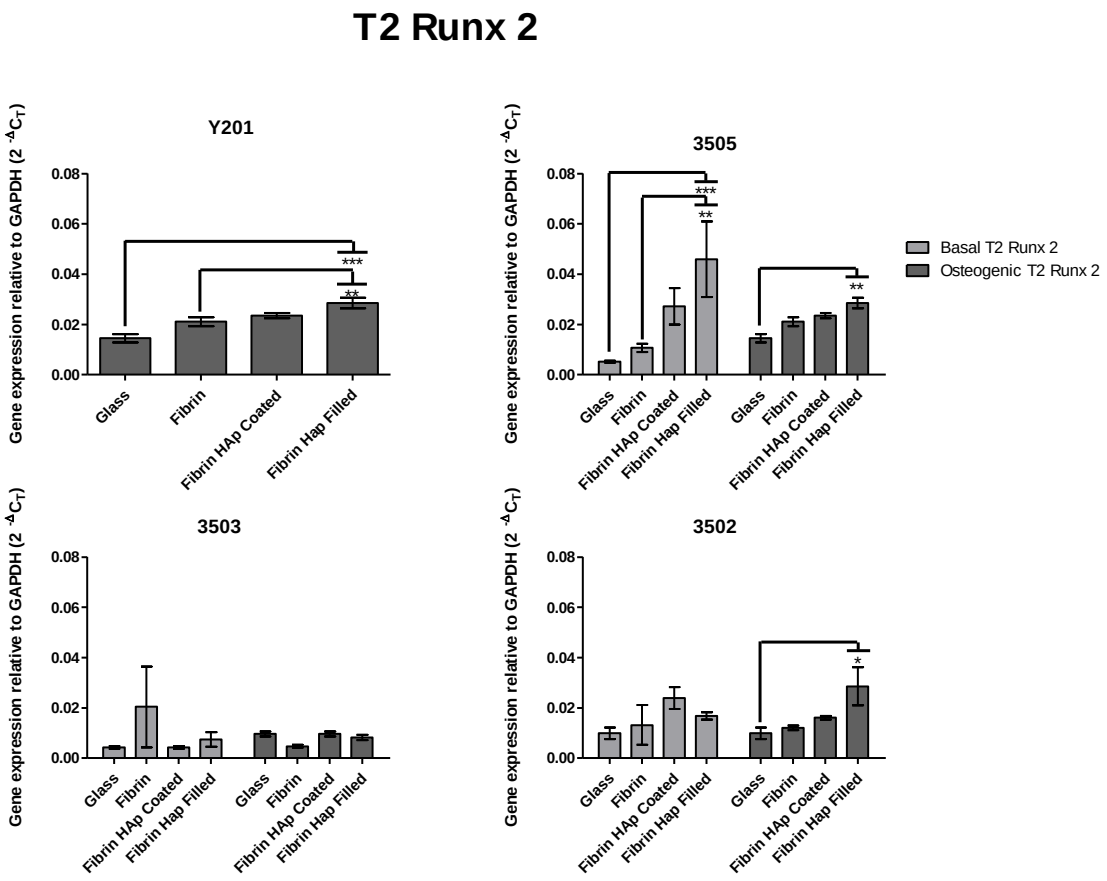

Figure 6-12: mRNA expression of T2 Runx 2 relative to GAPDH. Bars show average gene expression of Y201, 3505, 3503 and 3502 hMSC cells cultivated on glass, fibrin and fibrin/HAp coated and fibrin/HAp filled surfaces in basal and osteogenic media groups for 7 days. (n=5).

No significant differences in T2 Runx2 mRNA expression was observed in patient derived 3503 cells in both media groups on all substrates (figure ***6-12***). A significant increase in T2 Runx 2 expression was observed in 3505 cells cultivated on fibrin/HAp filled substrates in basal medium compared with both glass and fibrin surfaces. A statistical increase in T2 Runx 2 mRNA expression was found in Y201, 3505 and 3502 hMSC cultivated on fibrin filled substrates relative to glass in osteogenic medium (figure ***6-12***).

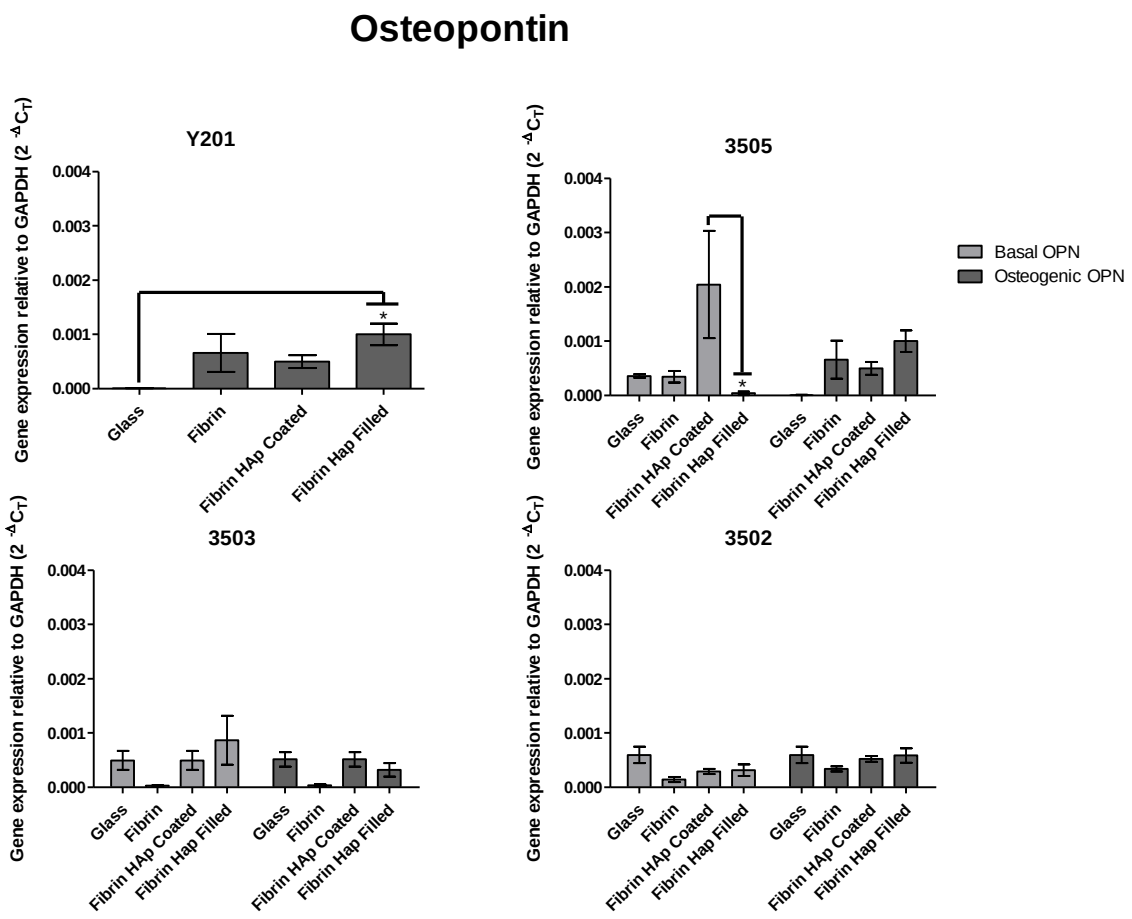

Figure 6-13: mRNA expression of OPN relative to GAPDH. Bars show average gene expression of Y201, 3505, 3503 and 3502 hMSC cells cultivated on glass, fibrin and fibrin/HAp coated and fibrin/HAp filled surfaces in basal and osteogenic media groups for 7 days. (n=5).

No significant differences in OPN mRNA expression was observed in patient derived 3503 and 3502 cells in both media groups on all substrates (figure ***6-13***). Y201 cells cultured on fibrin/HAp substrates had a significantly increased OPN mRNA expression relative to glass control (figure ***6-13***).

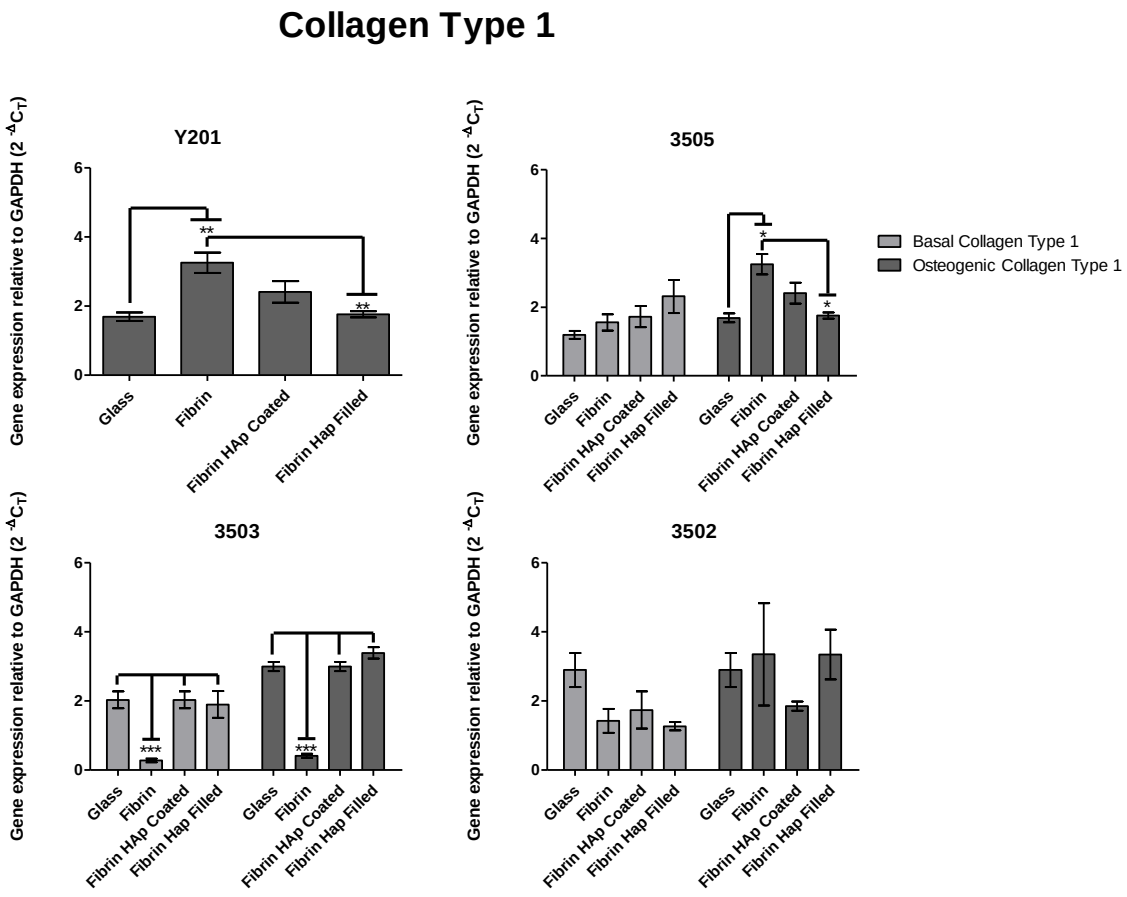

Figure 6-14: mRNA expression of T2 Runx 2 relative to GAPDH. Bars show average gene expression of Y201, 3505, 3503 and 3502 hMSC cells cultivated on glass, fibrin and fibrin/HAp coated and fibrin/HAp filled surfaces in basal and osteogenic media groups for 7 days. (n=5).

Significantly reduced collagen type 1 mRNA expression was found in 3503 hMSC cultivated on fibrin substrates in comparison to glass in both basal and osteogenic medium (figure ***6-14***). Y201 and 3505 cells demonstrated a significantly increased collagen type 1 mRNA expression when cultivated on fibrin compared with glass control (figure ***6-14***). Y201 and 3505 showed a significantly increased mRNA expression in fibrin substrates relative to glass and fibrin/HAp filled groups, in osteogenic medium (figure ***6-14***).

6.4 Discussion

This chapter describes the synthesis of 2D fibrin hydrogel materials with HAp produced from chapter 4 and subsequent *in-vitro* assessment. The processing approach resulted in relatively flat fibrin substrates and fibrin/HAp filled materials with some evidence of fibrin/HAp interaction. Morphological differences in patient derived hMSC were observed with an increase in surface area on fibrin based materials. Biological characterisation revealed good, but variable patient to patient hMSC growth kinetics on fibrin and HAp filled/coated materials. Results from hMSC cultivated on fibrin/HAp materials also demonstrated some differences in osteogenic gene expression.

6.4.1 *Fibrin/HAp substrates*

SEM characterisation of the fibrin/HAp surfaces revealed a uniform fibrin coating across the glass coverslip, however fibrin/HAp filled surfaces appeared to have subsurface irregularities. An area of bulge in the central region was observed in fibrin/HAp substrates, co-located with the initial droplet deposition (figure 6-2).

The irregularities are likely due to agglomeration of HAp within the fibrin matrix. There are a number of suggestions for the observed central bulge. 1. The fibrin formed within the droplet is large enough not to be sheared from the droplet location through the addition of the clean coverslip. 2. The inherent large surface area of the HAp could lead to adsorption of thrombin and/or, fibrinogen molecules creating a fibrinogen conversion region localised to deposits of HAp agglomerates (Nakamura *et al.* 2007; Hu *et al.* 2002). This would influence the crosslinking density in proximity to the HAp particles and agglomerates, however there is no direct evidence of increased fibrin fibril density.

The information drawn from the SEM observations is limited, further work to physically characterise these surfaces could include TEM observation to assess HAp particle dispersion within the fibrin/HAp matrix, AFM to measure substrate stiffness/profile and equilibrium water content to measure crosslinking density.

6.4.2 *Fibrin/HAp hMSC adherence and morphology*

SEM and immunofluorescent images of hMSC cultivated on fibrin and fibrin/HAp substrates revealed physical cell adherence and spreading across the materials (figure 6-3, figure 6-5 and figure 6-6 respectively). The images show hMSC extending pseudopodia and associated actin fibre stress filaments on the glass, fibrin and HAp filled fibrin substrates. Quantitative morphological assessment of patient derived hMSC showed increased spreading on fibrin compared with glass controls. It was also evident that a patient derived hMSC on fibrin/HAp filled surface spread to a lesser extent than on fibrin alone. Remarkably no large differences were observed in Y201 cell morphology on all material substrate groups.

Literature has previously demonstrated adherence and characteristic fibroblastic morphology of hMSC on 2D fibrin hydrogels with fibrinogen concentrations less than 18 mg/mL (Bensaïd *et al.* 2003). Increase in hMSC surface area on fibrin substrates relative to glass is likely due to differences in anchorage points for cell adhesion which is known to directly influence cell morphology (Yeung *et al.* 2005). Differences in crosslink density might explain why hMSC cultivated on fibrin/HAp filled materials had a higher surface area relative to glass control yet lower than the fibrin alone. In addition to the observed morphological changes, an increase in cell area and alteration of shape has been linked to lineage commitment of hMSC as reported by McBeath *et al.* (2004). Lack of morphological differences in Y201's to the various substrates could be a result of hTERT modification, leading to a loss in cell sensing characteristics.

The morphological quantification of hMSC immunofluorescence using a simple actin filament stain has its limitations. Actin staining allows for basic shape quantification, however it is not a measurement of cytoskeletal tension, which is known to be a determining factor in stem cell fate. Immunohistochemical staining for vinculin could have been used to quantify focal adhesion plaques which provides information on the level of cytoskeletal tension (Mcnamara *et al.* 2012).

6.4.3 *Fibrin/HAp hMSC growth kinetics*

The MTT assay allows us to determine that hMSC adhere to fibrin and fibrin/HAp substrates in densities similar to, or greater than glass control.

Relative cell number of all cell populations were statistically lower on fibrin/HAp coated surfaces relative to glass and fibrin/HAp filled substrates at day 7. The MTT assay also indicates cell proliferation and viability over a 7-day period with high variability observed across the different cell sources on the different material substrates (figure 6-9).

The data presented in this chapter is supported by literature showing hMSC proliferation on fibrin substrates (Catelas *et al.* 2006). The differences observed at day 7 between HAp filled and coated substrates could be due to a number of factors associated with the material and/or biological response. 1. The HAp organisation (dispersed vs agglomerated), quantity and presentation (covered in fibrin or exposed) in the two substrates is uncharacterised, but most likely different. 2. hMSC growth kinetics are known to alter with osteogenic lineage commitment and it could be an indication of early differentiation in the HAp coated materials (McBeath *et al.* 2004).

Differences observed in cell numbers between cell sources suggest donor cell heterogeneity which is highlighted by the relative cell number of 3505 cells at day 3 relative to other cell sources (figure ***6-9***). Likewise, inconsistencies in data across donor sources supports this presumption. Heterogeneity of hMSC populations reflect a variety of differentiated cells including progenitor osteoblast primed precursor cells, however knowledge regarding these populations is not fully understood (Phinney 2012). Therefore, differences in cell number are varied as different donor cell populations proliferate at different rates.

The limitations of using the MTT assay to quantitate relative cell number is well known, and is based upon the reduction capability of the cells mitochondria. The metabolism of hMSC at various stages of cell density, differentiation and donor age is known to vary and this could also explain variations in patient to patient 'relative cell number' (McBeath *et al.* 2004). Future work to assess the growth kinetics of hMSC cultivated on fibrin materials could include comparison of metabolic activity as discerned by MTT, to DNA quantity which could be measured using a fluorescence assay such as the PicoGreen assay (Singer *et al.* 1997).

6.4.4 *Fibrin/HAp – hMSC osteogenesis*

No obvious data trends were observed in hMSC ALP activity on fibrin/HAp substrates, however substrates were not inhibitory and ALP activity was increased in osteogenic media groups. Small differences were observed in hMSC osteogenesis with an increase in T2 Runx 2 mRNA levels at day 7 on fibrin/HAp filled substrates relative to control.

Results from the ALP assay with hMSC demonstrate high substrate variability, however cells demonstrated a response to osteogenic medium with higher ALP activity at day 7 compared with basal control. The ALP data gathered was not standardised to cell number thus limiting the inference from these experiments.

An increase in hMSC T2 Runx2 mRNA expression at day 7 was found in (figure 6-12) was found in two patient derived and the Y201 cells cultured on fibrin/HAp filled substrates relative to glass control in osteogenic medium. Previous studies have found that fibrin materials support hMSC growth and do not inhibit osteogenesis, with some evidence suggesting enhanced osteogenesis with increased fibrinogen concentrations (Catelas *et al.* 2006). An increase in fibrinogen (and crosslinking density) would increase the stiffness of fibrin and, as previously outlined is a major regulator for cell behaviour and differentiation (Park *et al.* 2011). The inclusion of HAp into this material could potentially lead to an increase in substrate stiffness, by acting either as a simple filler or through direct fibrin chain bonding as previously discussed (Nakamura *et al.* 2007; Hu *et al.* 2002).

6.5 Conclusion

This chapter has demonstrated the fabrication of relatively flat fibrin substrates, with and without HAp coating on the surface or filled within the matrix. Results have shown that hMSC cultivated on the surface of these materials adhere, proliferate and maintain their capacity to differentiate towards the osteogenic lineage. Experimental evidence also reveals variation in hMSC morphology and osteogenesis when cultured on fibrin/HAp filled substrates. This is possibly linked to substrate stiffness and organisation with the inclusion of HAp and/or fibrin crosslinking density, however further studies are required to elucidate the underlying mechanism for this observation.

Chapter 7 – Influence of 3D fibrin/HAp filled PLA constructs on hMSC behaviour *in-vitro*

7.1 Introduction

This chapter aims to investigate the combination of HAp synthesised using the approach discussed in chapter 4 with fibrin hydrogel as a delivery vehicle for hMSC into 3D printed PLA constructs. The seeding of the 3D printed PLA scaffolds was investigated using two different static seeding techniques. The next aim was to develop a viable cell delivery methodology using fibrinogen/thrombin system outlined in the chapter 5 and to investigate the influence of these HAp nanoparticles on hMSC within a 3D environment. Finally, the outcome of prolonged *in-vitro* culture was examined on hMSC gene expression and matrix deposition via histology.

The method of seeding of 3D scaffolds with cells can be split into two main approaches static and dynamic. Static seeding techniques include surface seeding and direct injection (Vitacolonna *et al*. 2015). Dynamic approaches involve the movement of cells in medium around and through the scaffolds to encourage better cell coverage than static seeding techniques (Thevenot *et al.* 2008). In this chapter two static seeding techniques were investigated for 3D printed PLA constructs.

The work presented in this chapter is similar to a study by Shao *et al*. (2006) which investigated the delivery of MSC using commercially available fibrin glue into a 3D printed PCL TCP composite scaffold. Localised delivery of hMSC laden hydrogels has a number of advantages over direct implantation of porous scaffold materials. Firstly, the immunomodulatory function of hMSC may help regulate host immune response to the implant and secondly hMSC are capable of differentiating into bone forming osteoblasts. To encourage these actions, the fibrin hydrogel can temporarily localise the hMSC within the implant site, allowing them to interact with the host's extracellular fluid. HAp fillings have been widely used to encourage osteogenesis in hMSC and is also reported to encourage angiogenesis, therefore HAp filled hydrogels have the potential to enhance bone regeneration (Rao *et al.* 2014). Cell laden fibrin hydrogel delivery methods also offer greater control over seeding processes and more uniform distribution, which in turn would be expected to produce a more uniform and complete osteogenesis (Schantz *et al.* 2005).

Hydrogels are not only limited to the delivery of cells. In a less related proof of concept *in-vivo* study, Lee *et al*. (2010) used TGFβ3 infused collagen type 1 hydrogel within a custom 3D printed PCL hydroxyapatite scaffold in a rabbit condyle model. The 3D printed scaffold had varied pore dimensions to specifically target various regions of the replaced tissue. Results demonstrated 130% more recruitment of cells in the TGFβ3 infused regenerated cartilage compared with control with no TGFβ3 using 5 mg/mL collagen type 1. This study demonstrates the versatility of using hydrogel delivery, which can be adapted to include growth factor release to enhance regional regeneration of tissues.

Similar to work by Shao *et al*. (2006) a biodegradable polymeric scaffold was fabricated using the additive manufacturing approach fused filament fabrication (FFF). Unlike the work presented in Shao *et al*. (2006), PLA was used as the biodegradable material for the scaffold. The scaffold was designed for the regeneration of cancellous subchondral bone region with a defect size of 8mm in diameter and 2 mm in depth. The hydrogel was investigated in an unconstrained (free floating) form and within the PLA scaffold. HAp produced from chapter 4 was also incorporated within the fibrin component to investigate its influence on hMSC in a 3D environment.

In the past decade nanotechnology has received a great deal of interest for a number of different applications. To date the number of nanoparticle-related publications have focus exclusively on the synthesis and physical characterisation of these nanomaterials. Previous literature has demonstrated the toxicity of some nanomaterials, which consequently has led to a focus on their mode of action in biology. An excellent review by Mahmoudi *et al*. (2011) describes in detail various processes for the internalisation of nanoparticles and their influence on the cell cycle.

Cells are known to internalise their surrounding extracellular molecules via a process of endocytosis. Typically, endocytosis can be divided into two categories phagocytosis and pinocytosis. All eukaryotic cells except erythrocytes perform pinocytosis, which is often called fluid-phase endocytosis when it does not involve specific receptors. This involves the internalisation of fluids, soluble material, or nanoparticles in the order of 100 nm (micropinocytosis) (Mahmoudi *et al*. 2011).

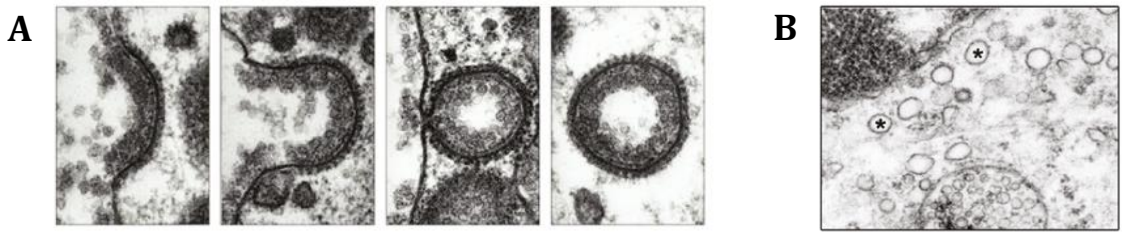

Figure 7-1: TEM image examples of A) of clathrin-dependent endocytosis and B) clathrin-independent endocytosis (Mahmoudi et al. 2011).

Clathrin dependent pinocytosis as the name suggests, involves the formation of a clathrin protein complex at the surface of the cell membrane. This complex is subsequently internalised, encapsulating the extracellular molecules into a cage-like structures figure 7-1A. This process is well known for its selective uptake of specific molecules through interaction with membrane receptors (Mahmoudi *et al*. 2011). Clathrin independent endocytosis is a poorly uncharacterised process, in which non-specific invagination and internalisation of surrounding bulk extracellular fluid leading to uncoated pinocytic vessels (figure 7-1B)(Mahmoudi *et al*. 2011).

A HAp concentration of 10 mg/mL was selected to give a 5 mg/mL final concentration, this was based on previous research by Rao *et al.* (2014) showing it gives better hydrogel mechanical properties than 0 – 2.5 mg/ml HAp fillers. When this material was studied using endothelial cells the 5 mg/mL appeared to have better capillary network formation than the 10 mg/mL hydrogel concentration.

The fibrin alone, has insufficient mechanical properties for load bearing applications. For this reason, a solid free form fabrication using FFF was used to process PLA into a cage with large pores. This was done to improve implant mechanical properties, whilst allowing nutrient diffusion and cell migration. The PLA construct would also promote osteogenesis based on its mechanical properties (Engler et al. 2006). FFF was selected as it allows for control over specific geometries of the scaffold material using a computer aided design (CAD) program.

7.2 Materials and Methods

The methods outlined in this section focus specifically on fused deposition modelling, histological staining and the live/dead assay.

7.2.1 *Fused filament fabrication (FFF)*

PLA constructs were fabricated with translucent PLA using a RapMan 3D Touch printer (Bits from Bytes, UK). The information for the parts to be printed using RapMan was contained in a G code file on an SD card. The G code was generated using Axon 2 (Axon 2.0 beta 2, Bits from Bytes, UK). Autodesk Inventor 2012 was used to CAD the PLA constructs used in experimentation.

7.2.2 *Histology*

Samples were prepared for histology by incubation in 10% formalin solution for 24 hours at 4^{o}C. Samples were then incubated with 70% ethanol for 24 hours before paraffin embedding. Dehydrated fibrin gels were transferred into fenestrated cassettes, smaller samples were wrapped in tissue prior to processing. Paraffin embedding was performed by Mrs Xin Xu – research technician at the Newcastle Biomedicine Biobank tissue processing services. Microtome sectioning of paraffin blocks and histological staining were processed by Sharon Watson - technician from Newcastle University, Institute of Cellular Medicine, Musculoskeletal Research Group. Specific protocols can be found in the materials and methods chapter 3.6.3 .

7.2.3 *TEM cell staining*

Samples were prepared for TEM staining by fixation in 2% glutaldehyde in cacodylate buffer <1h. Samples were rinsed cacodylate buffer twice for 10 minutes. Samples were rinsed in dH_2O twice for 120 minutes and fixed in 1% osmium tetroxide (diluted in dH_2O) for 30 minutes. Samples were then rinsed in dH_2O twice for 10 minutes each.

Samples were dehydrated in 20%, 50%, 75%, 100% and 100% acetone in dH_2O for 15 minutes each. TAAB epoxy resin kit was used to impregnate epoxy into the samples using 25%, 50% 75% resin in acetone for 30 minutes each. Samples were then incubated in 100% resin for 1 hour three times each. Samples were left on a rotator overnight and polymerised at 60^{o}C in an oven overnight before sectioning.

Sections were cut to 0.5 µm and stained with toluidine blue in 1% borax to visualise cells. Ultrathin sections ~70nm were cut using a diamond knife on a RMC MT-XL ultramicrotome or a Leica EM UC7 ultramicrotome. The sections were stretched using TCM to eliminate compression and mounted on Pioloform-filmed copper grids.

7.2.4 *Live dead staining*

A Live/Dead® Viability/Cytotoxicity kit (Molecular Probes, UK) was used to visualise cell viability. Calcein acetoxmethyl (Calcein, 0.05%) and Ethidium homodimer-1 (EthD-1, 0.2%) were diluted in PBS and incubated with samples for 20 minutes similar to (Catelas *et al.* 2006). Samples were viewed using the Leica DM4000B described in the materials and methods chapter, section 1.8.

The percentage of live cells within L/D images was calculated using ImageJ in a similar fashion to methods section 3.8 (figure 3-5). Images were split into RGB and green and red images were analysed. The image was first inverted and a threshold was set to include the fluorescent cells of the focal plane. Cells out of the focal plane were excluded by using this threshold. The particles were analysed using the "analyse particles option". Particles with and area of <140 µm^2 were excluded from analysis. Instances of cells in both green (live) and red (dead) were counted and a total cell number was used to determine the percentage live cells (equation ***7-1***)

$$Percentage\ live\ cells\ \% = \left(\frac{Number\ of\ live\ cells}{(Number\ of\ live\ cells + dead\ cells)}\right) 100$$

Equation 7-1: Calculation of percentage live cells.

7.2.5 *Confocal and stereo microscopy*

3D images of cells were captured using a Leica SP2 UV CLSM confocal microscope with x20 NA 0.5 dipping lens. Images were processed using LCS 2.61 software (Leica Microsystems Heidelberg GMBH Germany).

The 3D printed PLA scaffolds were imaged using a Leica M165FC with a two-armed gooseneck integrated LED spotlights. Images were acquired and processed using DFC310 FX camera Leica with the Application Suite (LAS) software (Leica Microsystems Heidelberg GMBH Germany).

7.3 Experimental procedures

The procedures outlined in this section were developed at Newcastle University using methods attained from a variety of different sources.

7.3.1 *PLA construct*

PLA cages were designed by Dr. Matt Benning at the Newcastle University, School of Mechanical and Systems Engineering, SAgE, Newcastle upon-Tyne, to produce interconnected channels of approximately 600 X 600 X 600µm.

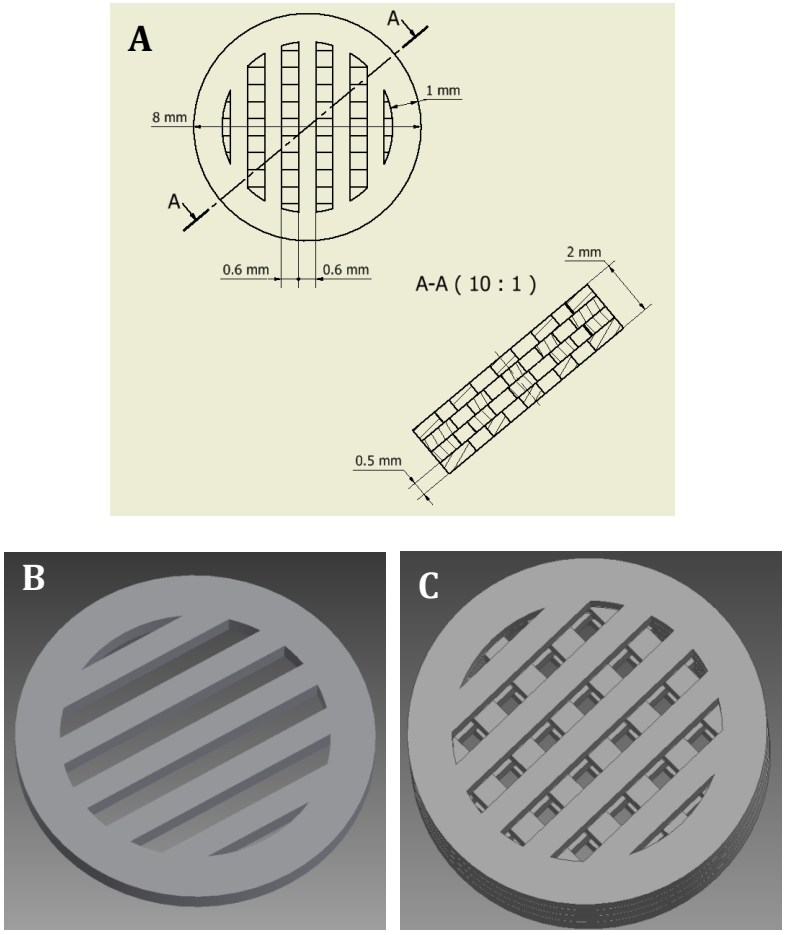

Figure 7-2: A) Design parameters of PLA constructs, B) Layer model and C) 4x multilayer model with 90^o rotation per layer. Designed by Dr. Matt Benning.

To improve the wettability, 3DP PLA constructs were first plasma treated using a compact plasma cleaner PDC-32G (EQ-PDC-32G) (MTI Corporation, US) with an 8CFM double step rotary vacuum pump (2TW-4C) (MTI Corporation, US). Samples were placed in a vacuum chamber and the vacuum was allowed to draw for a minimum of 10 minutes. The plasma treatment was performed for 3 minutes at medium intensity. Samples were UV sterilised, washed in PBS and incubated with hMSC medium for 1 hour prior to seeding.

In an attempt to reproducibly seed a quantifiable number of cells onto the PLA construct a mixture of methodologies were investigated. The hanging drop methodology is commonly used *in-vitro* for the production of cell spheroids (Kurosawa 2007). In this experiment 100,000 in 70 µL cells were added directly onto the PLA construct in a square petri dish cover. The cover was inverted over a PBS filled square petri dish, the liquid, including the PLA constructs hydrostatically adhered to the lid as a droplet and the samples were incubated at 37°C with 5% CO_2 for 7 days (figure 7-3).

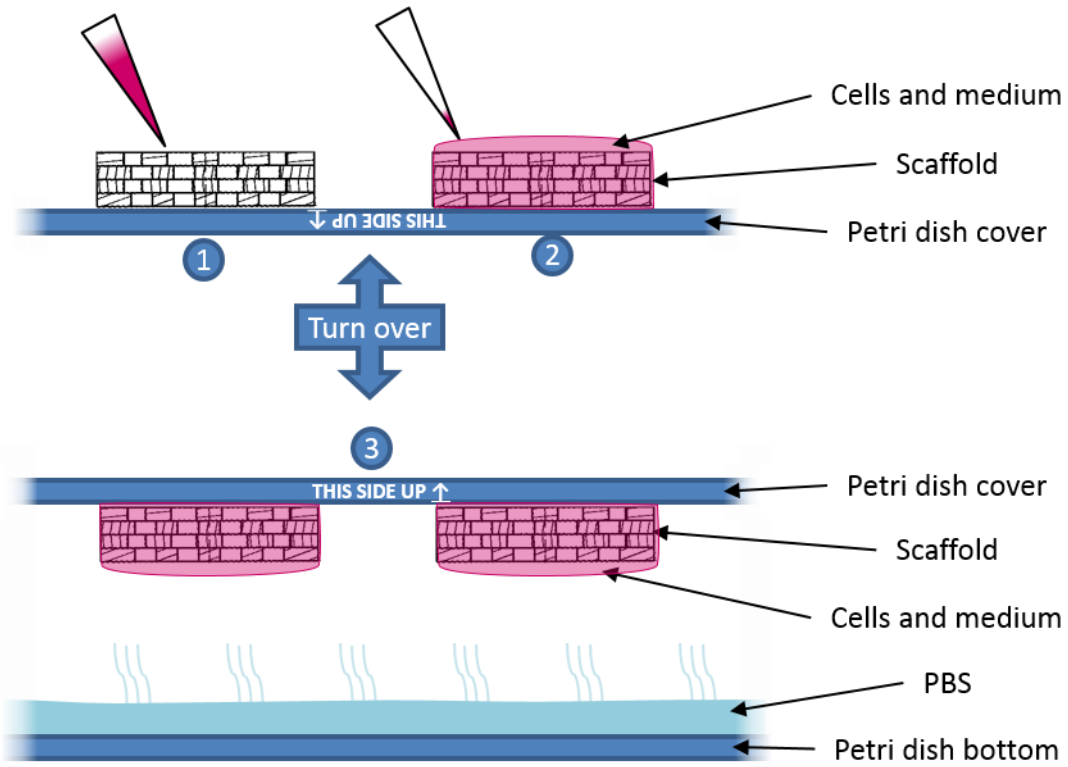

Figure 7-3: Illustration of hanging drop/static seeding methodology for PLA scaffolds.

7.3.2 *Fibrin hydrogels*

ID	Solution	Concentration	Solvent	Cell number	HAp mg/mL
A	Bovine thrombin (T4648)	13.25 U/L	DMEM	0	0
	Bovine fibrinogen (Millipore, 341573)	20 mg/mL	0.9% w/v NaCl in dH_2O	100,000	± 10
B	Bovine thrombin (T4648)	13.25 U/L	HBSS	0	0
	Bovine fibrinogen (Millipore, 341573)	20 mg/mL	hMSC media	100,000	± 10

Table 7-1: Fibrin precursor solutions and their constituents. Formulation A) (Rao et al. 2014) and formulation B) experiment.

Cell survivability was first investigated, in fibrin gel encapsulated hMSC fabricated using formulations outlined in table 7-1. The precursors were incubated at 37°C with 5% CO_2 to set for either 30 or 60 minutes in covered eight chamber microscope slides, before quenching with hMSC medium. Samples were immediately stained and visualised using live/dead protocol outlined in section 7.2.4 .

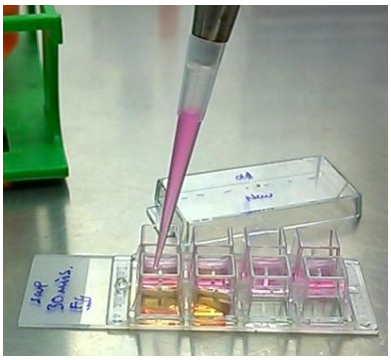

Figure 7-4: Fibrin gels fabricated in an eight chamber microscope slide.

Fibrin/HAp gels with hMSC for long-term *in-vitro* experiments were fabricated using Millicell Hanging Cell Culture Insert (Merk Millipore, PIHT12R48) with removed membranes as moulds. These inserts were pressed into a parafilm covered petri dish to create a seal and UV sterilised for 30 minutes. Gelation of hMSC/fibrin/HAp matrices were achieved using the formulation B with or without incorporation of HAp (table ***7-1***).

PLA constructs for fibrin/HAp cell delivery were first plasma treated as previously outlined in 7.2.1 , placed on a parafilm covered petri dish and UV sterilised for 30 minutes.

Gelation of hMSC/fibrin/HAp matrices were achieved using the formulation B with or without incorporation of HAp (table ***7-1***). 35 µL of the fibrinogen solution was added to the parafilm and mixed with 35 µL of the thrombin solution containing 100,000 hMSC and ± 10 mg/mL HAp. The 70 µL droplets were then immediately transferred into the moulds (figure ***7-5***A) and PLA scaffolds (figure ***7-5***C). The samples were incubated at 37°C in a humid atmosphere at 5% CO_2 for 30 minutes to polymerise.

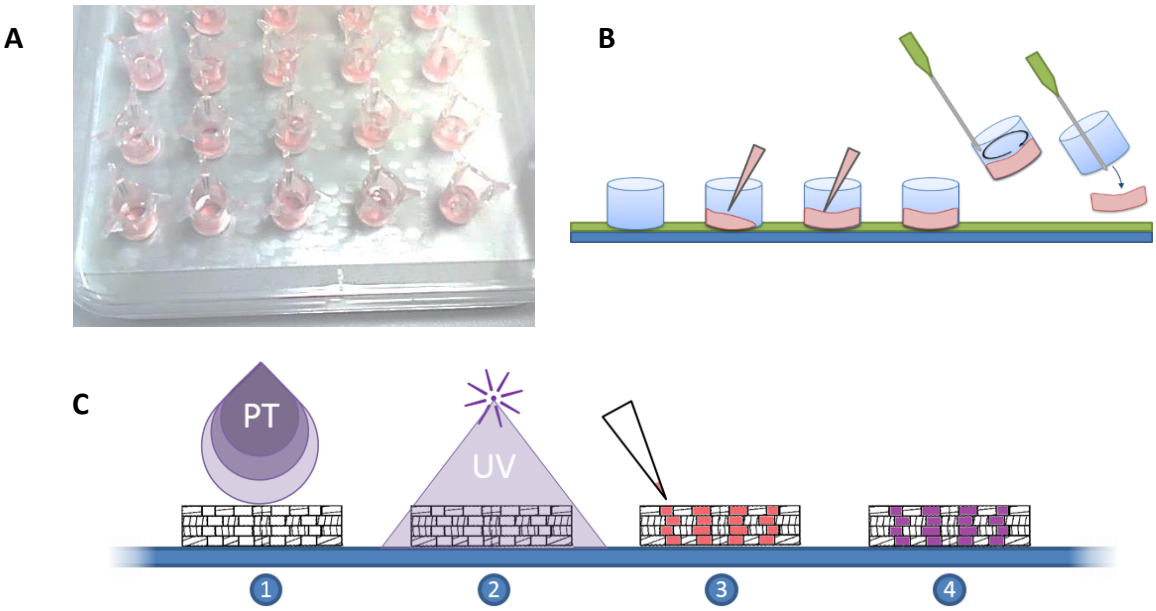

Figure 7-5: A) Fibrin gels post-gelation, B) schematic of fibrin gel fabrication/release and C) PLA scaffold processing and fibrin gel delivery 1- plasma treatment, 2 – UV sterilisation, 3 – fibrinogen/thrombin/cells/HAp mixture delivery and 4 – gelation.

Removal of fibrin/HAp gels from moulds was achieved using a sterile needle to dislodge the gel from the walls of the mould and samples were carefully push the samples out (figure 7-5 A-B). All samples were transferred into 24 well plates and incubated with 1 mL of basal or osteogenic hMSC media/well for 21 days; media was changed every 3 days.

7.3.3 *RNA extraction from 3D scaffolds*

TRIzol® lysates were obtained from non-caged fibrin gels by transferring samples using forceps into a 1.5 mL Eppendorf and homogenised using a 1.5 mL micro-centrifuge tube tissue grinder micro-pestle.

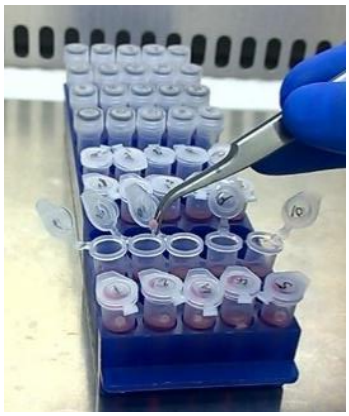

Figure 7-6: Image of fibrin gel harvesting for RNA isolation using TRIzol®.

TRIzol® lysates were obtained from PLA caged fibrin scaffolds by transferring samples using forceps into a 1.5 mL Eppendorf and freezing over night at -80^{o}C. Samples were then thawed at room temperature, once thawed the lysates were centrifuged at 13,000 rpm for 5 minutes and mixed before transferring the lysate into a fresh 1.5 mL Eppendorf. RNA was isolated and purified using methods outlined in chapter 2 section 3.6.5.1

7.4 Results

7.4.1 *PLA constructs*

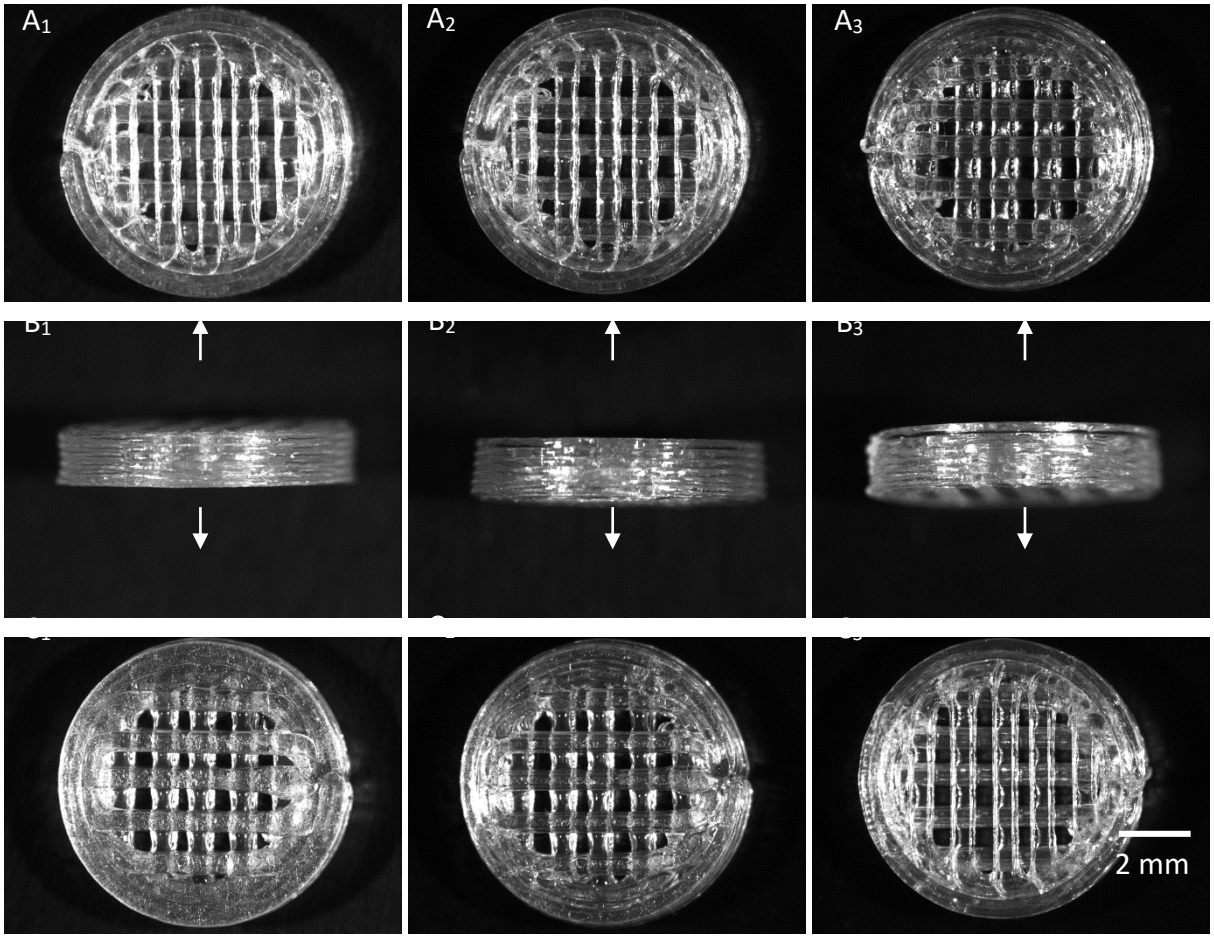

Figure 7-7: Stereomicroscope greyscale images of 3D printed PLA FFF scaffolds using design parameters (figure 7-2). A1-3) Top view, B1-3 side view and C1-3 bottom view. Numbers 1-3 demote the scaffold number.

Figure 7-7 demonstrates the morphology of the as printed PLA constructs produced using figure 7-2 design parameters. Images A_{1-3} show the top view show some very fine polymer filaments across the surface. The sides of the scaffolds do not appear to be uniform; some edges appear sloped with some curvature in the base layer. The base layer of the PLA scaffolds has indents and appears to have the largest diameter of the scaffold.

3D printed PLA scaffolds were originally investigated as a control for later cell culture experiments. Initial seeding experiments using a direct injection method demonstrated the need for plasma treatment to improve the wettability of the PLA scaffolds. The direct injection of cells suspended in hMSC medium into the PLA scaffold in tissue culture treated plastic resulted in preferential adherence to the well over the construct. Therefore, a combination of

direct injection and hanging drop method was employed to encourage cell interaction with the scaffold.

The seeding of PLA scaffolds was investigated using confocal microscopy to see the distribution of cells seeded using the procedure outlined in figure 7-3.

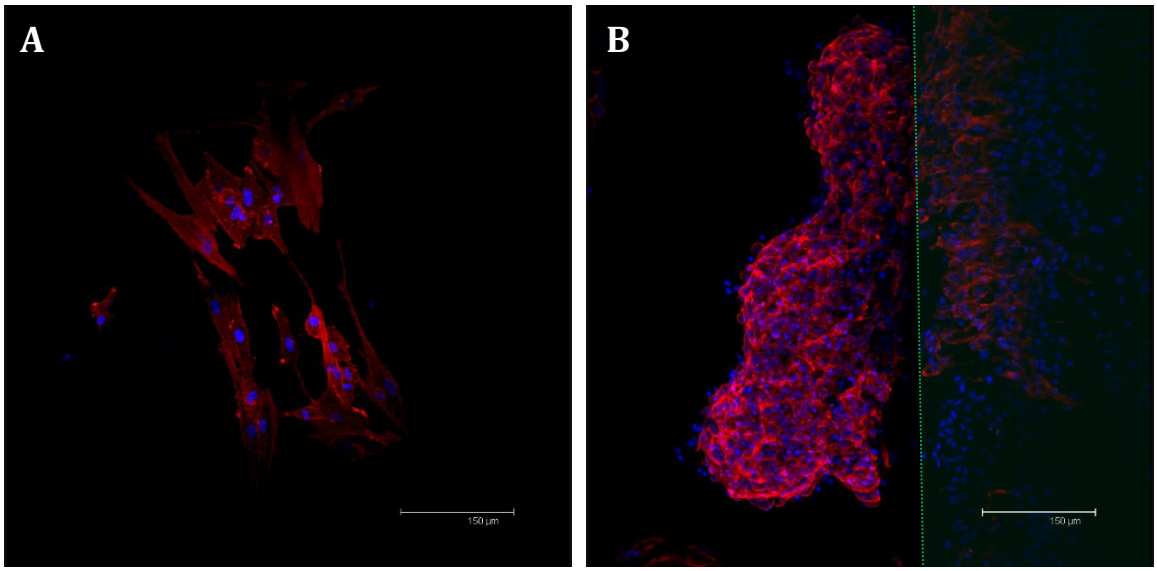

Figure 7-8: Confocal images of Y201 hMSC cultivated on PLA constructs for 7 days. A) hMSC coating PLA filament and B) a cluster of cells attached to a PLA filament. Red = rhodamine phalloidin, Blue = DAPI and Green line & shaded area = approximate location of PLA filament.

Microscopic analysis revealed spheroid formation within the vertical pores of the PLA constructs, however when the scaffolds were relocated into a 24 well plate with hMSC medium, the majority of the spheroids and non-clustered cells were not adhered to the PLA construct.

Confocal images of hMSC demonstrate hMSC adhesion along the PLA filament (figure 7-8 A), the majority of cells appeared to align with the direction of the PLA filament axis. Image B shows a cluster of hMSC within the vertical pore of the PLA scaffold adhering to the edge of a filament (green area and line), cells can be observed coating the PLA filament in a similar fashion to image A (figure 7-8). The images of areas demonstrating cell attachment were extremely sparse throughout PLA construct and was therefore abandoned for use as a control for later cell laden fibrin scaffold investigation.

7.4.2 *Fibrin hydrogels*

This section outlines results obtained for investigation into hMSC viability, 3D fibrin/HAp hMSC interaction, PLA/fibrin/HAp scaffold influence on hMSC gene expression and histology.

7.4.2.1 Fibrin encapsulated hMSC survival

Live/dead staining outlined in section 7.2.4 was used to demonstrate cell survival following fibrin encapsulation with two fibrin formulations outlined in 7.3.1 with two gelation times.

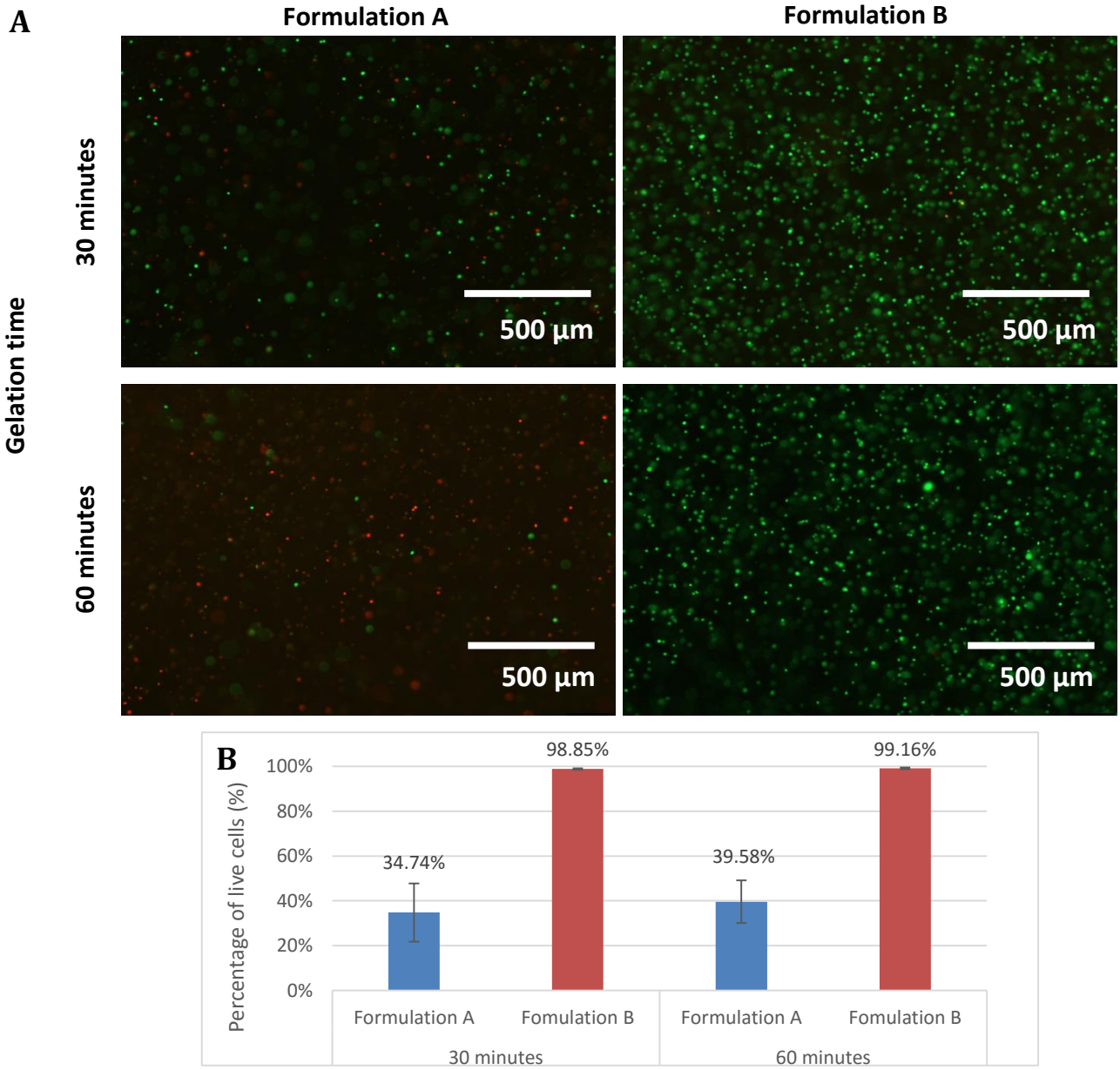

Figure 7-9: A) Live dead images of Y201 hMSC cells captured within a fibrin matrix. Fluorescence from cells polymerised with formulation A (left) and B (right) for 30 minutes

(top) and 60 minutes (bottom). Green = living; Red = dead. B) Graph showing the percentage of live cells relative to total live/dead cell count. Bars represent the mean ± SEM (n = 4).

Images of live dead staining revealed a relatively higher number of dead cells when encapsulated using formulation A, however this cell death appeared reduced with a decreased gelation time. Formulation B yielded high cell survivability following 30 and 60-minute gelation times (figure 7-9A).

One-way ANOVA demonstrated a significant increase in cell survival with formulation B compared with A at both incubation times (p-value = 9.94×10^{-7}) (figure 7-9B). No significant differences were observed in the percentage of live cells between different incubation times with both formulations A and B (figure 7-9B).

The influence of HAp on hMSC within a 3D fibrin environment at the nanoscale was investigated on TEM sections of hMSC cultivated within a fibrin/HAp matrix for 24 hours (figure 7-10).

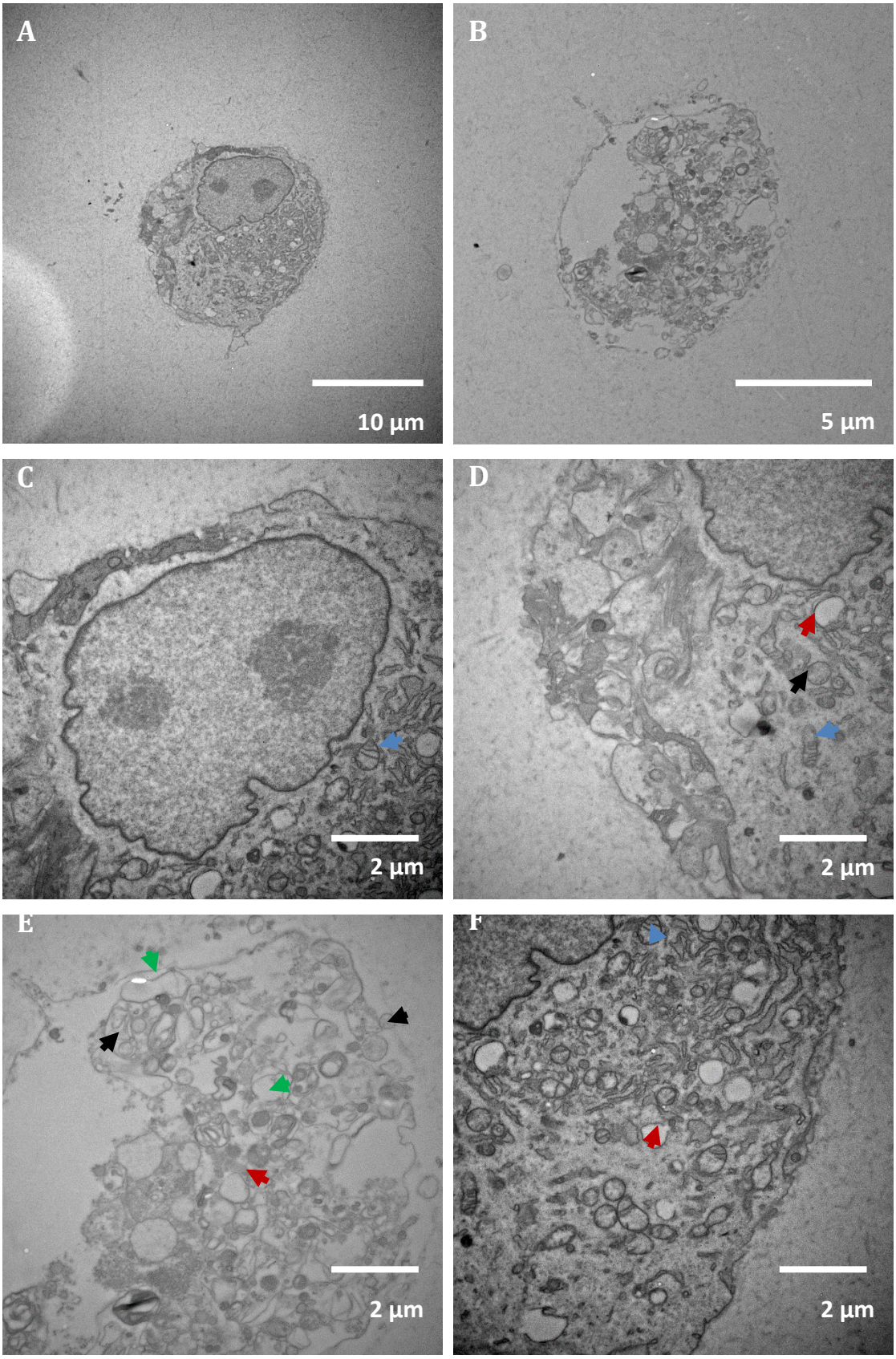

Figure 7-10: Transmission electron microscope images of 3505 hMSC incubated for 24 hours within a fibrin matrix. A) 2,600X, B) 4,600X and C - F) 10,500X magnification. Arrows: Red = vacuoles, green = peroxisomes, blue = mitochondria and black =lysosomes.

7.4.2.2 TEM – fibrin/HAp encapsulated hMSC

TEM cross-sections of hMSC embedded within a fibrin matrix showed spherical cell morphologies (figure 7-10 A & B). Nucleus morphology showed a definitive nuclear envelope with areas of condensed chromatin (figure 7-10 C). Within the cell cytoplasm a variety of organelles were observed including vacuoles (red arrows), peroxisomes (green arrows), lysosomes (black arrows) and mitochondria (blue arrows).

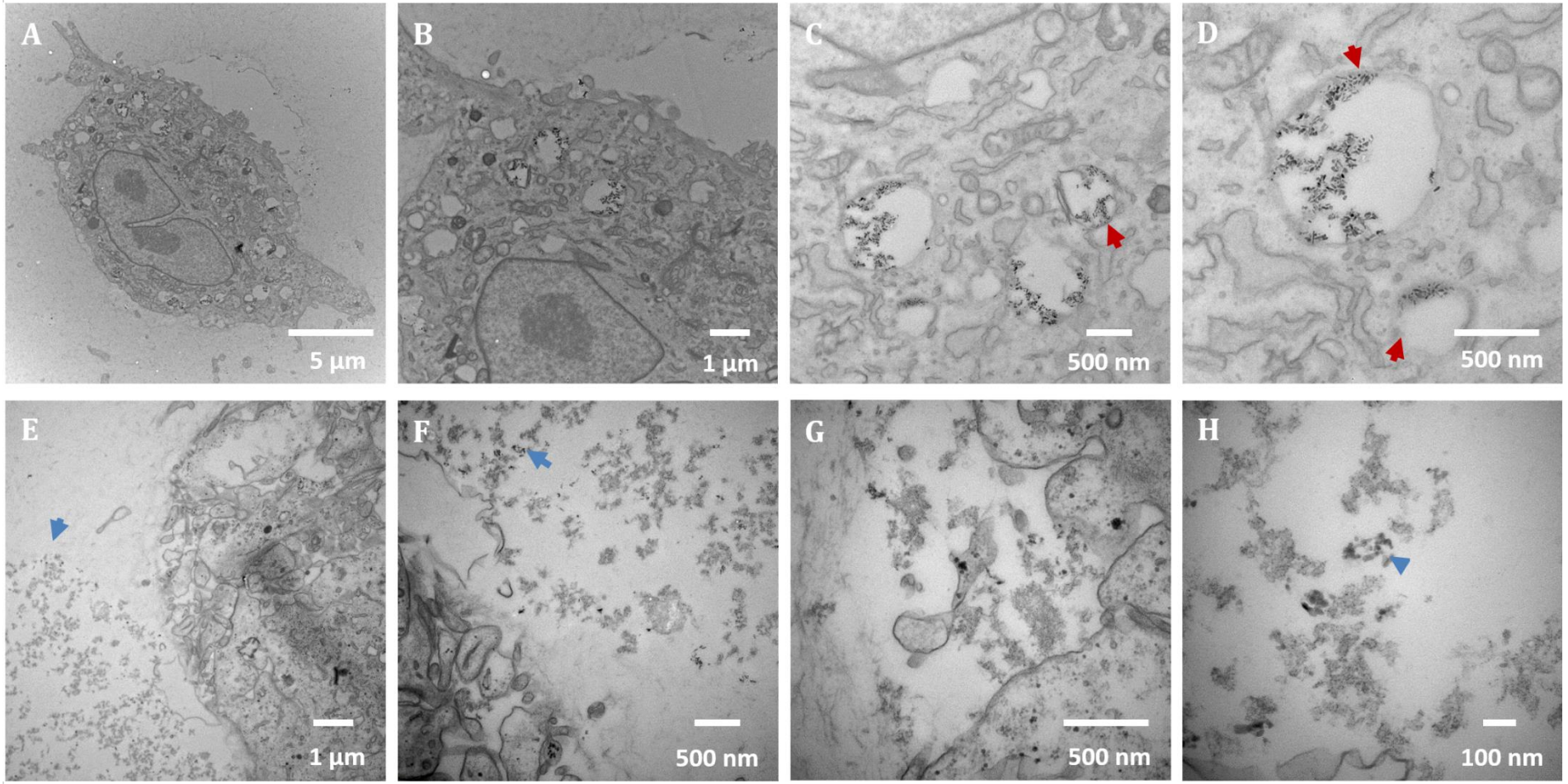

Figure 7-11: Transmission electron microscope images of 3505 hMSC incubated with HAp nanoparticles for 24 hours in a fibrin matrix. HAp synthesised using methodology A outlined in section 4.3.5 ***of chapter 4. A) 4,600X, B & E) 10,500X, C & F) 25,000X, D & G) 46,000X and H) 92,000X magnification. Arrows: Red = intracellular vacuole bound HAp and blue = extracellular HAp.***

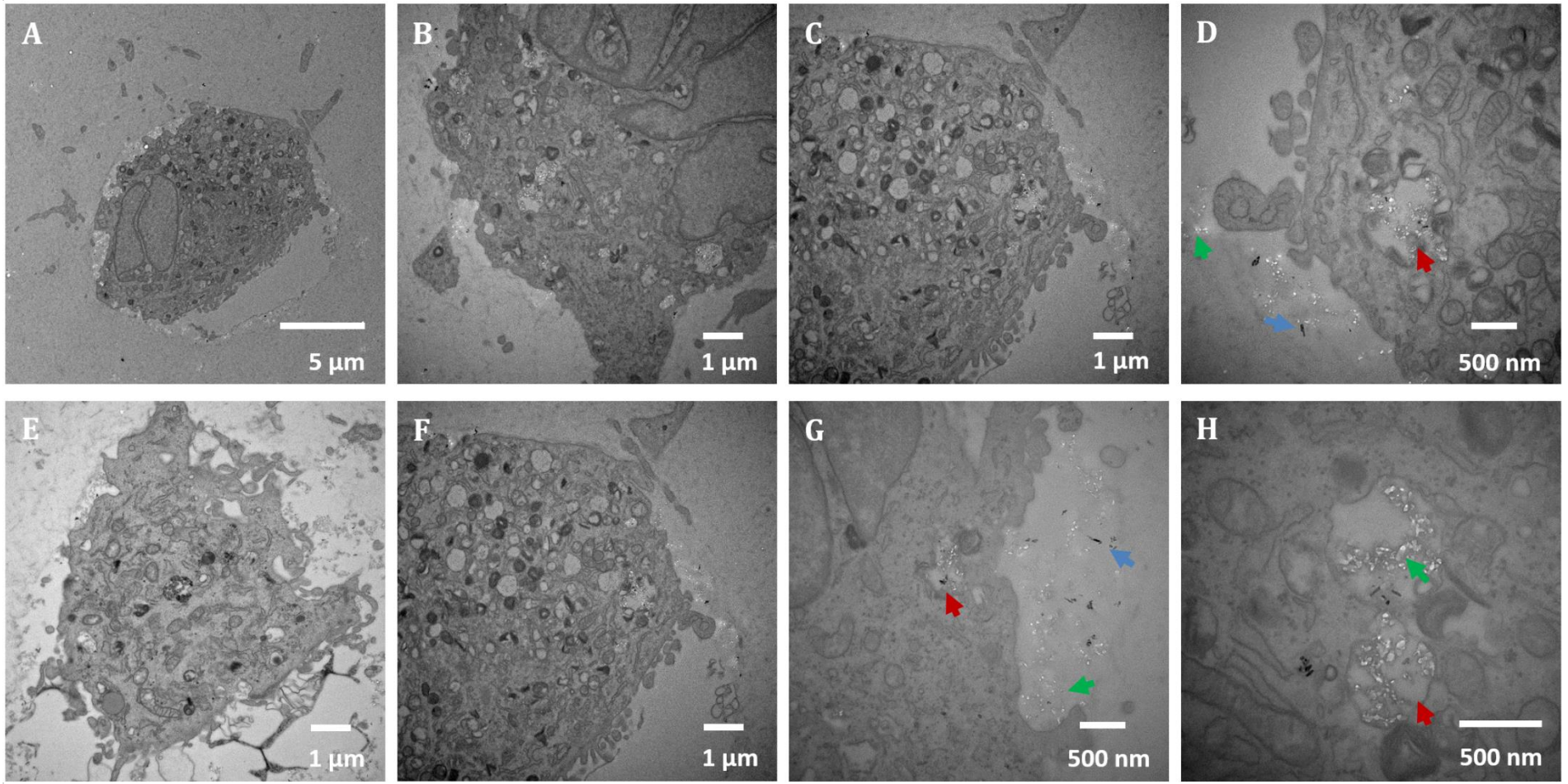

Figure 7-12: Transmission electron microscope images of 3505 hMSC incubated with HAp nanoparticles for 24 hours in a fibrin matrix. HAp synthesised using methodology B outlined in section 4.3.5 ***of chapter 4. A) 4,600X, B & C, E & F) 10,500X, D & G) 25,000X and H) 46,000X. Arrows: Red = intracellular vacuole bound HAp, green = unknown artefacts and blue = extracellular HAp.***

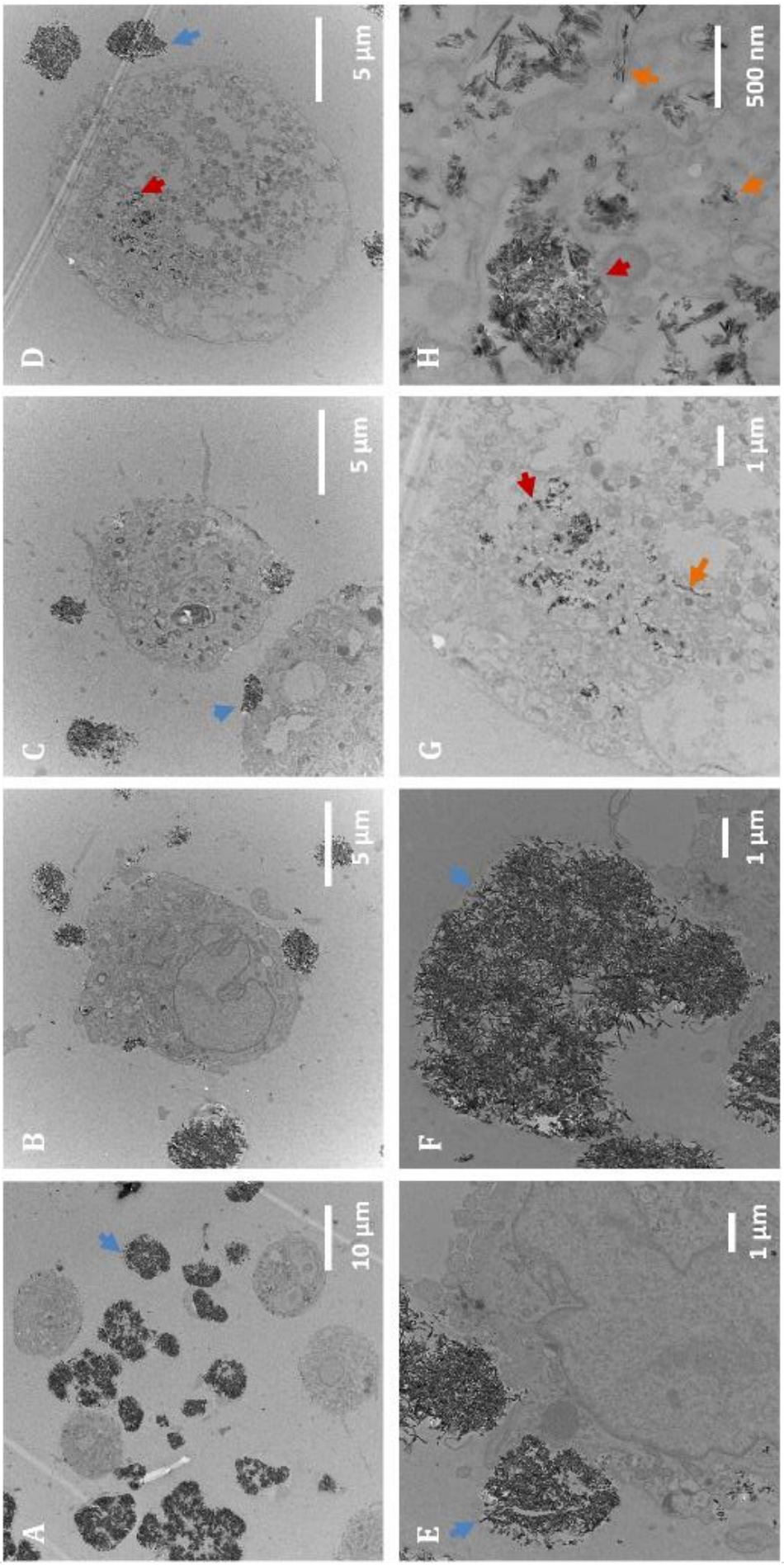

Figure 7-13: Transmission electron microscope images of 3505 hMSC incubated with HAp nanoparticles for 24 hours in a fibrin matrix. HAp synthesised using methodology C outlined in section 4.3.5 ***of chapter 4. A) 1,950X, B-D) 4,600X, E – G) 10,500X and H) 46,000X. Arrows: Red = intracellular vacuole situated HAp, green = unknown artefacts, orange = intracellular tubulovesicular situated HAp and blue = extracellular***

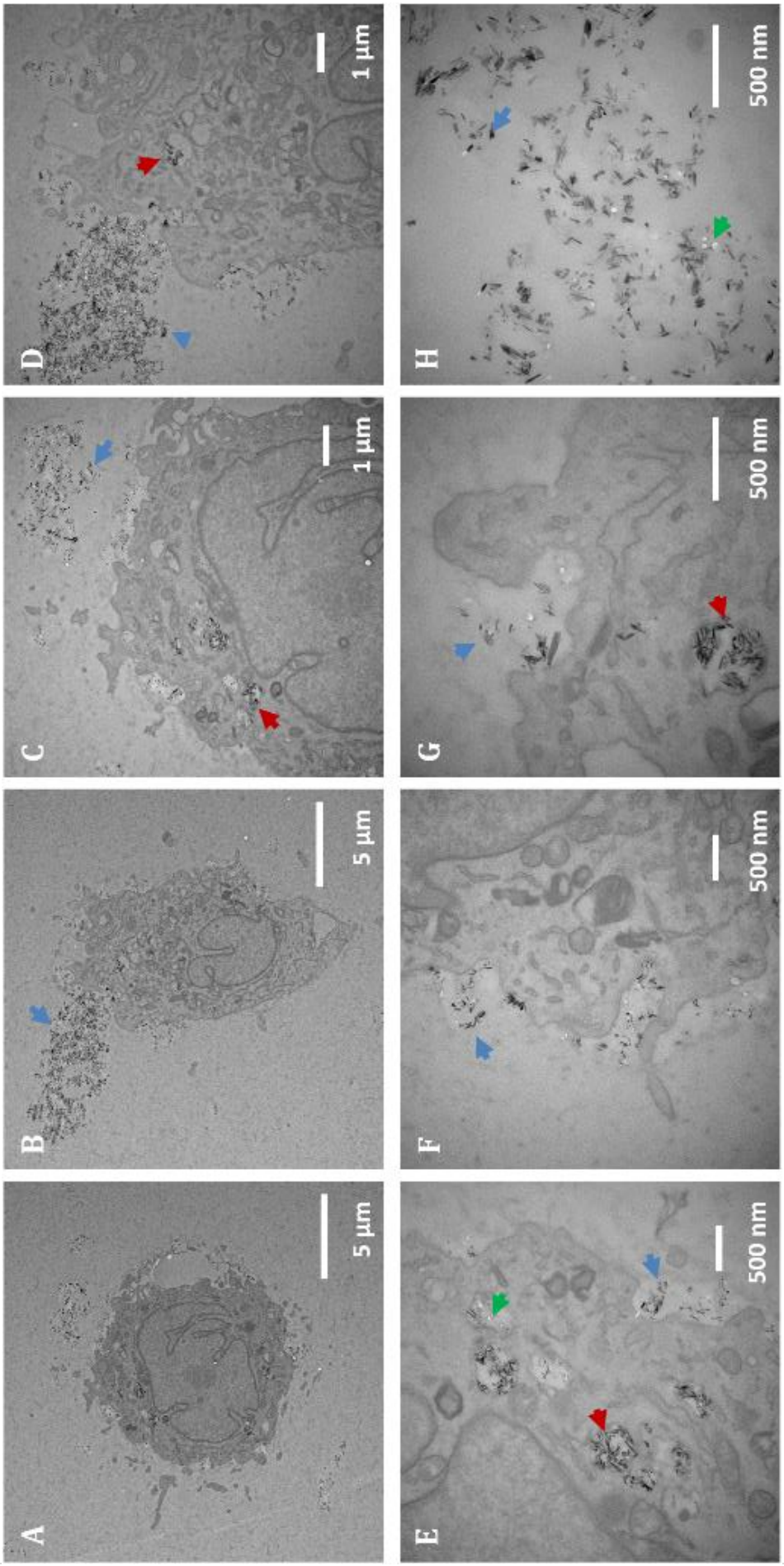

Figure 7-14: Transmission electron microscope images of 3505 hMSC incubated with HAp nanoparticles for 24 hours in a fibrin matrix. HAp synthesised using methodology D outlined in section 4.3.5 ***of chapter 4. A & B) 4,600X, C & D) 10,500X E & F) 25,000X and G & H) 46,000X.***

Arrows: Red = intracellular vacuole situated HAp, green = unknown artefacts and blue = extracellular HAp.

To examine the effect of including HAp, synthesised using the four distinct approaches described earlier (chapter 4) in the fibrin studies were performed to investigate 3D HAp – hMSC interaction.

TEM cross-sections of hMSC incubated with HAp encapsulated within a fibrin matrix for 24 hours showed HAp A–D nanoparticles in vacuoles (**red** arrows) within the cell cytoplasm. The presumed HAp can be clearly observed in figure 7-14F at various processes of internalisation, of which appears to be absent of characteristic clathrin dependent complexes at the plasma membrane.

Cross-sections also revealed debris in the extracellular vicinity with varied nanoscale morphologies (**blue** arrows) (figure 7-11, figure 7-12, figure 7-13 and figure 7-14).

HAp B and D appeared heterogeneous in contrast with associated lighter shaded unknown artefact particles (**green** arrows), where as in HAp A and C presumed particles appeared with a darker contrast with no evidence of lighter particles. TEM also revealed large agglomerates of HAp within the fibrin matrix as is most clearly visible in figure 7-12.

Images from HAp C (figure 7-12) show HAp not only limited to spherical membrane bound vesicles, but within the tubulovesicular system of the cytoplasm characterised by the elongated cavities (**orange** arrows) (Mahmoudi *et al.* 2011).

7.4.2.3 Gene expression

RT-PCR was used to quantify osteogenic differentiation at a transcriptional level, assessing lineage-specific to assess the influences different 3D environments on hMSC differentiation. Changes in mRNA levels were quantified in hMSC cultured in fibrin/HAp filled and PLA fibrin/HAp matrices following 21 days growth in both basal and osteogenic media.

Reverse transcriptase – polymer chain reaction (RT-PCR) was used to quantify osteogenic differentiation at a transcriptional level. Messenger ribonucleic acid (mRNA) expression of lineage-specific markers were analysed to assess the influences of fibrin/HAp ± PLA scaffolds on hMSC differentiation.

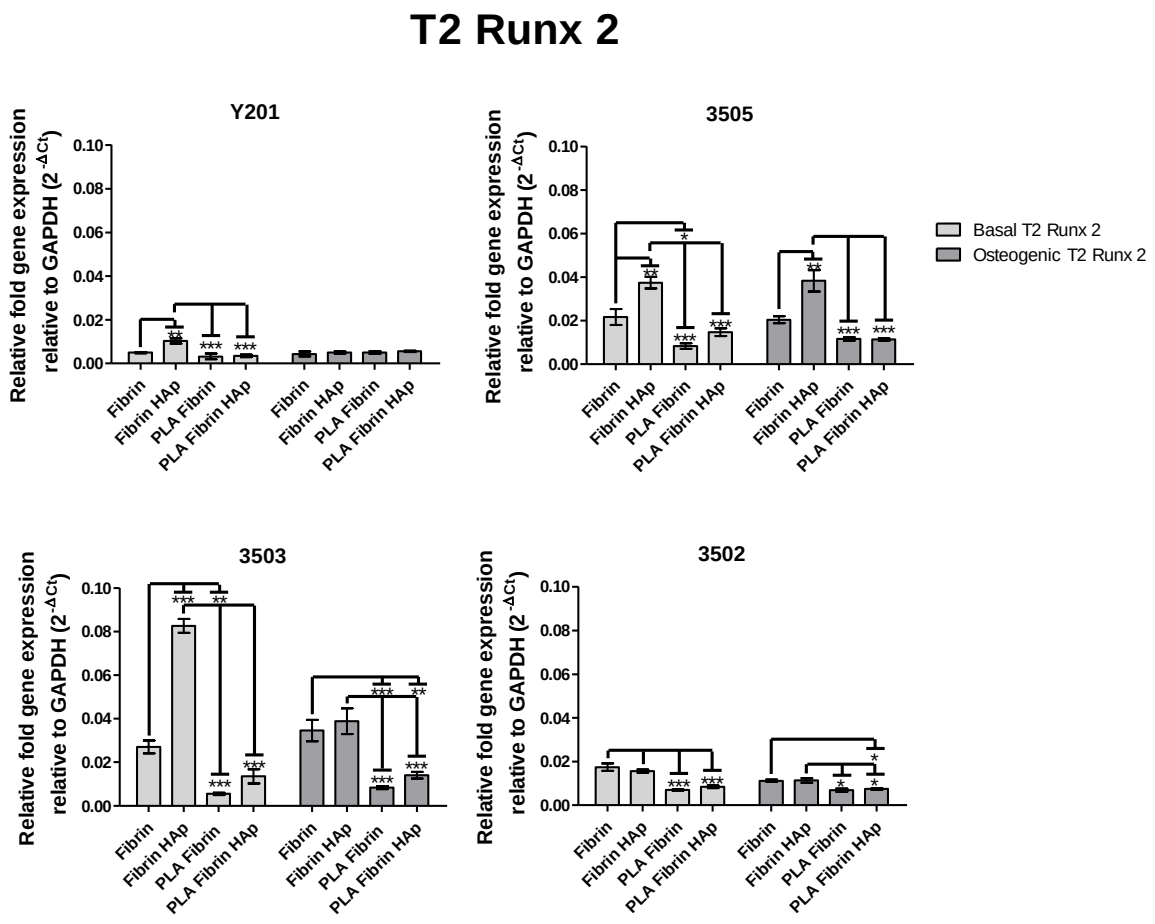

Figure 7-15: mRNA expression of T2 Runx 2 relative to GAPDH. Bars show average gene expression of Y201, 3505, 3503 and 3502 hMSC cells cultivated in fibrin, fibrin/HAp, PLA fibrin and PLA fibrin/HAp in basal and osteogenic media groups for 21 days. (n=5).

No significant differences in T2 Runx 2 expression was found in Y201 cultivated in osteogenic medium between all material groups. The hMSC cultivated in PLA caged fibrin/HAp groups demonstrated a significant reduction in T2 Runx 2 expression relative to fibrin/HAp in 3505, 3503 and 3502 in both media groups. A statistical increase T2 Runx 2 mRNA expression was found in hMSC cultivated in fibrin/HAp materials relative to fibrin controls; this trend was also observed in Y201, 3505 and 3503 basal medium groups.

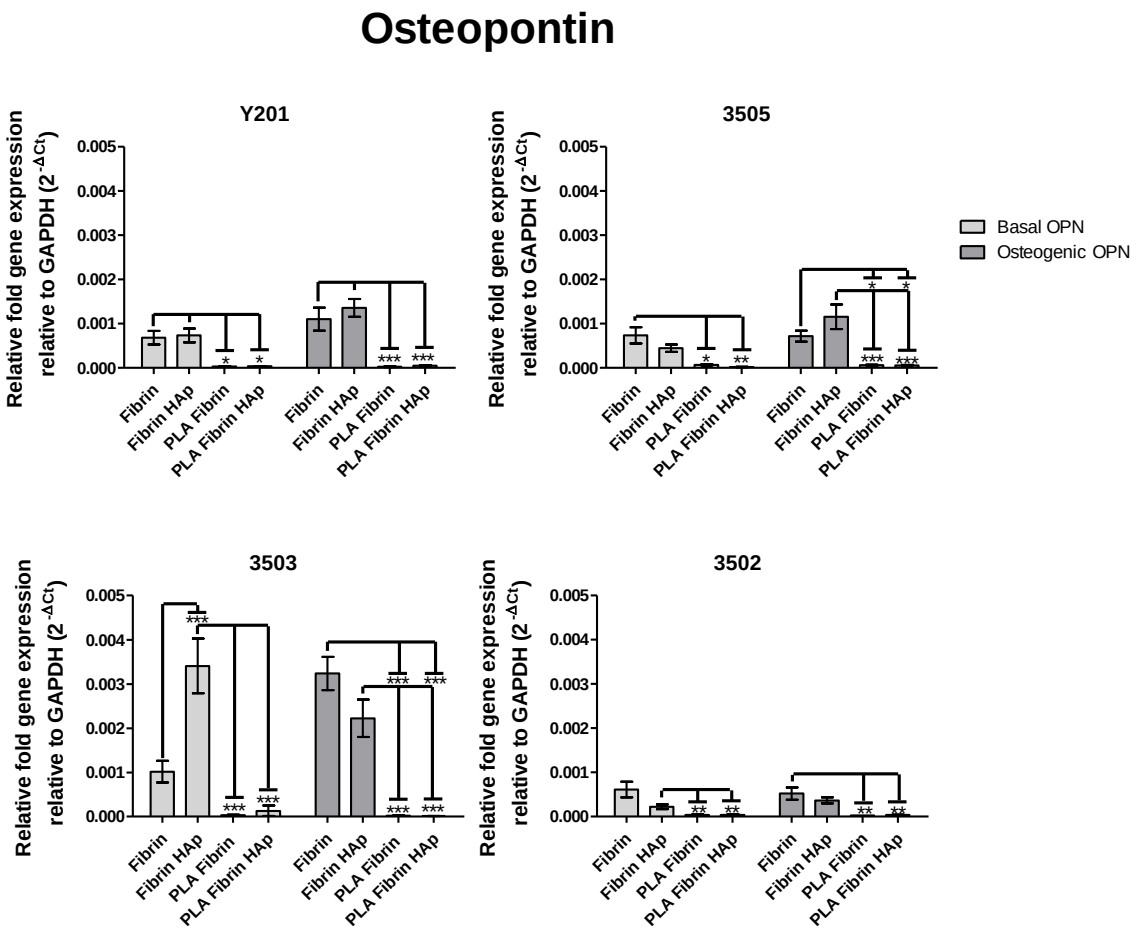

Figure 7-16: mRNA expression of OPN relative to GAPDH. Bars show average gene expression of Y201, 3505, 3503 and 3502 hMSC cells cultivated in fibrin, fibrin/HAp, PLA fibrin and PLA fibrin/HAp in basal and osteogenic media groups for 21 days. (n=5).

Data demonstrates significant reduction in OPN mRNA levels in all hMSC cultivated in PLA caged fibrin/fibrin/HAp constructs in all media groups relative to non-caged fibrin/HAp.

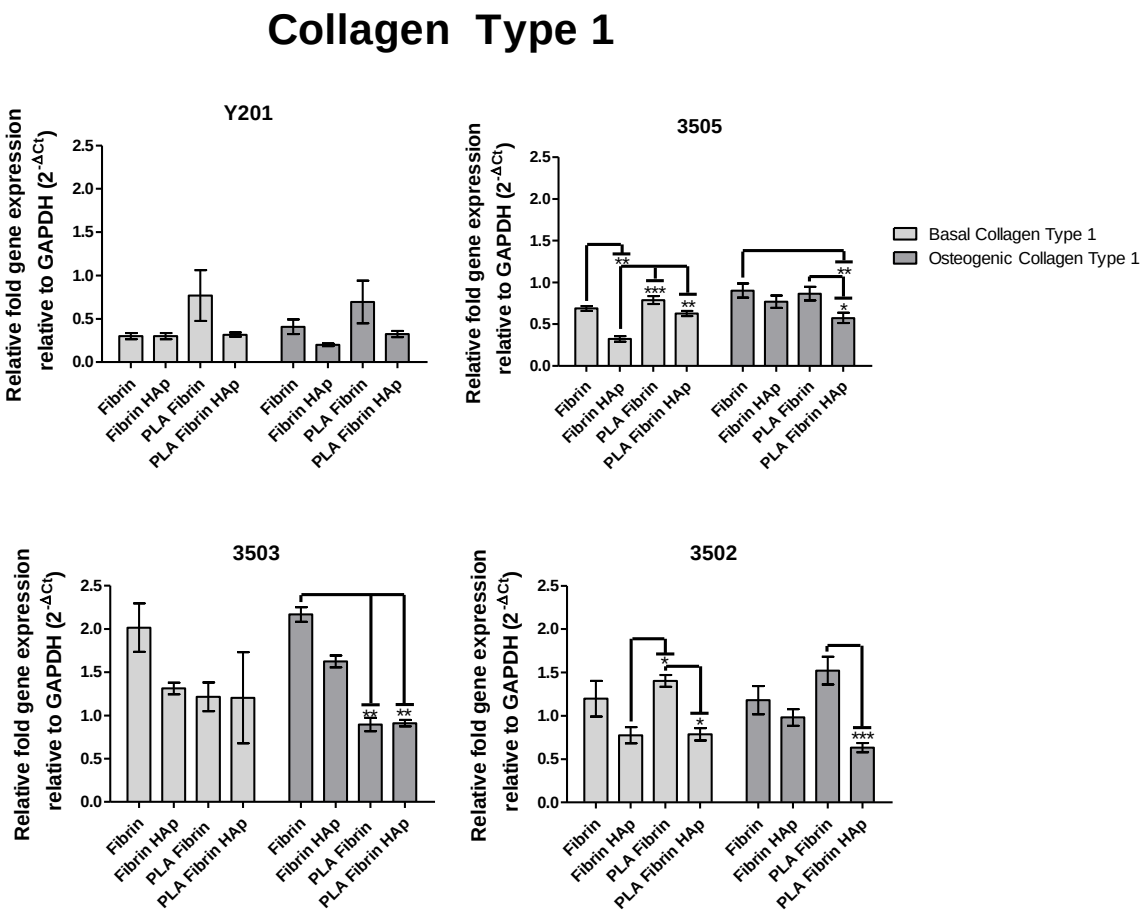

Figure 7-17: mRNA expression of collagen type 1 relative to GAPDH. Bars show average gene expression of Y201, 3505, 3503 and 3502 hMSC cells cultivated in fibrin, fibrin/HAp, PLA fibrin and PLA fibrin/HAp in basal and osteogenic media groups for 21 days. (n=5).

Collagen type 1 mRNA levels of hMSC appear to be reduced in HAp containing groups, this trend appears to be similar across the majority of donor sources and media groups.

7.4.2.4 Histology

Histological examination was performed on hMSC encapsulated in a fibrin matrix with and without HAp following cultivation in basal and osteogenic media for 21 days. Histology was aimed to identify changes in the cell – matrix structure and organisation.

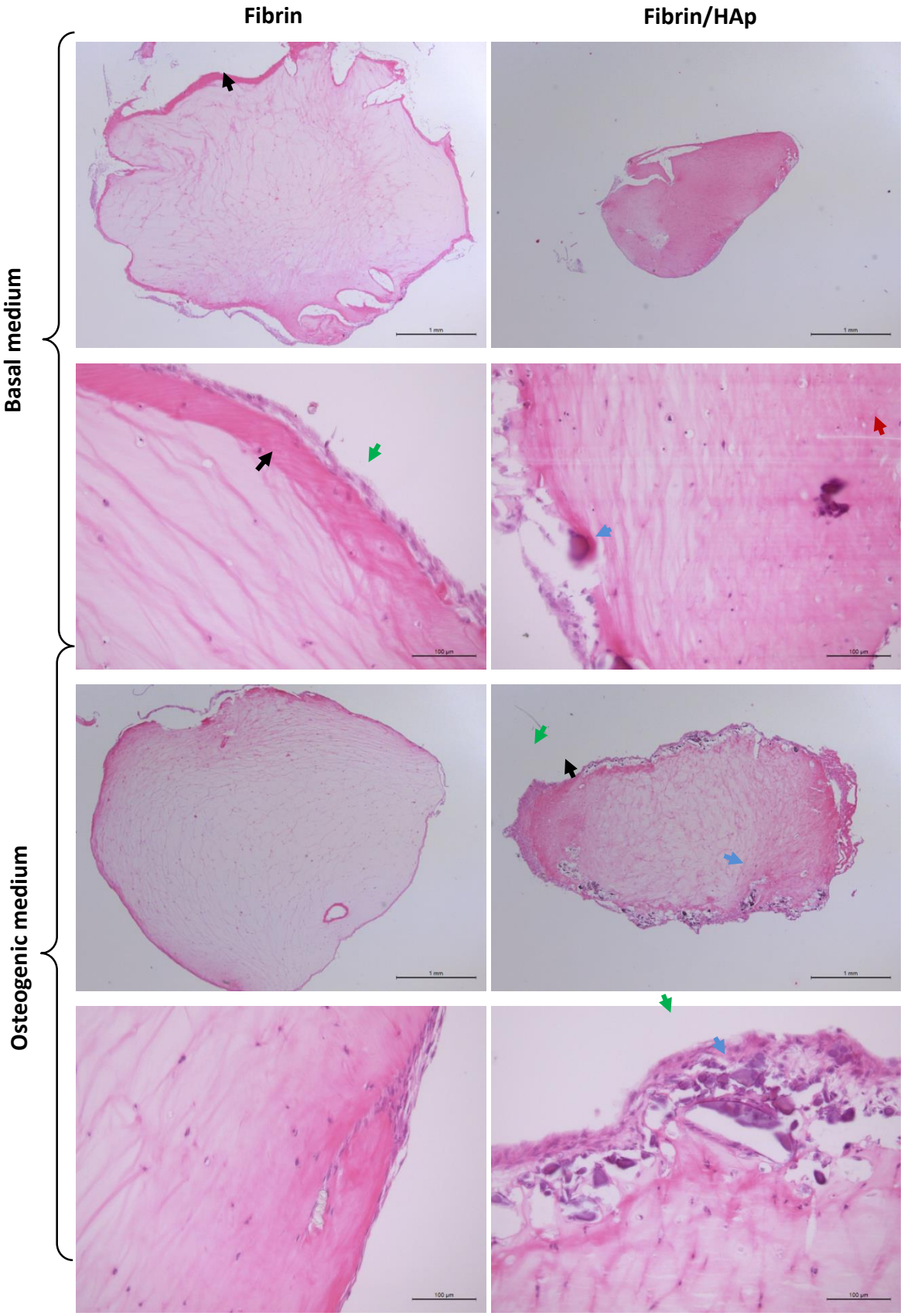

Figure 7-18: Histological Mayer's haematoxylin staining of Y201 hMSC cultured for 21 days. A-D = fibrin and A_1-D = fibrin/HAp. A-B = basal medium and C-D = osteogenic medium.

Arrows: green = layers of cells, black = high matrix deposition, red = sectioning streaks and blue = stained crystal structures.

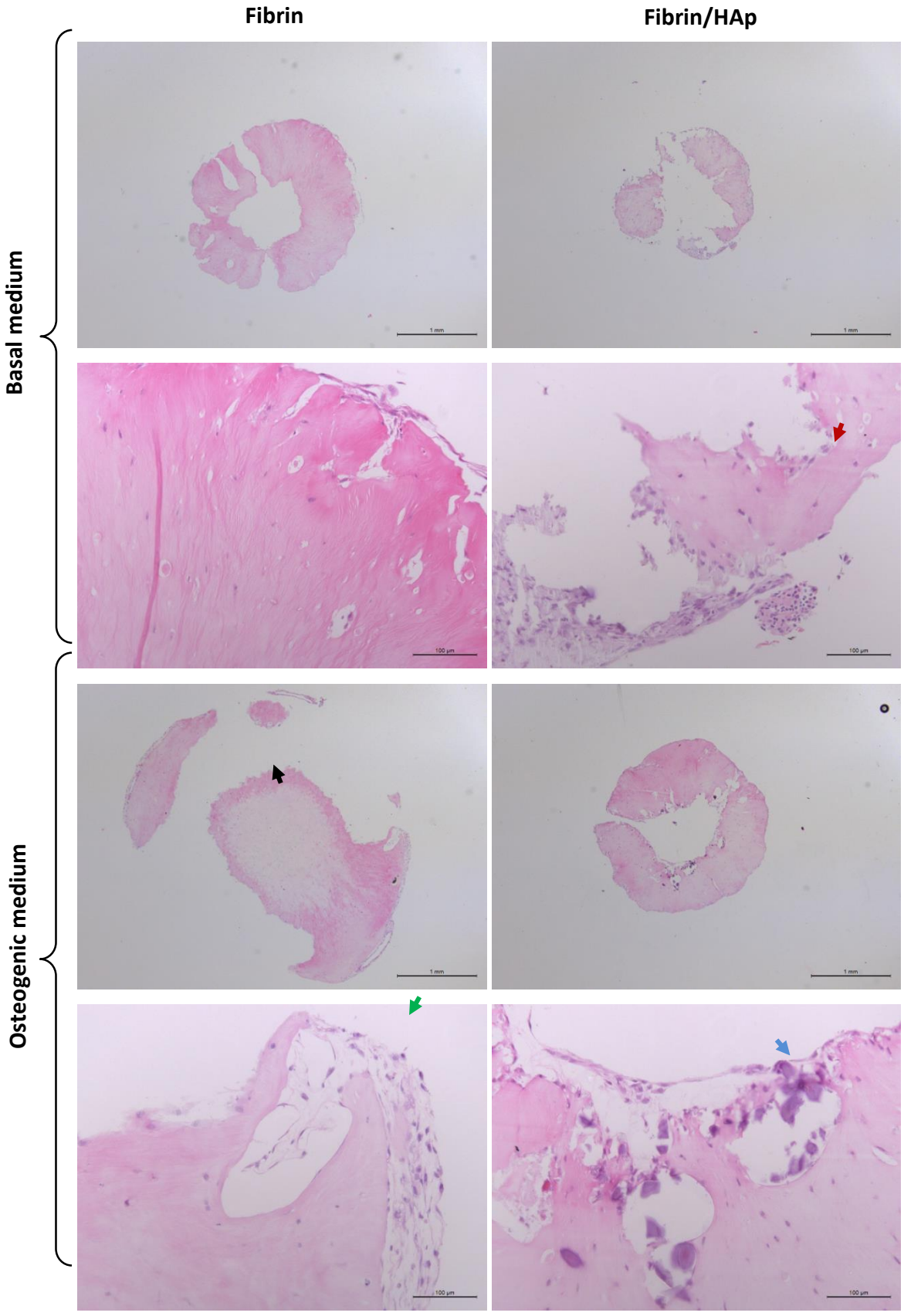

Figure 7-19: Histological Mayer's haematoxylin staining of 3505 hMSC cultured for 21 days. A-D = fibrin and A_1-D = fibrin/HAp. A-B = basal medium and C-D = osteogenic medium. Arrows: green = layers of cells, black = high matrix deposition, red = sectioning streaks and blue = stained crystal structures.

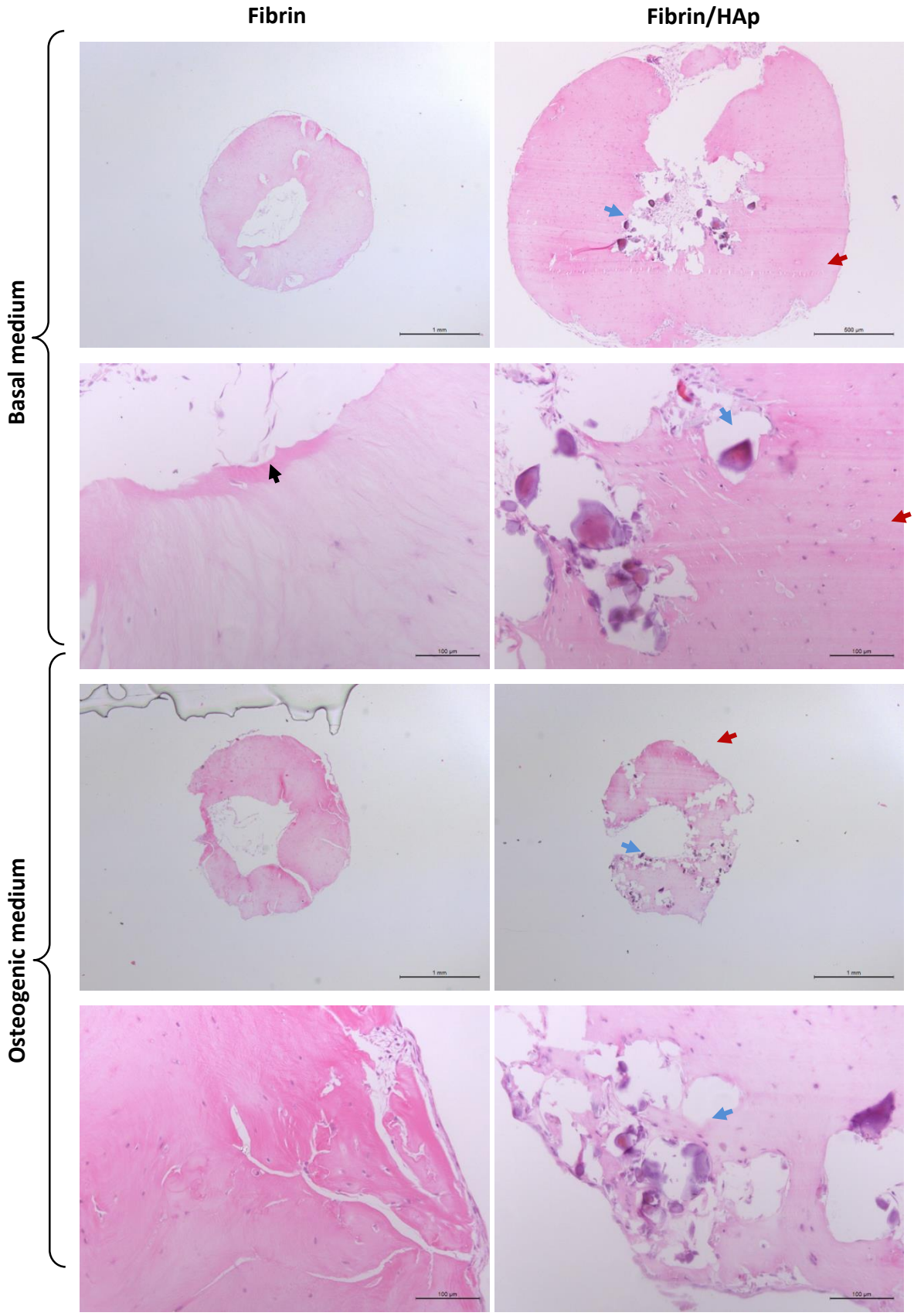

Figure 7-20: Histological Mayer's haematoxylin staining of 3503 hMSC cultured for 21 days. A-D = fibrin and A_1-D = fibrin/HAp. A-B = basal medium and C-D = osteogenic medium.

Arrows: green = layers of cells, black = high matrix deposition, red = sectioning streaks and blue = stained crystal structures.

Histological sections of fibrin and fibrin/HAp gels following 21 days of culture in basal and osteogenic medium revealed some differences in matrix deposition (figure 7-18, figure 7-19 and figure 7-20). The majority of sections displayed highest matrix deposition around the periphery of the gels (**black** arrows), with layers of cells on the outside of the material (**green** arrows).

In fibrin/HAp groups purple stained crystals (**blue** arrows) were observed at periphery which appeared to correlate with enhanced matrix deposition and higher numbers of cell populated regions. Sectioning streaks could also be observed around the regions these crystals appeared (**red** arrows).

7.5 Discussion

This chapter has shown some of the challenges associated with *in-vitro* cell seeding of 3DP PLA scaffolds. Results have also demonstrated a potential delivery vehicle for viable hMSC using a fibrin hydrogel formulation. Investigation into hMSC - HAp interaction within a fibrin matrix revealed nanoparticle agglomeration and uptake into hMSC cytoplasm after 24 hours. A significant increase in T2 Runx2 expression was observed in hMSC cultured in non-caged fibrin/HAp compared with fibrin alone. The hMSC cultured in fibrin and fibrin/HAp gels had statistically lower gene expression of T2 Runx2 and OPN at day 21 in caged gels compared with non-caged gels. Histological examination of hMSC embedded fibrin/HAp hydrogels following 21 days showed distinct regions of increased matrix deposition of which contained mineral crystals in HAp containing gels.

7.5.1 *PLA & fibrin*

The morphology of the printed PLA constructs demonstrated morphological differences from the top, side and base layer images (figure 7-7). The fine polymer filaments observed in figure 7-7 A_{1-3} are likely ligature marks from the hot end nozzle of the extrusion process. The differences observed with the side of the scaffolds is likely due to the rate cooling of the polymer, which will differ from the base layer on the heated print bed.

The combination of hanging drop and static seeding of PLA scaffolds was performed to encourage cell adherence to the PLA scaffolds alone. The observations and confocal images from the PLA seeded constructs allows us to determine that even with a combination of methodologies seeding efficiency was limited and was therefore eliminated as a control for later experiments (figure 7-8). Other dynamic seeding methods could have be utilised such as seeding cells in suspension with the PLA scaffold on an orbital shaker similar to Thevenot *et al.* (2008). A centrifugation approach by Thevenot *et al.* (2008) would have been inappropriate for this scaffold as the structure of the scaffold would have resulted in cells passing through the scaffold entirely.

The quantitative representation of the live/dead performed on hMSC within fibrin formulations and varied gelation time demonstrated a significant increase in cell survival with formulation B compared with A (figure 7-9). Sodium chloride salt used in formulation A is likely to produce a hypertonic medium for the cells, removing water from the cell cytoplasm via osmosis inducing cell death. The HBSS and the hMSC medium is designed to be isotonic and

would therefore maintain an osmotic balance. Further investigation could include incremental time-point analysis and the influence of HAp filling on L/D quantification. Alternatively, confocal microscopy or fluorometry of digested cells could have been used to more accurately quantify live/dead ratios of hMSC cultured in fibrin gels.

7.5.2 ***Fibrin/HAp***

From the TEM cross-sectional images of hMSC cultivated within a fibrin/HAp matrix for 24 hours we can observe that HAp is taken into hMSC via clathrin-independent pinocytosis. Images from all types of HAp demonstrate internalisation into the cytoplasm via membrane bound vesicles. These vesicles, whilst forming, display no signs of clathrin mediated receptor – ligand complexes which would have been stained along with the other cell structures with the osmium tetroxide and uranyl acetate during TEM cell staining.

Subtle differences were observed in the location of HAp within the cytoplasm and varied between HAp A and HAp C (figure 7-11 and figure 7-13). With HAp A, B and D the nanoparticles appeared restricted to definitive vacuoles, whereas images from HAp C demonstrate HAp within the tubulovesicular system of the cell cytoplasm (figure 7-11, figure 7-12, figure 7-13 and figure 7-14). This is likely due to the absorptive endocytosis process, in which pinocytic vesicles fuse with endosomes and begin a degradation process in which the pH is lowered via the action of ATPase proton pumps to pH ~4.5. This process matures the endosome for later fusion with lysosomes containing hydrolytic enzymes to degrade the endocytosed material (Mahmoudi *et al*. 2011; Motskin *et al*. 2011).

Previous work investigating various agglomerates of HAp and their uptake into human monocyte macrophages have demonstrated degradation of HAp through the fusion of vacuole bound HAp and lysosomes (Motskin *et al.* 2011; Motskin *et al.* 2009). It is likely that most of the HAp absorbed into the cell will undergo this process, but it is not fully evident from the images of hMSC 24 hours post incubation. Further investigation into different time points could help to pin point the specific degradation pathway for these nanoparticles. Inhibition of specific endocytic pathways could also be investigated to determine the specific mode of HAp uptake into the cell (Kastl *et al.* 2013).

Clathrin-independent pinocytosis remains a poorly characterised process, however there are a number of articles that display nonspecific nanoparticle uptake, which have been attributed

to their electrostatic status (Wilhelm *et al.* 2003; Barnett *et al.* 2007). It is postulated that electrostatic interaction with the phospholipid bilayer lead to the formation of invaginations, encapsulating the nanoparticles though direct membrane bending and disruption (Barnett *et al.* 2007). Cai *et al.* (2007) investigated the influence of HAp size and morphology on hMSC uptake, they reported limited penetration of larger particle sizes (~200-500 nm length and ~30-80 nm width rod-like morphology) with rapid absorption with small rounded HAp ~20 nm.

The aspect ratio of nanoparticles have been shown to influence cellular uptake (Qiu *et al*. 2010). However a recent study into the influence of HAp on cells demonstrated no correlation between aspect ratio and cellular uptake (Müller *et al.* 2014). Cellular uptake of nanoparticles and release of ions are the likely modes of action for calcium phosphate nanoparticles. Since hydroxyapatite does not dissolute under physiological conditions, it is likely that the cellular uptake of HAp is the mechanism for the observed influences on cell biology (Ha *et al*. 2015). However, there appears to be an ambiguity surrounding nanoparticle characteristics that enable cellular uptake. Quantum dots with a higher aspect ratios were found to uptake slower into the cell than spherical nanoparticles (Soenen *et al.* 2011). The internalisation of gold nano-rods also appeared to diminish with greater aspect ratios (Soenen *et al.* 2011). HAp with aspect ratios of ~1-5 have been observed internalising into a number of different cell types *in-vitro* (Motskin *et al.* 2011; Müller *et al.* 2014; Motskin *et al.* 2009). In summary it is likely that a myriad of nanoparticle properties including, morphology, surface area, aspect ratio, zeta potential, protein absorption and elemental composition are responsible for the observation of HAp uptake into hMSC (Motskin *et al.* 2011; Müller *et al.* 2014).

The noted debris surrounding the cell (figure 7-11, figure 7-12 and figure 7-14) are of a similar size to the HAp nanoparticles and are electron dense, this debris could be a result of degradation as the cell begins to digest the surrounding matrix.

The unknown artefacts which appear to be in proximity to HAp nanoparticles observed with HAp synthesised at pH 8 (HAp B and D) could be due to ionic dissolution of a less stable Ca/P ordered nanostructure as previously postulated in chapter 4. Highly crystalline hydroxyapatite materials are known to further apatite deposition in simulated body fluid (SBF) experiments and *in-vivo*. The nanocrystalline forms of HAp are likely more vulnerable to cellular degradation processes. Further investigation might include a dissolution study to measure the effect of lower pH environments of HAp A, B C and D ion release over time in SBF medium.

Data collected from RT-PCR analysis allows us to determine that there is a significant increase in T2 Runx 2 gene expression in hMSC cultivated in fibrin/HAp compared with fibrin alone following 21 days incubation in basal medium. Collagen type 1 mRNA levels demonstrated variability in all data sets, however a trend can be observed showing reduced expression in all cells cultivated with HAp, respective of their fibrin controls.

Due to the temporal nature of the investigated genes and lack of previous time points, it is unclear whether levels of expression recorded at day 21 are from lack of stimulation, or the initiation/termination of the expression sequence. Differences observed in gene expression between cell sources adds to evidence from previous chapters of donor cell heterogeneity. Heterogeneity in adherence isolated hMSC is a reported phenomenon (Phinney 2012).

The histological examination allows us to determine that there was matrix deposition, which appeared to be located around the periphery of the hydrogel following 21 days cultivation with a variety of hMSC cell sources. Crystalline minerals were also observed in areas co-located with areas of high matrix deposition and cell activity in HAp containing fibrin hydrogels.

Cell matrix deposition around the periphery is a common occurrence with 3D static cultivation conditions (Wu *et al.* 2014). This observation is possibly due to mass transport limitations with the static culture conditions. Further study may include the use of a perfusion bioreactor system to improve mass transport or modification of the fibrin gel to improve permeability.

The influence of HAp filled hydrogels has been investigated on capillarity network formation using co-cultures of MSC and endothelial cells in a fibrin/collagen composite scaffolds. The results demonstrated inhibition of capillary network formation *in-vitro* with constrained hydrogels, however with unconstrained hydrogels an increase in total network length was measured with 2.5 mg/mL HAp filling (Rao *et al.* 2014).

7.5.3 *PLA caged fibrin/HAp*

A significant reduction in T2 Runx 2 expression was found in hMSC cultivated in PLA caged fibrin/HAp constructs following 21 days incubation relative to fibrin/HAp in all medium groups. Expression of OPN at day 21 revealed significantly reduced mRNA levels in hMSC cultivated in PLA caged fibrin/HAp constructs, biologically however the levels were low relative to previous reports OPN expression at ~ 0.25 $2^{-\Delta Ct}$ GAPDH (Köllmer *et al.* 2013). Again

due to the single time point of measurement it is indistinguishable whether these results are suggestive of any positive or negative biological influences.

In most studies conducted *in-vitro* the 3D hydrogels are constrained preventing remodelling and compaction by contractile forces exerted by the cells. In this chapter hMSC embedded within the fibrin ± HAp were either unconstrained or constrained by a PLA scaffold. It has been suggested that unconstrained gel compaction leads to increased matrix density and associated increase in matrix stiffness (Rao *et al*. 2014). This information may explain the observed reduction in osteogenic associated gene expression in the PLA caged fibrin groups compared with non-caged fibrin groups (figure 7-15, figure 7-16 and figure 7-17).

In a study by Endres & Hutmacher (2003) fibrin was used as a vehicle for hMSC delivery into 3D printed polymeric scaffolds. No significant differences were observed in this study following 3 weeks *in-vitro* incubation with honeycomb PCL and PCL hydroxyapatite scaffolds.

An article by Jung *et al.* (2014) investigated the osteogenic potential of rat MSC within a fibrin HAp (Ostim™) filled matrix caged within a 3-D mesh scaffold. Their results showed an increase in ALP activity from day 14-21 and cell cytotoxicity from day 1-14. More experiments are required to compare results from this chapter with this work, however the delayed osteogenic response could have implications for future work.

7.6 Conclusion

The results from this chapter demonstrate a variety of challenges with static *in-vitro* cultivation of 3D constructs. Fibrin hydrogels were successfully used as a delivery vehicle for viable patient derived hMSC. Fibrin/HAp matrices displayed hMSC nanoparticle uptake following 24 hours cultivation, with some morphological differences in HAp from different synthesis methods outlined in chapter 4. Osteogenic gene expression data requires further investigation, however it did demonstrate an increase in T2 Runx2 expression in hMSC cultivated in non-caged fibrin/HAp relative to control. PLA caged fibrin and fibrin HAp materials appeared to have a significant influence on T2 Runx2 and OPN expression compared with non-caged counterparts. Histology demonstrates regions of cell activity corresponding with increased matrix deposition from cells located at the periphery of the fibrin hydrogel. Mineral deposits were also observed within fibrin/HAp hydrogels following 21 days static cultivation, however their origin and composition requires further elucidation.

Chapter 8 – Discussion

8.1 Summary of Results

Chapter 4 describes the synthesis and characterisation of HAp synthesised using an automated component addition rate and pH regulation sol-gel synthesis methodology. Results demonstrated control of HAp particle a-axis (width) by the modification of the reaction pH during titration. The availability of calcium present during HAp formation, through alteration in either titration methods or rates, appeared to significantly influence HAp crystal c-axis (length). HAp lattice carbonate ion absorption was found to decrease in HAp synthesised at higher rates and with the simultaneous addition titration methodology. The cytotoxicity of the HAp to hMSC indicated ≥75% viability to various forms and concentrations of synthesised HAp.

Results from chapters 5 and 6 provide evidence of the maintenance of hMSC capacity to adhere, grow and differentiate when cultivated on 2D PLA, fibrin and HAp filled/coated materials. Differentiation towards the osteoblast lineage was observed in hMSC cultured on fibrin/HAp filled substrates with differences in hMSC cell morphology and an increase in osteogenic gene induction. Donor hMSC morphology, proliferation and gene expression changes however varied notably from patient-to-patient, illustrating that despite broadly similar trilineage potential and flow marker profile, the significant heterogeneity of these cells.

8.2 Novelty

As introduced in the literature survey, there are currently a number of systems to produce nanoscale apatite derivatives. The experimental methods used in chapter 4 provide a systematic evaluation of parameters known to influence sol-gel HAp crystal nucleation and growth providing greater insight into titration variation than previously published studies.

Other research articles have used DMF as a dispersant solvent for HAp prior to polymeric incorporation and composite fabrication (Deng *et al*. 2001; Deng *et al*. 2007; Patlolla *et al*. 2010). However, the novelty described here is in the processing. Dispersion of HAp followed by PLA incorporation, gelation, DMF removal and composite powder fabrication is a new approach to the fabrication of monodispersed nanocomposite materials. As demonstrated in chapter 4 the composite powder was used in a pressure moulding technique yielding a monodisperse solid nanocomposite PLA/HAp bar.

The dispersion and phase transfer of nanoparticles using a surfactant aided process is not a novel process. Previous research using the phase transfer of gold and silver nanoparticles has been widely reported. However, the application of this technique to HAp is a novel approach for HAp polymer nanocomposite fabrication.

The use of 3D printed PLA scaffold followed by fibrin/HAp hydrogel hMSC encapsulation and infiltration is a novel combination of materials.

8.3 Implications for tissue engineering

8.3.1 *2D vs 3D models*

Investigations into 2D material substrates were designed to include a number of principles associated with a 3D biodegradable scaffold surface. Firstly cytoskeletal tensions are known to influence hMSC lineage commitment on substrates of different elasticities (Engler *et al*. 2006).

Gupta *et al*. (2015) proposed a number of theories regarding the adaptive nature of the cell cytoskeleton depending on substrate stiffness. Images of hMSC cultured on the glass PLA and PLA HAp substrates in chapter 5 (figure 5-21 and figure 5-22) clearly demonstrate cells with a nematic cytoskeletal arrangement (figure 2-8A). Whereas images of hMSC cultivated on fibrin and fibrin HAp coated substrates in chapter 6 (figure 6-5 and figure 6-6) appear to show isotropic characteristics (figure 2-8A) of less stiff substrates. This appears to happen due to inherent differences in substrate stiffness, however further investigation is required to give a definitive answer. Figure 8-1 demonstrates hypothetical differences in substrate elasticity as a result of subsurface particle agglomeration.

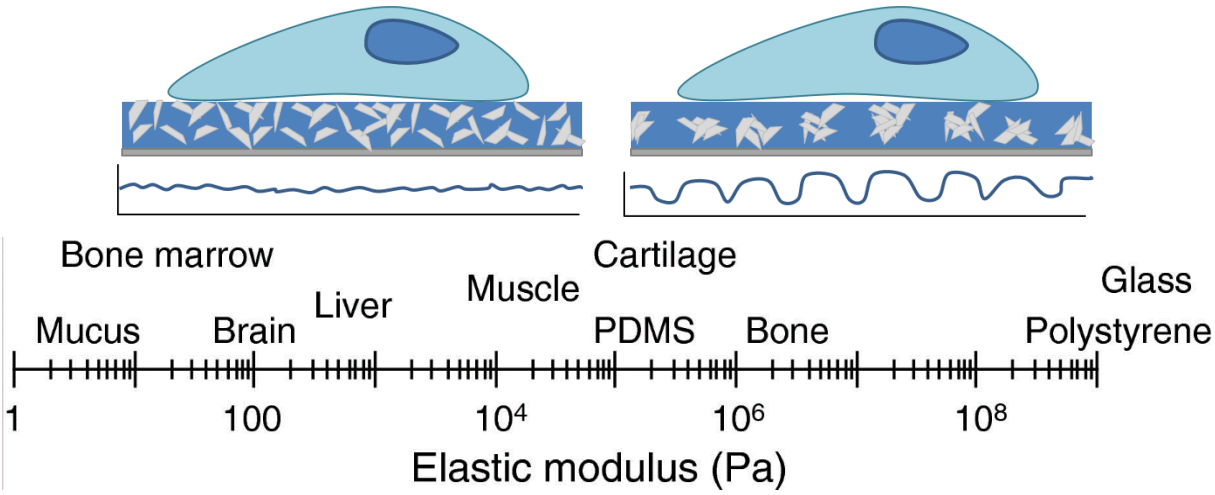

Figure 8-1: A) Illustration of dispersed vs agglomerated HAp filled matrices with hypothetical changes in elasticity across the surface illustrated below.

As previously introduced the substrate stiffness can have a variety of influences on cell biology, such as proliferation, apoptosis, migration and stem cell differentiation (Engler *et al*. 2006; Park *et al*. 2011; Yeung *et al*. 2005).Current studies investigating the influence of mechanical anisotropy have utilised pillars of deformable materials such as silicon nanowires (Park *et al*. 2016), however the influence of anisotropic substrate stiffness patterns

irrespective of surface topography has not yet been investigated. In the body, cells are exposed to a number of different micro and nano substrate patterns of elasticity. A good example of this would be in the bone, where collagen fibres are intercalated with HAp. This nanoscale range of mechanical anisotropy in bone is likely masked by the dense distribution of HAp within the collagen fibres. However, in an elegant study by McNamara *et al. (*2014) hMSC were found to directly sense 8 nm high pillars using nanoscale membrane projectors, demonstrating the extremely sensitive nature extracellular interaction. The threshold of the cells mechanosensing apparatus is no doubt limited within a range of biological substrate stiffness's. Therefore, it is plausible that the size and mechanical properties of fillers within artificial polymeric matrices will influence cell behaviour, given that the materials can be subject to deformation by cell contractile processes.

For the literature the elastic modulus of PLA substrates vary from 1.9 – 2.7 GPa depending on the content of L/D isomers (Middleton & Tipton 2000). The Natureworks PLA used in this thesis according to the data sheet has an elastic modulus of 3.45 GPa. Results from chapter 5 did not specifically address the differences in substrate elasticity due to difficulties with HAp dispersion within PLA. However, one cell viability assay demonstrated no significant difference between PLA and PLA (non-dispersed) HAp. Further investigations are required in order to determine any potential effects of this principle. However, it is likely that the inherent stiffness of PLA hides any elasticity changes caused by HAp inclusion to the hMSC.

Fibrin substrate stiffness can vary from 16.1 – 80.9 kPa depending on fibrinogen and thrombin concentrations (Thomson *et al.* 2013). This is within the range for a number of other biological tissues, including liver, muscle and cartilage. Results from chapter 6 demonstrate hMSC responses to fibrin and fibrin/HAp filled substrates. As was evident from SEM and TEM images, the HAp within the fibrin was agglomerated. Results from morphological analysis of hMSC demonstrated some decrease in cell spreading on fibrin/HAp compared with fibrin substrates. It is probable that differences observed between fibrin and fibrin/HAp substrates are due in part to changes in substrate elasticity (Guthold *et al*. 2007).

Further investigation could use techniques such as AFM and nanoindentation to directly measure differences in substrate elasticity as a result of HAp filling.

Secondly, protein adhesion is a fundamental facilitator of cell adhesion. Figure 8-2 demonstrates hypothetical differences in protein binding on HAp filled and coated substrates.

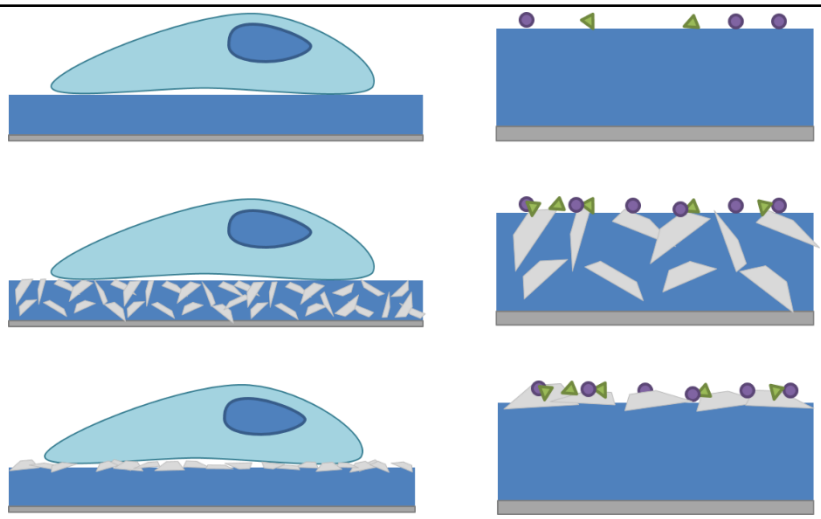

Figure 8-2: Illustration of protein absorption on material surface and HAp filled coated substrates.

Chapter 5 investigated the differences between HAp coated and non-coated PLA substrates. Results showed 50% of the hMSC donors had higher levels of proliferation on PLA+ HAp coated vs. PLA+ control. However, results from fibrin experiments demonstrated the exact opposite with a reduction in proliferation on HAp functionalised substrates. These results could be due to a number of factors including degree of adhesion and likelihood of triggering differentiation, the population doublings each cell line had to have sufficient cells for the experiment. More targeted investigations are required to determine any potential influences of this theory.

SEM analysis revealed topographical differences between control substrates and HAp filled/coated materials. Topography is known to influence osteoblast adhesion and differentiation making it a factor requiring further characterisation.

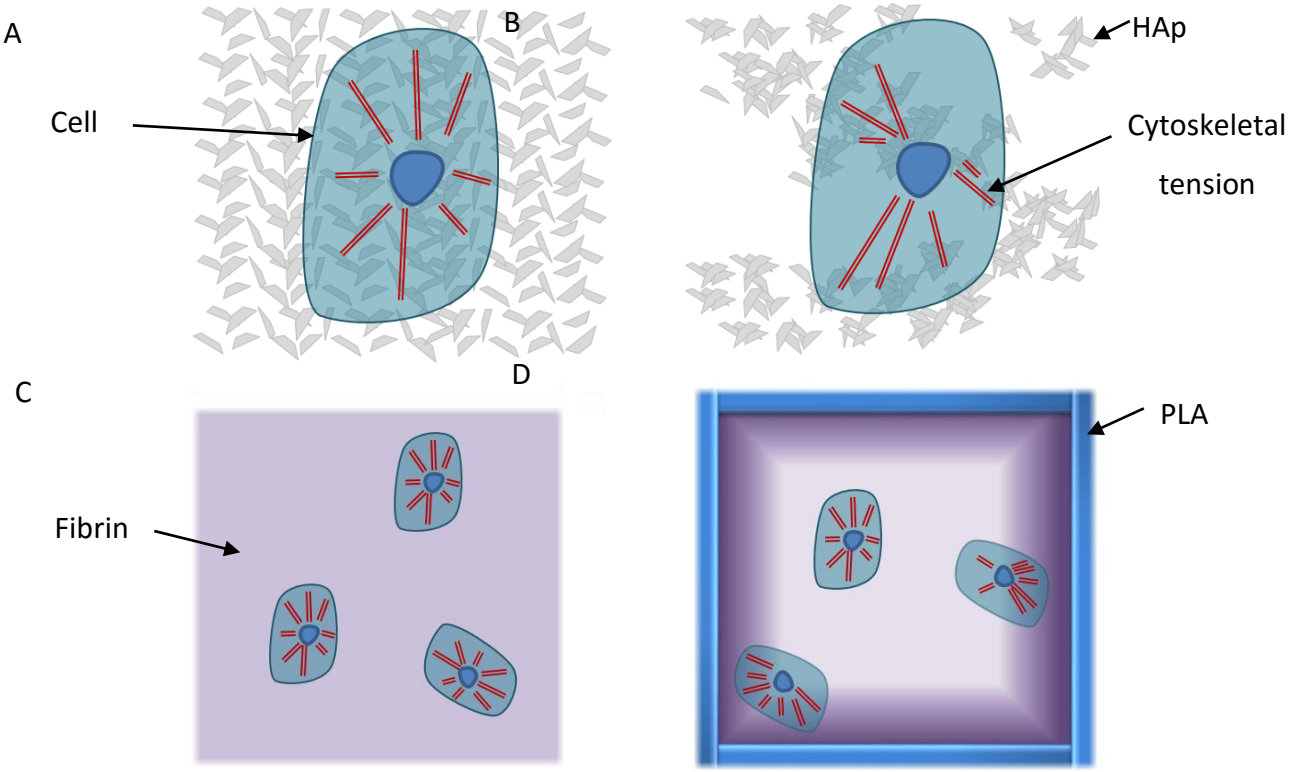

Figure 8-3: Illustration of the theoretical 3D influence of; A) dispersed HAp, B) agglomerated HAp, C) unconfined fibrin and D) PLA confined fibrin matrix on cells in 3D.

Figure 8-3 demonstrates the 3D equivalence of figure 8-1. Chapter 7 demonstrated the influence of HAp within a 3D matrix, although the role of particle dispersion was not specifically investigated, it is likely to cause regional differences in substrate stiffness. In a similar fashion, cells encapsulated within a uniform fibrin matrix are likely to have homogenous cytoskeletal tensions depending on the cross-link density. Whereas fibrin confined within a PLA pore is likely to have distinct regions of increased cross-link density closer to the PLA filaments. The effect of heterogeneous cytoskeletal tensions could be a determining factor in the gene expression results observed in chapter 7. It is also possible that the marked differences in hMSC mRNA expression as a result of PLA confinement is caused by differences in mass transport throughout the fibrin matrix.

8.3.2 *HAp*

The influence of HAp on cell behaviour is the primary motive for its use in bone tissue engineering. Remarkably, the effects of HAp on cell function is relatively unknown. Recently, Ha *et al.* (2015) demonstrated modulation of a specific gene expression regulatory programme through promotor methylation by HAp in osteoblasts. This is the first exciting report unravelling the mode of action for HAp on cell biology. With the recognised dissimilarities between 2D and 3D cell behaviour it would be interesting to see if this result is reciprocated in a 3D environment.

Chapter 5 shows HAp uptake by hMSC encapsulated within a fibrin matrix following 24 hours incubation. HAp uptake into cells is not new to tissue engineering, however uptake into hMSC within a 3D matrix is. Stem cells are known to have enhanced protective mechanisms to avoid damage and maintain their 'stemness' (Bosco *et al.* 2015). The result demonstrates that hMSC actively sample their surrounding microenvironment and are likely subject to similar effects as terminally differentiated cell types in response to HAp.

The influence of substrate stiffness has recently been linked to changes in the cells ability to endocytose (Missirlis 2014). In the study by Missirlis (2014) clathrin dependent endocytosis was measurably lower in fibroblasts cultured in substrates with an elasticity modulus of 5 kPa compared with 40 and 85 kPa. Although there was no evidence for clathrin-dependent endocytosis demonstrated in chapter 7, this information may have implications to the field of nanoparticle research for biological applications.

8.3.3 *Polymer cages for 'soft' materials within a 'hard' scaffold*

Previous literature has investigated the use of relatively hard polymer cages to house hydrogel encapsulated cells for bone tissue engineering (Shao *et al*. 2006; Lee *et al*. 2010). Data from chapter 6 demonstrates the ability of hMSC to modify their environment with enhanced matrix deposition and mineralisation observed in groups cultured in fibrin/HAp hydrogels.

The contraction of fibrin/HAp hydrogel discs following culture with hMSC is likely due to cell induced contraction of the ECM. Within the PLA caged scaffolds the fibrin is likely to more robustly anchor to the PLA filaments locally increasing the network strength within the PLA structure. An increase in cytoskeletal tension is known to enhance hMSC osteogenesis (Mcnamara *et al.* 2012).

The mass transport limitations with current static tissue culture practices makes the growth of large tissues *ex-vivo* unlikely. Bone is a highly vascularised tissue and, without the simulation of interstitial fluid flow or *in-vivo* experimentation, it is difficult to determine the effectiveness of 3D materials on the regeneration of bone tissue.

The observed crystalline structures in histology images (figure 7-18, figure 7-19 and figure 7-20) could potentially be the original HAp filled within the fibrin matrix. However, their size and morphology are more representative of a large crystalline hydroxyapatite. TEM examination in figure 7-12 demonstrated agglomerates of HAp nanoparticles with an approximate size of 5 – 20 μm. Minerals observed in histological examination ranged from 20 – 50+ μm in size with what appears to be large planar surface features. Alternatively, apatite formation of Ca^{2+} and PO_3^{2-} ions from the culture media may have amalgamated the nanoparticles into a single planar structure. Further examination of these minerals by TEM and EDX are required to pinpoint their origin.

The results from RT-PCR analysis and histological examination raise a number of interesting questions: 1. Are the observed differences in mRNA expression due to the late *in-vitro* time point or is it due to the mobility, communicative and proliferative capability of cells embedded within these matrices? 2. What are the reasons for the observed differences in mRNA expression with the hMSC within the PLA scaffolds? 3. Are the minerals observed in the histological images new or agglomerated forms of the HAp introduced within the material from the beginning?

To address these questions, a number of further studies are required: 1. To elucidate the mobility, communicative potential of hMSC within the fibrin matrix. 2. To investigate the proliferation and differentiation of hMSC in respect to their seeding density and HAp quantity per mm^3. 3. Further investigation into previous time points is required to clarify the differences observed in hMSC mRNA levels over the 21-day period. 4. To investigate the final mineral content either through quantification of total calcium using AES-ICP or with EDX.

8.3.4 *Isolated human OA MSCs*

The hMSC that were used in this thesis were isolated from OA patients that had undergone total hip replacement. All the samples that were used were from female patients (table 3-2) simply because there was higher percentage of female hips that were received. It was noticed that there was a higher prevalence for females to undergo THR from the data that our

department has acquired (figure 0-16). It has been reported that oestrogens related genes are associated with the risk of severe OA of the large joints of the lower limbs (Riancho *et al*. 2010).

In chapter 5, chapter 6 and chapter 7, it was shown that the patient derived hMSC did not behave in the same manner on or inside the matrices sometimes providing inconclusive results. This could be a consequence of the nature of cell isolation. First of all, using the specific isolation protocol not all the cell population have the same purity, so possible contamination from other cell populations could have an influence. In addition, at every isolation a different number of cells will adhere on the tissue culture plastic. This means that the cells from passage 0 to passage 1 have undergone different number of cell population doublings and this can result in discrepancies in the number of cell doublings for the same theoretical passage number. It has been demonstrated that replicative senescence starts from the first passage and it is a continuous process influencing the phenotype and differentiation potential of the cells (Wagner *et al*. 2008).

A way to limit these issues of senescence mentioned above would have been to count and calculate the number of cell doublings that the cells undergone from passage 0. Then, only cells with similar number of doublings could have been used. However, this plan was not feasible taking into consideration the number of samples that were collected, the researchers that need them, the length of time needed to expand the cells and do the experiments.

The results gathered from experiments using patient derived hMSC presented in this thesis demonstrates the complexity of patient variability. Using a variety of hMSC from a number of patients certainly holds greater value that investigations using a clonally expanded cell lines, however may be prohibitive to the discovery of specific cell response mechanisms. *In-vitro* experimentation is far removed from conditions present with *in-vivo* studies but is a useful model for assessing the potential of biomaterials,

8.4 Implications for the treatment of osteoarthritis

A more consistent positive response over multiple donors and hence better cell selection would be required in order to develop cell-material combinations for clinical application. Types of treatment for OA that could be developed from the elements described in this work are the reconstruction of defects that include the subchondral bone region by using a multiphase bioresorbable scaffold. Specifically, this could contain a load bearing

nanocomposite material with graded mechanical properties/porosity coupled with the delivery of autologous cells within a gel to locally stabilise within the load bearing device. These therapies could be combined with an approach to regenerate the cartilage region, such as ACI.

With FDA approval for the use of PLA, fibrin and HAp materials already in place; the hurdle from bench to bedside is only dependent on pre-clinical trials. Work performed by our group with collaborators from the Karolinska Institute Sweden using these 3D printed PLA constructs *in-vivo* has already demonstrated their biocompatibility and osteogenic potential in a mouse calvarial defect model (figure 8-4).

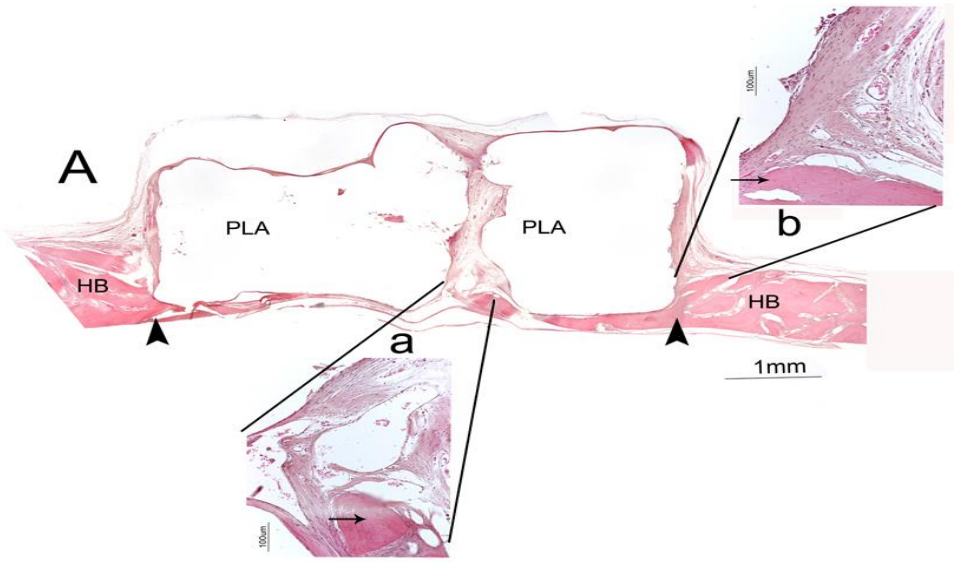

Figure 8-4: "The representative morphology of the calvarial defects treated with PLA discs, 12 weeks after surgery; overview image. (A) HB – host bone; defect margins indicated by arrow heads; Bar = 1 mm; (a) and (b) new bone formation indicated by arrows; Bar = 100 µm. Haematoxylin & Eosin staining." Dr Ion Tcacencu - 24-month review - Restoration FP7 project in Karolinska Institute Sweden.

8.5 Conclusions

8.5.1 *Hydroxyapatite nanoparticle synthesis*

- The controlled low temperature synthesis of nanocrystalline forms of HAp was achieved using a well-regulated sol-gel synthesis methodology.
- HAp can be tailored using reaction pH, titration speed and addition methodology.
    - The important parameters for governing the width and length of HAp using a sol-gel synthesis method were OH^- and Ca^{2+} ion availability respectively.
    - Decreased titration rates yield increased HAp lattice carbonation.
    - Ca/P ratio can be altered through the control of HAp formation, namely by regulation of pH and titration rate.

8.5.2 *Nanocomposites*

- A novel processing route was demonstrated using DMF as a solvent to disperse HAp within PLA matrices, subsequent processing resulted in a near monodispersed nanocomposite material.
- The novel CTAB aided fabrication of nanocomposite surfaces resulted in good nanoscale dispersion, however results in cytotoxic responses from hMSC following >7 days in culture.

8.5.3 *Biological responses to PLA/fibrin/HAp scaffolds*

- hMSC uptake of HAp nanoparticles was observed following 24 hours incubation encapsulated within a fibrin/HAp filled matrix.
- The delivery of cells using fibrin into a PLA 3D printed construct appears to be a useful way to provide implanted materials with a locally situated, stabilised, specific cell type for tissue regeneration.
- Responses gained from donors was too variable to determine any potential influences of the effect of HAp on hMSC behaviour.

References

Adamczyk, Z., 2003. Particle adsorption and deposition: Role of electrostatic interactions. *Advances in Colloid and Interface Science*, 100-102(SUPPL.), pp.267–347.

Ahmed, T.A.E., Dare, E. V & Hincke, M., 2008. Fibrin: A Versatile Scaffold for Tissue Engineering Applications. *Tissue Engineering Part B: Reviews*, 14(2), pp.199–215. Available at: http://www.liebertonline.com/doi/abs/10.1089/ten.teb.2007.0435.

Alberts, B. et al., 2008. *Molecular Biology of the Cell, 5th Edition*,

Alkilany, A.M. et al., 2009. Cellular uptake and cytotoxicity of gold nanorods: molecular origin of cytotoxicity and surface effects. *Small (Weinheim an der Bergstrasse, Germany)*, 5(6), pp.701–8. Available at: http://www.ncbi.nlm.nih.gov/pubmed/19226599 [Accessed June 2, 2014].

Althues, H., Henle, J. & Kaskel, S., 2007. Functional inorganic nanofillers for transparent polymers. *Chemical Society reviews*, 36(9), pp.1454–65. Available at: http://www.ncbi.nlm.nih.gov/pubmed/17660878 [Accessed June 16, 2014].

Asri, R.I.M. et al., 2016. A review of hydroxyapatite-based coating techniques: Sol-gel and electrochemical depositions on biocompatible metals. *Journal of the Mechanical Behavior of Biomedical Materials*, 57, pp.95–108. Available at: http://dx.doi.org/10.1016/j.jmbbm.2015.11.031.

Bagambisa, F.B. & Joos, U., 1990. Preliminary studies on the phenomenological behaviour of osteoblasts cultured on hydroxyapatite ceramics. *Biomaterials*, 11(1), pp.50–56.

Bahney, C.S. et al., 2015a. The Multifaceted Role of the Vasculature in Endochondral Fracture Repair. *Frontiers in Endocrinology*, 6(February), pp.1–10. Available at: http://www.frontiersin.org/Bone_Research/10.3389/fendo.2015.00004/abstract.

Bahney, C.S. et al., 2015b. The Multifaceted Role of the Vasculature in Endochondral Fracture Repair. *Frontiers in Endocrinology*, 6(February), pp.1–10.

Bakan, F., Laçin, O. & Sarac, H., 2013. A novel low temperature sol-gel synthesis process for thermally stable nano crystalline hydroxyapatite. *Powder Technology*, 233, pp.295–302.

Barnett, B.P. et al., 2007. Magnetic resonance-guided, real-time targeted delivery and imaging of magnetocapsules immunoprotecting pancreatic islet cells. *Nature medicine*, 13(8), pp.986–91. Available at: http://www.ncbi.nlm.nih.gov/pubmed/17660829 [Accessed June 11, 2014].

Basu, B., Sabareeswaran, A. & Shenoy, S.J., 2015. Biocompatibility property of 100% strontium-substituted SiO2 -Al2 O3 -P2 O5 -CaO-CaF2 glass ceramics over 26 weeks implantation in rabbit model: Histology and micro-Computed Tomography analysis. *Journal of biomedical materials research. Part B, Applied biomaterials*, 103(6), pp.1168–79. Available at: http://www.scopus.com/inward/record.url?eid=2-s2.0-84937521610&partnerID=tZOtx3y1.

Bensaïd, W. et al., 2003. A biodegradable fibrin scaffold for mesenchymal stem cell transplantation. *Biomaterials*, 24(14), pp.2497–2502. Available at: http://linkinghub.elsevier.com/retrieve/pii/S014296120200618X [Accessed June 11, 2014].

Best, S. et al., 1997. The dependence of osteoblastic response on variations in the chemical

composition and physical properties of hydroxyapatite. *Journal of Materials Science: Materials in Medicine*, 8(2), pp.97–103.

Best, S.M. et al., 2008. Bioceramics: Past, present and for the future. *Journal of the European Ceramic Society*, 28(7), pp.1319–1327. Available at: http://linkinghub.elsevier.com/retrieve/pii/S0955221907005961 [Accessed May 27, 2014].

Bigi, A. et al., 1997. Chemical and structural characterization of the mineral phase from cortical and trabecular bone. *Journal of Inorganic Biochemistry*, 68(1), pp.45–51.

Bigi, A. et al., 1992. The role of magnesium on the structure of biological apatites. *Calcified Tissue International*, 50(5), pp.439–444.

Billiet, T. et al., 2012. A review of trends and limitations in hydrogel-rapid prototyping for tissue engineering. *Biomaterials*, 33(26), pp.6020–6041.

Bin, Y. et al., 2003. Development of Highly Oriented Polyethylene Filled with Aligned Carbon Nanotubes by Gelation / Crystallization from Solutions. *Society*, pp.6213–6219.

Blake, G.M. et al., 1986. Sr-89 therapy: Strontium kinetics in disseminated carcinoma of the prostate. *European Journal of Nuclear Medicine*, 12(9), pp.447–454. Available at: http://dx.doi.org/10.1007/BF00254749.

Blombäck, B. et al., 1994. Fibrin in human plasma: Gel architectures governed by rate and nature of fibrinogen activation. *Thrombosis Research*, 75(5), pp.521–538.

Borchert, H. et al., 2005. Determination of nanocrystal sizes: A comparison of TEM, SAXS, and XRD studies of highly monodisperse CoPt 3 particles. *Langmuir*, 21(5), pp.1931–1936.

Bosco, D.B. et al., 2015. Human Mesenchymal Stem Cells Are Resistant to Paclitaxel by Adopting a Non-Proliferative Fibroblastic State. *Plos One*, 10(6), p.e0128511. Available at: http://dx.plos.org/10.1371/journal.pone.0128511.

Bose, S., Vahabzadeh, S. & Bandyopadhyay, A., 2013. Bone tissue engineering using 3D printing. *Materials Today*, 16(12), pp.496–504. Available at: http://dx.doi.org/10.1016/j.mattod.2013.11.017.

Bouyer, E., Gitzhofer, F. & Boulos, M.I., 2000. Morphological study of hydroxyapatite nanocrystal suspension. *Journal of materials science. Materials in medicine*, 11(8), pp.523–31. Available at: http://www.ncbi.nlm.nih.gov/pubmed/15348004.

Bruder, S.P., Jaiswal, N. & Haynesworth, S.E., 1997. Growth kinetics, self-renewal, and the osteogenic potential of purified human mesenchymal stem cells during extensive subcultivation and following cryopreservation. *Journal of cellular biochemistry*, 64(2), pp.278–94. Available at: http://www.ncbi.nlm.nih.gov/pubmed/9027588.

Buehler, J. et al., 2001. Strontium ranelate inhibits bone resorption while maintaining bone formation in alveolar bone in monkeys (Macaca fascicularis). *Bone*, 29(2), pp.176–179.

Burridge, K. & Chrzanowska-Wodnicka, M., 1996. Focal Adhesions, Contractility, and Signaling. *Annual Review of Cell and Developmental Biology*, 12(1), pp.463–519. Available at: http://www.annualreviews.org/doi/abs/10.1146/annurev.cellbio.12.1.463.

Cai, Y. et al., 2007a. Role of hydroxyapatite nanoparticle size in bone cell proliferation. *Journal of Materials Chemistry*, 17(36), p.3780.

Cai, Y. et al., 2007b. Role of hydroxyapatite nanoparticle size in bone cell proliferation. *Journal*

of Materials Chemistry, 17(36), p.3780. Available at: http://xlink.rsc.org/?DOI=b705129h [Accessed July 20, 2011].

Camarero-Espinosa, S. et al., 2016. Directed cell growth in multi-zonal scaffolds for cartilage tissue engineering. *Biomaterials*, 74, pp.42–52. Available at: http://dx.doi.org/10.1016/j.biomaterials.2015.09.033.

Carlevaro, M.F. et al., 2000. Vascular endothelial growth factor (VEGF) in cartilage neovascularization and chondrocyte differentiation: auto-paracrine role during endochondral bone formation. *Journal of cell science*, 113 (Pt 1, pp.59–69.

Carlisle, E.M., 1970. Silicon: a possible factor in bone calcification. *Science (New York, N.Y.)*, 167(3916), pp.279–80. Available at: http://www.ncbi.nlm.nih.gov/pubmed/5410261.

Catelas, I. et al., 2006. Human Mesenchymal Stem Cell Proliferation and Osteogenic Differentiation in Fibrin Gels in Vitro. *Tissue Engineering*, 12(8).

Caverzasio, J., 2008. Strontium ranelate promotes osteoblastic cell replication through at least two different mechanisms. *Bone*, 42(6), pp.1131–1136.

Chavassieux, P. et al., 1993. Fluoride increases rat osteoblast function and population after in vivo administration but not after in vitro exposure. *Bone*, 14(5), pp.721–725.

Cheang, P. & Khor, K. a., 1996. Addressing processing problems associated with plasma spraying of hydroxyapatite coatings. *Biomaterials*, 17(5), pp.537–544.

Chen, F.M. & Liu, X., 2014. Advancing biomaterials of human origin for tissue engineering. *Progress in Polymer Science*, 53, pp.86–168. Available at: http://dx.doi.org/10.1016/j.progpolymsci.2015.02.004.

Chen, Y. et al., 2013. Mechanical characterization of interfaces in epoxy-clay nanocomposites by molecular simulations. *Polymer (United Kingdom)*, 54(2), pp.766–773.

Clarke, B., 2008. Normal bone anatomy and physiology. *Clinical journal of the American Society of Nephrology : CJASN*, 3 Suppl 3.

Cunniffe, M. et al., 2010. The synthesis and characterization of nanophase hydroxyapatite using a novel dispersant-aided precipitation method. *Microscopy*, pp.1142–1149.

D'Lima, D.D. et al., 1998. Bone response to implant surface morphology. *The journal of arthroplasty*, 13(8), pp.928–934.

Davies, J.E., 2007. Bone bonding at natural and biomaterial surfaces. *Biomaterials*, 28(34), pp.5058–67. Available at: http://www.ncbi.nlm.nih.gov/pubmed/17697711 [Accessed November 29, 2014].

Delgado-López, J. & Rodríguez, I., TWO CRYSTALLIZATION ROUTES TO SYNTHESIZE CARBONATE-APATITE NANOPARTICLES FOR BIOMEDICAL APPLICATIONS. *aidic.it*, 4, pp.2–5. Available at: http://www.aidic.it/isic18/webpapers/246Delgado-Lopez.pdf [Accessed December 4, 2014].

Deng, C. et al., 2007. Choice of dispersants for the nano-apatite filler of polylactide-matrix composite biomaterial. *Current Applied Physics*, 7(6), pp.679–682.

Deng, X., Hao, J. & Wang, C., 2001. Preparation and mechanical properties of nanocomposites of poly(D,L-lactide) with Ca-deficient hydroxyapatite nanocrystals. *Biomaterials*, 22(21), pp.2867–73. Available at: http://www.ncbi.nlm.nih.gov/pubmed/11561892.

Deville, S., Saiz, E. & Tomsia, A.P., 2006. Freeze casting of hydroxyapatite scaffolds for bone

tissue engineering. *Biomaterials*, 27(32), pp.5480–5489.

Dikovsky, D., Bianco-Peled, H. & Seliktar, D., 2006. The effect of structural alterations of PEG-fibrinogen hydrogel scaffolds on 3-D cellular morphology and cellular migration. *Biomaterials*, 27(8), pp.1496–1506.

Dominici, M. et al., 2006. Minimal criteria for defining multipotent mesenchymal stromal cells. The International Society for Cellular Therapy position statement. *Cytotherapy*, 8(4), pp.315–317.

Ducheyne, P. & Qiu, Q., 1999. Bioactive ceramics: the effect of surface reactivity on bone formation and bone cell function. *Biomaterials*, 20(23-24), pp.2287–303. Available at: http://www.ncbi.nlm.nih.gov/pubmed/10614935.

Ducy, P. et al., 1997. Osf2/Cbfa1: a transcriptional activator of osteoblast differentiation. *Cell*, 89(5), pp.747–54. Available at: http://www.ncbi.nlm.nih.gov/pubmed/9182762.

Elliott, J., Wilson, R. & Dowker, S., 2002. Apatite structures. *Advances in X-ray Analysis*, 45(c), pp.172–181. Available at: http://scholar.google.com/scholar?hl=en&btnG=Search&q=intitle:APATITE+STRUCTURES#0 [Accessed December 3, 2014].

Endres, M. & Hutmacher, D., 2003. Osteogenic induction of human bone marrow-derived mesenchymal progenitor cells in novel synthetic polymer-hydrogel matrices. *Tissue engineering*, 9(4), pp.689–701. Available at: http://online.liebertpub.com/doi/abs/10.1089/107632703768247386.

Engler, A.J. et al., 2006. Matrix Elasticity Directs Stem Cell Lineage Specification. *Cell*, 126(4), pp.677–689.

Farley, J.R., Wergedal, J.E. & Baylink, D.J., 1983. Fluoride directly stimulates proliferation and alkaline phosphatase activity of bone-forming cells. *Science (New York, N.Y.)*, 222(4621), pp.330–2. Available at: http://www.ncbi.nlm.nih.gov/pubmed/6623079.

Farley, S.M.G. et al., 1987. Fluoride therapy for osteoporosis: Characterization of the skeletal response by serial measurements of serum alkaline phosphatase activity. *Metabolism*, 36(3), pp.211–218.

Fernández-Tresguerres-Hernández-Gil, I. et al., 2006. Physiological bases of bone regeneration I. Histology and physiology of bone tissue. *Medicina oral, patología oral y cirugía bucal.*, 11(1), pp.47–51.

Fu, S.Y. et al., 2008. Effects of particle size, particle/matrix interface adhesion and particle loading on mechanical properties of particulate-polymer composites. *Composites Part B: Engineering*, 39(6), pp.933–961.

Gerhardt, L.-C. & Boccaccini, A.R., 2010. Bioactive Glass and Glass-Ceramic Scaffolds for Bone Tissue Engineering. *Materials*, 3(7), pp.3867–3910. Available at: http://www.mdpi.com/1996-1944/3/7/3867.

Gericke, a et al., 2005. Importance of phosphorylation for osteopontin regulation of biomineralization. *Calcified tissue international*, 77(1), pp.45–54. Available at: http://www.pubmedcentral.nih.gov/articlerender.fcgi?artid=1451414&tool=pmcentrez&rendertype=abstract [Accessed December 1, 2014].

Gibson, I.R., Best, S.M. & Bonfield, W., 1999. Chemical characterization of silicon-substituted hydroxyapatite. *Journal of biomedical materials research*, 44(4), pp.422–8. Available at:

http://www.ncbi.nlm.nih.gov/pubmed/10397946.

Gilbert, S.F., 2000. Developmental Biology -- NCBI Bookshelf. *Developmental Biology*. Available at: http://www.ncbi.nlm.nih.gov/bookshelf/br.fcgi?book=dbio.

Gilbert, S.F., 2010. *Developmental Biology,* Ninth Edit., Sunderland, MA: SP MAIK Nauka/Interperiodica. Available at: http://dx.doi.org/10.1134/S1062360411050043.

Glantz, S.A. & Slinker, B.K., 1990. *Primer of Applied Regression and Analysis of Variance*, McGraw-Hill.

Granqvist, C.G., 2012. Preparation of thin films and nanostructured coatings for clean tech applications: A primer. *Solar Energy Materials and Solar Cells*, 99, pp.166–172. Available at: http://dx.doi.org/10.1016/j.solmat.2011.11.048.

Gumbiner, B.M., 1996. Cell adhesion: the molecular basis of tissue architecture and morphogenesis. *Cell*, 84(3), pp.345–57. Available at: http://www.ncbi.nlm.nih.gov/pubmed/8608588.

Gupta, M. et al., 2015. Adaptive rheology and ordering of cell cytoskeleton govern matrix rigidity sensing. *Nature communications*, 6(May), p.7525. Available at: http://www.nature.com/ncomms/2015/150625/ncomms8525/full/ncomms8525.html.

Guthold, M. et al., 2007. A comparison of the mechanical and structural properties of fibrin fibers with other protein fibers. *Cell Biochemistry and Biophysics*, 49(3), pp.165–181.

Guzm, C., 2005. Stoichiometric hydroxyapatite obtained by precipitation and sol gel processes. , 51(3), pp.284–293.

Ha, S.-W. et al., 2015. Nano-hydroxyapatite modulates osteoblast lineage commitment by stimulation of DNA methylation and regulation of gene expression. *Biomaterials*, 65, pp.32–42. Available at: http://linkinghub.elsevier.com/retrieve/pii/S0142961215005530.

Hannink, G. & Arts, J.J.C., 2011. Bioresorbability, porosity and mechanical strength of bone substitutes: What is optimal for bone regeneration? *Injury*, 42(SUPPL. 2), pp.S22–S25. Available at: http://dx.doi.org/10.1016/j.injury.2011.06.008.

Hench, L.L., 1991. Bioceramics: From Concept to Clinic. *Journal of the American Ceramic Society*, 74(7), pp.1487–1510. Available at: http://doi.wiley.com/10.1111/j.1151-2916.1991.tb07132.x.

Hong, Z. et al., 2007. Composites of poly(lactide-co-glycolide) and the surface modified carbonated hydroxyapatite nanoparticles. *Journal of Biomedical Materials Research Part A*, 81A(3), pp.515–522. Available at: http://dx.doi.org/10.1002/jbm.a.31038.

Hong, Z. et al., 2004. Grafting polymerization of l-lactide on the surface of hydroxyapatite nano-crystals. *Polymer*, 45(19), pp.6699–6706. Available at: http://linkinghub.elsevier.com/retrieve/pii/S0032386104007086 [Accessed June 16, 2014].

Hu, W.J. et al., 2002. Molecular basis of biomaterial-mediated foreign body reactions (vol 98, pg 1231, 2001). *Blood*, 99(11), p.3908. Available at: <Go to ISI>://000175804700005.

Huang, C. & Ogawa, R., 2010. Mechanotransduction in bone repair and regeneration. *FASEB journal : official publication of the Federation of American Societies for Experimental Biology*, 24(10), pp.3625–32. Available at: http://www.ncbi.nlm.nih.gov/pubmed/20505115 [Accessed June 16, 2014].

Huang, Y. et al., 2012. Micro-/nano- sized hydroxyapatite directs differentiation of rat bone marrow derived mesenchymal stem cells towards an osteoblast lineage. *Nanoscale*, 4(7), pp.2484–90. Available at: http://www.ncbi.nlm.nih.gov/pubmed/22371072.

Hussain, F., 2006. Review article: Polymer-matrix Nanocomposites, Processing, Manufacturing, and Application: An Overview. *Journal of Composite Materials*, 40(17), pp.1511–1575.

Hutmacher, D.W., 2000. Scaffolds in tissue engineering bone and cartilage. *Biomaterials*, 21(24), pp.2529–43. Available at: http://www.ncbi.nlm.nih.gov/pubmed/11071603.

Hutmacher, D.W. et al., 2007. State of the art and future directions of scaffold-based bone engineering from a biomaterials perspective. *Journal of Tissue Engineering and Regenerative Medicine*, 1(4), pp.245–260.

Ito, E. et al., 2009. Potential use of cetrimonium bromide as an apoptosis-promoting anticancer agent for head and neck cancer. *Molecular pharmacology*, 76(5), pp.969–83. Available at: http://molpharm.aspetjournals.org/content/76/5/969.long.

Iyyappan, E. et al., 2016. Role of triton X-100 and hydrothermal treatment on the morphological features of nanoporous hydroxyapatite nanorods. *Materials Science and Engineering: C*, 63, pp.554–562. Available at: http://linkinghub.elsevier.com/retrieve/pii/S0928493116301679.

Jacob, M.M.E. & Arof, a. K., 2000. FTIR studies of DMF plasticized polyvinyledene fluoride based polymer electrolytes. *Electrochimica Acta*, 45, pp.1701–1706.

Jadalannagari, S. et al., 2011. Low temperature synthesis of hydroxyapatite nano-rods by a modified sol-gel technique. *Materials Science and Engineering C*, 31(7), pp.1534–1538. Available at: http://dx.doi.org/10.1016/j.msec.2011.07.001.

Jahromi, M.T., Yao, G. & Cerruti, M., 2013. The importance of amino acid interactions in the crystallization of hydroxyapatite. *Journal of the Royal Society, Interface / the Royal Society*, 10, p.20120906. Available at: http://www.scopus.com/inward/record.url?eid=2-s2.0-84873624761&partnerID=tZOtx3y1.

Jaiswal, N. et al., 1997. Osteogenic differentiation of purified, culture-expanded human mesenchymal stem cells in vitro. *Journal of cellular biochemistry*, 64(2), pp.295–312. Available at: http://www.ncbi.nlm.nih.gov/pubmed/9027589.

Janmey, P. a. & Miller, R.T., 2011. Mechanisms of mechanical signaling in development and disease. *Journal of cell science*, 124(Pt 1), pp.9–18. Available at: http://jcs.biologists.org/cgi/doi/10.1242/jcs.071001.

Jevtic, M., Mitric, M. & Skapin, S., 2008. Crystal structure of hydroxyapatite nanorods synthesized by sonochemical homogeneous precipitation. *Crystal Growth and …*. Available at: http://pubs.acs.org/doi/abs/10.1021/cg7007304 [Accessed December 15, 2014].

Jung, O.L.E. et al., 2014. Osteogenic Differentiation of Mesenchymal Stem Cells in Fibrin-Hydroxyapatite Matrix in a 3-Dimensional Mesh Scaffold. , 482, pp.477–482.

Kalfas, I.H., 2001. Principles of bone healing. *Neurosurgical focus*, 10(4), p.E1.

Kanno, T. et al., 1999. Characteristics of the carbonate ions incorporated into calcium-, partially-strontium-substituted and strontium apatites. *Journal of Materials Science Letters*, 18(16), pp.1343–1345.

Karageorgiou, V. & Kaplan, D., 2005. Porosity of 3D biomaterial scaffolds and osteogenesis. *Biomaterials*, 26(27), pp.5474–91. Available at: http://www.ncbi.nlm.nih.gov/pubmed/15860204 [Accessed May 23, 2014].

Kastl, L. et al., 2013. Multiple internalization pathways of polyelectrolyte multilayer capsules into mammalian cells. *ACS Nano*, 7(8), pp.6605–6618.

Kemp, K. et al., 2010. Chemotherapy-induced mesenchymal stem cell damage in patients with hematological malignancy. *Annals of hematology*, 89(7), pp.701–13. Available at: http://www.ncbi.nlm.nih.gov/pubmed/20119670 [Accessed June 16, 2014].

Kim, H.M., 2003. Ceramic bioactivity and related biomimetic strategy. *Current Opinion in Solid State and Materials Science*, 7(4-5), pp.289–299.

Kim, H.-W., Lee, H.-H. & Knowles, J.C., 2006. Electrospinning biomedical nanocomposite fibers of hydroxyapatite/poly(lactic acid) for bone regeneration. *Journal of Biomedical Materials Research Part A*, 79A(3), pp.643–649. Available at: http://doi.wiley.com/10.1002/jbm.a.30866.

Kishi, S. & Yamaguchi, M., 1994. Inhibitory effect of zinc compounds on osteoclast-like cell formation in mouse marrow cultures. *Biochemical pharmacology*, 48(6), pp.1225–30. Available at: http://www.ncbi.nlm.nih.gov/pubmed/7945416.

Kister, G., Cassanas, G. & Vert, M., 1998. Effects of morphology, conformation and configuration on the IR and Raman spectra of various poly(lactic acid)s. *Polymer*, 39(2), pp.267–273.

Köllmer, M. et al., 2013. Markers Are Shared Between Adipogenic and Osteogenic Differentiated Mesenchymal Stem Cells. *Journal of developmental biology and tissue engineering*, 5(2), pp.18–25. Available at: http://www.pubmedcentral.nih.gov/articlerender.fcgi?artid=3765027&tool=pmcentrez&rendertype=abstract [Accessed June 19, 2015].

Kumar, R. et al., 2004. Temperature driven morphological changes of chemically precipitated hydroxyapatite nanoparticles. *Langmuir*, 20(13), pp.5196–5200.

Kumta, P. et al., 2005. Nanostructured calcium phosphates for biomedical applications: novel synthesis and characterization. *Acta Biomaterialia*, 1, pp.65–83. Available at: http://www.sciencedirect.com/science/article/pii/S1742706104000133 [Accessed December 6, 2014].

Kurosawa, H., 2007. Methods for inducing embryoid body formation: in vitro differentiation system of embryonic stem cells. *Journal of bioscience and bioengineering*, 103(5), pp.389–98. Available at: http://www.ncbi.nlm.nih.gov/pubmed/17609152 [Accessed June 6, 2014].

Lazić, S., 1995. Microcrystalline hydroxyapatite formation from alkaline solutions. *Journal of crystal growth*, 147, pp.147–154. Available at: http://www.sciencedirect.com/science/article/pii/0022024894005877 [Accessed December 5, 2014].

Lee, C.H. et al., 2010. Regeneration of the articular surface of the rabbit synovial joint by cell homing: A proof of concept study. *The Lancet*, 376(9739), pp.440–448. Available at: http://dx.doi.org/10.1016/S0140-6736(10)60668-X.

Lee, J.H. & Shofner, M.L., 2013. Copolymer-mediated synthesis of hydroxyapatite

nanoparticles in an organic solvent. *Langmuir*, 29(34), pp.10940–10944.

LeGeros, R., Lin, S. & Rohanizadeh, R., 2003. Biphasic calcium phosphate bioceramics: preparation, properties and applications. *Journal of materials …*, 4, pp.201–209. Available at: http://link.springer.com/article/10.1023/A:1022872421333 [Accessed December 8, 2014].

Lester, E. et al., 2006. Reaction engineering: The supercritical water hydrothermal synthesis of nano-particles. *The Journal of Supercritical Fluids*, 37(2), pp.209–214. Available at: http://linkinghub.elsevier.com/retrieve/pii/S0896844605001750 [Accessed November 21, 2014].

Li, H., Chen, Y. & Xie, Y., 2003. Photo-crosslinking polymerization to prepare polyanhydride/needle-like hydroxyapatite biodegradable nanocomposite for orthopedic application. *Materials Letters*, 57(19), pp.2848–2854.

Li, H.Y., Chen, Y.F. & Xie, Y.S., 2004. Nanocomposites of cross-linking polyanhydrides and hydroxyapatite needles: Mechanical and degradable properties. *Materials Letters*, 58(22-23), pp.2819–2823.

Link, S., Mohamed, M.B. & El-Sayed, M.A., 1999. Simulation of the Optical Absorption Spectra of Gold Nanorods as a Function of Their Aspect Ratio and the Effect of the Medium Dielectric Constant. *The Journal of Physical Chemistry B*, 103(16), pp.3073–3077. Available at: http://dx.doi.org/10.1021/jp990183f\nhttp://0-pubs.acs.org.jabega.uma.es/doi/pdfplus/10.1021/jp990183f.

Linnes, M.P., Ratner, B.D. & Giachelli, C.M., 2007. A fibrinogen-based precision microporous scaffold for tissue engineering. *Biomaterials*, 28(35), pp.5298–306. Available at: http://www.pubmedcentral.nih.gov/articlerender.fcgi?artid=2140252&tool=pmcentrez&rendertype=abstract [Accessed May 30, 2014].

Liu, D.-M., Troczynski, T. & Tseng, W.J., 2001. Water-based sol–gel synthesis of hydroxyapatite: process development. *Biomaterials*, 22(13), pp.1721–1730. Available at: http://linkinghub.elsevier.com/retrieve/pii/S014296120000332X.

Lovald, S.T. et al., 2009. Mechanical design optimization of bioabsorbable fixation devices for bone fractures. *Journal of Craniofacial Surgery*, 20(2), pp.389–398. Available at: http://www.embase.com/search/results?subaction=viewrecord&from=export&id=L355052202\nhttp://dx.doi.org/10.1097/SCS.0b013e31819b96fb\nhttp://sfx.ub.rug.nl:9003/sfx_local?sid=EMBASE&issn=10492275&id=doi:10.1097%2FSCS.0b013e31819b96fb&atitle=Mechanical+desig.

Luckham, P.F., 2004. Manipulating forces between surfaces: Applications in colloid science and biophysics. *Advances in Colloid and Interface Science*, 111(1-2 SPEC. ISS.), pp.29–47.

Luyten, F.P., 2004. Mesenchymal stem cells in osteoarthritis. *Current opinion in rheumatology*, 16(5), pp.599–603.

Mahmoudi, M. et al., 2011. Effect of nanoparticles on the cell life cycle. *Chemical Reviews*, 111(5), pp.3407–3432.

Mantila Roosa, S.M. et al., 2010. The pore size of polycaprolactone scaffolds has limited influence on bone regeneration in an in vivo model. *Journal of Biomedical Materials Research - Part A*, 92(1), pp.359–368.

Marković, S. et al., 2011. Synthetical bone-like and biological hydroxyapatites : a comparative

study of crystal structure and morphology. , 045005.

Mathieu, L., Bourban, P. & Manson, J., 2006. Processing of homogeneous ceramic/polymer blends for bioresorbable composites. *Composites Science and Technology*, 66(11-12), pp.1606–1614. Available at: http://linkinghub.elsevier.com/retrieve/pii/S0266353805004355 [Accessed June 16, 2014].

Maurin, A.. et al., 2002. Role of polyunsaturated fatty acids in the inhibitory effect of human adipocytes on osteoblastic proliferation. *Bone*, 31(1), pp.260–266. Available at: http://www.sciencedirect.com/science/article/pii/S8756328202008050.

McBeath, R. et al., 2004. Cell shape, cytoskeletal tension, and RhoA regulate stem cell lineage commitment. *Developmental Cell*, 6(4), pp.483–495.

McNamara, L.E. et al., 2014. Investigation of the limits of nanoscale filopodial interactions. *Journal of tissue engineering*, 5(JANUARY), p.2041731414536177. Available at: http://www.pubmedcentral.nih.gov/articlerender.fcgi?artid=4046805&tool=pmcentrez&rendertype=abstract.

Mcnamara, L.E. et al., 2012. Nanotopographical Control of Stem Cell Differentiation. *Tissue Engineering*.

Middleton, J.C. & Tipton, A.J., 2000. Synthetic biodegradable polymers as orthopedic devices. *Biomaterials*, 21(23), pp.2335–2346. Available at: http://www.sciencedirect.com/science/article/pii/S0142961200001010.

Missirlis, D., 2014. The effect of substrate elasticity and actomyosin contractility on different forms of endocytosis. *PLoS ONE*, 9(5).

Monchau, F. et al., 2002. In vitro studies of human and rat osteoclast activity on hydroxyapatite, beta-tricalcium phosphate, calcium carbonate. *Biomol Eng*, 19(2-6), pp.143–152. Available at: http://www.ncbi.nlm.nih.gov/pubmed/12202175\nhttp://ac.els-cdn.com/S1389034402000230/1-s2.0-S1389034402000230-main.pdf?_tid=b42efeca-6fd0-11e4-9b9c-00000aab0f27&acdnat=1416390469_3eaeb9a98ad952d198cac31c43d37fd3.

Monmaturapoj, N., 2008. Nano-size Hydroxyapatite Powders Preparation by Wet-Chemical Precipitation Route Particle sizes and density were analyzed by. , 18(1), pp.15–20.

Montel, G. et al., 1981. New concepts in the composition, crystallization and growth of the mineral component of calcified tissues. *Journal of Crystal Growth*, 53(1), pp.74–99.

Mosesson, M.W., 2005. Fibrinogen and fibrin structure and functions. *Journal of thrombosis and haemostasis : JTH*, 3(8), pp.1894–904. Available at: http://www.ncbi.nlm.nih.gov/pubmed/16102057.

Motskin, M. et al., 2009. Hydroxyapatite nano and microparticles: Correlation of particle properties with cytotoxicity and biostability. *Biomaterials*, 30(19), pp.3307–3317. Available at: http://dx.doi.org/10.1016/j.biomaterials.2009.02.044.

Motskin, M. et al., 2011. The sequestration of hydroxyapatite nanoparticles by human monocyte-macrophages in a compartment that allows free diffusion with the extracellular environment. *Biomaterials*, 32(35), pp.9470–9482. Available at: http://dx.doi.org/10.1016/j.biomaterials.2011.08.060.

Müller, K.H. et al., 2014. The effect of particle agglomeration on the formation of a surface-connected compartment induced by hydroxyapatite nanoparticles in human monocyte-derived macrophages. *Biomaterials*, 35(3), pp.1074–88. Available at: http://www.pubmedcentral.nih.gov/articlerender.fcgi?artid=3843813&tool=pmcentrez&rendertype=abstract [Accessed June 16, 2014].

Munarin, F. et al., 2015. Micro- and nano-hydroxyapatite as active reinforcement for soft biocomposites. *International Journal of Biological Macromolecules*, 72, pp.199–209. Available at: http://dx.doi.org/10.1016/j.ijbiomac.2014.07.050.

Muraglia, a, Cancedda, R. & Quarto, R., 2000. Clonal mesenchymal progenitors from human bone marrow differentiate in vitro according to a hierarchical model. *Journal of cell science*, 113 (Pt 7, pp.1161–1166.

Murphy, C.J. et al., 2008. Gold Nanoparticles in Biology: Beyond Toxicity\rto Cellular Imaging. *Accounts Of Chemical Research*, 41(12).

Nakamura, M. et al., 2007. Interaction of a blood coagulation factor on electrically polarized hydroxyapatite surfaces. *Journal of Biomedical Materials Research - Part B Applied Biomaterials*, 82(1), pp.29–36.

Nampoothiri, M.K., Nair, N.R. & John, R.P., 2010. An overview of the recent developments in polylactide (PLA) research. *Bioresource Technology*, 101(22), pp.8493–8501. Available at: http://dx.doi.org/10.1016/j.biortech.2010.05.092.

Nukavarapu, S.P. & Dorcemus, D.L., 2013. Osteochondral tissue engineering: Current strategies and challenges. *Biotechnology Advances*, 31(5), pp.706–721. Available at: http://dx.doi.org/10.1016/j.biotechadv.2012.11.004.

Olejnik, S., Posner, a. M. & Quirk, J.P., 1971. The i.r. spectra of interlamellar kaolinite-amide complexes-I. The complexes of formamide, N-methylformamide and dimethylformamide. *Clays and Clay Minerals*, 19, pp.83–94.

Osathanon, T. et al., 2008. Microporous nanofibrous fibrin-based scaffolds for bone tissue engineering. *Biomaterials*, 29(30), pp.4091–9. Available at: http://www.pubmedcentral.nih.gov/articlerender.fcgi?artid=2610368&tool=pmcentrez&rendertype=abstract [Accessed June 16, 2014].

Palmer, L.C. et al., 2009. Biomimetic Systems for Hydroxyapatite Mineralization Inspired by Bone and Emalel. *Materials Science*, 108(11), pp.4754–4783.

Park, J.S. et al., 2011. The effect of matrix stiffness on the differentiation of mesenchymal stem cells in response to TGF-β. *Biomaterials*, 32(16), pp.3921–30. Available at: http://www.pubmedcentral.nih.gov/articlerender.fcgi?artid=3073995&tool=pmcentrez&rendertype=abstract [Accessed May 23, 2014].

Park, Y.-S. et al., 2016. Deflection induced cellular focal adhesion and anisotropic growth on vertically aligned silicon nanowires with differing elasticity. *NPG Asia Materials*, 8(3), p.e249. Available at: http://www.nature.com/doifinder/10.1038/am.2016.5.

Patlolla, a, Collins, G. & Arinzeh, T.L., 2010. Solvent-dependent properties of electrospun fibrous composites for bone tissue regeneration. *Acta biomaterialia*, 6(1), pp.90–101. Available at: http://www.ncbi.nlm.nih.gov/pubmed/19631769 [Accessed June 16, 2014].

Peng, S. et al., 2009. Strontium promotes osteogenic differentiation of mesenchymal stem cells through the Ras/MAPK signaling pathway. *Cellular physiology and biochemistry :*

international journal of experimental cellular physiology, biochemistry, and pharmacology, 23(1-3), pp.165–74. Available at: http://www.ncbi.nlm.nih.gov/pubmed/19255511.

Perez, R.A. & Mestres, G., 2016. Role of pore size and morphology in musculo-skeletal tissue regeneration. *Materials Science and Engineering C*, 61, pp.922–939.

Phinney, D.G., 2012. Functional heterogeneity of mesenchymal stem cells: Implications for cell therapy. *Journal of Cellular Biochemistry*, 113(9), pp.2806–2812.

Pirraco, R.P., Marques, a P. & Reis, R.L., 2010. Cell interactions in bone tissue engineering. *Journal of cellular and molecular medicine*, 14(1-2), pp.93–102. Available at: http://www.ncbi.nlm.nih.gov/pubmed/20050963 [Accessed June 16, 2014].

Qiu, Y. et al., 2010. Surface chemistry and aspect ratio mediated cellular uptake of Au nanorods. *Biomaterials*, 31(30), pp.7606–7619. Available at: http://dx.doi.org/10.1016/j.biomaterials.2010.06.051.

Ramesh, S. et al., 2015. Characteristics and properties of hydoxyapatite derived by sol-gel and wet chemical precipitation methods. *Ceramics International*, 41(9), pp.10434–10441. Available at: http://dx.doi.org/10.1016/j.ceramint.2015.04.105.

Rao, R.R. et al., 2014. Effects of hydroxyapatite on endothelial network formation in collagen/fibrin composite hydrogels in vitro and in vivo. *Acta Biomaterialia*, 10(7), pp.3091–3097. Available at: http://dx.doi.org/10.1016/j.actbio.2014.03.010.

Ratnayake, J.T.B., Mucalo, M. & Dias, G.J., 2016. Substituted hydroxyapatites for bone regeneration: A review of current trends. *Journal of Biomedical Materials Research Part B: Applied Biomaterials*, p.n/a–n/a. Available at: http://doi.wiley.com/10.1002/jbm.b.33651.

Redey, S.A. et al., 1999. Osteoclast adhesion and activity on synthetic hydroxyapatite, carbonated hydroxyapatite, and natural calcium carbonate: Relationship to surface energies. *Journal of Biomedical Materials Research*, 45(2), pp.140–147.

Reffitt, D.M. et al., 2003. Orthosilicic acid stimulates collagen type 1 synthesis and osteoblastic differentiation in human osteoblast-like cells in vitro. *Bone*, 32(2), pp.127–135.

Rehman, I. & Bonfield, W., 1997. Characterization of hydroxyapatite and carbonated apatite by photo acoustic FTIR spectroscopy. *Journal of Materials Science: Materials in …*, 8, pp.1–4. Available at: http://link.springer.com/article/10.1023/A:1018570213546 [Accessed December 3, 2014].

Riancho, J.A. et al., 2010. Common Variations In Estrogen-Related Genes Are Associated With Severe Large Joint Osteoarthritis: A Multicenter Genetic And Functional Study. *Osteoarthritis Cartilage*. Available at: http://www.ncbi.nlm.nih.gov/entrez/query.fcgi?cmd=Retrieve&db=PubMed&dopt=Citation&list_uids=20417295.

Richardson, J., 2015. BOA 2015. In *Clinical Trials for Cartilage Repair*.

Riss, T.L. et al., 2013. Cell Viability Assays. *Eli Lilly & Company and the National Center for Advancing Translational Sciences*. Available at: http://www.ncbi.nlm.nih.gov/books/NBK144065/.

Rogers, C.M. et al., 2014. A novel technique for the production of electrospun scaffolds with tailored three-dimensional micro-patterns employing additive manufacturing.

Biofabrication, 6(3), p.35003. Available at: http://stacks.iop.org/1758-5090/6/i=3/a=035003?key=crossref.0fc7f67e1beeae9eb87b2d9a8da2f4c6\nfile:///Users/Nakazawa-lab/Documents/Papers-shere/Articles/2014/Rogers/Biofabrication 2014 Rogers.pdf\npapers2://publication/doi/10.1088/1758-5082/6/3/035003\nht.

Roohani-Esfahani, S.I. et al., 2010. The influence hydroxyapatite nanoparticle shape and size on the properties of biphasic calcium phosphate scaffolds coated with hydroxyapatite-PCL composites. *Biomaterials*, 31(21), pp.5498–5509. Available at: http://dx.doi.org/10.1016/j.biomaterials.2010.03.058.

Royer, A. et al., 1993. Stoichiometry of hydroxyapatite: influence on the flexural strength. *Journal of Materials Science: Materials in Medicine*, 4(1), pp.76–82. Available at: http://dx.doi.org/10.1007/BF00122982.

Rozenberg, B.A. & Tenne, R., 2008. Polymer-assisted fabrication of nanoparticles and nanocomposites. *Progress in Polymer Science (Oxford)*, 33(1), pp.40–112.

Rusu, V.M. et al., 2005. Size-controlled hydroxyapatite nanoparticles as self-organized organic-inorganic composite materials. *Biomaterials*, 26(26), pp.5414–26. Available at: http://www.ncbi.nlm.nih.gov/pubmed/15814140 [Accessed June 21, 2011].

Safadi, B., Andrews, R. & Grulke, E.A., 2002. Multiwalled carbon nanotube polymer composites: Synthesis and characterization of thin films. *Journal of Applied Polymer Science*, 84(14), pp.2660–2669.

Salimi, M.N. et al., 2012. Effect of processing conditions on the formation of hydroxyapatite nanoparticles. *Powder Technology*, 218, pp.109–118. Available at: http://linkinghub.elsevier.com/retrieve/pii/S003259101100670X [Accessed June 10, 2014].

Sanosh, K.P. et al., 2009. Preparation and characterization of nano-hydroxyapatite powder using sol-gel technique. *Bulletin of Materials Science*, 32(5), pp.465–470.

Sarugaser, R. et al., 2009. Human mesenchymal stem cells self-renew and differentiate according to a deterministic hierarchy. *PloS one*, 4(8), p.e6498. Available at: http://www.pubmedcentral.nih.gov/articlerender.fcgi?artid=2714967&tool=pmcentrez&rendertype=abstract [Accessed June 3, 2014].

Savioli Lopes, M., Jardini, a. L. & Maciel Filho, R., 2012. Poly (lactic acid) production for tissue engineering applications. *Procedia Engineering*, 42(August), pp.1402–1413.

Schantz, J.T. et al., 2005. Osteogenic differentiation of mesenchymal progenitor cells in computer designed fibrin-polymer-ceramic scaffolds manufactured by fused deposition modeling. *Journal of Materials Science: Materials in Medicine*, 16(9), pp.807–819.

Semino, C., 2008. Self-assembling peptides: from bio-inspired materials to bone regeneration. *Journal of dental research*, pp.606–616. Available at: http://jdr.sagepub.com/content/87/7/606.short [Accessed January 15, 2015].

Shao, X. et al., 2006. Repair of Large Articular Osteochondral Defects Using Hybrid Scaffolds and Bone Marrow-Derived Mesenchymal Stem Cells in a Rabbit Model. *Tissue Engineering*, 12(6), pp.1539–1551. Available at: http://www.liebertonline.com/doi/abs/10.1089/ten.2006.12.1539.

Shepherd, J.H., Shepherd, D. V & Best, S.M., 2012. Substituted hydroxyapatites for bone repair. *Journal of materials science. Materials in medicine*, 23(10), pp.2335–47. Available

at: http://www.ncbi.nlm.nih.gov/pubmed/22389101 [Accessed June 13, 2014].

Shi, Z. et al., 2009. Size effect of hydroxyapatite nanoparticles on proliferation and apoptosis of osteoblast-like cells. *Acta Biomaterialia*, 5(1), pp.338–345. Available at: http://dx.doi.org/10.1016/j.actbio.2008.07.023.

Sicchieri, L.G. et al., 2012. Pore size regulates cell and tissue interactions with PLGA-CaP scaffolds used for bone engineering. *Journal of Tissue Engineering and Regenerative Medicine*, 6(2), pp.155–162.

Singer, V.L. et al., 1997. Characterization of PicoGreen reagent and development of a fluorescence-based solution assay for double-stranded DNA quantitation. *Analytical biochemistry*, 249(2), pp.228–38. Available at: http://www.ncbi.nlm.nih.gov/pubmed/9212875.

Sinha Ray, S. & Okamoto, M., 2003. Polymer/layered silicate nanocomposites: A review from preparation to processing. *Progress in Polymer Science (Oxford)*, 28(11), pp.1539–1641.

Ślósarczyk, A., Paszkiewicz, Z. & Paluszkiewicz, C., 2005. FTIR and XRD evaluation of carbonated hydroxyapatite powders synthesized by wet methods. *Journal of Molecular Structure*, 744-747, pp.657–661. Available at: http://linkinghub.elsevier.com/retrieve/pii/S0022286004009706 [Accessed December 3, 2014].

Sodek, J., Ganss, B. & McKee, M.D., 2000. Osteopontin. *Critical Reviews in Oral Biology & Medicine*, 11(3), pp.279–303.

Soenen, S.J. et al., 2011. Cellular toxicity of inorganic nanoparticles: Common aspects and guidelines for improved nanotoxicity evaluation. *Nano Today*, 6(5), pp.446–465.

Stankovich, S. et al., 2006. Graphene-based composite materials. *Nature*, 442(7100), pp.282–286.

Street, J. et al., 2002. Vascular endothelial growth factor stimulates bone repair by promoting angiogenesis and bone turnover. *Proceedings of the National Academy of Sciences of the United States of America*, 99(15), pp.9656–9661.

Šupová, M., 2009. Problem of hydroxyapatite dispersion in polymer matrices: a review. *Journal of Materials Science: Materials in Medicine*, 20(6), pp.1201–1213.

Tai, H. et al., 2007. Control of pore size and structure of tissue engineering scaffolds produced by supercritical fluid processing. *European cells & materials*, 14, pp.64–77. Available at: http://www.ncbi.nlm.nih.gov/pubmed/18085505.

Tanaka, H. et al., 1999. TPD, FTIR, and Molecular Adsorption Studies of Calcium Hydroxyapatite Surface Modified with Hexanoic and Decanoic Acids. *Journal of colloid and interface science*, 214, pp.31–37. Available at: http://www.ncbi.nlm.nih.gov/pubmed/10328893.

Tang, D. et al., 2016. Biofabrication of bone tissue: Approaches, challenges and translation for bone regeneration. *Biomaterials*, 83, pp.363–382. Available at: http://linkinghub.elsevier.com/retrieve/pii/S0142961216000260.

Thevenot, P. et al., 2008. Method to Analyze Three-Dimensional Cell Distribution and Infiltration in Degradable Scaffolds. *Tissue Engineering Part C: Methods*, 14(4), pp.319–331. Available at: http://www.pubmedcentral.nih.gov/articlerender.fcgi?artid=2913783&tool=pmcentrez

&rendertype=abstract.

Thomson, K.S. et al., 2013. Prevascularized microtemplated fibrin scaffolds for cardiac tissue engineering applications. *Tissue engineering. Part A*, 19(7-8), pp.967–77. Available at: http://www.pubmedcentral.nih.gov/articlerender.fcgi?artid=3589898&tool=pmcentrez&rendertype=abstract [Accessed June 16, 2014].

Tjong, S.C., 2006. Structural and mechanical properties of polymer nanocomposites. *Materials Science and Engineering: R: Reports*, 53(3-4), pp.73–197. Available at: http://linkinghub.elsevier.com/retrieve/pii/S0927796X06000544 [Accessed May 29, 2014].

Tsuchiya, K. et al., 2001. Effects of cell adhesion molecules on adhesion of chondrocytes, ligament cells and mesenchymal stem cells. *Materials Science and Engineering C*, 17(1-2), pp.79–82.

Tuin, S.A., Pourdeyhimi, B. & Loboa, E.G., 2013. Creating tissues from textiles : scalable nonwoven manufacturing techniques for fabrication of tissue engineering scaffolds. *Biomedical Materials*, 015017(11), p.15017. Available at: http://dx.doi.org/10.1088/1748-6041/11/1/015017.

Ugarte, J., Sena, L. & Pérez, C., 2005. Influence of processing parameters on structural characteristics of porous calcium phosphate samples: A study using an experimental design method. *Materials …*, pp.0–5. Available at: http://www.scielo.br/scielo.php?pid=S1516-14392005000100013&script=sci_arttext [Accessed December 3, 2014].

Underwood, S. & Mulvaney, P., 1994. Effect of the Solution Refractive Index on the Color of Gold Colloids. *Langmuir*, 10(3), pp.3427–3430.

Uskoković, V., Li, W. & Habelitz, S., 2011. Amelogenin as a promoter of nucleation and crystal growth of apatite. *Journal of Crystal Growth*, 316(1), pp.106–117. Available at: http://linkinghub.elsevier.com/retrieve/pii/S0022024810011516 [Accessed June 16, 2014].

Utara, S. & Klinkaewnarong, J., 2015. Effect of sonication time on the characteristics of nanophase hydroxyapatite crystals synthesised by the sol–gel technique. *Micro & Nano Letters*, 10(1), pp.1–4. Available at: http://digital-library.theiet.org/content/journals/10.1049/mnl.2014.0316.

Vázquez-Hernández, F. et al., 2010. Synthesis and characterization of hydroxyapatite nanoparticles and their application in protein adsorption. *Materials Science and Engineering B*, 174(1-3), pp.290–295.

Vieira, D. & Carmona-Ribeiro, A.M., 2006. Cationic lipids and surfactants as antifungal agents: Mode of action. *Journal of Antimicrobial Chemotherapy*, 58(4), pp.760–767.

Vitacolonna, M. et al., 2015. Effect of dynamic seeding methods on the distribution of fibroblasts within human acellular dermis. *Cell and Tissue Banking*, 16(4), pp.605–614.

Vitale-Brovarone, C., Baino, F. & Verné, E., 2010. Feasibility and tailoring of bioactive glass-ceramic scaffolds with gradient of porosity for bone grafting. *Journal of biomaterials applications*, 24(8), pp.693–712.

Wagner, W. et al., 2008. Replicative senescence of mesenchymal stem cells: A continuous and organized process. *PLoS ONE*, 3(5).

Wang, A. et al., 2007. Size-controlled synthesis of hydroxyapatite nanorods by chemical precipitation in the presence of organic modifiers. *Materials Science and Engineering C*, 27(4), pp.865–869.

Wang, P. et al., 2010. Effects of synthesis conditions on the morphology of hydroxyapatite nanoparticles produced by wet chemical process. *Powder Technology*, 203(2), pp.315–321. Available at: http://dx.doi.org/10.1016/j.powtec.2010.05.023.

Wang, Y. et al., 2006. Hydrothermal synthesis of hydroxyapatite nanopowders using cationic surfactant as a template. , 60, pp.1484 – 1487.

Webster, T.J. et al., 2000. Enhanced functions of osteoblasts on nanophase ceramics. *Cell Proliferation*, 21, pp.1803–1810.

Webster, T.J. et al., 2001. Enhanced osteoclast-like cell functions on nanophase ceramics. *Biomaterials*, 22(11), pp.1327–1333.

Webster, T.J. et al., 2004. Osteoblast response to hydroxyapatite doped with divalent and trivalent cations. *Biomaterials*, 25(11), pp.2111–2121.

White, L.J. et al., 2012. The effect of processing variables on morphological and mechanical properties of supercritical CO2 foamed scaffolds for tissue engineering. *Acta biomaterialia*, 8(1), pp.61–71. Available at: http://www.ncbi.nlm.nih.gov/pubmed/21855663 [Accessed June 5, 2014].

Wilhelm, C. et al., 2003. Intracellular uptake of anionic superparamagnetic nanoparticles as a function of their surface coating. *Biomaterials*, 24(6), pp.1001–1011.

Wu, J. et al., 2014. Oxygen transport and stem cell aggregation in stirred-suspension bioreactor cultures. *PloS one*, 9(7), p.e102486. Available at: http://www.pubmedcentral.nih.gov/articlerender.fcgi?artid=4102498&tool=pmcentrez&rendertype=abstract [Accessed May 22, 2015].

Xiao, Z.S. et al., 1998. Genomic structure and isoform expression of the mouse, rat and human Cbfa1/Osf2 transcription factor. *Gene*, 214(1-2), pp.187–197.

Yamada, Y. et al., 2003. Bone regeneration following injection of mesenchymal stem cells and fibrin glue with a biodegradable scaffold. *Journal of Cranio-Maxillofacial Surgery*, 31(1), pp.27–33. Available at: http://linkinghub.elsevier.com/retrieve/pii/S1010518202001439 [Accessed June 16, 2014].

Yang, D.-C. et al., 2011. Hypoxia inhibits osteogenesis in human mesenchymal stem cells through direct regulation of RUNX2 by TWIST. *PloS one*, 6(9), p.e23965. Available at: http://www.pubmedcentral.nih.gov/articlerender.fcgi?artid=3170288&tool=pmcentrez&rendertype=abstract [Accessed June 10, 2014].

Yeung, T. et al., 2005. Effects of substrate stiffness on cell morphology, cytoskeletal structure, and adhesion. *Cell Motility and the Cytoskeleton*, 60(1), pp.24–34.

Yoshida, Y. et al., 2000. Evidence of Chemical Bonding at Biomaterial-Hard Tissue Interfaces. *Journal of Dental Research*, 79(2), pp.709–714. Available at: http://jdr.sagepub.com/cgi/doi/10.1177/00220345000790020301 [Accessed November 29, 2014].

Yubao, L. et al., 1994. Morphology and composition of nanograde calcium phosphate needle-like crystals formed by simple hydrothermal treatment. *Journal of Materials Science: Materials in Medicine*, 5(6-7), pp.326–331. Available at:

http://www.springerlink.com/index/10.1007/BF00058956.

Zhang, C. et al., 2009. Hydroxyapatite Nano- and Microcrystals with Multiform Morphologies: Controllable Synthesis and Luminescence Properties. *Crystal Growth & Design*, 9(6), pp.2725–2733. Available at: http://pubs.acs.org/doi/abs/10.1021/cg801353n.

Zhang, X. & Lu, Y., 2014. Centrifugal Spinning: An Alternative Approach to Fabricate Nanofibers at High Speed and Low Cost. *Polymer Reviews*, 54(4), pp.677–701. Available at: http://www.tandfonline.com/doi/abs/10.1080/15583724.2014.935858.

Zhou, H. & Lee, J., 2011. Nanoscale hydroxyapatite particles for bone tissue engineering. *Acta biomaterialia*, 7(7), pp.2769–81. Available at: http://www.ncbi.nlm.nih.gov/pubmed/21440094 [Accessed June 17, 2011].

Appendix

8.6 Chapter 3

8.6.1 *Differential Scanning Calorimetry*

Differential scanning calorimetry (DSC) is a technique used to determine the thermal transition states of a material. Glass transition temperature and melting point of polymer composite materials can provide information into the changes between chemical bond strength within a material.

A Mettler Toledo DSC823 (Mettler-Toledo international inc., Greifensee, Switzerland) was used to analyse the thermal properties of PLA and PLA nanocomposites. Sample/reference aluminium crucibles and sample were weighed using a Mettler Toledo AJ100 analytical balance and loaded in to the sample chamber. The thermal cycle of the DSC comprised of two 10°C/min ramp cycles from 25°C – 200°C with 5-minute equilibrium plateaus (figure 0-1).

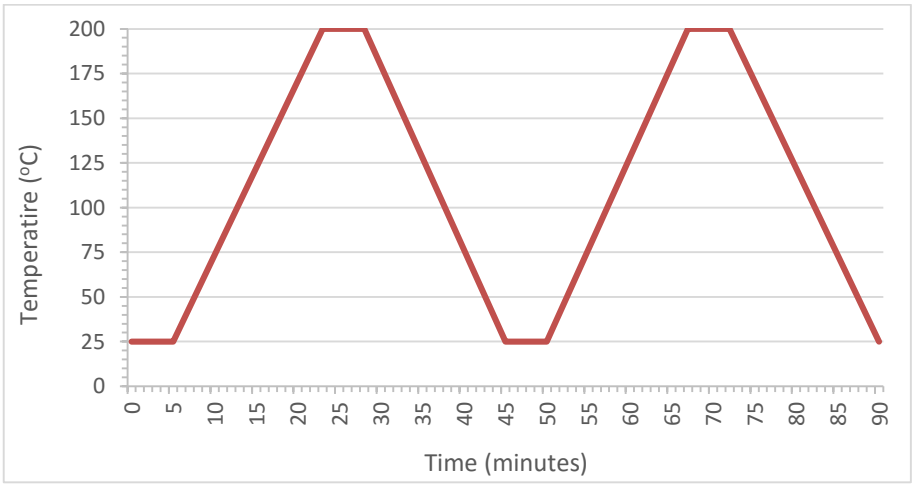

Figure 0-1: DSC melt and re-melt temperature program.

8.6.2 *Flow Cytometry*

The flow cytometry methodology uses lasers to simultaneously measure distinct fluorescent and morphological parameters of particles in a hydrodynamically focused stream of liquid. Development of multicolour systems has enriched the quantity of data provided at the cellular level. Cell surface marker expression can be characterised using this technique when combined with immunocytochemistry to target specific protein antigens using fluorescently conjugated antibodies. This method requires stringent control parameters to reproducibly distinguish between positive and negative results. Below outlines the antibodies/isotypes used for the characterisation of hMSC (Dominici *et al.* 2006) populations. Isotypes are required to ensure the absence of false positive detection.

Fluorochr-ome	Absorption/Emission wavelength nm	Isotype	Ag/control	Protein conc. (µg/mL)	Clone	Supplier	Catalogue number
PE (+)	488-585	mIgG1	CD73	12.5	AD2	BD	550257
			control	50	MOPC-21	BD	555749
APC (+)	635-660	mIgG1	CD105	100	266	BD	562408
			control	12.5	MOPC-21	BD	555751
FITC (-)	488-530	mIgG1	CD34	12.5	581/CD34	BD	555821
			CD45	50	2D1	BD	345808
			CD19	25	4G7	BD	345776
			control	50	MOPC-21	BD	555748
		mIgG2b	CD14	25	MϕP9	BD	345784
			control	50	27-35	BD	555742
PerCPCy5.5 (+)	488-670	mIgG1	CD90	50	5E10	BD	561557
			control	12.5	MOPC-21	BD	552834
APC-H7 (-)	635-750	mIgG2a	HLA-DR	50	L243	BD	641411
			control	200	G155-178	BD	560897

Table 0-1: List of antibodies used for flow cytometry characterisation of hMSC surface antigens.

A FACSCanto II (Becton Dickinson Biosciences, Oxford, UK) instrument was used to analyse cell surface markers. Compensation for various fluorochromes was achieved using a mixture of positively and negatively charged Compbeads® (table 0-2). The compensation was determined by manually setting median fluorescence channel of labelled and unlabelled beads for each fluorochrome.

Tube	Beads	Antibody	Volume
1 – Unstained	-ve	-	4 µl
2 – APC	-ve/+ve	APC-CD105	4 µl
3 – PerCP Cy5.5	-ve/+ve	PerCP Cy5.5 – CD90	4 µl
4 – FITC	-ve/+ve	FITC – CD45	4 µl
6 – APC-H7	-ve/+ve	APC-H7-HLA-DR	4 µl

Table 0-2: List of FACS tubes and components for compensation analysis.

Cells were cultured to confluence in a 75cm^2 flask. Upon confluence cells were raised from tissue culture plastic substrate using 0.05% trypsin-EDTA (Life-Technologies, UK) centrifuged at 200g and washed in 0.2 µm filtered FACS buffer containing 0.5% BSA w/v and 2mM EDTA in PBS. Cells separated into 3 FACS tubes and centrifuged at 200g. These pellets were suspended in 50µl FACS buffer incubated with various quantities (table 0-3) of antibodies/isotypes for 15 minutes in the dark at 4^{o}C.

Tube	Antibody/Isotype/DAPI	Volume
1 – Unstained	DAPI	50 µl
2 – Isotype	PE-mIgG1	1 µl
	APC-mIgG1	16 µl
	FITC-mIgG1	4 µl
	FITC-mIgG2b	2 µl
	PerCP Cy5.5-mIgG1	8 µl
	APC-H7-mIgG2a	1 µl
	DAPI	50 µl
3 – Test	PE – CD73	4 µl
	APC – CD105	2 µl
	FITC – CD14	4 µl
	FITC – CD19	4 µl
	FITC – CD34	4 µl
	FITC – CD45	4 µl
	PerCP Cy5.5 – CD90	2 µl
	APC-H7 – HLA-DR	4 µl
	DAPI	50 µl

Table 0-3: List of FACS tubes and components for testing hMSC surface marker expression.

Dead cells were excluded from analysis through using a double-strand nucleic acid intercalant DAPI (PARTC – Phywe Systeme GmbH, Göttingen, Germany). 5,000 to 10,000 events were acquired per test. The figures presented in this thesis show a representative experiment of three to four repeated experiments.

8.6.3 *Calibration curves*

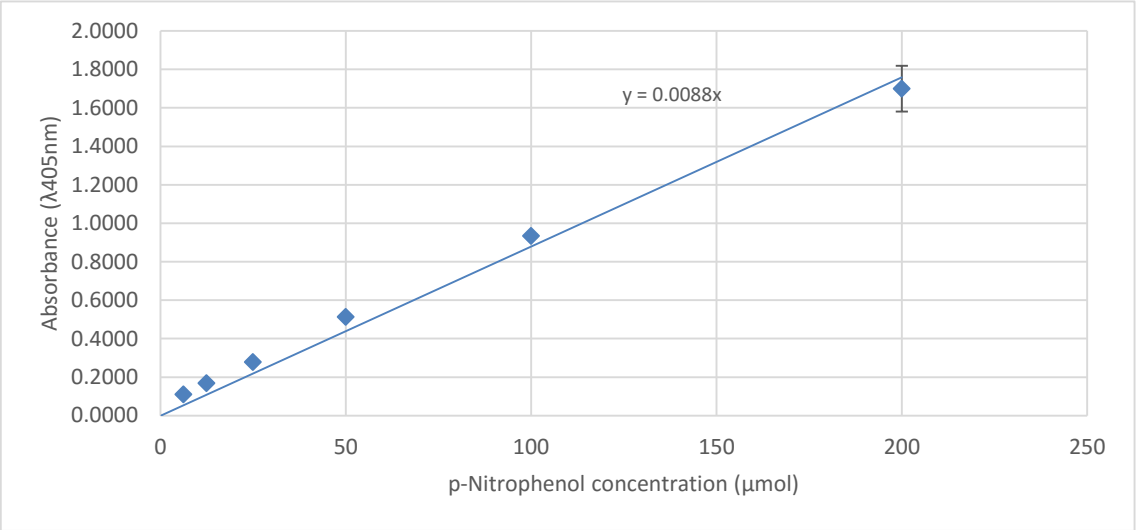

Figure 0-2: p-nitrophenol absorbance calibration curve at λ 405nm.

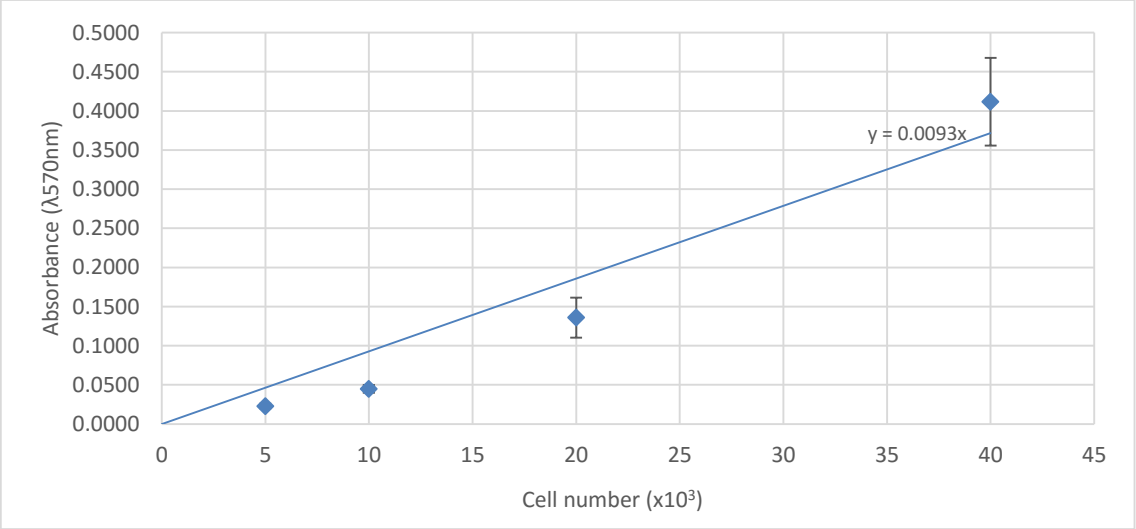

Figure 0-3: MTT assay formazan absorbance calibration curve at λ 570nm.

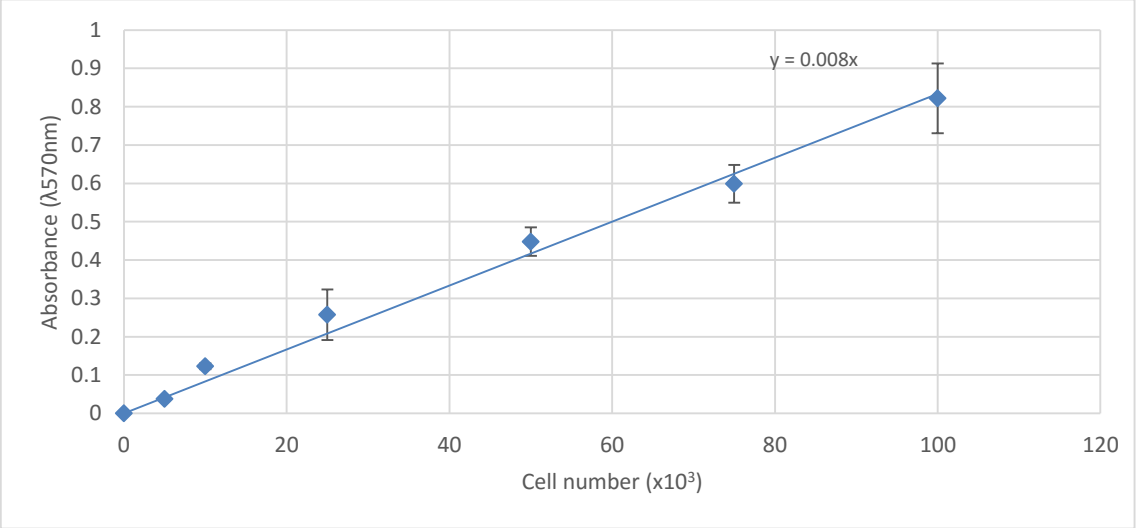

Figure 0-4: Crystal violet absorbance calibration curve at λ 570nm.

8.6.4 *Tri-lineage differentiation*

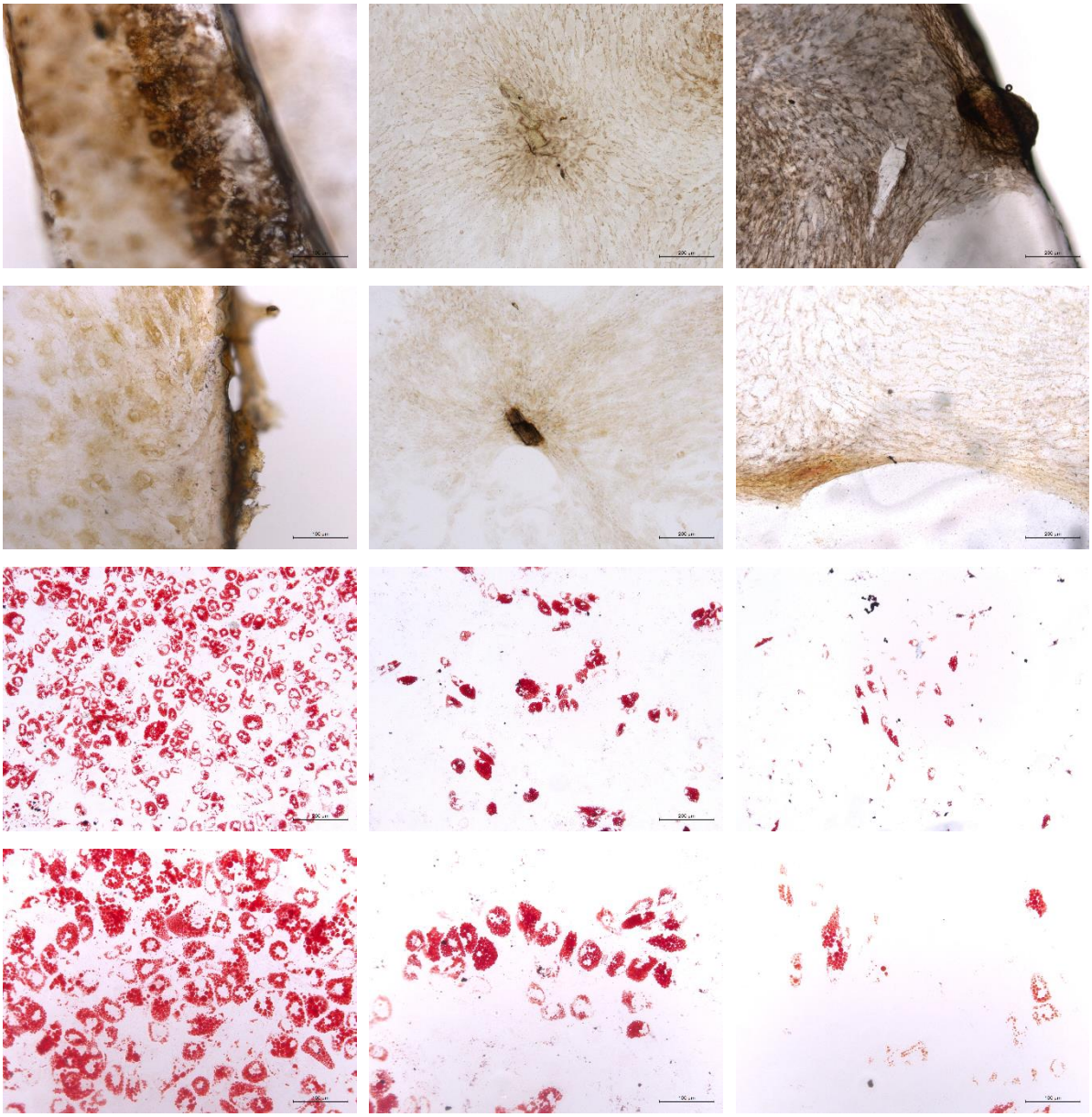

Sectioning/staining req	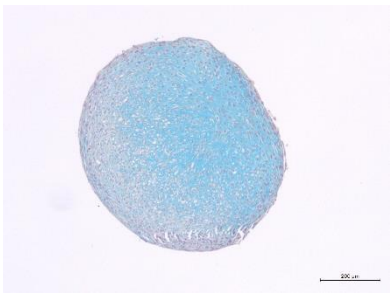	Sectioning/staining req
Sectioning/staining req	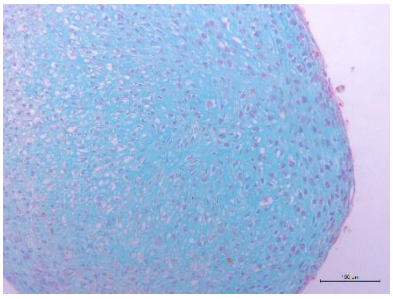	Sectioning/staining req

Figure 0-5: Trilineage differentiation of human mesenchymal stem cells A) 3503 P4, B) 3502 P4 and C) 3505 P4. A-C = 10x, A_1-C_1 = 20x magnification.

8.7 Chapter 4

8.7.1 *FWHM measurement from XRD spectra*

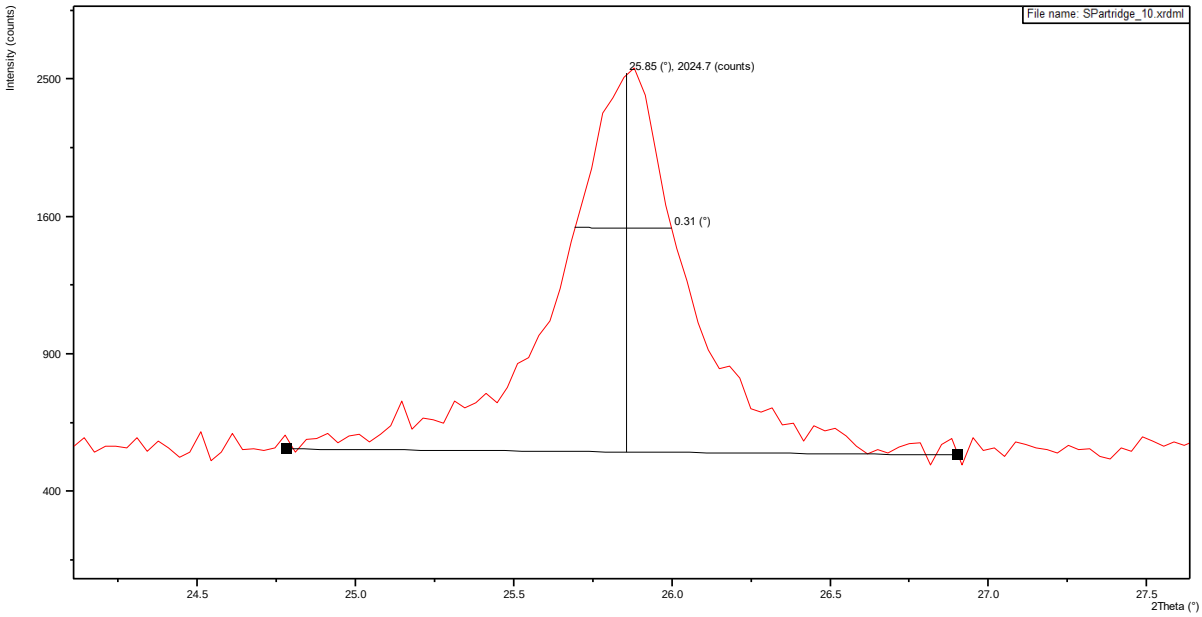

Figure 0-6: Representative measurement of the FWHM diffraction peak at position [002] on XRD HAp spectra.

Titration type	Crystal size (002)	SEM
Ca → P	45.420	1.459
P → Ca	54.390	7.851
Ca + P	70.040	8.116
	Crystal size (110)	SEM
Ca → P	16.340	1.176
P → Ca	28.374	0.330
Ca + P	25.942	0.483
	Crystal size (002)	
0.1 mL/min	45.420	1.459
1.0 mL/min	88.390	6.806
10 mL/min	70.390	11.201
	Crystal size (110)	
0.1 mL/min	16.340	1.176
1.0 mL/min	26.687	1.610
10 mL/min	26.253	0.770
	Crystal size (002)	
pH 10	45.42	1.46
pH 9	64.97	10.57
pH 8	66.04	7.77
	Crystal size (110)	
pH 10	16.34	1.18
pH 9	24.41	1.86
pH 8	34.05	5.33
	Crystal size (002)	
pH 10, 0.1 mL/min	45.420	1.459
pH 8, 0.1 mL/min	66.040	7.767
pH 10, 1.0 mL/min	88.390	6.806
pH 8, 1.0 mL/min	88.390	6.797
	Crystal size (110)	
pH 10, 0.1 mL/min	16.340	1.176
pH 8, 0.1 mL/min	34.047	5.330
pH 10, 1.0 mL/min	26.687	1.610
pH 8, 1.0 mL/min	28.068	0.640

Figure 0-***7: Numerical data from XRD HAp crystal measurements***

8.8 Chapter 5

8.8.1 *DSC*

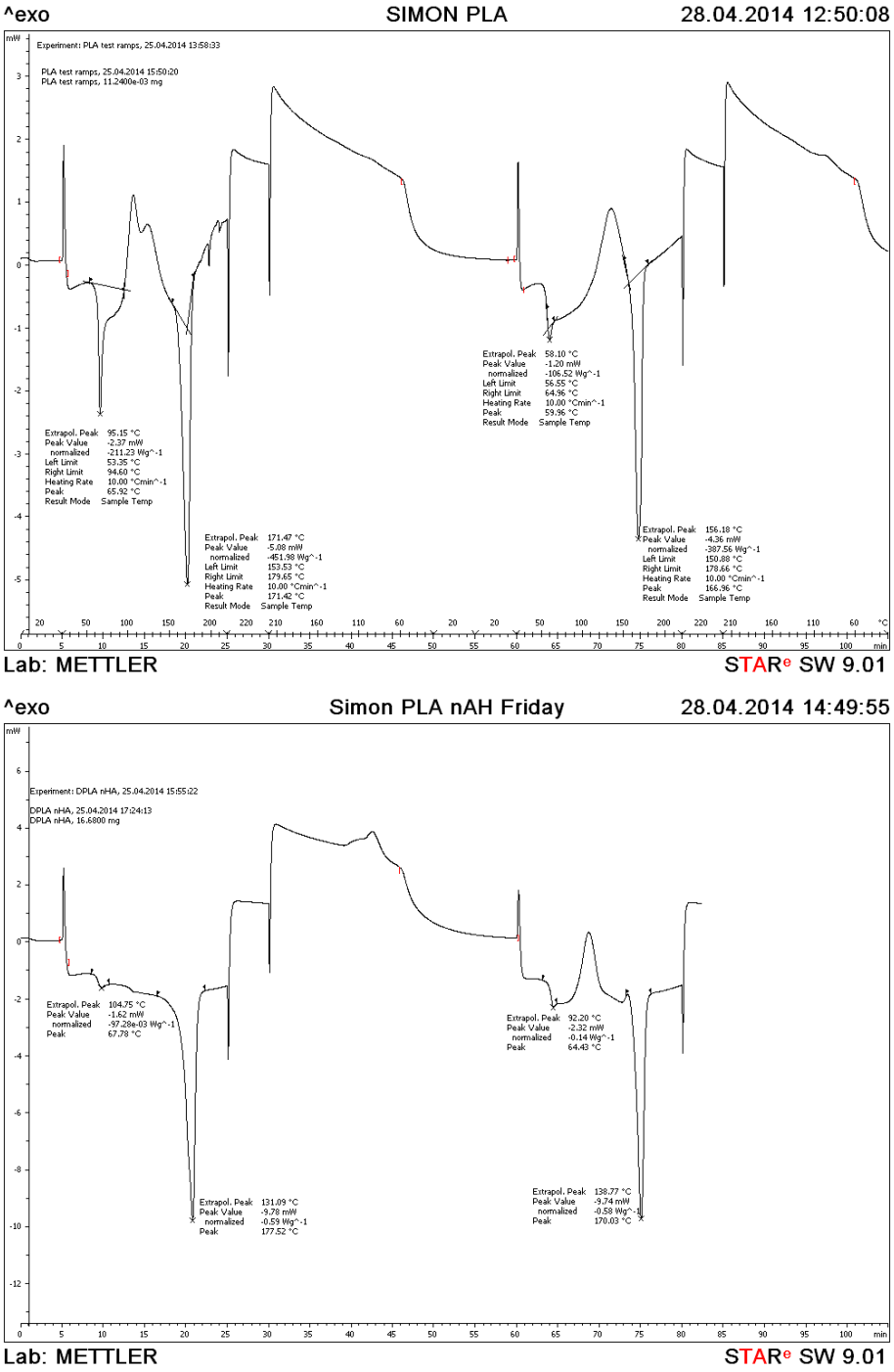

Figure 0-8: DSC graphs from DMF processed PLA and PLA/HAp 10% wt/v samples.

8.9 Chapter 7

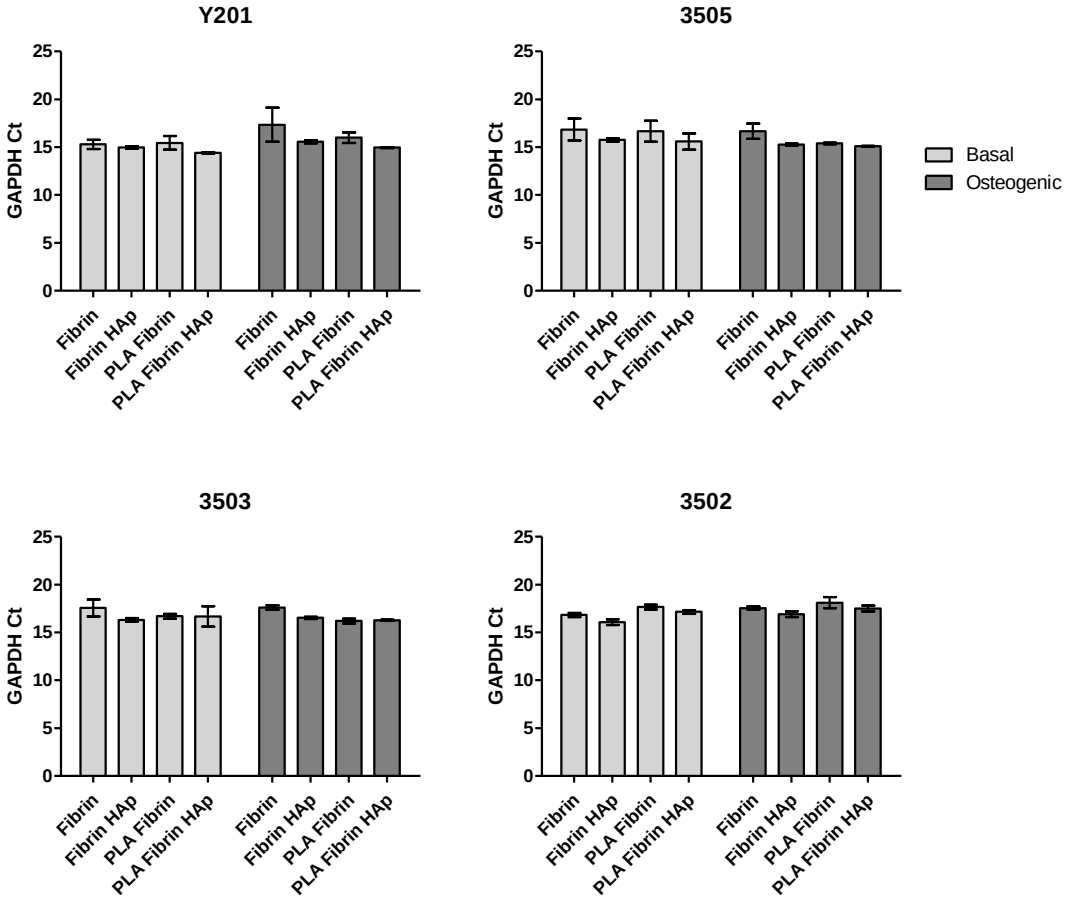

Figure 0-9: Average GAPDH Ct value of hMSC encapsulated in fibrin/HAp with and without PLA cage following 21 days in basal/osteogenic media.

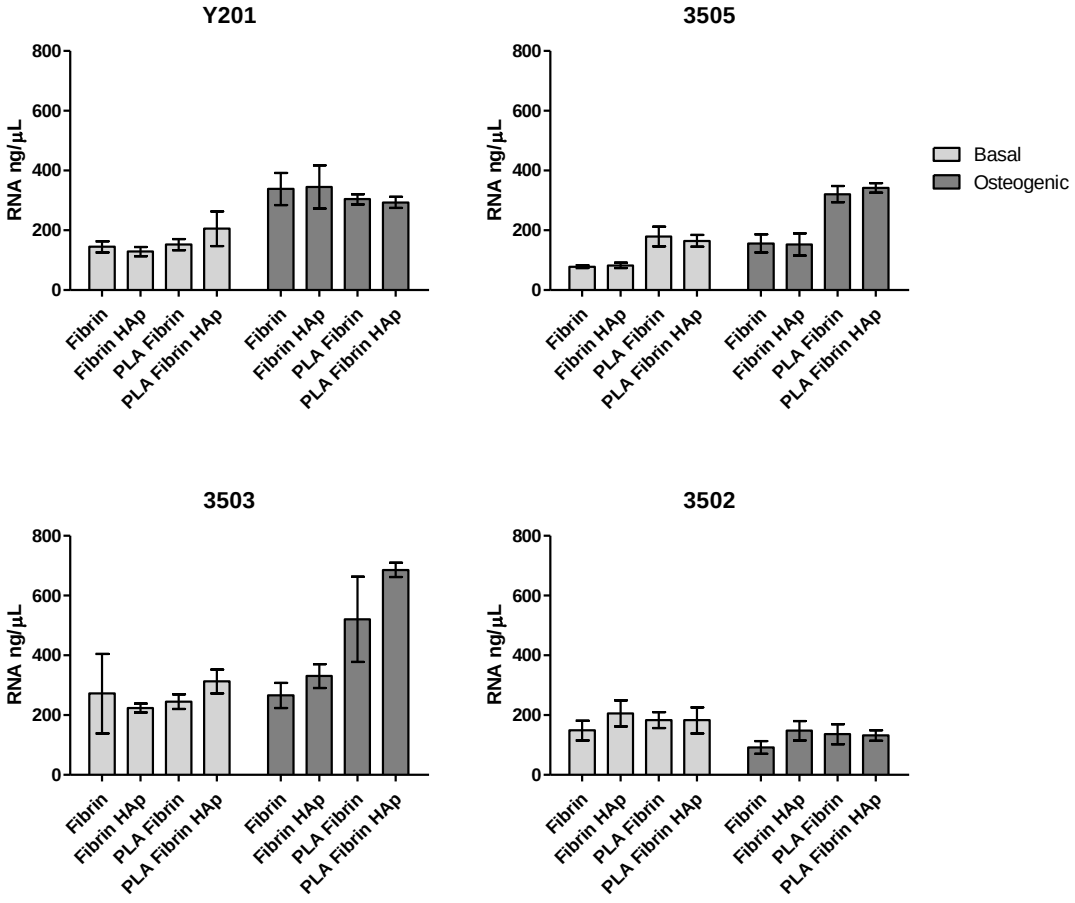

Figure 0-10: Total RNA isolated form hMSC encapsulated in fibrin, fibrin/HAp, PLA fibrin and PLA fibrin/HAp cultivated in basal and osteogenic media for 21 days.

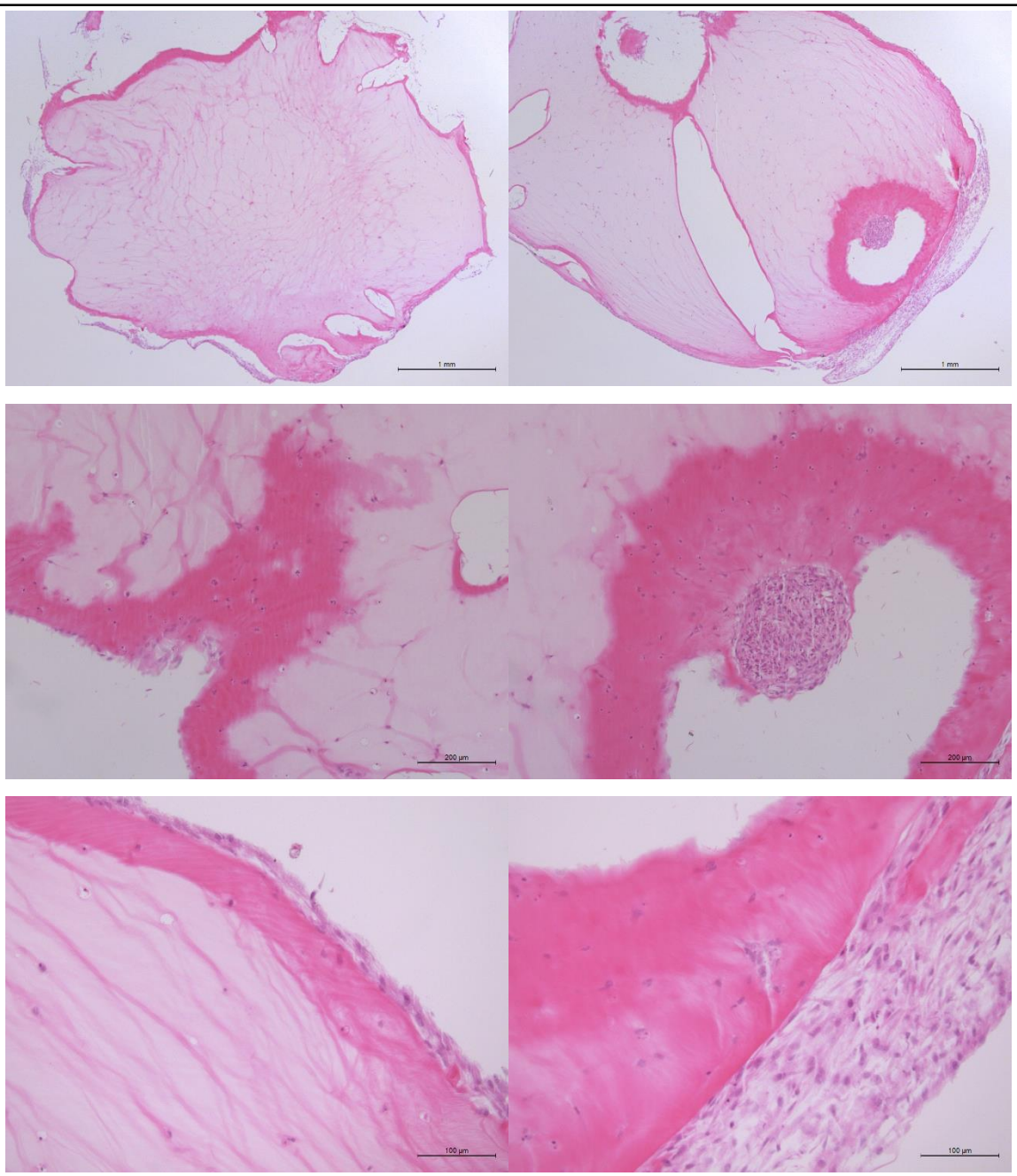

Figure 0-11: Histological Mayer's haematoxylin staining of Y201 hMSC cultured in basal medium for 21 days. FIBRIN

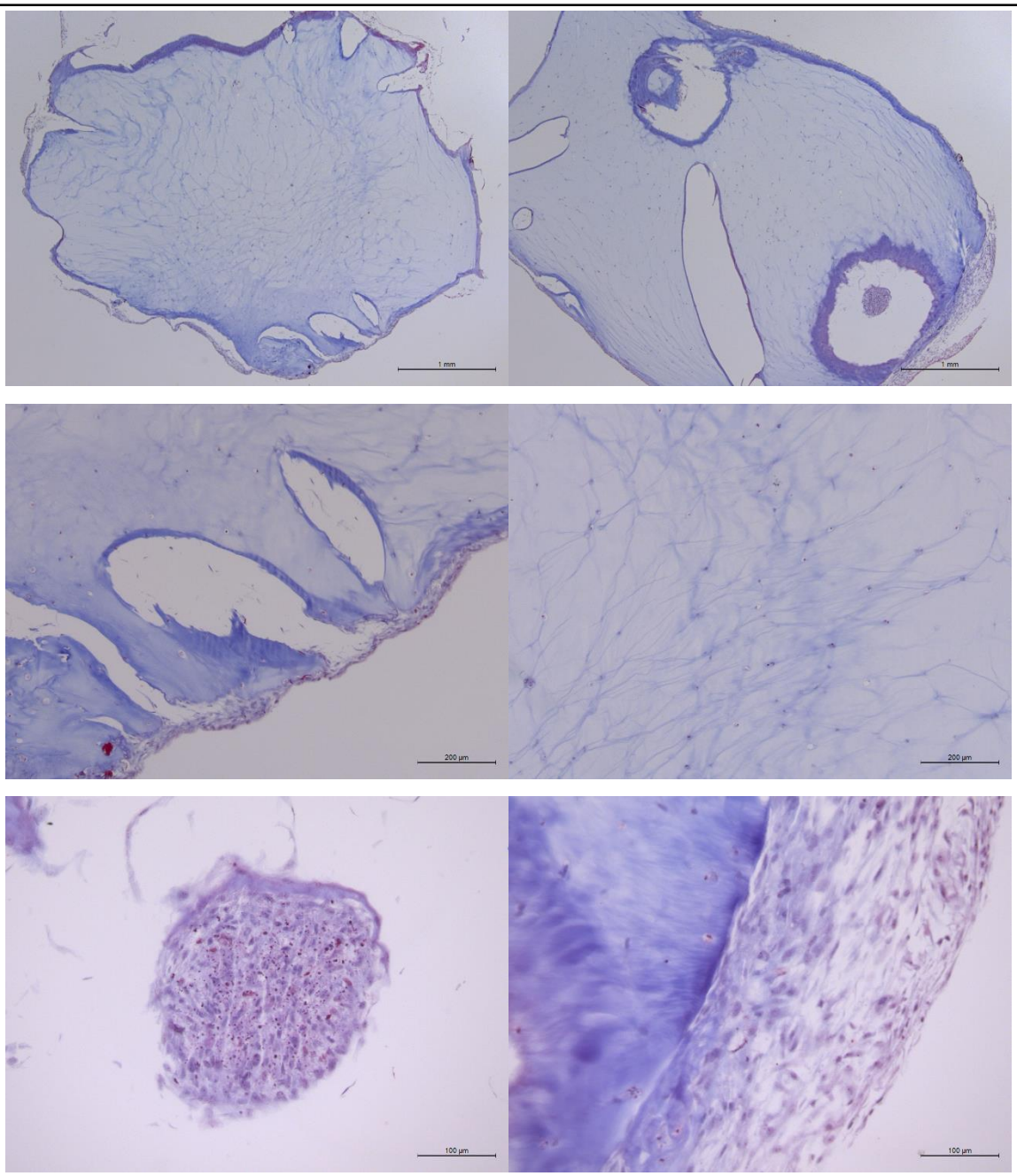

Figure 0-12: Histological Masson's trichrome staining of Y201 hMSC cultured in basal medium for 21 days. FIBRIN

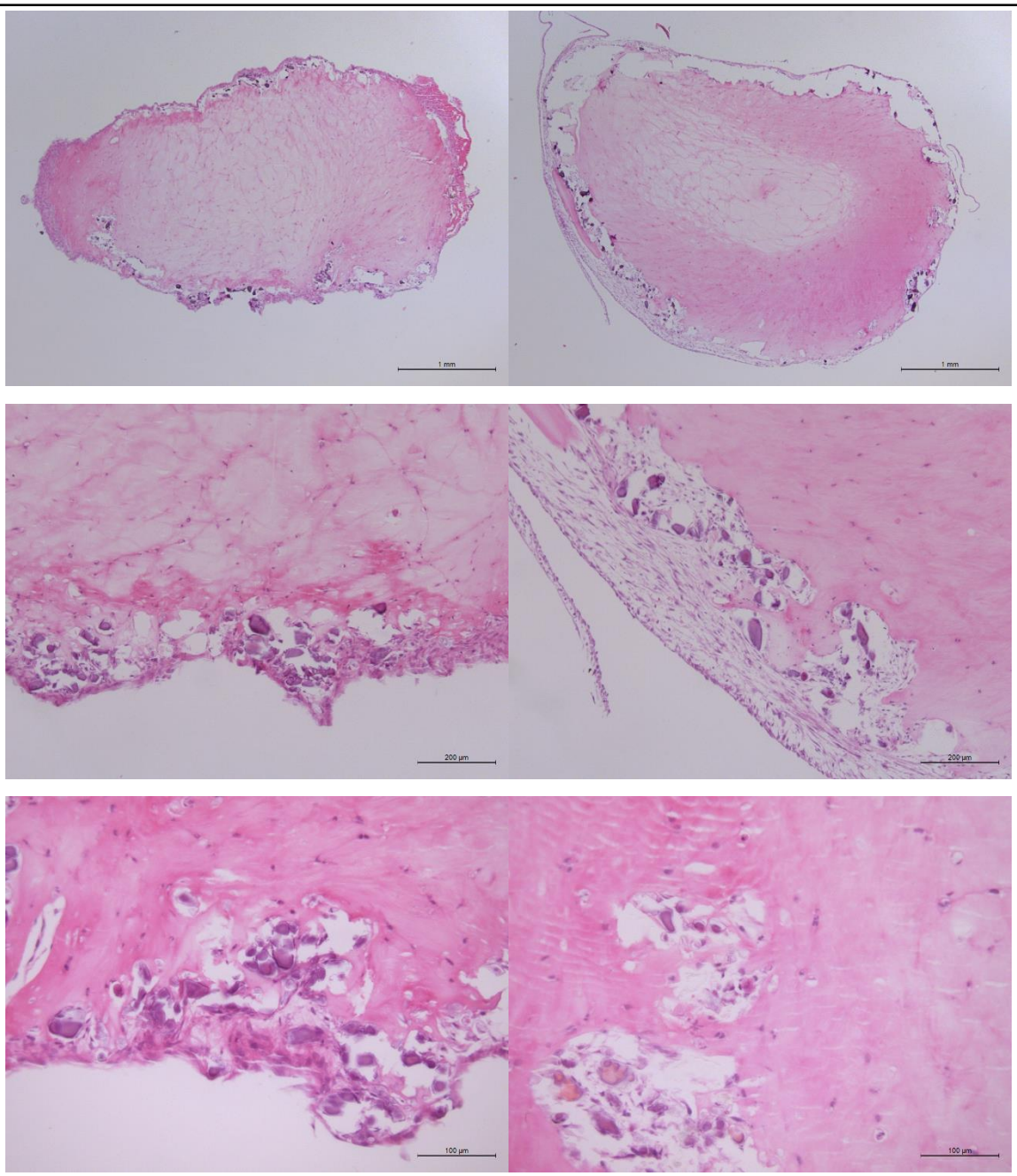

Figure 0-13: Histological Mayer's haematoxylin staining of Y201 hMSC cultured in osteogenic medium for 21 days. Fibrin/HAp

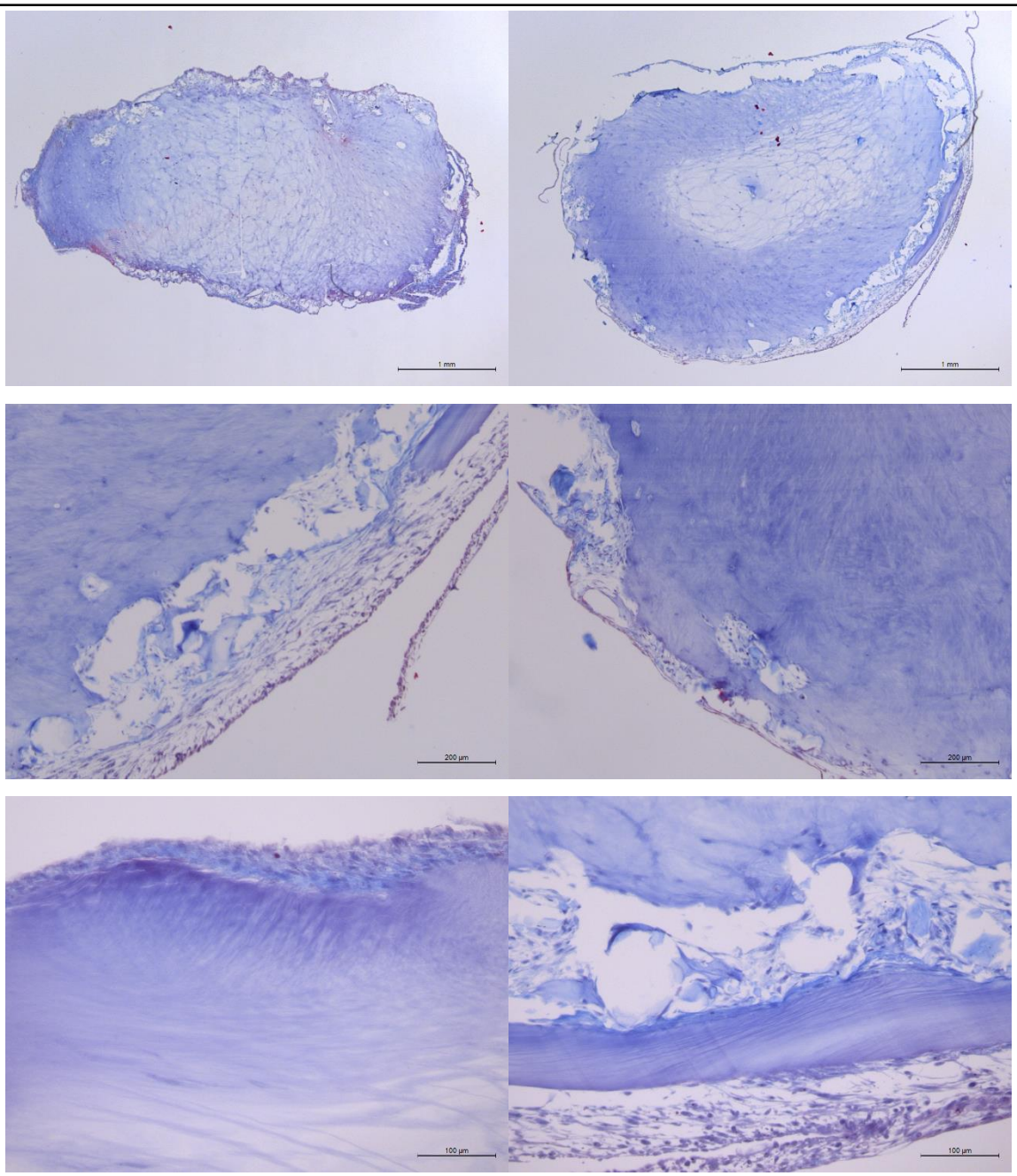

Figure 0-14: Histological Masson's trichrome staining of Y201 hMSC cultured in osteogenic medium for 21 days. Fibrin/HAp

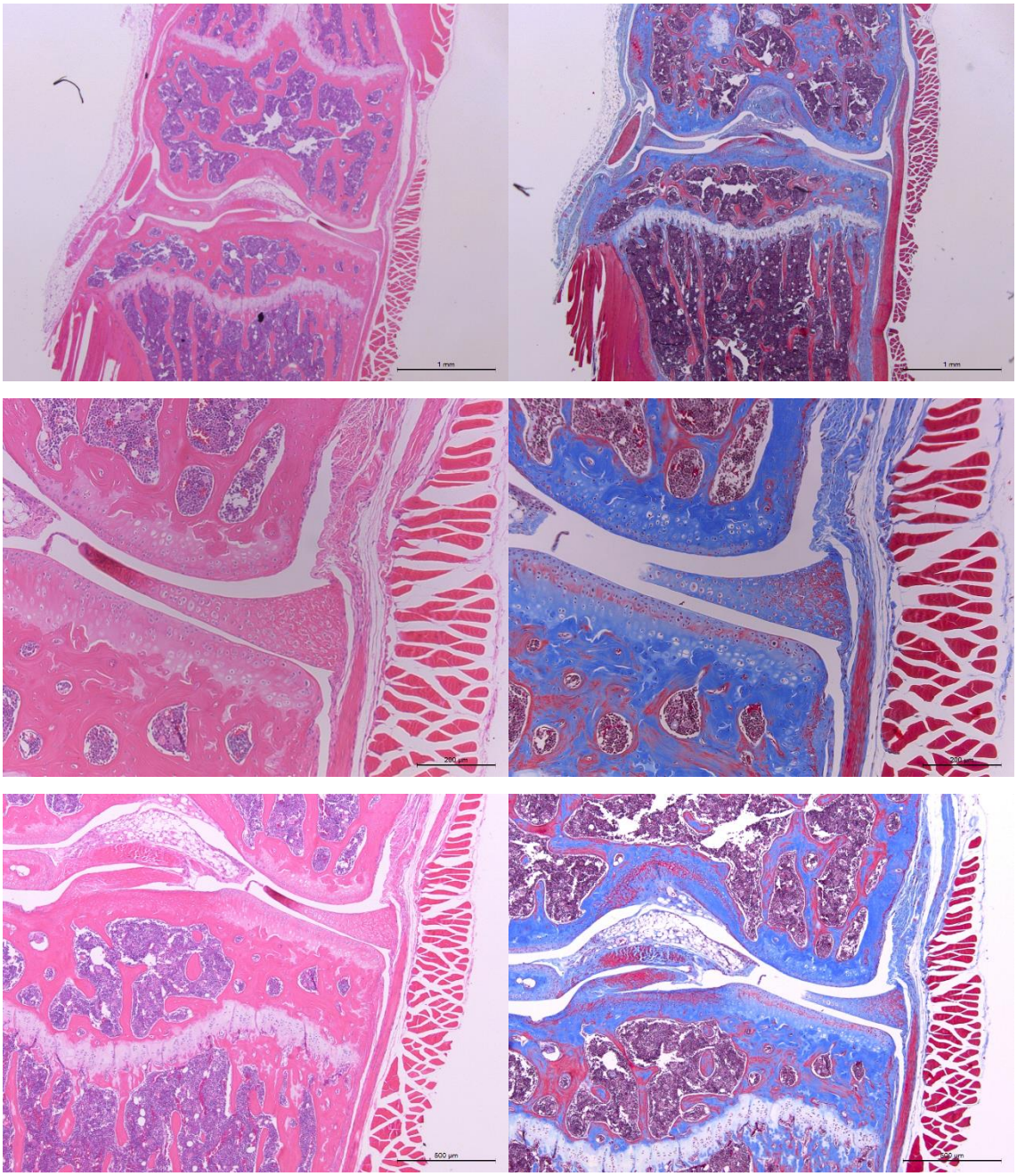

Figure 0-15: Histological staining controls of a rat knee. Left = Haematoxylin and right = Massons Trichrome. 25X, 50X and 100X magnifications.

8.10 Chapter 8

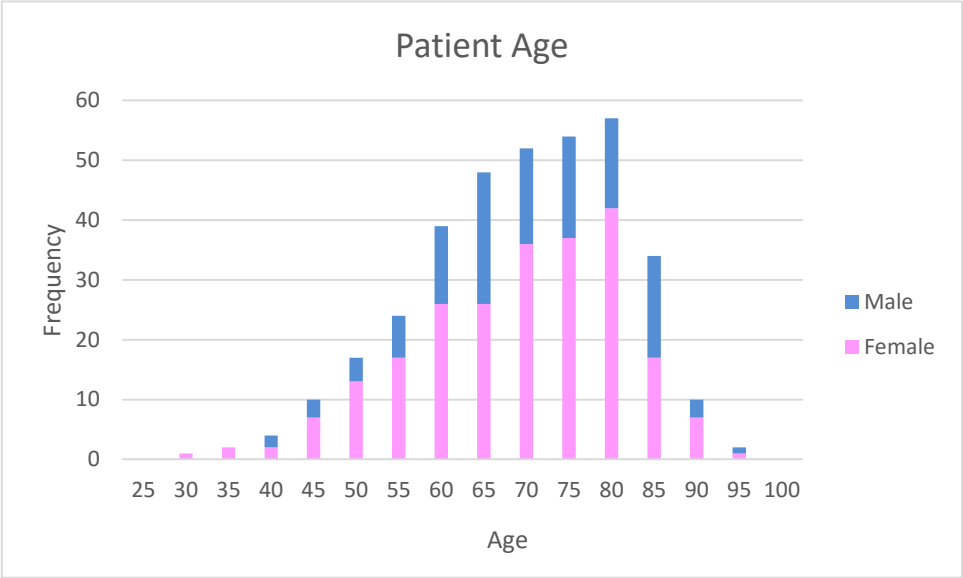

Figure 0-16: Patient age histogram of donated hips for hMSC isolation from 23/07/2012 – 27/03/2015. Female = 66.10 % and male = 33.90%. Range = 26 – 92 years. Average = 67.34 years. n = 354